

Gödöllő

**SZENT ISTVÁN UNIVERSITY**  
**FACULTY OF MECHANICAL ENGINEERING**

---

Release of

TRANS-TRIO SCIENCES



Gent • Gödöllő • Baia Mare

**R&D**

**MECHANICAL ENGINEERING LETTERS**

**2009**

**VOLUME 2**

# **Research & Development**

## **2009**

# Mechanical Engineering Letters, Szent István University

Technical-Scientific Journal of the Mechanical Engineering Faculty,  
Szent István University, Gödöllő, Hungary

Editor-in-Chief:  
Dr. István SZABÓ

Editor:  
Dr. Gábor KALÁCSKA

Executive Editorial Board:

Dr. István BARÓTFI	Dr. István HUSTI
Dr. János BEKE	Dr. Sándor MOLNÁR
Dr. István FARKAS	Dr. Péter SZENDRŐ
Dr. László FENYVESI	Dr. Zoltán VARGA

International Advisory Board:

Dr. Patrick DE BAETS (B)  
Dr. Radu COTETIU (Ro)  
Dr. Manuel GÁMEZ (Es)  
Dr. Klaus GOTTSCHALK (D)  
Dr. Yurii F. LACHUGA (Ru)  
Dr. Elmar SCHLICH (D)

Cover design:  
Dr. László ZSIDAI

HU ISSN 2060-3789  
CD-ROM ISSN 2060-3797

All Rights Reserved. No part of this publication may be reproduced, stored in a retrieval system or transmitted in any form or by any means, electronic, mechanical, photocopying, recording, scanning or otherwise without the written permission of Faculty.

Páter K. u. 1., Gödöllő, H-2103 Hungary  
dekan@gek.szie.hu, www.gek.szie.hu,

Volume 2 (2009)

Release of



## Preface

During the last two decades three co-operating institutes from three European regions carried out many fundamental and experimental researches supporting each other in the field of PhD projects, education and industrial expertizing. This period can be described as mutual engineering interest and assistance that resulted many successful projects and partnership. The joint work was named as:

„GGB Trans-Trio Sciences”  
Gent – Gödöllő – Baia Mare



From Gödöllő, Hungary: Szent István University, Faculty of Mechanical Engineering

From Baia Mare, Romania: University North, Faculty of Engineering

From Gent, Belgium: University Gent, Department of Mechanical Construction and Production

This release of „Mechanical Engineering Letters” contains - under the name of

*„Modelling and Solutions of Industrial Problems” -*

reviewed articles that can specially characterize the ramifying engineering topics in the field of:

- Materials
- Tribology
- Modelling
- Technologies
- Mechanical construction and maintenance

The articles were received and accepted between 1st March and 15th July 2009. They are available on CD ROM and online from [www.geti.gek.szie.hu](http://www.geti.gek.szie.hu).

This special release of „Mechanical Engineering Letters” Volume 2 is announced for the occasion of:

*„Synergy and Technical Development”*  
International Conferences in Agricultural Engineering,  
2009, Gödöllő.

Prof. Gábor KALÁCSKA  
Szent István University,  
Gödöllő  
Hungary

Prof. Patrick DE BAETS  
University Gent  
Belgium

Prof. Radu COTETIU  
North University,  
Baia Mare  
Romania

## Contens

Róbert KERESZTES, László ZSIDAI, Gábor KALÁCSKA, Patrick DE BAETS: Friction of polymer/steel gear pairs	1
Ibolya ZSOLDOS, Gyula KAKUK: Modelling of Carbon Nanotube Junctions	12
Wouter OST, Patrick DE BAETS, Stijn VAN AUTRÈVE, Jeroen VAN WITTENBERGHE, László ZSIDAI, Gábor KALÁCSKA: Tribotesting of large-scale specimens: the necessity of proper design	17
Sándor RAVAI NAGY, Mircea LOBONȚIU, Nicolae MEDAN: Issues on the design and construction of machinery for cleaning and maintenance of sewage system	27
Attila KÁRI-HORVÁTH, István VALASEK, Ibolya ZSOLDOS: The effect of the molecule manipulation on the lifetime of the product	34
Mátyás ANDÓ, Gábor KALÁCSKA, Tibor CZIGÁNY: Shore D hardness of cast PA6 based composites	42
Stijn VAN AUTRÈVE, Wouter OST, Patrick DE BAETS, Mia LOCCUFIER: Experimental investigation of the friction behaviour of engineering plastics on a rotating pin-on-disc type tribotester	47
Rajmund LEFÁNTI, József JANIK, Gábor KALÁCSKA: Plastic machine parts of small airplane: application and failure	56
Mircea LOBONTIU, Georghe Ioan POP, Alina Bianca (POP) BONTIU: Aspects regarding the simulation and the application of the finite element analysis in the designing process of the resistance structure of the adipur waste water treatment plants	61
Ibolya ZSOLDOS: Special algorithm of the Potts-model for the reconstruction of liquid foam structure	69
Attila KÁRI-HORVÁTH, István VALASEK: Machining: some new aspects	75
Koen BONNY, Patrick DE BAETS, Yeczain PEREZ, Jef VLEUGELS, Omer VAN DER BIEST, Bert LAUWERS: Impact of wire EDM on reciprocating sliding friction and wear response of WC based cemented carbides	88
Vasile NASUI, Radu COTETIU, Adriana COTETIU: The praxeologic pattern for the innovation in the field of the industrial actuators	105
Gellért FLEDRICH, István PÁLINKÁS: Machining questions of engineering ceramics (Zirconium-dioxide ZrO <sub>2</sub> )	114
Mátyás ANDÓ, Gábor KALÁCSKA, Tibor CZIGÁNY: The effects of humidity on surface resistance of magnesium catalyzed cast polyamide 6	120

Koen BONNY, Patrick DE BAETS, Yeczain PEREZ, Jef VLEUGELS, Omer VAN DER BIEST, Bert LAUWERS: Influence of secondary electro-conductive phases on the friction and wear response of ZrO <sub>2</sub> -based composites	126
Mircea LOBONȚIU, Alina Bianca (POP) BONȚIU, Gheorghe Ioan POP: The current stage of the cutting process simulation	139
László SZABADI, Lajos PÉK: Hot-dip galvanizing: further challenges	146
Gellért FLEDRICH, Károly PETRÓCZKI: Cutting engineering ceramics with normal edge tool (lathe machining of zirconium dioxide)	150
Quintelier JAN, Ost WOUTER, Patrick DE BAETS: Online monitoring of polymer matrix composites	155
László FÖLDI, László JÁNOSI: Design of electro-rheological flow control valve	161
Marius COSMA, Lucian BUTNAR, Vlad DICIUC, Sever POP The role of the tool path orientations in ball nose end milling	166
Ibolya ZSOLDOS: Loading simulations of nanotube networks	176
Gábor KALÁCSKA, Ottó EBERST, Sever POP, Patrick DE BAETS: Abrasive Wear of Different Polymer/Steel Gear Pairs	190
Jeroen VAN WITTENBERGHE, Patrick DE BAETS, Wim DE WAELE: Analysis of the make-up and break-out behaviour of api line pipe threaded connections	210
István OLDAL, László SZENTESI: Strength analysis of the frame of filter machine	220
Lucian BUTNAR, Marius COSMA, Otto EBERST, Gellért FLEDRICH: The effect of the punch clearance on the punched surface	226
Gyula KAKUK, Ibolya ZSOLDOS, István OLDAL, Ágnes CSANÁDY: The optimal milling energy in a planetary ball mill	232
Péter KAJTÁR, Péter SZENDRŐ, Andreas HAFFERT: Measuring the coefficient of friction of chopped materials	255
Mircea LOBONȚIU, Ciprian MELIAN: The quality of metal surface resulted after cutting with laser	260
László SZENTESI, István OLDAL, Gábor KALÁCSKA: Opportunities of developing cooler-heater system of food industrial tanks	266
Eszter SÁRKÖZI, László JÁNOSI: Ranking of various rapeseed sorts' oils by their fatty acid compositions according to the expectable physical properties	273
Wim VAN PAEPEGEM, Ali REZAEI, Wouter OST, Patrick DE BAETS, László ZSIDAI, Gábor KALÁCSKA: Numerical and experimental analysis of friction of large scale self lubricating radial bearings	277

Zoltán SZAKÁL, Ibolya ZSOLDOS: New algorithm for symmetry recognition in two-dimensional case	289
Gyula KAKUK, Ibolya ZSOLDOS, István OLDAL, Ágnes CSANÁDY: Energetics of the milling process in a planetary ball mill	301
Otto EBERST, Sever POP, Gábor KALÁCSKA, Róbert KERESZTES: Re-constructions with engineering polymers	310
Rajmund LEFÁNTI, József JANIK, Gábor KALÁCSKA: Landing gear leg breakdown and examination	315
Attila KÁRI-HORVÁTH, István VALASEK: Developing directions and utilization technology of cooling-oiling liquids from environmental effects	324



# Friction of polymer/steel gear pairs

Róbert KERESZTES, László ZSIDAI, Gábor KALÁCSKA

Szent Istvan University, Faculty of Mechanical Engineering

Patrick DE BAETS

University Gent, Department of Mechanical Construction and Production

## Abstract

Engineering plastics are often applied in tribological systems, where moving parts are subjected to severe friction and wear processes. Compared to metals engineering plastics are used because of their good friction and wear properties together with increased corrosion resistance and vibration damping ability. There are many sorts of technical polymers available of which sliding elements can be produced. To choose proper polymers for a given tribological application is not a simple task owing to many different parameters influencing the performance of a polymer sliding element.

## Keywords

gear, line of action, coefficient of friction.

## 1. Introduction

In many cases investigations on rigs in laboratory have to be used to reveal the tribological properties of different polymer/metal pairs. In our institutes also many investigations on the tribological properties of technical polymer/steel pairs were performed using different tribometers. It was stated that the ranking of polymer/steel pairs alters according to the friction and wear measured on different tribometers, therefore it would be difficult to choose the best polymer/steel pair to make a polymer gear for a given application. We started to approach of gear mesh with a real gear tests. We concluded that the change of the coefficient of friction during the meshing and the misalignment of gears made difficult to evaluate the actual friction coefficient between the teeth of polymer/steel gears. This problem was solved with the following test system.

## 2. Survey of formulations

The common normal to the tooth profile at the point of contact must always pass through a fixed point called the pitch point in order to maintain a constant angular velocity ratio of the two gears. The involute curve satisfied the law of gearing and is most commonly used for gear teeth profiles in the practice. Data of connecting involute profile gears:

- tooth number:  $z_1 = z_2 = 12$
- module:  $m = 10$  mm
- pressure angle:  $\alpha = 20^\circ$
- face width:  $b = 5$  mm (at polymer segment gear)

We can see from the data, that the used gears are undercut. We chose these gears with large module, because we can measure clearly the changing of force through line of connection. The forces arising from sliding and rolling tooth connection. Therefore we had to modify the addendum circle diameter. The value of maximal addendum circle diameter ( $d_{f\max}$ ):

$$d_{f\max} = 2 \cdot \sqrt{(a_w \cdot \sin \alpha)^2 + \left(\frac{d_o}{2} \cdot \cos \alpha\right)^2} \quad [\text{mm}] \quad (1)$$

where:

- $a_w$  – applied center distance [mm]
- $d_o$  – pitch circle diameter [mm]
- $\alpha$  – pressure angle [ $^\circ$ ]

The calculated engagement factor ( $\varepsilon$ ) with modified addendum circle diameter:

$$\varepsilon = \frac{\overline{AE}}{p_w \cdot \cos \alpha} \quad (2)$$

where:

- $\overline{AE}$  – length of connection section (A - the first, E - the last connection point) [mm]
- $p_w$  – base pitch [mm]

$$\overline{AE} = \rho_{a1} + \rho_{a2} - a_w \cdot \sin \alpha \quad (3)$$

where:

- $\rho_{a1}$  – radius of involute curvature of drive gear at E point [mm]
- $\rho_{a2}$  – radius of involute curvature of driven gear at A point [mm]
- $a_w$  – applied center distance [mm]

$$p_w = \pi \cdot m \quad (4)$$

where:

- $m$  – module [mm]

$$\rho_a = \sqrt{r_f^2 - r_a^2} \quad (5)$$

where:

$r_f$  – addendum radius [mm]

$r_a$  – base radius [mm]

The allowable tangential force  $F_{to\max}$  (N) at the pitch circle of polyamide spur gear can be obtained from the Lewis formula. However, the basic equations used are applicable to all other plastic materials if the appropriate values for the factors are applied.

$$F_{to\max} = m \cdot y \cdot b \cdot \sigma_b \cdot K_v \quad [\text{N}] \quad (6)$$

where:

$m$  – module [mm]

$y$  – form factor at pitch point

$b$  – face width [mm]

$\sigma_b$  – allowable bending stress [ $\text{N}/\text{mm}^2$ ]

$K_v$  – speed factor

The values of different factors can be found in the tables.

The surface strength using Hertz contact stress,  $\sigma_H$ , is calculated by this equation

$$\sigma_H = \sqrt{\frac{F_{to}}{b \cdot d_o} \cdot \frac{i+1}{i}} \cdot \sqrt{\frac{1.4}{\left(\frac{1}{E_1} + \frac{1}{E_2}\right) \cdot \sin 2\alpha}} \quad [\text{N}/\text{mm}^2] \quad (7)$$

where:

$F_{to}$  – tangential force on surface [N]

$i$  – gear ratio

$E_1, E_2$  – modulus of elasticity of material [ $\text{N}/\text{mm}^2$ ]

$\alpha$  – pressure angle [ $^\circ$ ]

The arising sliding velocity between contact teeth is difference of the tangential velocities ( $v_t$ ).

The sliding velocity determine the frictional heating and wear of teeth.

The  $v_s$  sliding velocity:

$$v_s = v_{t1} - v_{t2} \text{ OR } v_s = s \cdot (\omega_1 + \omega_2) \quad (8)$$

where:

$s$  – distance between pitch point and contact point on line of action [mm]

$\omega_1, \omega_2$  – angular velocity [rad/s]

Kozma earlier studied the friction phenomena between the gears and found that the forces and torque during the connection changed due to the friction. He distinguished two cases: the change of the teeth-force and torque in case of constant drive torque, and the change of teeth-force and torque in case of

constant driven torque. The latter can be seen in *Fig. 1*. In his theoretical studies he took constant friction between the surfaces, however we know from our previous research projects and from the literature that the friction between a polymer and steel surfaces was nearly never constant.

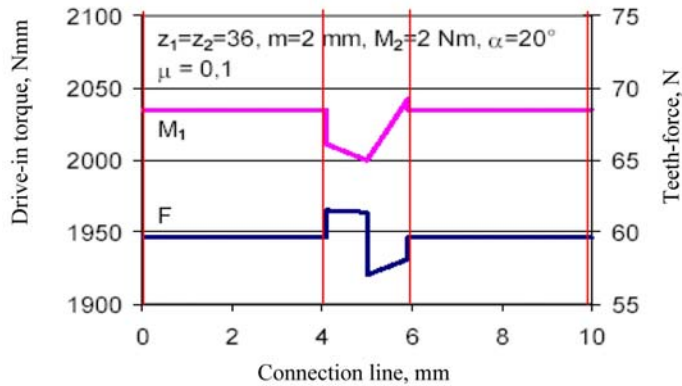


Figure 1. The theoretical change of teeth-force and torque during the connection line in case of constant driven torque and constant friction.

### 3. The test systems

We made a new gear connection test rig. The new test method (*Fig. 2.*) using large teeth was developed to measure the influence of friction on the tooth forces. In this method the rotation is limited; the variation of forces is measured during only one meshing cycle of a tooth pair. The three-teethed segments were made of the investigated polymers, but the mating steel gear must be prepared in full size due to balancing reasons.

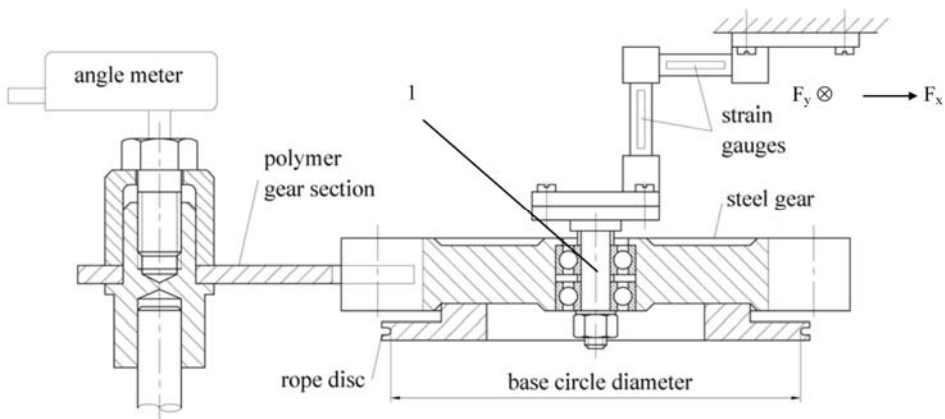


Figure 2. Drawing of test rig

### Measured and calculated forces

The forces on the axle 1 of steel gear ( $F_x$ ,  $F_y$ ) were measured with strain gauges, as it is shown in *Fig. 2*. The normal force ( $F_N$ ) was equal the applied load force ( $F_g$ ), because each line of forces were same.

If we consider the effect of friction along the connection section, it's clear that the direction of friction force changes at the pitch point (*Fig. 3*).

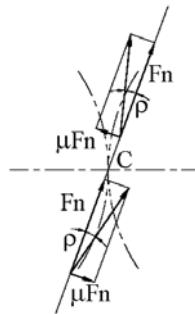


Figure 3. Influence of friction

The value of friction force is altering during tooth connection. We can evaluate it using the following phenomena. The value of normal force is equal to load force divided by two in the two teeth connection sections (AB and DE sections)  $F_n = F_g/2$  [N]. The arising friction forces ( $F_s$ ) are in both connecting point (*Fig. 4*.) but having opposed directions, so, they cause a torque breaking the rolling movement. This torque can not be measured correctly with our technical system.

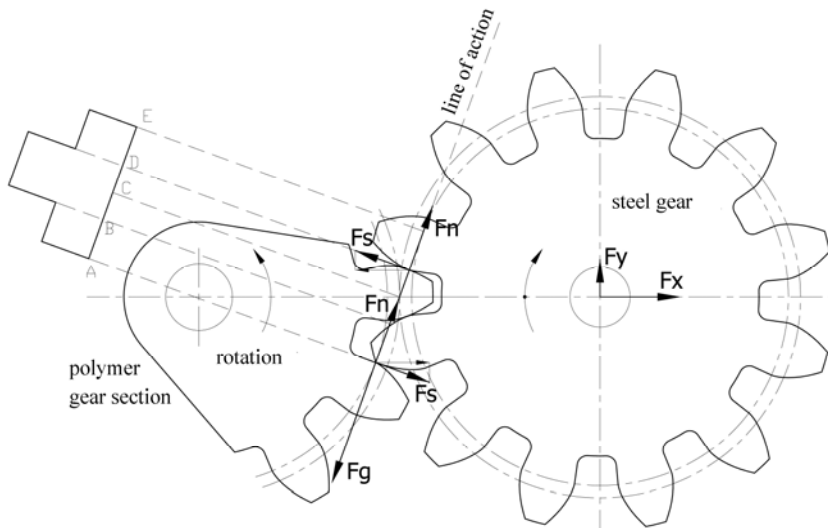


Figure 4. The arising forces at two teeth connection

There are two different section under one tooth connection. The pitch point (C) is in the center position. The value of normal force is equal to load force  $F_n = F_g$  [N]. There is a relationship between the friction force and the measured axle force (Fig. 5.). The axle force increasing until pitch point and decreasing after it. We can evaluate their relationship using the following equations:

in BD connection section:

$$F_x = F_s \cdot \cos \alpha \quad (9)$$

where:

$F_x$  – measured axel force [N]

$\alpha$  – pressure angle [°]

$F_s$  – friction force [N]

$$F_s = \frac{F_x}{\cos \alpha} \quad [N] \quad (10)$$

In this system we define a coefficient of friction between contact teeth. It is calculated by this equation.

$$\mu = \frac{F_s}{F_n} = \frac{F_x}{F_n \cdot \cos \alpha} \quad (11)$$

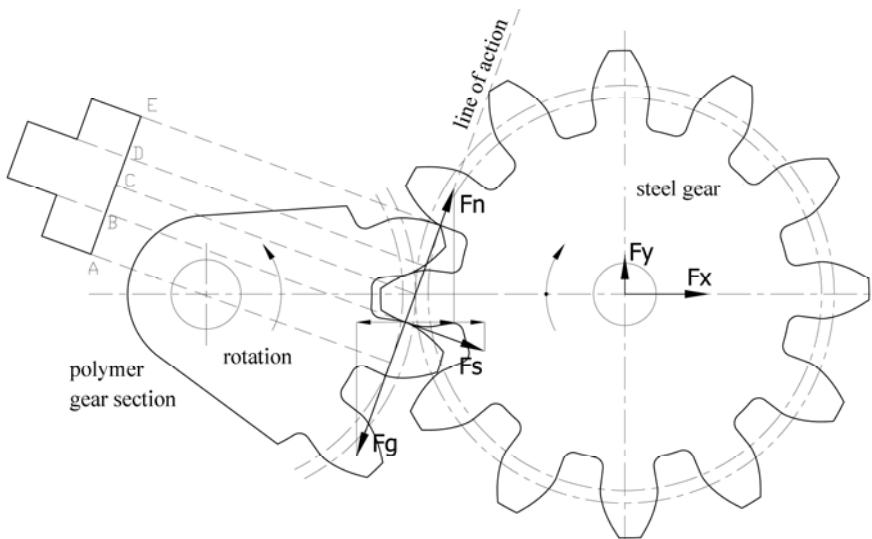


Figure 5. The arising forces at one tooth connection

At the *table 1*. we show the testing conditions.

Table 1. Parameters of the tests

Parameters	Tooth connection model tests
load, M [Nm]	1.1 / 5.5
angular velocity, $\omega$ [1/s]	0.1
test time, cycle	1 / 100 / 500 / 1000 / 2000 cycles
ambient temperature, T [°C]	24 °C
Relative humidity, RH [%]	50 %

### Tested materials

The properties of the investigated polymers are presented in the Table 2. The gear mating with polymer gears was made of structural steel S355 with a surface finish (CLA)  $R_a$  2,5  $\mu\text{m}$ .

Table 2. Properties of investigated polymers

Polymer	Elongation at rupture A (%)	Young modulus E (MPa)	Rockwell M hardness	Tensile strength $R_m$ (MPa)
PA 6G-Mg	40	3000	86	85
PA 6G-Na	25	3300	88	80
PA 66 GF30	7	5200	98	185
POM C	30	3000	86	70
PETP /PTFE	8	3200	94	75
Bakelite		7000	98	80

## 4. Results and discussion

Because of the large number of experiments and continuous monitoring of gear mesh friction many different graphs can be drawn about teeth surface processes.

As we have explained earlier in the test system the motion of the measurements were reciprocating (towards – upload, backwards –down load) between the mating teeth and from each cycle the upload process under „one-tooth” connection was grabbed to evaluate.

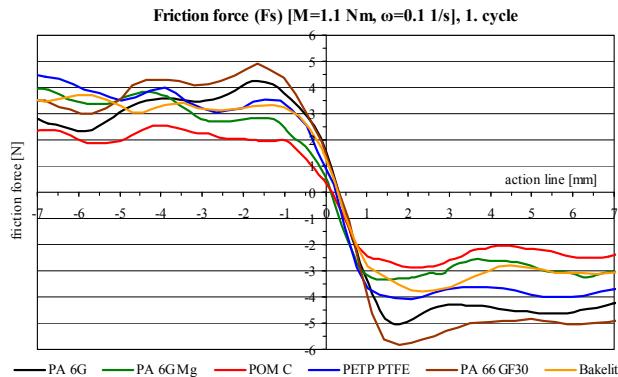


Figure 6. Friction forces during the first test cycle

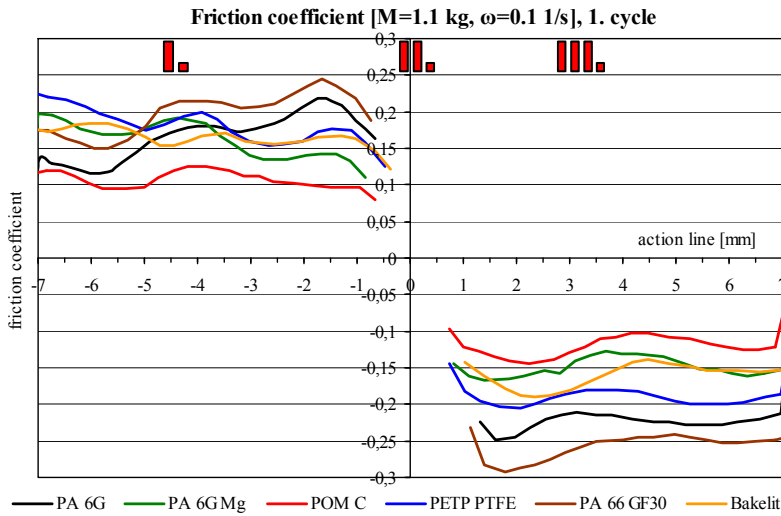


Figure 7. The calculated friction coefficients during the first test cycle

Fig.6. shows a summary about the measured friction force during the first cycle of drive in case of six different polymer materials meshing with S355 structural steels. The role of pitch point is very spectacular.

At the beginning of the measurements the POM-C performed the lowest friction and PA 66 GF30 gave relatively high friction force. If we compare the two cast polyamide versions - Na and Mg catalytic types – essential difference can be realized. The Mg catalytic cast polyamide 6 material is better performing much lower friction force.

In Fig.7. the calculated friction coefficients are shown. The main difference between the curves plotted in Fig 6. and Fig.7. is the domain. While friction forces are drawn as continuous functions along action line, curves of friction coefficients are interrupted at pitch point and its transition zone. The reason is the origin of friction movement. At pitch point and its transition zone the dominant form of friction is rolling instead of sliding. Before and after pitch point zone the friction is generated mainly from sliding, the rolling friction effect is much lower.

That means along the action line the friction form can be split to:

- I. – sliding zone before pitch point with decreasing sliding speed to reach pitch zone
- II. – pitch transition zone with mainly rolling movement
- III. – sliding zone after pitch point with increasing sliding speed leaving pitch zone

For further evaluation of gear mesh friction coefficient curves we introduce more values according to Fig. 8.

As an example of the evaluations Fig.9. shows the change with cycle numbers of local maximum friction coefficient values for the different polymer materials.

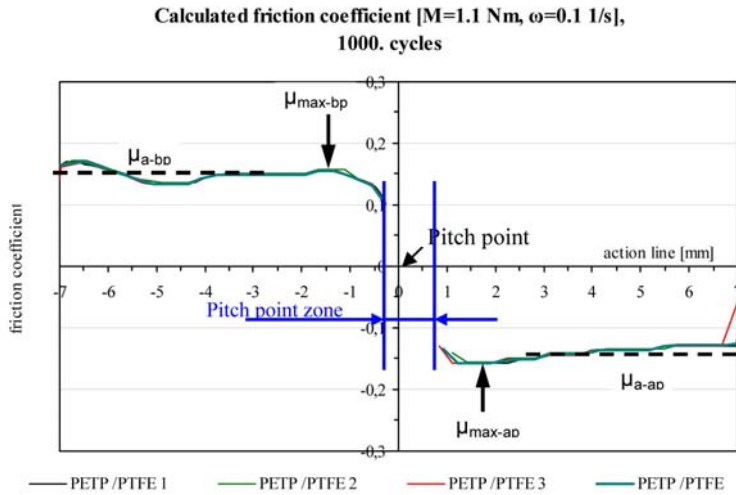


*Figure 8.* The calculated friction coefficients during the first test cycle  
 $\mu_{a-bp}$ : average friction coefficient before pitch zone,  $\mu_{max-bp}$ : local maximum of friction before pitch zone,  $\mu_{max-ap}$ : local maximum of friction after pitch zone,  $\mu_{a-ap}$ : average friction coefficient after pitch zone

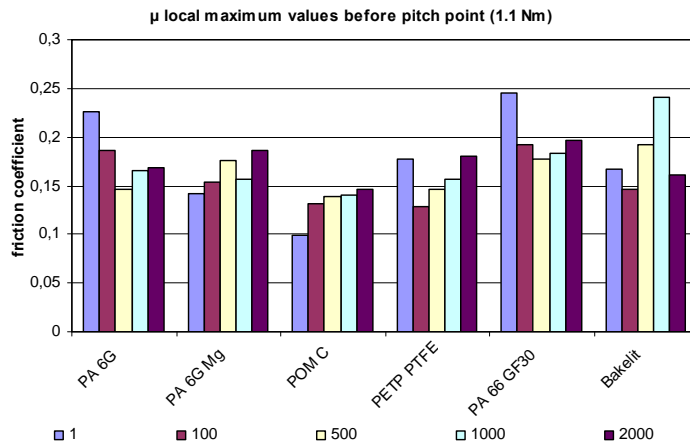


*Figure 9.* Local maximum values of friction before pitch zone under different cycle numbers

If we follow the different behaviour of friction values in the function running distance (number test cycles) we can distinguish four different groups.

1. Materials performing basin-like curves or columns (PA 6G, PETP/PTFE, PA 66 GF30, in *Fig 9.*): with increasing meshing time the friction first decreasing but after a certain running cycle it starts to elevate.
2. Material with continuously increasing friction with increasing meshing time (POM C in *Fig 9.*): according to the test condition (load and speed)

the function of friction increasing with different slopes during the gear mesh.

3. Material with low difference increasing tendency (PA 6G Mg)
4. Stochastic-like friction results with large differences in friction coefficients (bakelite)

Regarding the absolute values of friction coefficient in *Fig 9*, we can find POM C and PETP/PTFE the best ones. Comparing the two cast polyamide types we can state that the Na catalytic cast Pa (PA 6 G) performed higher friction than PA 6 G Mg.

## 5. Conclusions

- The developed test method is useful to study the friction process along the action line under „one-tooth” connection phase between polymer/steel gears.
- The theoretical friction can be discovered more in depth and described with a given friction pairs.
- The friction changes along the action line.
- The trends also change in the function of load and meshing time (test cycles)
- Different changing trends of friction means different change of efficiency of polymer/gear drive. In our database we set these trends.
- Pitch point rolling effect in the practice means pitch zone. The width of the pitch zone is different with different friction pairs due to the different adhesion and deformation.
- The comparison of local maximum friction and average sliding friction values gives information about „even” or „un-even” running of mesh, the sensitivity for „stick-slip” behaviour of gear drive. Where we find local maximum friction to be much higher to average friction values, that means potential „stick-slip” danger. That is typical for PA 6G under light load.
- Based on our new research method we discovered more material- and system-specific phenomena with polymer/steel gear pair friction and our new database can help to design and maintain such a kind of gear drives.

## 6. Acknowledgements

The research was supported by OTKA T42511, OTKA T37244, OTKA NI 62729 and Tét B-1/04 research funds.

## References

Antal – Fledrich – Kalácska – Kozma: *Műszaki műanyagok gépészeti alapjai, Műszaki műanyagok gépészeti alapjai*, Minerva-Sop Bt. Sopron, 1997

---

Benedict, G.H., and Kelley, B.W.: Instantaneous Coefficients of Gear Tooth Friction. ASLE Transactions, Vol. 4, No. 1, 1961. p. 59–70

Brian Rebbechi, Fred B Oswald, Dennis P. Townsend: Measurement of Gear Tooth Dynamic Friction. NASA Technical memorandum 107279, Army Research Laboratory, 1996

Kozma Mihály: A fogaskerekek súrlódási vesztesége. Gép okt. – nov., 2004

[www.quattroplast.hu](http://www.quattroplast.hu)

Yamaguchi Yukisaburo: Tribology of plastic materials. Amsterdam: Tribology series 16, Elsevier, 1990

# Modelling of Carbon Nanotube Junctions

Ibolya ZSOLDOS, Gyula KAKUK

Szent Istvan University, Faculty of Mechanical Engineering

## Abstract

Theoretical calculations prove that carbon nanotube junctions having optional number, type (zigzag or armchair), length and diameter of tubes are stable. The most characteristic examples (Y, T, X, tetrahedral, octahedral and icosahedral junctions) are studied in this work.

## Keywords

nano, carbon-tubes, modelling, junctions

## 1. Introduction

The straight carbon nanotubes have excited worldwide interest since their discovery in 1991 because of their exceptional mechanical and electrical properties. The straight carbon nanotubes consist of two basic groups: single-wall and multiwall nanotubes. The straight single-wall carbon nanotube is a configuration created by the perfect cylindrical rolling of a single atom-thick graphite-layer (graphene). The single-wall carbon nanotubes are the strongest of all materials presently known. The multiwall carbon nanotube is made up of multiple singlewall tubes placed concentrically into one another. Singlewall carbon nanotubes can be grouped into three categories depending on the mode of their graphite-layer rolling: armchair, zigzag and chiral nanotubes. The mode of rolling influences the electrical properties of singlewall nanotubes: all armchair configuration nanotubes have metallic attributes, only every third of the zigzag nanotubes has metallic attributes while others have semiconductor ones. Shortly after the discovery of straight nanotubes it was shown that further nanostructures can be built if pentagons and heptagons are also built into the hexagonal graphite structure: nanotube Y-junctions, bends, T-junctions, toruses and coils. First multiwall and then singlewall carbon nanotube coils were studied experimentally, and then were followed by various symmetrical and asymmetrical Y-junctions. Metallic and semiconductor nanotubes can be connected into one another by forming a bend which results in nanometric-sized diodes. The existence of the characteristic double or manifold nanospirals resembling the structure of DNS was also proved.

The rolling mode and the properties of various formations consisting of pentagons, hexagons and heptagons have been surveyed in the same way as to the straight nanotubes rolling from a planar hexagonal formation. The tube

structures consisting of pentagonal, hexagonal and heptagonal – so called haeckelite or azulenoïd – units can form different configurations.

One of the most interesting tasks in the production of carbon nanotubes is making junctions. One possible method of producing junctions is the connection of carbon nanotubes by chemical reactions. It has been shown that during the necessary cleaning at the time of their production, different functional groups containing oxygen appear at the ends of the opened nanotubes. The various T, Y, X-junctions are connected with these functional groups and with the functional groups produced on the nanotube casing by chemical reactions.

In this study we prove that carbon nanotube junctions having optional number, type (armchair or zigzag), length and diameter of tubes are stable.

## 2. Most typical junctions

In a previous work we demonstrated that carbon nanotube junctions consisting of optional number, type (zigzag and/or armchair) length and diameter of tubes can exist. A method for the geometric construction of their models has been shown. In this paper we show DTMM models and numerical results in the cases of the most characteristic examples (T, Y, X, tetrahedral, octahedral and icosahedral junctions).

In the DTMM (Desktop Molecular Modeller) system models of stable molecules can be created. The modelling method is based on molecular dynamics. In Figure 1 the DTMM models of T, Y, X, tetrahedral, octahedral and icosahedral junctions (with closed tube-ends) can be seen. The carton models (with opened ends) are displayed near the DTMM models.

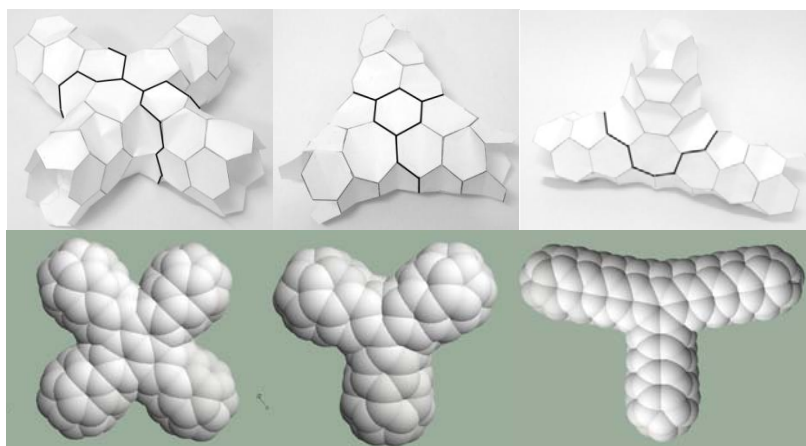
In Figure 2 the cohesive energy of the modelled junctions can be seen. The values of the cohesive energy were computed using the Stillinger-Weber potential [29]. In the case of the larger junctions (tetrahedral, octahedral and icosahedral) the value of the cohesive energy is between the values of the stable fullerene (C60) and graphene structures. In the case of the smaller junctions (X, T and Y) the value of the cohesive energy is a bit higher than the value of C60.

## 3. Conclusions

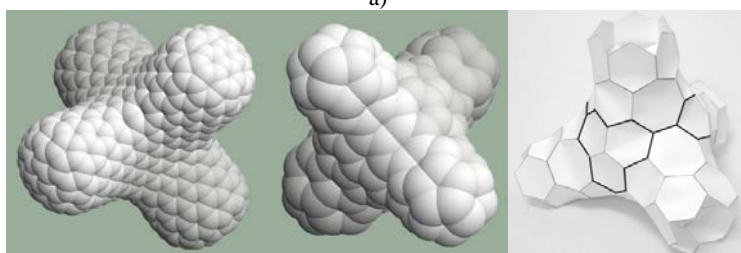
Molecular dynamic and energetic calculations prove that a set of new carbon nanostructures (the carbon nanotube junctions) are stable. The measured diode-like behaviour on a definite tubular structure [17] reassure us to expect other electronic devices based on the set of the new carbon nanotube junctions in the nanoscale range.

## 4. Acknowledgements

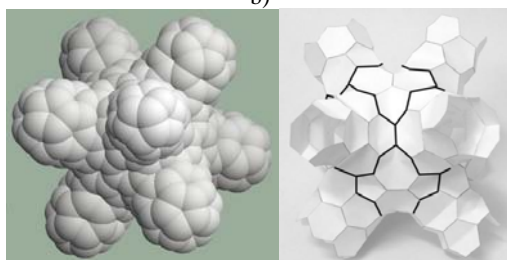
This work was supported by OTKA grants K 73776 in Hungary.



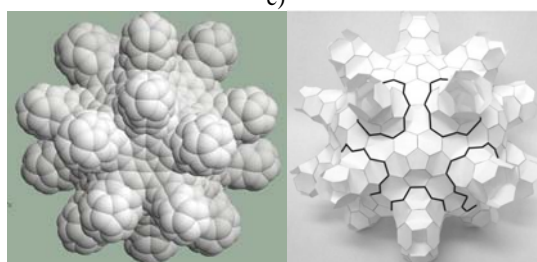
a)



b)



c)



d)

*Figure 1.* a: Carton and DTMM models of T, Y and X junctions. b: From left to right: carton model of a tetrahedral junction having two zigzag and two armchair type tubes, DTMM model of the same junction and DTMM model of a tetrahedral junction having larger diameter of tubes. c: Carton and DTMM models of an octahedral junction having four zigzag and four armchair type tubes. d: Carton and DTMM models of an icosahedral junction having ten zigzag and ten armchair type tubes.

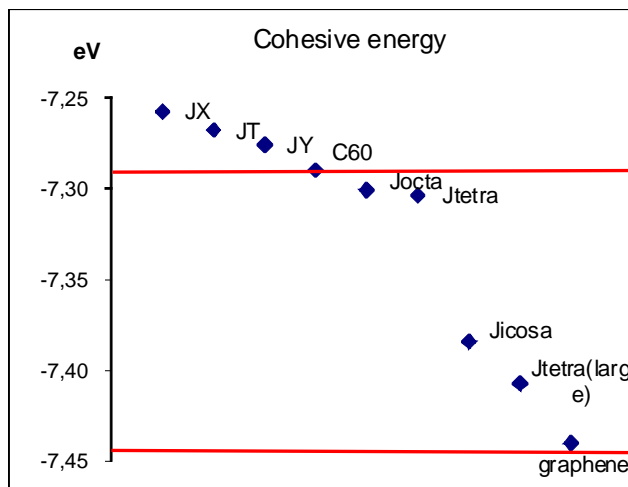


Figure 2. Cohesive energy of several carbon nanostructures: JX: X junction (Fig. 1a), JT: T junction (Fig. 1a), JY: Y junction (Fig. 1a), Jocta: octahedral junction (Fig. 1c), Jtetra: tetrahedral junction (Fig. 1b), Jicosa: Icosahedral junction (Fig. 1d), Jtetra(large): tetrahedral junction having larger diameter of tubes (Fig. 1b).

## References

- S. Iijima, Nature: 345, 56-58, 1991
- M.M.J.Treacy, T.W.Ebbesen, J.M.Gibson, Nature: 381, 678-680, 1996
- R.Saito, M.Fujita, G.Dresselhaus, M.S.Dresselhaus, App. Phys. Lett: 60, 2204-2206, 1992
- J.W.Mintmire, B.I.Dunlap, C.T.White, Physical Review Letters: 68, 631-634, 1992
- G.E.Scuseria, Chemical Physics Letters: 195, 534-536, 1992
- L.A.Chernozatonskii, Physics Letters A: 172, 173-176, 1992
- A.N.Andriotis et al., Applied Physics Letters: 79, 266-268, 2001
- B.I.Dunlap, Physical Review B. 46, 1933-1936, 1992
- I.Ponomareva et al., New Journal of Physics: 5, 119.1–119.12, 2003
- M.Menon, D.Srivastava, Physical Review Letters: 79, 4453-4456, 1997
- S.Ihara, S.Itoh, J.Kitakami, Physical Review B. 47, 12908-12911, 1993
- S.Ihara, S.Itoh, J.Kitakami, Physical Review B. 48, 5643-5647, 1993
- S.Amelinck et al., Science 265, 635, 1994
- L.P.Biró et al., Europhysics Letters. 50, 494-500, 2000

- L.P.Biró et al., *Diamond and Related Materials*. 11, 1081-1085, 2002
- Z.Osváth et al., *Chemical Physics Letters*. 365, 338-342, 2002
- Z.Yao, H.W.Ch.Postma, L.Balents, C.Dekker, *Nature*. 402, 273-276, 1999
- L.P.Biró et al., *Physical Review B*. 66, 165405-1 - 165405-6, 2002
- C-J.Su, D.W.Hwang, S-H.Lin, B-Y.Jin, L-P.Hwang, *Phys.Chem.Comm.* 5, 34-36, 2002
- D.Y.Ding et al., *Chemical Physics Letters*. 371, 333-336, 2003
- H.Terrones et al., *Physical Review Letters*. 84, 1716-1719, 2000
- I.László, A.Rassat, *International Journal of Quantum Chemistry*. 84, 136-139, 2001
- Ph.Lambin, G.I.Márk, L.B.Biró, *Physical Review B*. 67, 205413-1 - 205413-9, 2003
- Y.Zhang, Z.Shi, Z.Gu, S.Iijima, *Carbon*: 38, 15, 2055-2059, 2000
- Z.Kónya et al., *Chemical Physics Letters*. 360, 5-6, 429-435, 2002
- A.A. Koós et al., *Mat. Sci. Eng. C*, 23(6-8), 1007-1011, 2003
- F. Frehill et al., *J. Am. Chem. Soc.*, 124, 13694-13695, 2002
- I. Zsoldos et al., *Modelling and Simul. in Mater. Sci. and Eng. Ref: MSMS/180078/PAP/53960*
- F.H.Stillinger et al., *Physical Review B* 31, 5262, 1985, B 33, 1451, 1986

# **Tribotesting of large-scale specimens: the necessity of proper design**

Wouter OST, Patrick DE BAETS, Stijn VAN AUTRÈVE,  
Jeroen VAN WITTENBERGHE,  
University Gent, Department of Mechanical Construction and Production  
László ZSIDAI, Gábor KALÁCSKA  
Szent Istvan University, Faculty of Mechanical Engineering

## **Abstract**

Tribological tests have always been difficult and expensive to run, as the tests should as closely as possible mimic the application (Czichos, 1982). This has a number of implications: the tests cannot be sped up by applying higher contact pressure and/or velocity and the geometry and the environment of the test should match those of the application. Nonetheless most of the tribological tests are performed at small scale to minimize the cost of testing. This paper elaborates on the reasons why small scale testing, done on the cheap, often results in expensive mistakes.

## **Keywords**

Large scale, testing, tribology, bearing, radial bearing, polymer

## **1. Introduction**

There are a solid number of reasons to prefer small scale testing in tribology. Small scale testing is easier, test-rigs are cheaper, specimens are cheaper, handling of specimens and mounting is easier, tests can be performed faster and so on. Large scale testing is cumbersome and expensive. Nonetheless this paper will show that for a multitude of reasons it is a necessary bother as many effects in tribology cannot be scaled down.

This paper focuses on large scale civil and marine applications in which lubricating tribological contacts is often impossible or impractical. For these applications a number of self-lubricating materials are currently available, which provide benefits as low cost, no pollution due to lubricants and low maintenance. The traditional materials for these applications are bronze sintered with solid lubricant and bronze with holes in the surface filled with a solid lubricant (pockets). Nowadays more and more fibre (glass, carbon, polyester) reinforced polymer bearings are used, because they exhibit a lower coefficient of friction, are resistant to corrosion and are less sensitive to edge stresses resulting from misalignment of the bearing.

## 2. Maeslantkering (Netherlands)

The Maeslantkering which is the final part in a series of locks, gates bridges and dams built in the Netherlands which started after the breach of a number of dikes during spring tide in 1953. The Maeslantkering (commissioned in 1997) on the Nieuwe Waterweg (connecting the port of Rotterdam to the North Sea) is the last in this series.



*Figure 1. Aerial view of the maeslantkering (size indicated)*

Figure 1 shows an aerial view of the Maeslantkering, which consists of two circular walls connected by pylons to the abutments. When the lockgate is closed the walls are floated out into the channel and sunk. This implies that the connection of the pylons to the abutments should allow for two degrees of freedom in rotation.

The joint at the end of the pylons was designed as a large ball in socket joint (diameter 10 meters), in which a cast steel ball slides in a faceted cast steel socket. Both the ball and the socket were covered with a lacquer containing solid lubricant, to prevent steel to steel contact and adhesive wear. During test closings of the lock gate it was noticed however that steel on steel contact (and large adhesive wear and cold welding) occurred. So a new material choice was necessary. The requirements for the new material were stringent. As the new material could only be implemented as circular pads in round pockets, the contact pressure for the new design would be 150 MPa (original design pressure 30 MPa). Secondly the coefficient of friction should preferably be below 0.15 (absolute limit 0.25). In light of these requirements the best solution would be to select a polymer or a polymer composite with low coefficient of friction, but to provide for reinforcement features as the compressive strength of polymers and composites is normal below or far below 150 MPa.



Figure 2. UHMWPE with carbon fibre reinforcement ring.

After a number of static tests the following design was proposed for the pads: a UHMWPE disc with a diameter of 300 mm, fixed in a wound carbon fibre reinforcement ring to prevent sideways plastic flow of the UHMWPE. For these pads the coefficient of friction and the wear rate had to be determined. Due to the large contact pressure of 150 MPa and the combination of tribological material with reinforcement features this was next to impossible to test on small scale. A small scale test with a surface of 10 x 10 mm would imply a normal force of 15kN which is far beyond the capabilities of most small scale test-rigs. Moreover the speed at which the lock gate is moving amounts to only 2.75 mm/s. So in this case large scale testing was, although cumbersome, necessary.

The testing was carried out at the Laboratory Soete, which has a test-rig capable of producing 6500 kN normal load, 2500 kN friction load, 400 mm stroke and 5 mm/s velocity. Preliminary testing indicated that the carbon fibre ring of the pad design in figure 2 came into contact with the counterface, which produced higher coefficient of friction than expected and scratching of the counterplates due to the abrasive action of the carbon fibres. The design was changed in such way that a lip of UHMWPE covered the carbon fibre ring, lowering the coefficient of friction and preventing damage to the counterfaces.

Table 1. Coefficients of friction tested at large scale

Contact Pressure MPa	UHMWPE/Steel		UHMWPE/Painted Steel	
	$\mu_{\text{stat}}$ [-]	$\mu_{\text{dyn}}$ [-]	$\mu_{\text{stat}}$ [-]	$\mu_{\text{dyn}}$ [-]
15	0.12	0.11	0.12	0.09
30	0.11	0.10	0.09	0.08
60	0.08	0.07	0.07	0.04
90	0.06	0.05	0.05	0.03
120	0.05	0.04	0.04	0.03
150	0.04	0.03	0.03	0.02

Table 1 shows the coefficient of friction as measured on the large scale flat tribometer. From these results it is clear that the coefficient of friction is lower than the desired value, as the high contact pressure produces consistently low coefficients of friction. While this effect is already known from literature, the models for this effect taken from literature were found to be inaccurate, as they were fitted to data at much lower contact pressures.

### 3. Edge effects and heat input

The application presented in the previous section is somewhat special due to the extreme contact pressure. However, even for lower values of contact pressure small scale test results cannot be extrapolated to large scale applications. One of the reasons for this is the fact that the effect of the edges of the specimen (different mechanical properties, different contact pressure) is more pronounced for small scale specimens. This can be easily understood as follows. For a square with sides of length  $a$  the surface is equal to  $a^2$ , while the circumference is equal to  $4a$ . The ratio of circumference to area is therefore equal to  $4/a$ . This means that for small specimens the effect of the edges of the specimen is very much larger than for large scale tests. As an illustration a large scale specimen of a fibre reinforced composite of 150 x 150 mm is shown in figure 3. While the leading and trailing edges have disintegrated over 10 - 15 mm, the specimen is still functional. If this would have been tested at small scale (say 10 x 10 mm) the whole friction surface would have been damaged.



Figure 3. Edge disintegration of a reinforced polymer specimen after large scale friction test.

A third reason why large scale testing is often necessary is that even though care is taken to perform small scale tests at the same PV value as a large scale application, the wear rates and coefficients of friction taken from small scale test cannot be used for large scale applications. Table 2 shows typical values for contact pressure and velocity for a small scale test rig (commercially available plint TE77 is taken as an example) and a large scale application.

Table 2. Typical values for contact pressure and velocity for small scale tests and large scale applications.

Property	Small-scale testing	Large scale application
Contact surface [mm <sup>2</sup> ]	50	22,500
Normal force [N]	100	1,125,000
Contact pressure [MPa]	2	50
Velocity [mm/s]	500	20
P.v [MPa m/s]	1	1

Even when a correction is made for the fact heat transport is scale dependant (by using the dimensionless Peclet number) and for the differences in the relation between the geometry of the specimens and the sliding area (by using the dimensionless parameter G which is equal to the ratio of contact area to the circumference multiplied by the sliding stroke), small scale test testing is unable to accurately predict the wear rate and the coefficient of friction for large scale applications. This is illustrated in figure 4, in which the wear rate and coefficient of friction for small-scale and large scale are compared (bottom fitted line is in both cases large-scale). The coefficient of friction obtained from small scale testing does in no case match the coefficient of friction measured at large scale. As long as only mild wear is happening, the wear rates found at small scale correspond with the wear rates at large scale, but once softening of the polymer occurs this correspondence is lost.

#### 4. Oscillating radial bearing

For radial bearings under oscillating motion the location and the size of the sliding contact is not only dependent on the coefficient of friction, but also on the clearance of the bearing and the stiffness of the bearing material, all of which are to a large extent dominated by the size of the bearing. An overview of the forces acting on a radial bearing is shown in figure 5. The effect of clearance can be demonstrated as follows. When the shaft rotates around its own centre line it makes contact (a line contact is assumed for the calculations) with the bearing material at either  $\theta = -\alpha$  and  $\alpha$ , depending on the direction of motion of the shaft. At the reversal of motion the shaft purely rolls against the bearing, without slipping. The bearing will shift position (horizontal and vertical displacement) relative to the stationary shaft. When the angle position  $\alpha$  or  $-\alpha$  (which corresponds with a shaft rotation of  $\varphi_\alpha$  or  $\varphi_{-\alpha}$  according to equation 1) is reached slip occurs over a certain slip length.

$$\varphi_{2\alpha} = 2\alpha \cdot \frac{(R_s - R_b)}{R_s} = 2\alpha \frac{\text{clearance}}{\text{diameter}} \quad (1)$$

As a consequence wear will be unevenly distributed and will happen at the positions  $\theta = -\alpha$  and  $\alpha$ , while the rolling in between these positions will not result in wear. Due to the finite stiffness of the bearing, two contact zones will be formed at  $\theta = -\alpha$  and  $\alpha$ .

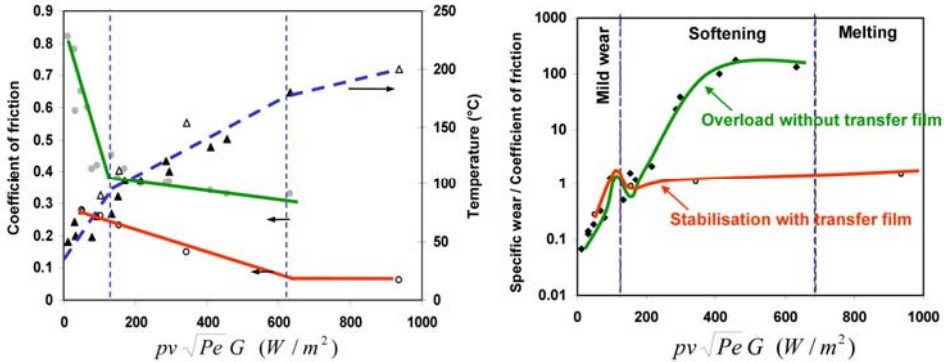
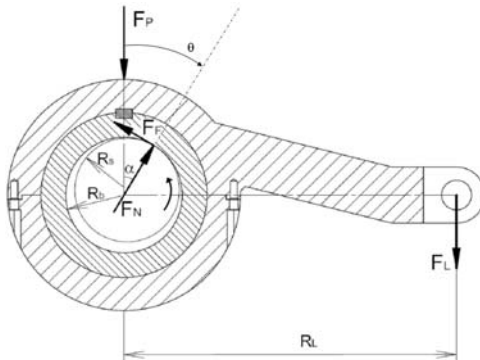


Figure 4. Effect of heat input on coefficient of friction and wear rate of POM.



- $F_L$ : force in the load-cell (8)
- $F_p$ : normal load
- $R_L$ : horizontal distance between the points of action of  $F_p$  and  $F_L$
- $R_b$ : bearing radius
- $R_s$ : shaft radius
- $\theta$ : angular displacement of the contact line between bearing and counter face
- $\alpha$ : transition point from rolling to sliding
- $F_f$ : tangential reaction force component
- $F_n$ : normal reaction force component

Total bearing play ( $2 \times (R_s - R_b)$ ) = bearing play (no load) + elastic deformation under load

Figure 5. Forces acting on a radial bearing.

The friction force when sliding of the shaft vs. the bearing material occurs can be calculated according to equation 2.

$$\mu = \frac{F_f}{F_n} = \tan \alpha = \frac{1}{\sqrt{\frac{1}{\sin^2 \alpha} - 1}} \quad , \quad \sin \alpha = \frac{R_L}{R_B} \frac{F_L}{F_p + F_L} \quad (2)$$

At the Laboratory Soete a test-rig is available which allows to test radial bearings at large scale. A schematic overview of this test rig is given in Figure 6. The test bearing (1) is fixed in a bushing (2) by means of a back-up ring (15). A lever arm (7) connects the bushing to a load-cell (8). These five components are all stationary and are not driven in any way during the conducted tests. Flanges can be fitted at the sides of the bushing to create an internal reservoir which can be filled with a test medium.

A counter face (14) is attached on the main shaft (3) which follows the reciprocating movement of the centre trunnion hydraulic cylinder (5) through a lever arm (6) and slides against the stationary test bearing. The trunnion pins of the hydraulic cylinder are carried by needle roller bearings, allowing the cylinder to pivot, following the motion of the lever arm while the actuator's displacement is changing. The main shaft is carried by two self-aligning double row spherical roller bearings which are each part of a stationary support (4), fixed to the ground.

The radial load on the test bearing is applied by a vertical hydraulic actuator (9) via a load transmission trolley (11) and is measured with a load-cell (10). A spherical pressure plate (13) allows small misalignments of the vertical hydraulic actuator and ensures that the load is transmitted in the radial direction to the bushing. To pull the trolley back up a threaded flange (12) is screwed on the load-cell threads and bolted to the trolley. The vertical actuator is connected to a stationary supporting frame. Limit switches are placed around the cylinder of the vertical actuator to ensure its vertical alignment.

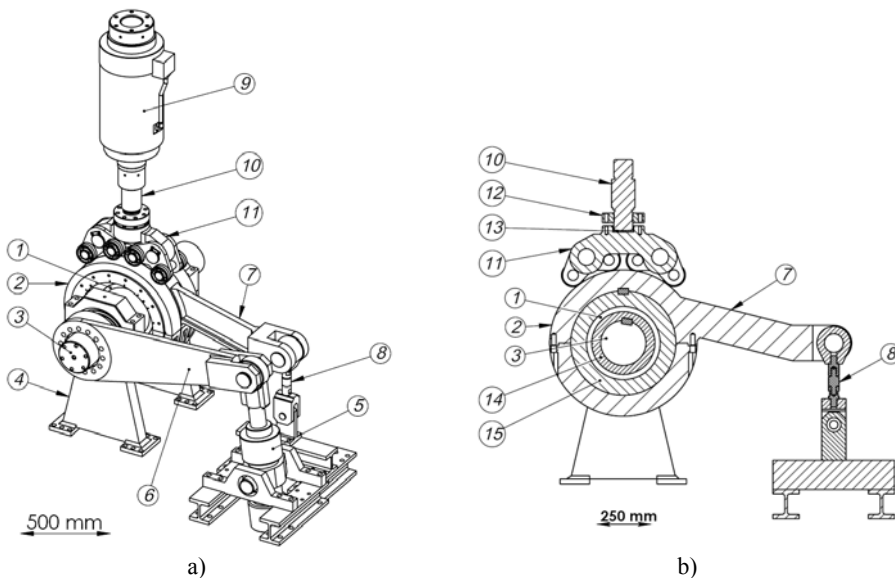


Figure 6. Large scale radial bearing test-rig.  
 a) isometric view b) section view.

Figure 7 shows the measured values of the displacement of the piston (saw tooth curve), force on the load arm ( $F_L$ ) and horizontal displacement of the bearing, together with the calculated friction force  $F_F$ , normal force  $F_N$  and horizontal displacement of the bearing (for a measured unloaded bearing play of 1.1 mm). As can be observed in Figure 7.b the measured total bearing play differs from the theoretical predicted value due to the elastic deformation under load. The latter can be corrected by taking into account the measured additional bearing play under load.

Figure 8.a gives an example of a friction-displacement characteristic (wherein the arrows indicate the time evolution of the cycles) used to calculate the static and dynamic COF. Because of the build up of the saw tooth displacement of the piston at the beginning of the test, the friction-displacement characteristic starts with a smaller cycle and then evolves to cycles with a shaft rotation amplitude of almost  $0.26^\circ$ . Figure 8.b shows the calculated COF and displacement of the drive piston versus time. At the moment the rotation of the shaft reverses the calculated value of the COF drops to a low value (rolling instead of sliding).

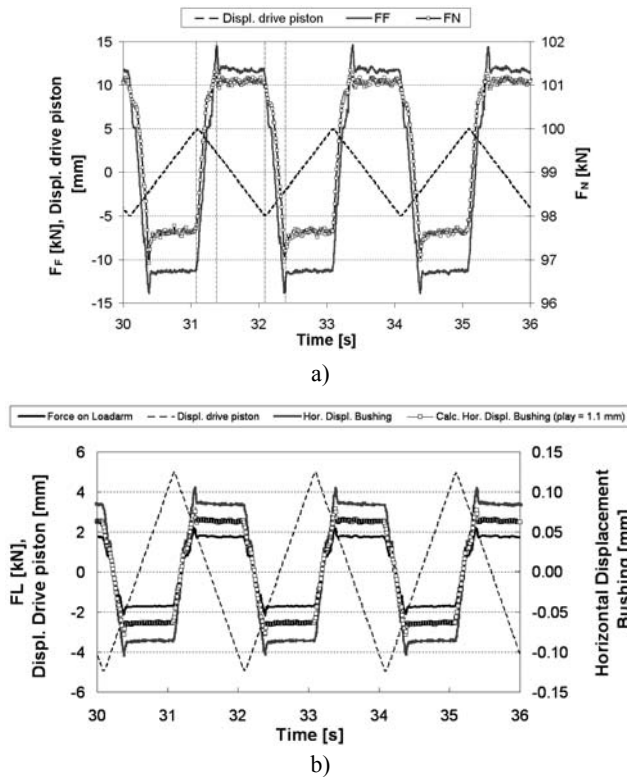


Figure 7. a) Displacement of the drive piston, friction force  $F_F$  and normal force  $F_N$ , b) displacement of the drive piston,  $F_L$  and horizontal displacement of the bearing (measured and calculated).

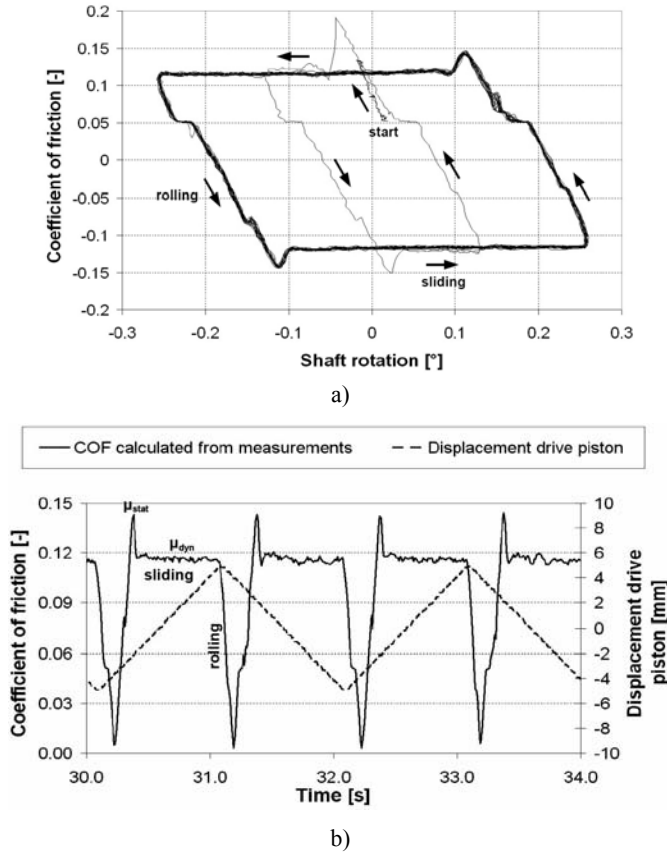


Figure 8. a) COF versus shaft rotation, b) calculated COF and displacement of drive piston versus time.

## 5. Conclusions

There is a multitude of reasons that make large scale testing, although expensive, slow and cumbersome a necessity. The first reason is geometrical features such as reinforcements, grooves, solid lubricant pockets which cannot be scaled down. A second reason is the influence of the edges (different material properties, different contact pressure). This is less pronounced at large scale, while a small scale specimen is basically all edges.

A third reason can be found in the fact that while testing at small scale and large scale can be done for the same  $P.v$  values, the absolute values for pressure and the absolute value for the velocity is often different for large and small scale testing. This results in different contact pressures and different wear rates.

A fourth reason is the effect clearance and stiffness have on the tribological and kinematic behaviour of radial bearings. In the case of radial bearings it is shown that as the tribological behaviour and the kinematic behaviour influence each other it is impossible to scale down test for radial bearings.

All this does not make tribological testing any easier, but full scale testing on large specimens is a luxury that cannot be dispensed with for large scale applications.

## **References**

Czichos H (1982), Reibung und verschleiß von werkstoffen, bauteilen und konstruktionen: ursachen, analyse, optimierung, Expert Verlag, Berlin.

# **Issues on the design and construction of machinery for cleaning and maintenance of sewage system**

Sándor RAVAI NAGY, Mircea LOBONȚIU, Nicolae MEDAN  
North University of Baia Mare, Faculty of Engineering

## **Abstract**

This paper presents an overview of the issues regarding the development of designs for the machinery family for cleaning and maintenance of sewage system. It presents a design approach based on parametric modelling and design, with the result of decreased, short product assimilation period, with the possibility of concept and design error observation prior to the implementation of the product. In addition, we discuss the structure and the functions of these machines for cleaning and maintenance of sewage system.

## **Keywords**

Cesspit emptier, Washing machinery, parametric design, Structure of cesspit emptier, Functions of machinery for cleaning and maintenance of sewage system.

## **1. Introduction**

The emptying systems have the function to clean and maintain sewage systems, to remove alluvia, sediments from clogged channels, to empty and maintain septic tanks, to clean the drinking water wells. For easy access and quick intervention, the emptying system, as superstructure, is installed on a chassis, which will provide energy necessary for the drives of different elements of the superstructure (pumps, engines, pistons, electrical systems etc.).

It can be said about the existing sewage system in Romania that it has to be re-designed to avoid intense physical damage, and to maintain its proper operating parameters.

The sewage system clogs and blocks up, leading to overcharge. To remove damage, periodic maintenance is required.

To realize this, depending on the real situation on the field, specialized technological systems have to be used. These are divided into 3 major groups of specialized equipment for sewage and transport:

1. Sewer cleaning machines,
2. Suction machines,
3. Combined machines.

## 2. The structuring of special machinery for sewer system cleaning

The block scheme of such machines has the form shown in fig. 1. The superstructure, composed of subassemblies, which meet the requirements of the client by their operation, is positioned on a proper chassis.

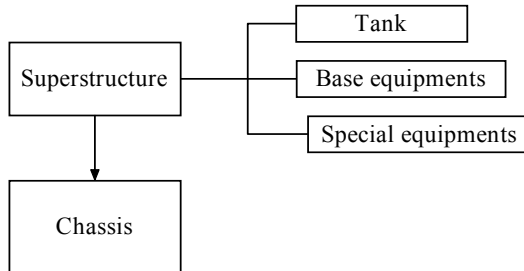
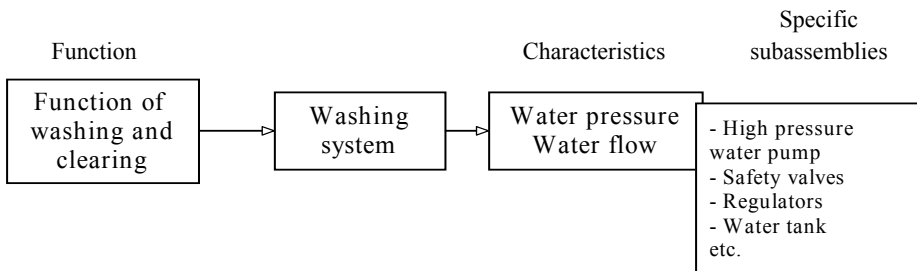


Figure 1. The structuring of special machinery for sewage system cleaning

General functions that must be satisfied by such machinery are:

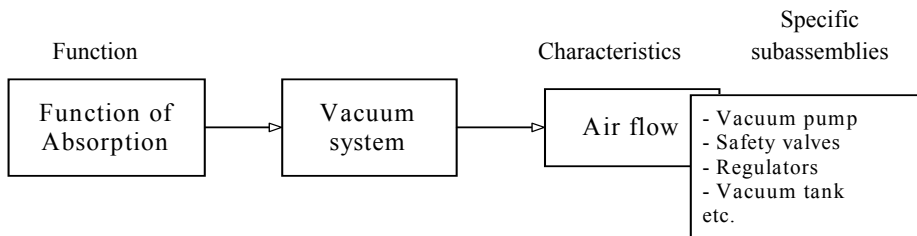
- washing and clearing the sewage pipes
- absorption of solids from the sewage system
- the transport of extracted solids to the WWTP
- the transport of water necessary for clearing the sewage system.

The function of washing and clearing, serves for cleaning of sewage pipes by pressurized water yet. The water pressure and the water flow rate are provided by a high-pressure water pump.



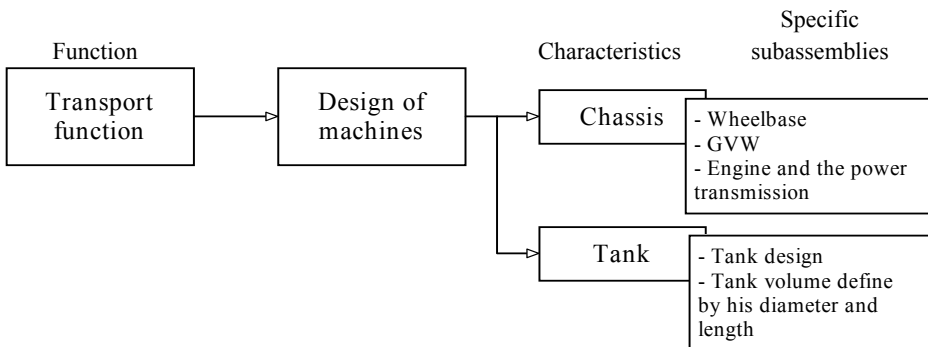
The high pressure pump is driven by a rim or cardan drive from the chassis gearbox via PTO (Power Take Off). The pump is supplied with water from the water tank of the machinery, creating a washing pressure of approx. 200 bars. The high-pressure pump is provided with protection systems to prevent its destruction. With washing hose, wrapped around a drum located generally on the rear part of the machinery, the pipe and channel clearing is realized. At the end,

the hose is provided with different washing heads, which secures the movement of the hose in the channel and removes the encountered blockages. Depending on the character of the blockages, a proper washing head must be used.



The absorption function is to extract the solids and the aqueous matter from the sewage system. This is done with absorption hoses, connected to the vacuum tank, in which depressurization is realized by a vacuum pump. The vacuum pump is driven by rim or cardan drive from the chassis gearbox via PTO. For high parameter operation and maximal safety, the absorption system contains a number of components having the role of protecting the service personnel, the machinery and provides a series of information regarding equipment operation.

The vacuum system can also be used for emptying the sludge tank by reversing the air circulation direction through the system. In this case, pressure is created inside the tank, which will force its content to evacuate through a discharge nozzle.



The transport function is based on the chassis, on which the tank specific superstructure was built, within which the material is transported. A very important characteristic of the tank is that of sealing, because the transported material is liquid or watery mixture.

### 3. Equipment structuring in accord with the functions of the machinery

To obtain a high performance equipment to satisfy all user needs, you have to realize a harmonious mixture of components so that the functions of the machinery will be balanced. By balancing the functions I mean, that none of the components is undersized to foster an unjustified increase of a component to obtain machinery with false high performance. (For ex.: To increase the capacity of the tank on a chassis with a given weight and engine power, you mount an undersized, but very light pump, which will not meet the demands, or the basic working time will increase significantly. It will result machinery having low functional characteristics with a big tank, which may mislead the clients with less knowledge and experience. It may lead to bankrupt a newly started business.)

### 4. The structure of the design process of sewage system cleaning machinery

Taking into consideration the facts presented above, prior to a purchase investment of one or some sewage system cleaning machinery, one should consider the possibilities and needs of the business and the situation on the field. These requirements are converted in ENTRIES for the design of such machinery. The synthetic scheme of emptying machinery design is presented in fig. 2.

As EXITS from the system, we can consider the functions satisfied by the design. These functions are modified until a consensus is achieved between the client and the machinery manufacturer, due to the feedback obtained by the designer from the project management (decision-making forum), respective from the client via project management.

The entries in the design system are the ones presented by the client, needs, which have to be filtered and clarified to obtain clear and precise entries.

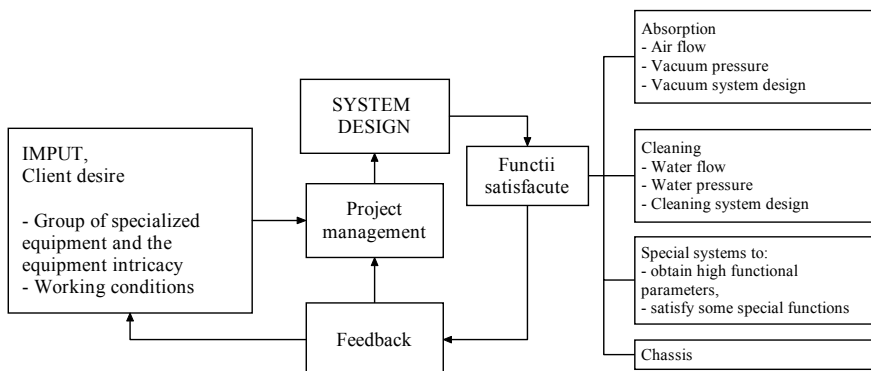


Figure 2. Synthetic scheme of sewage system cleaning machinery design

To launch the design act for a sewage clearing, one has to set the group of equipment and operating conditions and its destination, in concordance with identifying the client's needs.

The operating conditions can be grouped as it follows:

- sewage diameter
- the type of material the sewage is made of
- the type, character of clogging
- maximal depths of the cleaning system
- distances between manholes
- the configuration of access ways

To realize the parametric design of these technological systems, first the common components and subassemblies will be identified, respective the ones, obtained from the specialist companies producing only subassemblies (pumps, hydraulic equipments, etc.) To settle the design problem, the solution is parametric design and modelling. The components of machineries are modelled. These equipments are common in proportion of 75-80%, being identical for the machinery. The rest, in proportion of 20-25%, represents connection elements, necessary to form different systems. By connecting subassemblies, the machinery model is obtained. (fig. 3.)

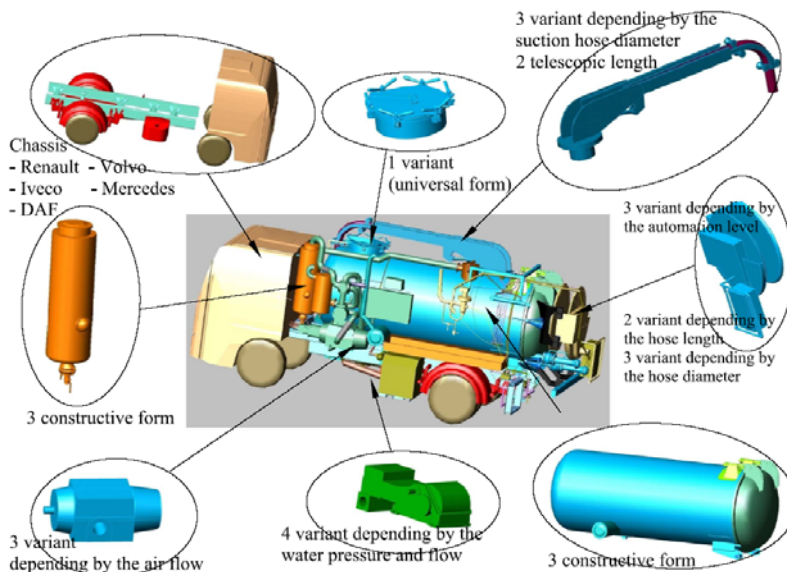
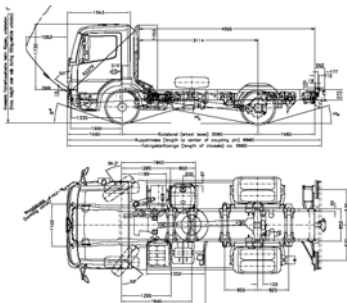
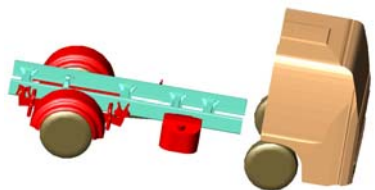
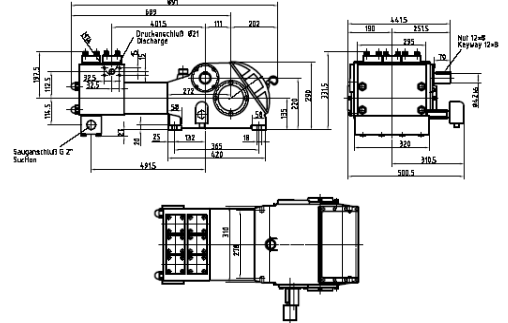
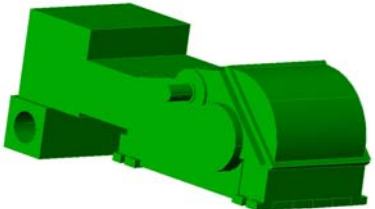


Figure 3. Modular structure of sewage system cleaning machinery

The documentation about subassemblies, which form the machinery's vertebra, depending on the manufacturer, can be a 3D model or 2D drawings in CAD form or just paper form. In case the subassembly's documentation is 2D, it has to be transformed in 3D model, Table 1.

Table 1. Modelling levels

Existing documentation	3D model
	
	

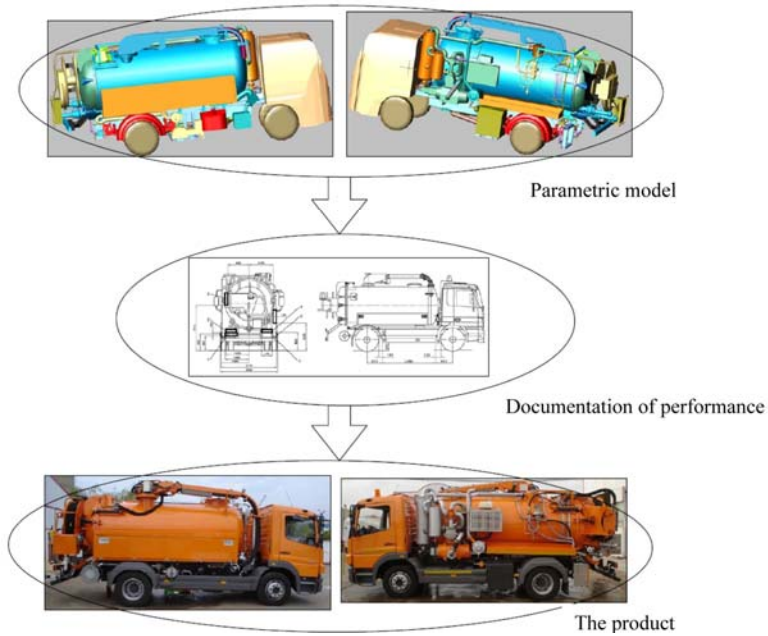


Figure 4. Machinery completion stages

After completion of parametric models of designed, respective purchased subassemblies, the machinery's model is formed, the construction documentation is worked out and the designed machinery is manufactured. (fig. 4.)

Using the parametric model of the machinery, the followings can be realized:

- the survey of equipment prior to its launching into design implementation and certification
- the work out of construction documentation (overall and construction drawings)
- management and marketing aspects.

## 5. Conclusions

The parametric design and 3D models lead to high accuracy construction documentation of the design.

By this type of design:

- construction flexibility is provided
- scraps and disturbances are reduced by over 70%
- the assimilation period of the product is very short
- the 3D modelling is used for design control and certification
- the gauges, possible collisions are verified, respective movement, construction simulations can be made, using rapid prototyping processes, it may even form the base of graphical presentation of the product, even before its manufacture.

## References

Big. R. ș.a. Difuzia tehnologică / Managementul proiectelor tehnologice. Editura Limes, 2008.

Loboțiu M. ș.a. Inovarea –sursă de dezvoltare antreprenorială. Inovarea tehnologică. Editura Limes, 2007.

\*\*\* [www.daf.com](http://www.daf.com)

\*\*\* [www.gdwittig.de](http://www.gdwittig.de)

\*\*\* [www.hpp.it](http://www.hpp.it)

\*\*\* [www.huwer.com](http://www.huwer.com)

\*\*\* [www.iveco.com](http://www.iveco.com)

\*\*\* [www.kamat.de](http://www.kamat.de)

\*\*\* [www.mbbi.co.uk](http://www.mbbi.co.uk)

\*\*\* [www.renault-trucks.com](http://www.renault-trucks.com)

# The effect of the molecule manipulation on the lifetime of the product

Attila KÁRI-HORVÁTH, István VALASEK, Ibolya ZSOLDOS  
Szent Istvan University, Faculty of Mechanical Engineering

## Abstract

In this work we show the results of our experiments in which we investigated the effect of different factors of the cooling system – the lubricant, the dosage of the lubricants and several complementary cooling factors as the spontaneously, the induced emission and the Doppler-cooling – for the demand of energy of the cutting. We have found that numerous variations of the different factors can decrease the demand of energy. The effects for the grain structure of the active volume of the cutting have been investigated, as well.

## Keywords

cooling systems, cutting, lubricant, Doppler cooling, MOL

## 1. Introduction

The energy imported into the cut and the changes occurring of its effect belong to the domain of the macro-physics and over this, the friction process - which gives the basis of the detachment of chip – belongs to the domain of the macro-physics, from this fact the development trend of this work was deduced.

The development of the elements in the machine-tool – tool – lubricant – work-piece system is not even. The improvement of one element forces the development of the others thus resulting in the progress of the whole system. The researchers have established that the application of the liquid coolants-lubricants is inevitable in the case of certain machining technologies therefore they have proven the necessity, the thrift and the realization of the MQL (Minimum Quantity of Lubricant) with experiments. This process aided the development of the machine-tools and the technologies.

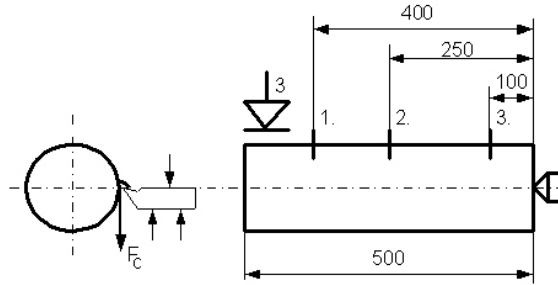
## 2. The short presentation of the research and development works

*The objectives of the research are:*

The interpretation of some theoretic issues of the energy conversion proceeding in the course of the cutting process putting on new theoretical bases and to explain several theoretical questions, to search several possibilities in the transitional section between the wet and dry machining which:



The measuring sets and places



**Measuring instruments**

traditional micrometer (measuring range: 50 - 75mm and 75-100mm)  
 traditional caliper (1/20 – 150mm)  
 metal microscope (Zeits Axi imager 1M, and Axiovision 4.7)  
 WA33 (TYP PRLTA13) scale (accuracy: 0,001g) for measuring of the insert mass  
 inductive odometer for measuring cutting force (type: TR102)  
 revolution counter for measuring revolution (own construction)  
 measuring-data collector (spider8 control)  
 IGA 300 infra thermometer  
 Mitutoyo SJ 201P diamond headed surface profilometer.  
 instruments generating photon electrons: photo-emission with visible light, laser cooling (laser: 1 mW,  $\lambda = 630-680$  nm): either the Doppler-cooling or side-strip cooling

**Measured data**

The measuring places signed by '1', '2', and '3':  
 $D_1$  [mm],  $D_2$  [mm],  $D_3$  [mm],  
 $R_a$  [μm],  $R_z$  [μm],  $R_q$  [μm],  $R_y$  [μm],  
 $n$  [min<sup>-1</sup>],  $F_c$  [N],  $T$  [°C]

**Calculated data**

$D_a$  [mm],  $v_c$  [m/min],  $s$  [m],  $V_f$  [mm<sup>3</sup>/s],  $VB$  [mm],  $P_c$  [kW]

We took into consideration the shaping period of the tool from the start to the end of the step and the average value was calculated by the mathematical function of the Excel 2003 program. We fixed the result received so in the table. We prepared the following functions based on these table data then  $R_a - V_f$  (the average surface roughness – quantity of detached sliver),  $VB - s$  (the measure of back abrasion – length of tool path),  $VB - V_f$  (the measure of back abrasion - quantity of detached sliver). We determined the stability of the diameters and the specific cutting force from measured cutting forces which are drawn in diagrams, as well. We examined the different effects in MQL lubrication circumstances of 50 g/h and 30 g/h of oil use. We examined the effect of the viscosity, the molecular structure and the dopes of the oils in manipulated and not manipulated molecular circumstances.

## 4. Results

The largest part of the chipping energy is needed for the balancing of the exceptionally complicated deformation and the tensile state, the smaller part 3% is needed for the crystal modification. From the prepared polished samples we present the modifications in the grain structure with the application of the following method.

The description of the examinational method:

Step 1. The cutting of the sample from the workpiece with metallographic rapid chopping under water cooling

Step 2. The embedding of the piece (with warm embedding, into a substance having bakelite basis– 3 min, 160 °C -)

Step 3. Preparation

- polishing (wet polishing with SiC basis mixture with water cooling)
- polishing with diamond suspension (9µm, 3µm and 1µm)
- in the end with colloid silica of 0,05µm

Step 4. Etching (with alcoholic nitric acid –NITAL- having concentration of 3-5 %)

Step 5. Microscopic examination (with an objective with own magnification of 20x, 50x and 100x).

The patterns of the samples having measure of 50 µm are presented in the following figures. A darker domains show the ground layers, the clearer domains show the layer where the effect of the shaping is observable.

Figure 2 shows the case when we applied emulsion of 5 % as lubrication and spontaneous emission to cool the workpiece. The size of the grains is big, the grains at the transition are deformed, the translational plane is visible in small rate.

In Figure 3 the workpiece was cooled with dry lubrication and spontaneous emission. The size of the grains is big, the grains at the transition are deformed, the translational plane is visible good.

In Figure 4. the sample of the experiment made with dry lubrication and with induced emission can be seen. The size of the grains is big, however high deformation at the transition cannot be seen, the translational plane is not visible.

In Figure 5 the sample of the experiment made with dry lubrication and Doppler cooling can be seen. The size of the grains is smaller than it was in the case of the induced emission, however the size of the grains at the transition is smaller and deformations are smaller, the translational plane cannot be seen.

We used MQL lubrication with spontaneous emission in the case of a market product which is shown in Figure 6. The size of the grains is big, deformation at the transition can not be seen, but the translational plane can be seen well.

Figure 7. shows the sample of the experiment where we used MQL lubrication with the solution prepared by us, with induced emission. The use of the lubricant was 50 g/h. The size of the grains is smaller, high deformation can be observed at the transition. The translational plane is visible mildly. In terms of a friction and abrasion the structure is favourable.

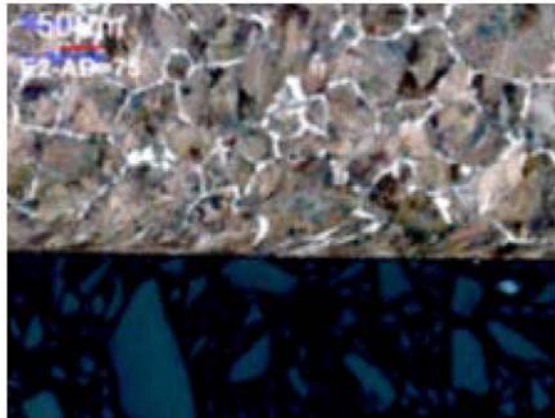


Figure 2. 5% emulsion

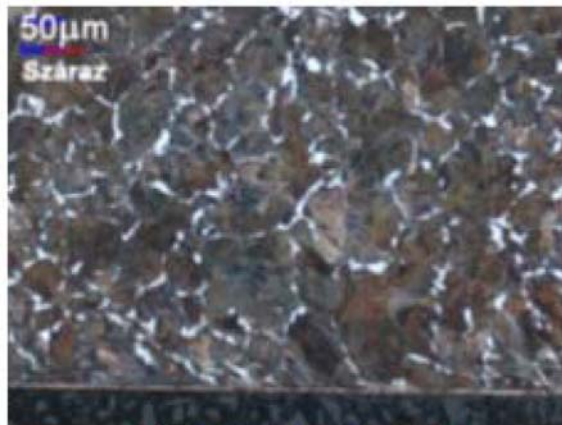


Figure 3. Dry-lubrication



Figure 4. Dry-lubrication (induced emission)

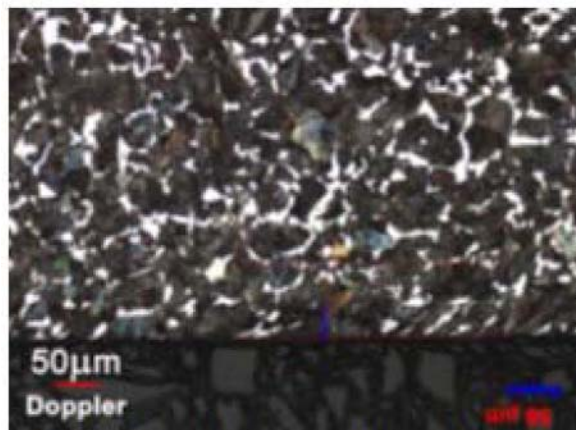


Figure 5. Dry-lubrication (Doppler-cooling)



Figure 6. MOL-lubrication (50 g/h)

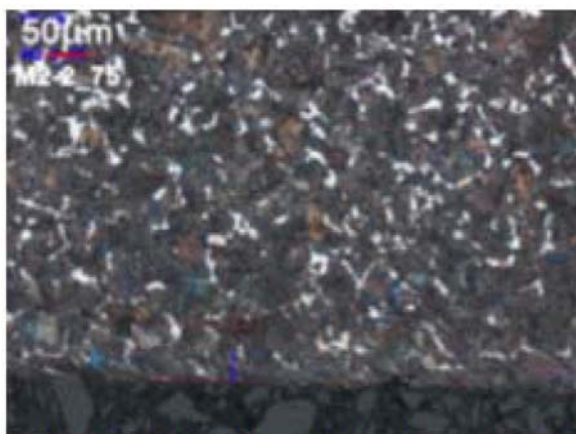


Figure 7. MOL-lubrication (M2-2, induced emission, 50 g/h)

Figure 2, 3 and 6 the translation plane is visible and the deformation of the grains is considerable at the transition. But when we carried out the molecule manipulation with induced emission or Doppler-cooling (Figure 4, 5 and 7), the grain structure is smoother, the translational plane is not or only narrowly visible and the deformation of the grains at the transition is small.

The crystal modifications during the chipping are not unconditional harmful, as it is known, that in the case of a directed strain a very good grain structure having good friction properties and effect which decreases the abrasion develops.

In cases, when the grain modification is rough and the dislocation develops at the maximum value of the tensile ( $\tau = 0,47 \cdot a$ ), the fatigue time starting from the surface – which appearances as the so called pitting – decreases.

In the case of a chill, if the depth of the chilled layer is the same as the plane of the maximum  $\tau$ , the fatigue speeds up and in certain cases, after 5-6 hours, total destruction of the surface can occur.

The deleterious effects of the modifications in the substance can be avoided with optimal technological parameters with MQL lubrication.

The most important result of the research and development work is the recognition, that it is not enough to study the sliver detachment process in the level of a phenomenon, but it is necessary to analyse the process in molecular level in parallel, as well. We may claim that a new theory was born, which is exact, rightfully and complements the earlier sliver detachment theory and which constitutes uniform whole one with it. We proved that the enormous energy reserves of the chipping are in the regulation of the energy conversion process. The revealed theory gives a safe method for the specialists dealing with MQL lubrication, and it offers a method for the treatment wet and dry transitional section. The research works continue according to a program, we inform the representatives of the trade about the results continuously.

## 5. Summary

The development of the elements in the machine-tool – tool – lubricant – work-piece system is not even. The improvement of one element forces the development of the others thus resulting in the progress of the whole system. The aim of the present paper is to shed light on the facts that the lubrication technologies used today are inefficient and pollute the environment. Therefore development of this area is inevitable. Among the present-day developmental trends MQL (Minimum Quantity of Lubricant) is one that promises immediate results. Hopefully, it will also bring about the total paradigm shift in the machine manufacture technology.

## References

Bartz, W.J. és 70 szerzőtárs: Kühlschmierstoffe und Zerspanung, Renningen-Malmsheim, expert-Verlag 2000.

---

Valasek I., Tóth I.: Megmunkálás - tribológia, Budapest, Tribotechnik Kft., 2003.

Csizmazia Ferencné: Anyagvizsgálat, Győr, 1999.

Csizmazia Ferencné, Fodor László: Anyagismeret és Technológia gyakorlatok (anyagvizsgálatok), Tankönyvkiadó, Budapest, 1987.

# Shore D hardness of cast PA6 based composites

Mátyás ANDÓ, Gábor KALÁCSKA,  
Szent Istvan University, Faculty of Mechanical Engineering  
Tibor CZIGÁNY  
Budapest University of Technology and Economics

## Abstract

Shore-D hardness gives additional help for tribological analysis of engineering polymers and their composites. On the basis of the tested samples it was determined that additives below 10% does not have significant effect on hardness of the samples. However with softening additives between 10 and 25%, hardness decreases in great extent. A particular rate of rigidity decrease can be advantageous as the particle embedding ability of friction surface arises in abrasive wear systems.

## Keywords

cast polyamide 6 composites, additives, hardness

## 1. Introduction

One of the advantageous field of the material developments is the friction and wear materials. Its importance is given by the fact that the wear and different friction phenomena in the long run can cause huge losses during the operation. Energy and wear losses can be reduced directly with materials of lower friction coefficient, but in long-term use in contaminated area the abrasion resistance is also very important. Tribological processes are complex due to many acting operational factors (mating material parts, surface macro and micro geometry, third-body behaviour, sliding speed, contact pressure, ambient temperature etc). For better understanding the tribological test results of different polymer composites, there is a need for other examinations. For plastics one of those examinations is the Shore-D hardness measurement. With Shore D hardness measurement it is possible to approach the embedding ability – how the polymer surface react against moving hard particle on it -, which has basic importance in abrasive friction systems. The hardness of plastic surface also plays important role in evaluating of wear volume and wear mechanism in case of hard mating surface, too.

This article gives a brief review about the results of Shore-D measurements by magnesium catalyzed polyamide 6 composites having different additives.

## 2. Base materials

PA6 is a strategic engineering plastic, which has quite good mechanical and tribological characteristics, and is used on several fields of engineering life. The material developing process, composite research, is supported by industrial company, thus, the selected base matrix is the magnesium catalyzed cast polyamide 6. This material is produced by Quattroplast Kft. under the name of DOCAMID 6G-H.

The basic raw material of the natural product is caprolactame ( $C_6H_{11}NO$ ), which is available among chemical products.

In Germany PA6 was first produced in 1938. This is a polycondensational procedure, during water exit (Kalácska 2007). Natrium-catalyzed PA6 was developed only later, but it did not fulfil the requirements. It was not appropriate for fibre production but it was excellent for block casting. The use of the magnesium catalyzer did not solve the problem of the fiber production, it only modified the characteristics of PA6. The Quattroplast Kft. produces cast PA6 with an unique production technology in the world, in industrial volumes. It takes the advantage of ring opening polymerisation without water exit (Macskási 1996). The natural cast material perform in average a tensile strength of 85 MPa, Charpy impact strength of  $8 \text{ kJ/m}^2$ , and Shore-D hardness of 83. In the present stage of the composite development, different quantity of montmorillonite, graphite and TA52 softening materials are added to the base matrix.

One of the new additive materials to achieve better fire-safe composite is the montmorillonite (Pál 2006). Montmorillonite is a clay mineral, which is modified in a way that the layers in the clay are extended so that the polymers are able to diffuse between them. If the distance is increased further, the contact between the layers ceases to exist and they are dissolved in a homogeneous way in the base matrix. It was shown several times that during the burning process it decreases HRR (Heat Release Rate  $\text{kW/m}^2$ ).

Graphite was several times used as additive to increase the conductive ability of plastics. Novák (2004) found out on the basis of his measurements that by adding graphite independently from the base matrix (polyurethane and epoxy resin), antistatics can be reached with the addiction of more than 20%.

TA52 is used originally for polyurethane production, in our case its role to increase the toughness and abrasive wear resistance. With TA52 application the molecule chain consists of 3 elements (A-B-A). The original aim of the additives was to increase the toughness and impact strength.

## 3. Shore-D hardness measurement

Shore-D hardness measurement is standardized in MSZ EN ISO 868:2003 [Plastics and ebonite. Determination of indentation hardness by means of a durometer (Shore hardness)]. The principle of the method is simply: pushing a needle into the material with given force for a given time, and the deepness of

the indentation is measured. The value of the indentation hardness is in inverse proportion to the intrusion and highly depended on the form of the pushing needle. For the measurements, in accordance with the recommendation, the D type needle was selected. The measurements were carried out on samples in accordance with the standard, applying 9 measurement points. The results - 1 second after the intrusion of the needle – were recorded (according to the standard, 2nd indication technique). The hardness durometer were made with Zwick/Roell HO4 3150 type equipment (Fig. 1).



Figure 1. Shore-D hardness durometer

#### 4. Measurement results

The results of the Shore-D hardness measurements are affected by the humidity content of the sample. Therefore the measurements were made with dry samples, which were worked out from the same location of the cast blocks. The outrageous faults were excluded from the results. The results were between 40 and 90 Shore-D hardness, therefore on the diagram this range is shown.

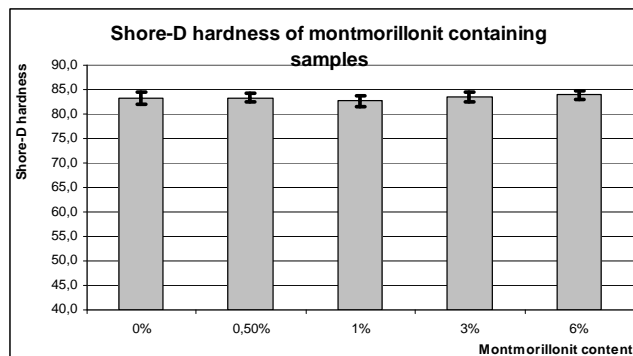


Figure 2. Shore-D hardness of montmorillonite containing samples

In case of montmorillonite and graphite containing samples the additive was below 10 %, and in this range it is not possible to show any tendencies between the additive content and hardness (results are shown in the Fig. 2 and 3). The value of the hardness is nearly the same as the base material has. On the basis of this, it can be expected that in the tribological systems their embedding ability will be similar to the base material’s ability. (This expectation is going to be tested during the research project later.) The additives can modify the tribological systems in case of not abrasive-type wear processes, too. (Graphite is often used as lubricant).

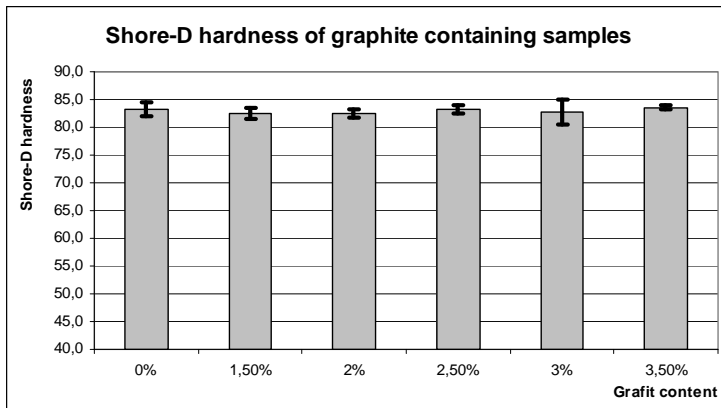


Figure 3. Shore-D hardness of graphite containing samples

In case of adding the TA52 softening material rigidity has changed significantly. On figure 4 it can be seen how TA52 influences the hardness of the cast PA 6 composites.

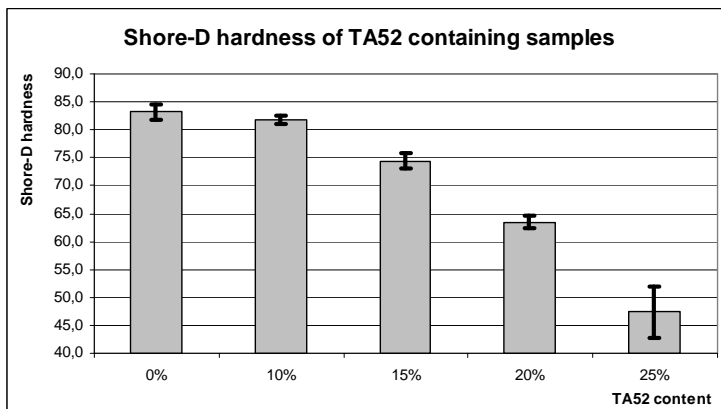


Figure 4. Shore-D hardness of TA52 containing samples

It can be seen that higher content of the TA52 softening material can decrease the hardness continuously. Between 0 -10% of TA52 additive the change of hardness is about 4 %, but over 10 % additive the decrease of the hardness is more progressive. In case of 25 % additive the hardness is only 50% of the natural version. Based on former experiments it can be considered advantageous in some abrasive circumstances due to the probably increased embedding property (this statements is going to be controlled with further measurements in the project). Extreme decrease of surface hardness of polymers can be disadvantageous in normal sliding systems due to the decreased load-carrying capacity and higher strain. The transition rate, the limit of additive percentage should be clarified by not abrasive wear tests. Also important to clarify the resulting effects of the toughness and hardness on friction and wear.

## 5. Summary

For safety and economical use of machines it is important to decrease different types of losses. One possible solution is the specialized materials for different applications. In plastic industry the composite developments can offer many advantageous new materials fit to challenges. Cast polyamide 6 as strategic, general engineering polymer has unique casting technology with magnesium catalyser. We launched a broad project to develop some special composites on that material to achieve better tribological, electrical (antistatics, ESd) and fire retardant versions. To evaluate the tribological behaviour in abrasive and adhesive sliding systems some other properties have to known. Among them the Shore-D hardness of composites has highlighted importance due to embedding ability. That feature is essential in abrasive systems. After getting to know the different hardness values the control tribological tests are going to be launched.

## References

- Kalácska G. : Műszaki polimerek és kompozitok a gépészmérnöki gyakorlatban, 2007, Gödöllő 3C-Grafika Kft.
- Macskási L., Műanyagok előállításának kémiai és műveleti alapjai, 1996, Budapest, Abigél Bt.
- Novák I., Krupa I., Electro-conductive resins filled with graphite for casting applications, 2007 European Polymer Journal, 40 (7) 1417-1422
- Pál Károlyné.: Műanyagok éghetőségének csökkentése töltőanyaggal, 2006, Műanyagipari Szemle, 3 (6) 33-41

# Experimental investigation of the friction behaviour of engineering plastics on a rotating pin-on-disc type tribotester

Stijn VAN AUTRÈVE, Wouter OST, Patrick DE BAETS  
University Gent, Department of Mechanical Construction and Production  
Mia LOCCUFIER  
University Gent, Department of Electrical Energy,  
Systems and Automation

## Abstract

Engineering plastics are increasingly used as bearing materials in applications demanding high contact loads and low sliding velocities. In these circumstances low and stable friction behaviour is desirable. In the present paper the frictional behaviour of some basic types of engineering plastics (PA6-G, POM and PET-P) and the influence of load and lubricant impregnation thereupon is experimentally investigated using a pin-on-disc type tribotester.

It is found that POM-C internal lubricated with a solid lubricant shows the most favourable friction behaviour in comparison with the other tested materials. Adding internal lubrication may stabilize the friction behaviour but is not always the case.

## Keywords

frictional instability, stick-slip, engineering plastics, experimental

## 1. Introduction

Bearing units in large-scale systems which require accurate positioning such as cranes or lock gates used in the civil as well as the off-shore industry mainly operate under relatively high contact pressures and low sliding velocities. Under these conditions and combined with the relative low stiffness of the large-scale positioning system, the friction between the mating bearing materials can give rise to friction-induced vibrations (i.e. stick-slip). This has a negative influence on the functioning of the positioning system and can lead to damage of the constructions to be positioned or even the bearing itself.

Bulk polymers (e.g. PA, POM, etc.) are normally used as bearing material because of their low cost. Nowadays, self-lubricating engineering plastics are increasingly used in order to have lower friction. Unfortunately, data concerning their stick-slip behaviour is scarce which makes it difficult to make a valid prediction of the friction behaviour at certain operating conditions. Experiments

on adequate testing equipment are needed in order to quantify their suitability for applications such as described above.

In the present study a number of engineering plastics (different types of PA6-G, POM and PET-P) are tested and their behaviour with respect to frictional stability (stick-slip) as well as the influence of some mechanical (load) and tribological parameters (lubricant impregnation) thereupon is investigated. Experiments are performed on a pin-on-ring type tribotester on which low speeds and high contact pressures can be applied.

In earlier studies already a series of experiments with engineering plastics were conducted on reciprocating large-scale and small-scale test setups (De Baets et al., 2000; Zsidai L. et al., 2002). Although it is not evident to compare results of different testing scales (this may result in important errors and many effects are scale dependent such as pocket distribution, misalignment...), small-scale test results can provide a ranking of the materials.

The main objective of the paper is to be helpful to the selection of a proper material which can operate optimal in comparison with other engineering plastics for the given operating conditions as described above.

## 2. Experimental

### *Description of the test-setup*

A schematic view of the pin-on-disc test apparatus is given in Figure 1. The main components of interest are numbered.

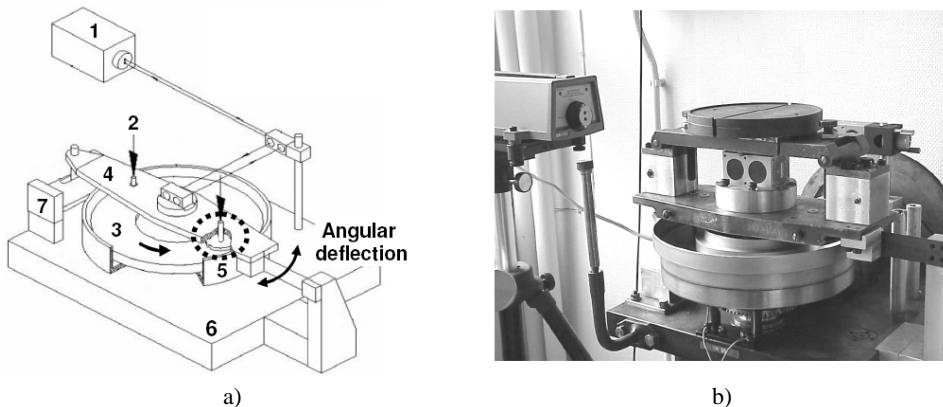


Figure 1. The pin-on-disc tribotester: schematic view (a) and view as present in laboratory (b)

Two symmetrical opposed sliding shoes (specimen holders) (5) which contain the specimens (engineering plastics) (5) are mounted in a rotating arm (4) which is fixed on the one end with low stiffness to the frame (6) by means of a leaf spring. The sliding shoes are pressed against a steel ring (3) by means of a

loading pin (2). The loading pins slide in linear bearings affixed to the rotating arm. This guide mechanism allows the loading pin to slide up and down the linear bearings without play. Calibrated dead weights provide the normal force which is transmitted, for each sliding shoe, onto the loading pins. The angular deflection (i.e. vibrations) of the arm is measured with a laser measurement device (1). The steel ring is driven by an electric motor of which the rotational speed is controlled by an inverter. The electric motor is part of a larger drive mechanism which is not shown in Figure 1. The rotating arm is on the other end connected to an external hydraulic damping unit (7). The latter was not used for the purpose of the present study while earlier studies showed that damping is compulsory to avoid vibrations (Van De Velde F., 1998; Ost W. 2006).

The test-rig described above can be modelled as an equivalent linear one degree of freedom mechanical model as shown in Figure 2. Only the tangential system motion of the system is described by this model. It is generally used in literature to investigate the occurrence of friction-induced vibrations (Van De Velde F., 1998; Ost W. 2006). The model corresponds to the following equation of motion:

$$m\ddot{x}(t) + c\dot{x}(t) + kx(t) = F = 2F_N\mu(t) \quad (1)$$

In equation 1,  $F$  represents the tangential friction force,  $F_N$  the normal force on one sliding shoe (the factor 2 in equation 1 originates from the fact that there are two sliding shoes as can be seen in Figure 1.a),  $\mu$  the friction coefficient,  $x$  the equivalent linear deflection of the arm,  $\dot{x}$  the velocity,  $\ddot{x}$  the acceleration,  $m$  the equivalent linear mass of the system,  $c$  the damping coefficient,  $k$  the equivalent linear stiffness of the system and  $t$  the time. Since the damping unit of the friction tester was not used in the experiments described in the present paper, the second term on the left side of equation 1 is negligible.

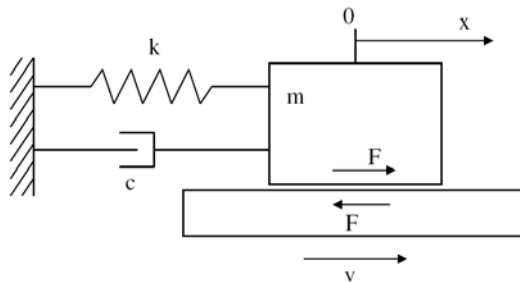


Figure 2. Linear mechanical (mass-spring-damper) model of the rotating pin-on-disc tribotester

Some main and specific characteristics used in the present study are gathered in Table 1.

Table 1. Some characteristics of the test-rig

Electric AC motor	Power: 1.5 kW
Used stiffness for leaf spring	$\pm 65$ N/mm (values vary slightly with each new mounting)
Used normal loads	150, 500 N per sliding shoe (max 1 kN applicable)
Rotating ring	Average radius: 100 mm Linear speed range: 0.2 -1940 mm/s (at 100 mm radius)
Laser measurement device	Range: $\pm 20^\circ$ Accuracy: $\pm 0.2$ %
Sliding shoe and specimen	Diameter frictional surface specimen: 6 mm Radius centreline: 100 mm

*Used test specimens*

An example of the used test materials is given in Figure 3.

Specimens used are polyethylene terephthalate (PET-P), acetal polyoxymethylene (POM) Copolymer and Homopolymer and cast nylon grade 6 (PA6-G) with and without internal lubrication (solid lubricant and /or oil). All polymers mentioned above are thermoplastic, semi-crystalline polyesters with high strength and stiffness.

In Figure 3.a below we can see that the top of the specimen has a smaller diameter than the bottom, which is fitted in the sliding shoes (shown above Figure 3.a). The top diameter determines the mean apparent contact pressure.

The rotating ring as shown in Figure 3.b is made of machine construction steel according to German "Werkstoff Nr." 1.5217; composition: 0.16 - 0.22 % C, 0.10 - 0.50 % Si, 1.3 - 1.7 % Mn,  $P \leq 0.035\%$ ,  $S \leq 0.035\%$ , 0.10 - 0.20% V. The two lateral faces of the ring were machined to an average surface roughness of 2.5 – 3  $\mu\text{m}$ , perpendicular to the machining grooves), in such a manner that the machining grooves are perpendicular to the sliding direction. The roughness is measured along the sliding direction.

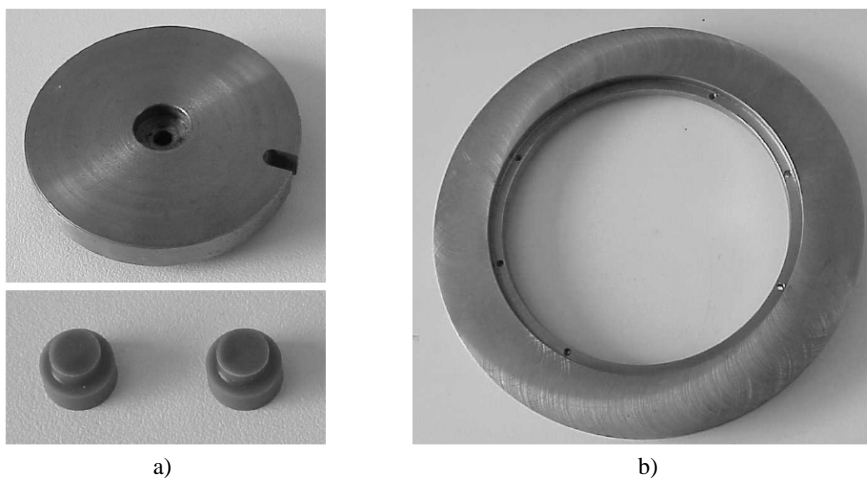


Figure 3. Specimens and sliding shoe (a), rotating steel ring (b)

### Test procedure

The tests are performed under dry conditions (no external lubrication was added). The used test conditions are gathered in Table 2.

The tangential friction between the specimens and the rotating ring originates from the relative motion between the bath with ring and the specimen holders, which are held up by the rotational arm and the leaf spring. When the equivalent linear spring stiffness  $k$  and the equivalent linear mass  $m$  are known, the friction force (more precisely the coefficient of friction) between the steel ring and the specimens can be obtained by means of equation 1 from the measured angular deflection/acceleration of the arm which is converted in a linear equivalent unit ( $x$  and  $\ddot{x}$ ).

Tests were performed with two different normal loads: 150 and 500 N. For each load, two different linear disc velocities were imposed (see Table 2) resulting in two main test conditions (C1 and C2 in Table 2).

The test was started according to condition C1 imposing a linear disc speed of 51 mm/s. The coefficient of friction was measured after 5', after 2h and after 3.5h. The speed of the pin-on-disc tribotester was then reduced to 5 mm/s and the coefficient of friction was measured after 5' and after 30'.

After testing at condition C1 the friction tester was stopped, the weights and speed were adjusted and the test was started again to continue according to condition C2 with an imposed linear disc speed of 164 mm/s. The coefficient of friction was measured after 5' and after 1h. After this the speed was again reduced to 5 mm/s and the coefficient of friction was determined after 5' and after 30'.

Table 2. Test conditions

Temperature rotating ring = 23°C			
CONDITION C1 $p_N = 17.7$ MPa (500 N)		CONDITION C2 $p_N = 5.3$ MPa (150 N)	
$v = 51$ mm/s	$v = 5$ mm/s	$v = 168$ mm/s	$v = 5$ mm/s

### 3. Results and discussion

The most important results of the conducted tests as described above are summarized in Table 3 showing the influence of normal load and internal lubrication. The values in the table are those taken at test condition C1 for an imposed disc velocity of 5 mm/s and after 30 minutes of testing.

Materials for which stick-slip is observed only show this behavior at the lowest imposed linear disc velocity of 5 mm/s. An example for PET-P with and without internal lubrication is given in Figure 4. It shows the angular displacement in function of time and the coefficient of friction in function of the

relative sliding velocity ( $v_{rel} = v - \dot{x}$ ). Typical stick-slip curves can be observed as during the stick-phase the relative sliding velocity remains zero and the friction coefficient increases in time until the recalling spring force of the leaf spring becomes larger than the static friction force. From that moment on, the slip-phase starts and the specimen will accelerate at first until the moment the reacting spring force will slow down the slip movement of the specimen and starts to decelerate. From the moment the relative sliding velocity between specimen and rotating ring reaches zero again, a new stick-episode begins.

*Table 3.* Test results summarized

material	Bulk*		Solid lubrication*		Oil lubrication*		v ~ and p <sub>N</sub> ↓			
	SS	μ <sub>b</sub>	SS	μ <sub>s</sub>	SS	μ <sub>o</sub>	SS	μ <sub>b</sub>	μ <sub>s</sub>	μ <sub>o</sub>
PA6-G	Yes	0.21	Yes	0.089	Yes	0.12	↓	0.35	0.081	0.12
POM-C	No	0.20	No	0.086	-	-	-	0.25	0.121	-
POM-H	No	0.20	-	-	-	-	-	0.31	-	-
PET-P	Yes	0.11	Yes	0.073	-	-	↓	0.14	-	-

\* Conditions:  $v = 5$  mm/s,  $p_N = 17.35$  MPa and test time = 30'

We can see in Figure 4 that the stick-slip amplitude increases with a percentage of approximately 84 % ( $\Delta_b \rightarrow \Delta_i$ ) when PET-P is internal lubricated with solid lubricant additives. This is an opposite effect as was observed in earlier studies (Zsidai et al., 2002; De Baets et al., 2000) which state that addition of polytetrafluorethylene (PTFE) lowers the (average coefficient of friction) and reduces the chance of the material to be prone to stick-slip. The former can be confirmed (see Table 3), while the latter is in contrast with what is observed in Figure 4.

Impregnation of PA6-G with oil or a solid lubricant lowers the coefficient of friction. In the case of impregnation with oil a higher coefficient of friction is obtained in comparison with the case of impregnation with a solid lubricant. This can be due to the fact that oil escapes more easily from the sliding area than in the case when the material is impregnated with a solid lubricant.

For all types of POM (-C, -H and lubricated) no stick-slip behaviour was observed for all test conditions. POM-C impregnated with a solid lubricant shows the lowest coefficient of friction in comparison with the other tested materials.

There are two main mechanisms that can contribute to the friction force between a thermoplastic and steel: adhesion (more pronounced on smooth surfaces) in the contact zone and deformation (more pronounced on rough surfaces) of the polymer (Zsidai et al., 2002). In the present study a rotating ring with rough surface is used for which we can say that the friction component resulting from deformation increases. Zsidai et al. stated that the influence of adhesion decreases with increasing load and surface roughness.

As can be seen in Table 2 the coefficient of friction decreases for almost all materials when the normal load (or apparent contact pressure) increases. This is also observed in (Zsidai et al., 2002; Van De Velde and De Baets P., 1997). For PA6-G impregnated with a solid lubricant the coefficient of friction increases little with an increase of the normal load, while impregnated with oil the coefficient of friction remains approximately the same for both normal loads. This can be due to the high rigidity of PA6-G resulting in little deformation at higher normal loads. Result is that less lubricant is squeezed out of the bulk while more lubricant is squeezed out of the sliding contact. The latter has a higher influence on oil than on the solid lubricant.

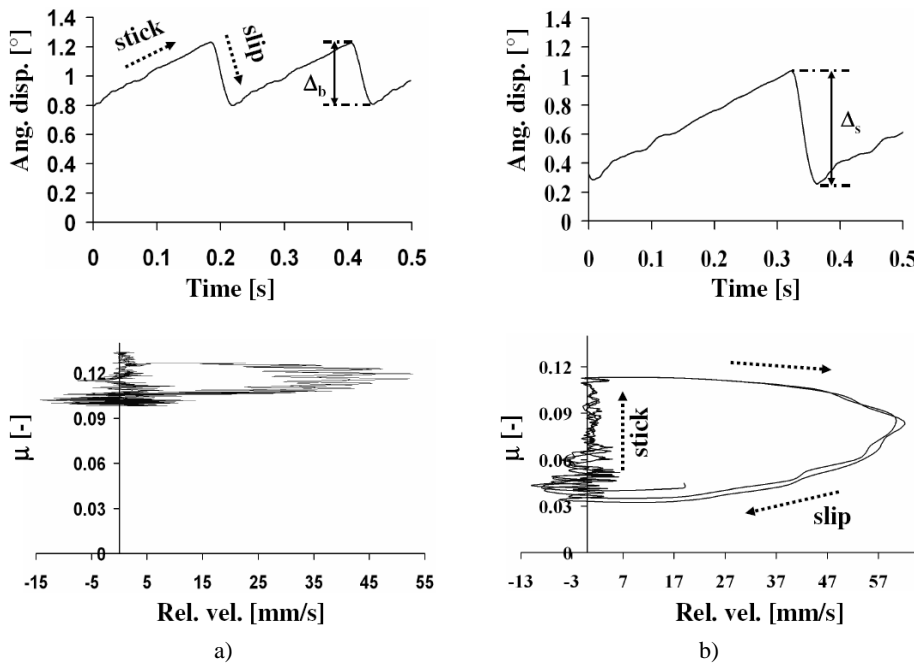


Figure 4. Stick-slip behaviour of PET (a) and PET-P + solid lubricant (b) ( $v = 5 \text{ mm/s}$ ,  $p_N = 17.35 \text{ MPa}$  and test time = 30')

#### 4. Conclusions

In general, lowering the contact pressure tends to increase the coefficient of friction, while adding internal lubrication to the material tends to decrease it.

Stick-slip was found to occur only at the lowest velocity (5 mm/s), but not for all materials. It is known from literature (Van De Velde F. and De Baets P., 1997) that PA6-G is sensitive to stick-slip motion which is also verified during the present study. The same conclusion can be made for PET-P. For all types of POM (-C, -H and with solid lubricant) no stick-slip behaviour is observed for all test conditions.

Impregnation of PET-P with a solid lubricant has a destabilizing effect on the stick-slip behaviour as has been observed above. No immediate and conclusive explanation could be found for this phenomenon as in (De Baets P. et al., 2000) the addition of PTFE had a stabilizing effect on stick-slip motion of pure PET-P.

POM-C impregnated with a solid lubricant is found to perform best under the chosen test conditions, showing the lowest average coefficient of friction in comparison with all the other tested materials and stable frictional behaviour at low velocity. This makes the material most suitable to use in applications operating under high contact loads and low sliding velocities.

## 5. Nomenclature

$p_N$	mean apparent contact pressure	MPa
$v$	linear sliding velocity of steel ring	mm/s
$v_{rel}$	relative sliding velocity	mm/s
$x$	equivalent linear deflection arm	mm
$\dot{x}$	equivalent linear velocity arm	mm/s
$\ddot{x}$	equivalent linear acceleration arm	mm/s <sup>2</sup>
$k$	equivalent linear stiffness of system	N/mm
$m$	equivalent linear mass of system	kg
$t$	time	s
Greek letters		
$\mu$	average coefficient of friction	-
$\Delta$	amplitude of angular deflection vibration	[°]
Subscripts		
b	bulk material	
s	internally lubricated with solid lubricant	
o	internally lubricated with oil	
Abbreviations		
SS	stick-slip	-

## 6. Acknowledgements

This work was by the Fund for Scientific Research Flanders (FWO) under project number G.0225.06. The authors would like to thank Quadrant Engineering Plastics Belgium for supplying the material specimens.

## References

Van De Velde, F. (1998), Characterization of stick-slip movement of rubbing metal surfaces, Doctoral Thesis, Faculty of Engineering (Ghent university).

De Baets, P., Van Parys, F., Kalacska, G. and Zsidai, L. (2000), The friction and wear of different polymers under high load conditions, Proc. 7<sup>th</sup> Int. Conf. on Tribology, Budapest, Hungary, September 4-5, 2000, pp. 237-242.

Zsidai, L., De Baets, P., Samyn P., Kalacska G., Van Peteghem A.P., and Van Parys P. (2002), The tribological behaviour of engineering plastics during sliding friction investigated with small-scale specimens, Wear, Volume 253, pp. 673-688.

Van De Velde F. and De Baets P. (1997), The friction and wear behaviour of polyamide 6 sliding against steel at low velocity under high contact pressures, Wear, Volume 209, pp. 106-114.

Ost W., Tribology and vibrations of wet clutches (2006), Doctoral Thesis, Faculty of Engineering (Ghent university).

## Plastic machine parts of small airplane: application and failure

Rajmund LEFÁNTI, József JANIK, Gábor KALÁCSKA  
Szent Istvan University, Faculty of Mechanical Engineering

### Abstract

Our daily life is strongly connected to the modern materials e.g. polymers and composites. These materials play more and more important role in airplane and aviation technologies. Not only the common places but load-carrying machine elements are produced of light-weight and wear resistant plastics as well. In the aviation the machine reliability especially is important, so, the good friction and wear properties together with increased corrosion resistance and vibration damping ability, as well low mass features are essential. There are many sorts of technical polymers available of which sliding and load-carrying elements can be produced. To choose proper polymers for a given tribological application is not a simple task owing to many different parameters influencing the performance of a polymer sliding element.

### Keywords

small airplane, plastic part, landing gear-leg, shaft support

### 1. Plastic applications in the aviation engineering

Plastic machine elements are often used in the aviation engineering. A special segment of the engineering activity at that field is the maintenance of single-engined- or small aircrafts having some critical elements.



Figure. 1. Polymer aircraft

The figure 1. and figure 2. shows a new single-engined polymer aircraft, which is a designed and built on different composite polymer. The previous releases of such a kind of planes are considered as transitions between the traditional metal-based constructions and the new composite models. That means in the age between 20 – 30 years of a small aircraft we can already find some hardwearing, strongly loaded polymers elements.



Figure 2. Polymer aircraft

## 2. Plastic machine elements are in small plane

Based on the list of the elements produced in the 1960-70-years regarding the commonly used CESSNA family, we can classify the plastic applications.

- Average contact pressure (10 – 50 MPa) applications (e.g. cable sheaves coming from the civil and mechanical engineering). Mainly tough polyamides are applied for that. (fig.2. aileron, side and depth rudder plate moving rope disc)
- High contact pressure moving surfaces: typical the rolling or rolling/sliding polymer surfaces mainly mating with steels. (fig.3., fig. 4.)



Figure 3. Polymer rope disc

- Pure sliding surfaces subjected to severe dynamic impacts (e.g. slide bearings and linear supports of landing-gear leg silent block)
- Covers and housing elements (PP, PE). Typically they are not mechanically loaded but light-weight is essential for them.

It is a fact that many of the small airplanes between 20 – 30 years are still in use worldwide. Comparing the engineering materials built in those old aircrafts to the new design versions shown in figure 1. we can find some typical engineering places to be resolved or redesigned during the maintenance.



Figure 4. Polymer spur gear

### 3. Landing-gear leg support

Studying the register of the maintenance activities a weak point can be found at CESSNA 172 aircraft. As time goes by the reliability of the landing-gear leg support (fig.5 and fig.6) becomes critical and after a certain number of friction load the original support pad cracks and wears extremely fast. This part is considered to be important aviation safety point, nowadays we a good engineering possibility to renew the old structure with better and higher performance engineering polymers.



Figure 5. Position of longing rein on Cessna 172 type aircraft

The figure 6. and figure 7. show the landing-gear leg support.



Figure 6. Landing-gear leg support in the aircraft



Figure 7. The failed PUR component

## References

- Antal – Fledrich – Kalácska – Kozma (1997): *Műszaki műanyagok gépészeti alapjai, Műszaki műanyagok gépészeti alapjai*, 47-79. p.
- Benabdallah H. (2003): Friction and wear of blended polyoxymethylene sliding against coated steel plates. *Wear*, Vol. 254 1239-1246. p.
- Kislinder E. (1999): Polimer súrlódó felületek tribológiai tulajdonságainak vizsgálata. *Gép*, 50 (11) 50-53. p.
- Oláh ZS., Szirmai L., Resofszki G. (2004): A new aspect of the evaluation of diesel fuel lubricity properties. 8th International Conference on Tribology. In: *Proceedings*. 2004. június 3-4. Veszprém 194-197. p.

Zsidai L. et al. (2002): The tribological behaviour of engineering plastics during sliding friction investigated with small-scale specimens, *Wear*, Vol. 253 673-688. p.

[www.quattroplast.hu](http://www.quattroplast.hu)

<http://index.hu/kultur/életmod/balloszog/> Repülőgyár a homokbuckák között

# Aspects regarding the simulation and the application of the finite element analysis in the designing process of the resistance structure of the adipur waste water treatment plants

Mircea LOBONTIU, Georghe Ioan POP,  
Alina Bianca (POP) BONTIU  
North University of Baia Mare, Faculty of Engineering

## Abstract

This paper presents the benefits of the parametric design in the process of ADIPUR waste water treatment systems design made by ADISS company, and the finite element analysis application on their resistance structures behaviour.

## Keywords

parametric design, FEM, waste water, treatment

## 1. Description of the waste water treatment system – adipur

The compact waste water ADIPUR treatment plants – are treating domestic wastewater for schools, camps, camping, hotels, cottages, houses, also for towns up to 6000 people, these plants being built by four basic modules, which, associated reach the maximum capacity .

The waste water treatment plant is designed with continuous supply and advanced filtering. It consists of the following components (see Figure 1):

- The homogenization modulus and the pumping station for waste water;
- ADIPUR cleaning equipment;
- Sludge storage tank.

The homogenization modulus and the pumping station for waste water, consist of:

- Homogenization tank – which is a stainless confection of steel metal underground mounted;
- Manual cleaning grate with 10 mm slots;
- Wastewater pumping station with chopper and steadily low;
- Mixing with air.

ADIPUR cleaning equipment consists of:



The virtual prototypes parameters establish, reduce considerably the modification time needed or even the basic concept replacement.

In addition to other CAD applications as: Autodesk Inventor, SolidWorks, Unigraphics, Pro-Engineering, the Catia V5 product from Dassault System, is considered to be one of the most complete software regarding designing, analysis, 2D documentation preparation and product data management.

Due to the large number of components of this system of purification, we chose to design CAD software Catia V5. Thus, from the basic idea of cleaning was created virtual prototype then were analyzed the assembly and disassembly component parts. In order to verify the behaviour of structures given by the working of the whole biological modulus, the finite element analysis was used.

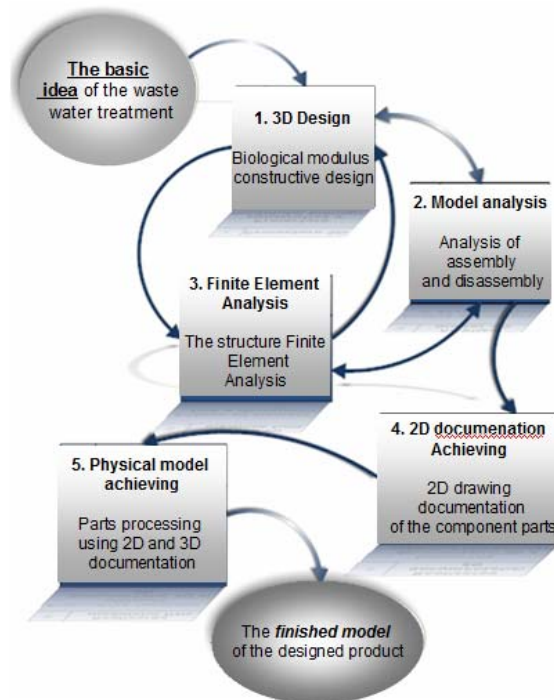


Figure 2. Stages of the designing process of the waste water systems

In this paper it is studied the behaviour in service of the homogenization tank elements when it is filled with water. The achievement of this study was carried out using finite element applications of CATIA V5 R16 and ANSYS Workbench software.

The parametric design of the waste water system allows the resistance structure analysis in terms of the components assembly method. Thus in this paper we will analyze the behaviour of the resistance structure and tank tightening- an essential part of the biological tank (Figure 2).

We consider two cases regarding the tank assembly components: the resistance structure consisting of an OL37 pipes network of 100x100x5 mm<sup>2</sup>.

The two cases of assembling components parts of the basin are:

- A. Between the welded tubes structure and the interior basin sheets which are welded tightening, there does not exist relative movement (they are welded between them) (Figure 4 a);
- B. Between the welded tubes structure and the interior basin sheets which are welded tightening, exist relative movement – friction (Figure 4 b).

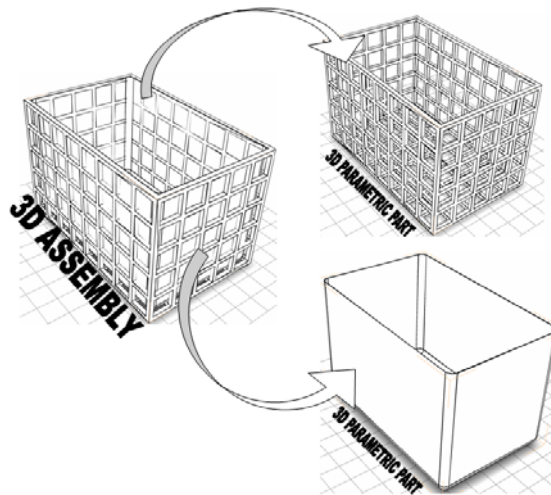


Figure 3. The tank components parametric design

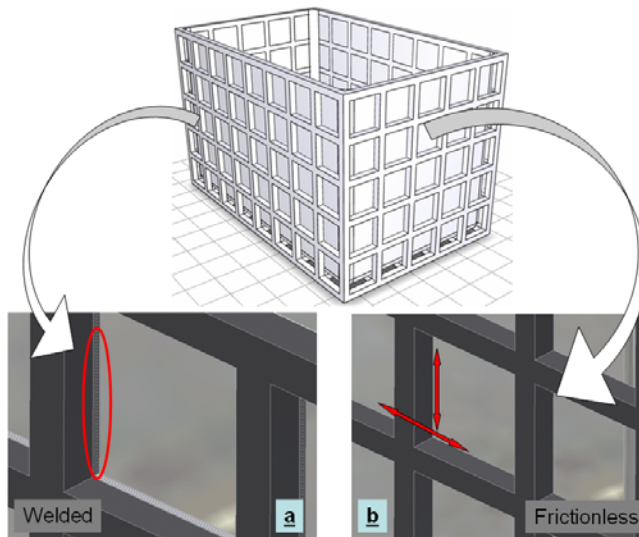


Figure 4. The tubes structure and the interior sheets assembly

In the case B, for the welds is necessary that the material for the tubes structure and for the sheets has to be the same.

The chosen material for these 3D models is stainless steel with the characteristics presented in table 1. These characteristics are used by the ANSYS calculation algorithm.

Table 1. Mechanical characteristics of stainless steel

Stainless Steel – X5CrNi18-10	
Young Modul [Pa]	1,93e+011
Density [Kg/m3]	7750
Tensile Yield Strength [Pa]	2,07e+008
Compressive Strength [Pa]	2,07e+008
Tensile Ultimate Strength [Pa]	5,86e+008

Figure 5 shows the initial conditions applied to the parametric model. On the tank walls which is fixed on its base, it acts, as can be seen in figure, a hydrostatic pressure of approximately 28 MPa - on the bottom of the tank, but on the top, its value dropping to zero. These conditions are identical for the two situations: in which the sheet and the tube is welded, and the other – in which between the two there is relative motion.

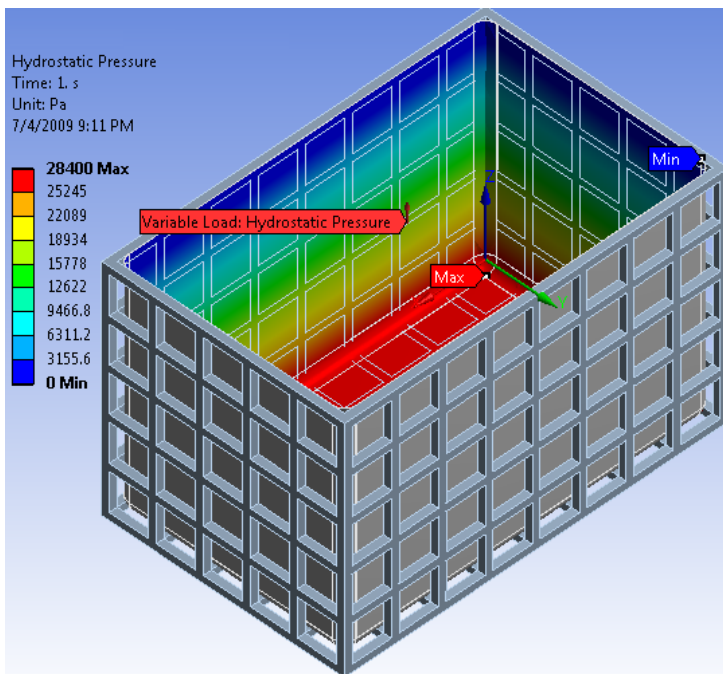


Figure 5. The initial conditions applied to the tank

In Figure 6 are graphically indicated the results obtained from finite element analysis of the tank structure, where, between the tubes and sheets exists welding. It can be noted that the area with the largest deformation is concentrated in the upper tank although the maximum pressure is on the base.

These strains occur due to lack of support points at the top.

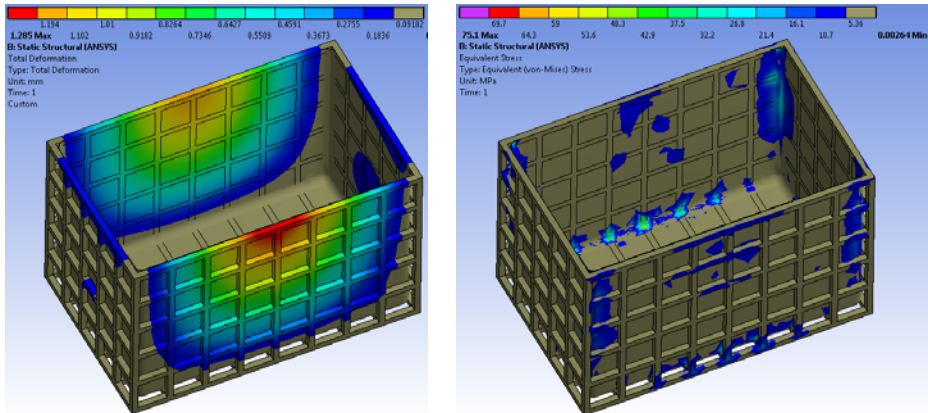


Figure 6. The strains and stress state within the tank structure

In Figure 7 are shown graphically the results obtained from finite element analysis of tank structure, where, between the tubes and the sheets there is a relative motion.

The reason for using this method of assembly is the economical one (materials used may be different).

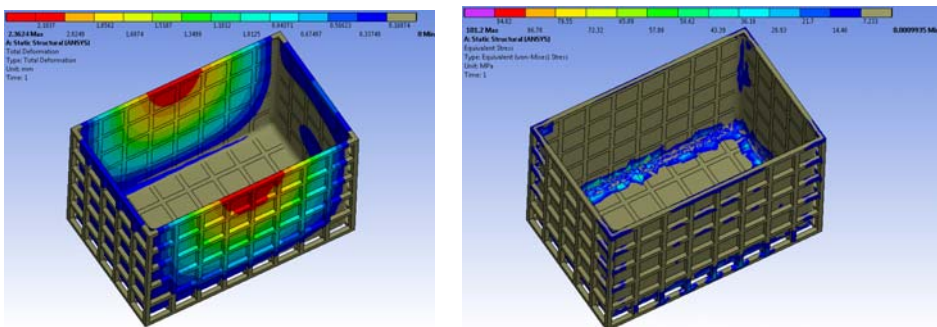
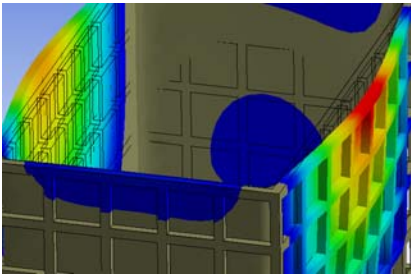
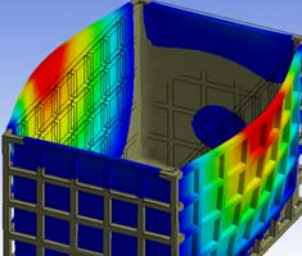
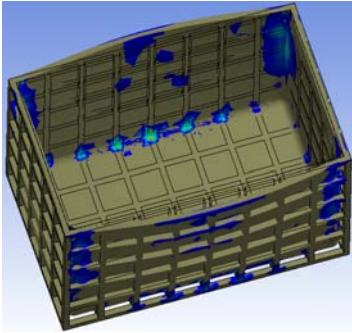
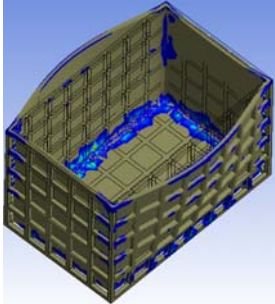


Figure 7. The strains and stress state within the tank structure

Due to relative movement between the two parts of the tank, we have observed a double increase of deformation, and a tensions increase with about 25 MPa.

Regarding the stress distribution, this is concentrated at the bottom of the tank, in the second case, by contrast, we have a better distribution in the first case of tension (Table 2).

Table 2. The maximum strains and stresses

Assembly type	A. By welding	B. Relative motion between parts
Maximum strain	 <p>Maximum displacement is 1,28 mm.</p>	 <p>Maximum displacement is 2,36mm</p>
Maximum stresses	 <p>Stress maximum value is 75, 1 MPa.</p>	 <p>Stress maximum value is 101 MPa.</p>

Note: the graphical representation is amplified by 200%.

Following the two situations analysis of the tank components, result that the assembly manner of the two components of the tank is particularly important in terms of strains and stresses occurring in them.

Since the finite element analysis is a part of the whole process of designing and using 3D parametric models, we can optimize the structure in parallel both minimize strains and tensions, and economic factor in terms of consumption and type of the material used.

### 3. Conclusions

1. Using parametric design and virtual prototypes, has a great influence on the time and on the budget to develop a product.

2. Using the finite element analysis in the equipment design for waste water treatment is useful because it allows the designer to analyze and determine the component benchmarks in terms of space and the environment they work in a minimum time interval.
3. The influence of the assembling ways of the resistance structure components, on the strains and stresses is evident, and these results may be adapted with minimal resources and other components of such equipment.
4. As direction of research using the parametric design in conjunction with finite element analysis, we can study too, other dimensions of the resistance structures of different technological equipment.

## References

Zienkiewicz, O., C., Taylor, R., L., *The Finit Element Method, Vol.2, Solid Mechanics*, 2000, Elsevier Butterworth-Hienemann, ISBN 0 7506 6321 9.

Hutton, D., v., *Fundamentals of Finite Element Anlaysis*, 2004, McGrawHill, ISBN 0-07-112231-1.

Stolarski, T., Nakasone, Y., Yoshimoto, S., *Engeneering Analysis with ANSYS Software*, 2006, Elsevier Butterworth-Heinemann, ISBN 0 7506 6875 X.

Marin, C., Hadar, A., Popa, I., F., Albu, L., *Modelarea cu elemente finite a structurilor mecanice*, 2002, Editura Academiei Române, ISBN 973-27-0957-X.

POP, GH., I, BONȚIU (POP) ALINA BIANCA, *CAD and FEA optimization of ADIPUR Equipment*, ERIN, Ostrava 2009.

# Special algorithm of the Potts-model for the reconstruction of liquid foam structure

Ibolya ZSOLDOS

Szent Istvan University, Faculty of Mechanical Engineering

## Abstract

In the case of the liquid foams the MRI imaging method has a problem: only the edges can be seen and the surfaces of the bubbles are not visible in the images. The problem is solved by a special reconstruction algorithm of the Potts model in 2-D case where the vertexes are known from an MRI image and the edges of the cells have to be reconstructed. We have shown that the similar special algorithm of the Potts model has an applicability limit in general 3-D froths because of the existence of the so called unfavourable growth directions. However the algorithm has to work well in the case of real liquid foams where the Plateau law is valid for the angles at meeting surfaces and edges in the cell system.

## Keywords

foam, cell, modelling

## 1. Introduction

Investigation of the foam structures is very interesting research field because the foams show a very interesting dynamical behaviour. To solve the laws of this dynamical behaviour motivates a lot of researcher. For example the liquid foams exhibit a complex dynamics in which gas passes from bubbles of higher pressure to lower pressure bubbles. Since smaller bubbles tend to have higher pressures because of geometric constraints, bubbles gradually disappear and the pattern coarsens. The same general phenomena with additional complications occur in metallic polycrystals, sintered ceramics, ferromagnets, micelles, ferrofluids and biological tissues and organs. Domain growth is a common feature of most of these patterns, though the time scales differ depending on the diffusion mechanisms controlling boundary motion. If the initial conditions are reasonably homogeneous, most of these materials develop geometrically similar structures. Thus, understanding the kinetics and geometry of a coarsening foam can provide information a broad class of important materials.

Investigating the three-dimensional structure and dynamics of foams remains an important problem. Foam rules *e.g.* the relationship between a bubble's shape and its rate of growth or shrinkage (its growth law) are not known exactly today,

chiefly because determining the three-dimensional structure of a foam is difficult. The naked eye cannot observe foam structure and dynamics because foams scatter light extremely effectively and most experimental techniques do not give enough information to reconstruct the real three-dimensional structure. Optical tomography is only possible for very dry foams, in which the Plateau borders but not the faces are visible. Magnetic resonance imaging (MRI) can also reveal a foam's three-dimensional structure. MRI measures the nuclear magnetic resonance (NMR) signal from protons in the hydrogen in the water present in the sample. However, since foams contain very little water, which mostly concentrates in the Plateau borders, the MRI signal is very weak elsewhere so we obtain an image of the Plateau borders, a skeleton of the foam.

The raw image is missing crucial information, *e.g.*, the bubble volumes, because of the absence of the bubble walls (films). The same problem of 3-D image segmentation can occur in confocal microscopy of cells, CT, MRI and ultrasound imaging of tissues and X-ray and neutron imaging of solids. An added difficulty is that the signal-to-noise ratio of such images is often close to one.

Vasconcelos et.al. have created a semi-empirical method to reconstruct foam structure in 2-D. They started from 2-D MRI images of foams where only the vertexes were visible and they reconstructed the missing edges with their algorithm based on the Potts model. In this paper we report about the first experiences of the 3-D reconstruction algorithm where the missing surfaces have to be reconstructed.

## 2. The 3-D algorithm

The 3-D reconstruction algorithm is built similar to the 2-D case. It is based on the Potts model which works with the minimization of a special case of the Hamiltonian.

The Potts Model is a generalization of the Ising model to more than two spin components. Although initially proposed to study critical phenomena in statistical physics, the Potts Model finds a wide variety of applications, including the simulation of metallic grain growth, soap foams, magnetic froths and biological cells.

We map the foam structure onto a cubic lattice containing  $N_x * N_y * N_z$  sites. Each lattice site contains an integer  $\sigma$  (a spin) which corresponds to a particular bubble. Number of bubbles = number of spins,  $\sigma=1, 2, 3, \dots, N$  where  $N$  is the number of bubbles,  $N \ll N_x * N_y * N_z$ . The boundary between two bubbles is the set of links between lattice sites associated to the spins of those bubbles. The Potts Model generally has two steps: In the first step we define the seeds of the cells, the centres of the bubbles assigning several sites around the bubble centres with  $\sigma$ . Every other site has  $\sigma=0$ , that means this site does not belong to any bubbles initially. In the second step we run the numbers of Monte Carlo steps. In a Monte Carlo step we select the boundary sites (initially: around the seeds) at random and randomly propose to change their spin to the value of one of the

neighbouring spins. If the resulting change of energy is less than or equal to zero, we accept the new spin configuration. However if the change in energy is positive, we accept the new configuration with Boltzmann probability:

$$P = \exp\left(-\frac{\Delta E}{kT}\right) \quad (1)$$

where T is the temperature assigned to allows for thermal fluctuation to overcome local energy minima. We define a Monte Carlo step as a sequence of  $N_x * N_y * N_z$  random site selection. The resulting bubble structure evolves after numbers of Monte Carlo steps.

The Hamiltonian including surface energy, the volume constraint and the so called pinning field has the following form in our special case ( $E=H$ ):

$$H = J \sum_{i,j} (1 - \delta_{\sigma_i, \sigma_j}) + \lambda \sum_k (V_k - V_k^t)^2 - \gamma \sum_{i,j} \left(1 - \delta_{\sigma_i, \sigma_j} \frac{1}{r_i}\right) \quad (2)$$

The first term in Eq. (2) accounts for the surface energy. The sum in i runs over all the sites in the lattice and the sum in j runs over sites neighbouring i. The parameter J sets the energy/unit surface area. The second term is the volume constraint. The sum in k runs over all the bubbles in the pattern.  $\lambda$  is a parameter specifying the strength of the volume constraint,  $V_k$  is the current volume of the kth bubble, and  $V_k^t$  is the target volume of the same bubble, because of the energy, each bubble's volume is usually smaller than its target volume during its growth. The third term is the assurance that the cells growth towards the edges (known from MRI layer images) in the Potts model.  $F(x,y)=\gamma/r_i$  is a continuous attractive pinning field around a point size at each known edge pin in the source image.  $\gamma$  is a constant that determines the pinning coupling strength and  $r_i$  is the distance from the site i to the closest edge pin.

### 3. Results

We are in the first stage of this research work. We have built the 3-D algorithm, we have created their computer codes and we have some experiences on their run.

First we have found that the reconstruction method based on the Potts model has a geometrical limit, it can not be applied in general case. In the Potts model a cell grows around its seed from site to site to different directions defined by the cubic lattice. The directions towards the known edges are the most important growth directions because the cell has to grow towards the known edges. In the Potts model the third term in Eq. (2) works so that the known edges attract the cells during the growth. In general case there can be unfavourable growth

directions where a cell can grow toward the edges of a neighbour cell and we show this applicability limit on an example of a random Voronoi froth.

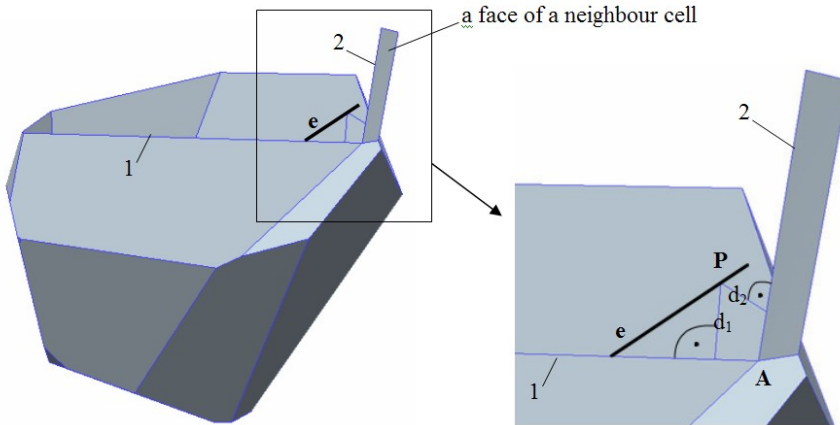


Figure 1. Example of the unfavourable growth direction for a random Voronoi cell.

In Figure 1 a random Voronoi cell can be seen. In order to see inside of the cell, its top surface is removed. We assume that the edges of the cell are known from MRI and the surfaces should be reconstructed. Let us assume that the cell grows along the direction shown by the thick black line signed by  $e$  (defined by the cubic lattice in the Potts model). At the beginning of the growth this is a favourable growth direction because if the cell follows it from inside it will be closer and closer to the edge signed by 1 (edge 1 is the closest edge for the sites along the given direction in the Potts model). This tendency is valid until the cell gets to the point  $P$  which is closest to the edge signed 1 (the distance between edge 1 and line  $e$  is signed by  $d_1$  in Figure 1). But here this point is already closer to edge signed 2 which already belongs to a neighbour cell (the distance between edge 2 and line  $e$  is signed by  $d_2$  in Figure 1 and  $d_2 < d_1$ ) and the attractive field of edge 2 is stronger than at the point  $P$ . Accordingly if the cell grows along this direction it will grow in the neighbour cell. The line  $e$  is an unfavourable direction in this special case of the Potts model. The existence of the unfavourable growth directions can be explained with the fact that the angles between the neighbour cell faces can be small in general froths. For example in Figure 1 the angle between the removed top face and the neighbour cell face is small (about  $90^\circ$ ) and the connecting edges at the vertex  $A$  have small angles, too.

In the case of the real liquid foams the Plateau law is valid which means that the angles of the meeting surfaces at an edge are  $120^\circ$  and the edges meet at tetrahedral angles. We mean that there are not unfavourable growth directions in the case of the real liquid foams (because of the large surface angles) and the new 3-D reconstruction method has to be applicable for real liquid foams. We

have run the new algorithm for the Kelvin froth. Every cell of the froth is uniform as it can be seen in Figure 2 a and b.

We assume that the edges of the cells are known from MRI. The first step of the Potts model is to define the seed of the sells. A cell seed is given as 27 sites around the centre of a given cell in our example, Figure 2 c. In the second step of the Potts model we have run about 100 Monte Carlo steps and after the run the shape of the cells has developed. The Kelvin froth could be reconstructed exactly, Figure 2 d. The reconstructed cell surfaces are planes because every cell has the same measure.

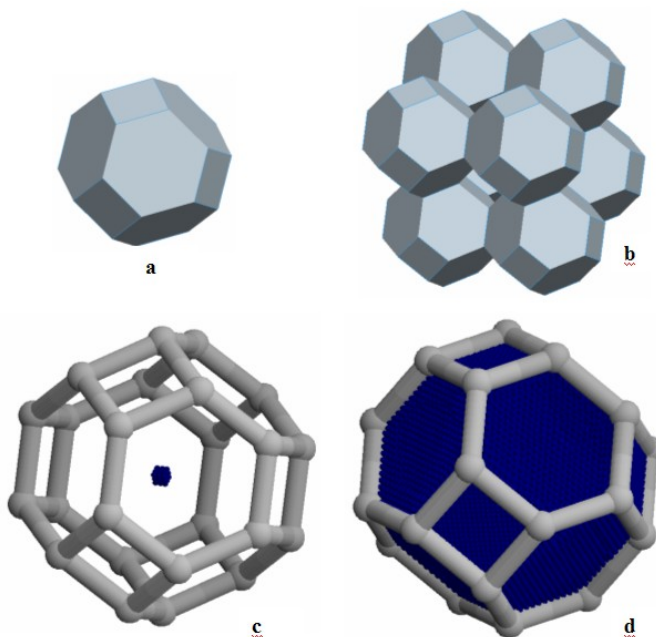


Figure 2. a: the Kelvin cell, b: the Kelvin froth, c: the cell seed for the starting of the Potts model, it is assumed that only the edges are known, d: the reconstructed cell is the exact Kelvin cell.

One of the advantages of the Potts model is that the curvatures of the cell surfaces can be shown with it, as well. The Kelvin froth is not enough to show this advantage. Curved surfaces occur in foams consist of bubbles having different sizes. The continuation of this work will be the studies of real liquid foams starting from their real MRI images.

#### 4. Conclusions

The special reconstruction algorithm of the Potts model has an applicability limit in general 3-D froths because of the existence of the so called unfavourable growth directions. However the algorithm has to work well in the case of real liquid foams

where the Plateau law is valid for the angles at meeting surfaces and edges in the cell system. We have shown a successful run result for the Kelvin froth where every cell has the same size. The continuation of this work will be creating run results of the new algorithm starting from MRI images of real liquid foams.

## 5. Acknowledgement

This work was supported by OTKA grants K 73776 in Hungary. The authors express their thanks to James A. Glazier and Ariel Balter from the Biocomplexity Institute of the Indiana University for their helpful consultations.

## References

- D. Weaire, N. Rivier, Soap, cells and statistics – random patterns in 2 dimensions, *Contemp. Phys.* 25 (1984) 59–99.
- H.V. Atkinson, Theories of normal grain-growth in pure single-phase systems, *Acta Metall. Mater.* 36 (1988) 469–491.
- G. Reiter, Dewetting of thin polymer-films, *Phys. Rev. Lett.* 68 (1992) 75–78.
- D\_Arcy W. Thomson, *On Growth and Form*, Cambridge University Press, Cambridge, 1942.
- K.J. Dormer, *Fundamental Tissue Geometry for Biologists*, Cambridge University Press, Cambridge, 1980.
- V.E. Fradkov, A.S. Kravchenko, L.S. Shvindlerman, Experimental investigation of normal grain-growth in terms of area and topological class, *Scripta Metall. Mater.* 19 (1985) 1291–1296.
- D.J. Durian, D.A. Weitz, D.J. Pine, Multiple light-scattering probes of foam structure and dynamics, *Science* 252 (1991) 686–688.
- D.J. Durian, D.A. Weitz, D.J. Pine, Scaling behavior in shaving cream, *Phys. Rev. A* 44 (1991) R7902–R7905.
- C. Monnereau, B. Prunet-Foch, M. Vignes-Adler, Topology of slightly polydisperse real foams, *Phys. Rev. E* 63 (2001), Art. no. 061402.
- C.P. Gonatas, J.S. Leigh, A.G. Yodh, J.A. Glazier, B. Prause, Magnetic-resonance images of coarsening inside a foam, *Phys. Rev.Lett.* 75 (1995) 573–576.
- I.F.Vasconcelos, I.Cantat, J. A. Glazier, Dynamics and topological aspects of a reconstructed two-dimensional foam time series using Potts Model on a pinned lattice, *Journal of Computational Physics* 192 (2003) 1-20
- F.Y. Wu, The Potts Model, *Rev. Mod. Phys.* 54 (1982) 235–268.

# Machining: some new aspects

Attila KÁRI-HORVÁTH, István VALASEK  
Szent Istvan University, Faculty of Mechanical Engineering

## Abstract

I examine in this paper the machining of steels by means of turning process, the chip removal and friction phenomenon during machining. I deal with energy's balance sheet of cutting of steel and I suggest a newer direction the machining technology based on friction and energetic effects.

## Keywords

machining, turning, chips, energy during cutting, friction

## 1. Introduction

The energy applied in cutting and the changes owing to this energy belong to macrophysics, the frictional process – presenting the vital part of cutting – belongs to microphysics. During my present-work I deduced from this the practice widely used in cutting nowadays as well as the direction of development.

The development of elements is not equal in the machine – cutting tool – cooling lubricant – workpiece system, but one of the elements always enforces the development of the other system-elements, which result in the collective system development. Researchers established that in certain cutting technologies the use of cooling lubricants is inevitable therefore were proved with experiments the necessity and economic efficiency as well as the realization of the minimal quantity lubrication. That process initiated the development of machine-tools and technologies, too.

### *Cutting with geometrically determined cut*

Cutting is a method of exact machining, the workpiece gets its desired shape, dimension by removing the machining allowance in smaller- bigger particles till the workpiece gets its planned shape. During cutting the workpiece and the cutting tool move on one another under force until the desired amount of material layer becomes detached from the workpiece. That detached getting out from the machining zone layer stays in a more or less unbroken piece. That detached layer is the chip. Complicated stress and deformation states are present in the cutting zone, Fig.1 shows this.

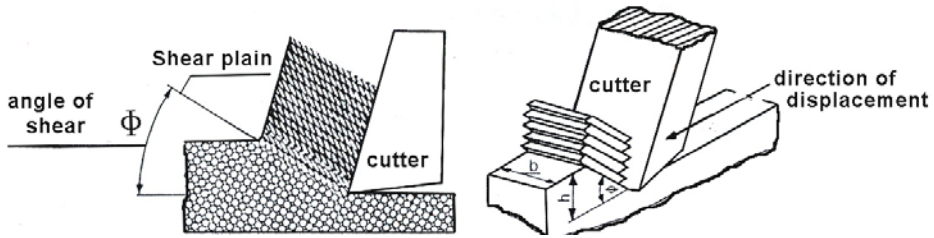


Figure 1. Process of cutting (the inside friction)

- As the cutter penetrates into the workpiece material it plastically deforms the material particles near the edge of the cutter. The particles slide on one another generally at one definite plane (shear plane) in the „h” thick layer. The chip-removal can be divided into three characteristic phases from a tribological point of view. These are:
- Internal friction arises in the material machined as a result of the sliding of particles on one another along the shear plane. The stress in the material layer near the edge of the cutter will be higher and higher, it reaches a critical level that the material can't resist and the material ruptures. That material rupture is called unconditional rupture, as it happens in every case independently from the cutting conditions. Two new surfaces are formed during material rupture: the chipped surface and the inner surface of the chip. The rupture can extend to the shear zone at certain conditions but only after the completion unconditional rupture. This is called conditional rupture.
- The removed particle (chip) slides mainly on the tool-face and a lesser amount on the tool-back from the deformation zone while friction resistance and wear are formed. This is called solid (external) friction. (Fig.2.)
- Fusions and solid material particles are also formed at the cutting edge of the tool, some part of which leaves between the tool-back and the fresh-machined surface, causing back-wear and surface damage.

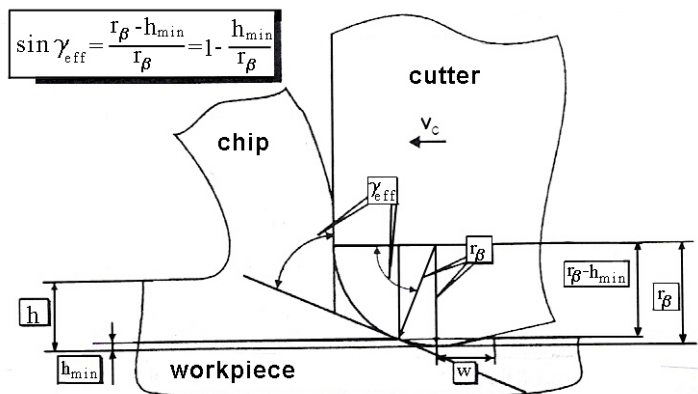


Figure 2. The solid-state friction

### Energy balance of chipping

As it is known the work necessary to overcome the friction (regardless of the type of that the friction whether internal or external) is a loss in the energy balance. Examining the further fate of the friction it can be established that it is a dissipation process, that is conversion of energy takes place on the friction surfaces and as a consequence the friction-work almost completely changes into friction-heat. Translating that conversion of energy into numbers: ~97%-of the cutting-energy (W[kWh]) changes into heat-energy (Q[J]) (Fig.3.) while the remaining ~3% stays in the workpiece as internal stress. (Fig.4.)

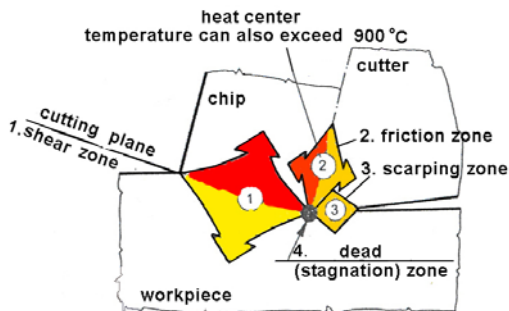


Figure 3. The main heat flows in the chip detachment zone

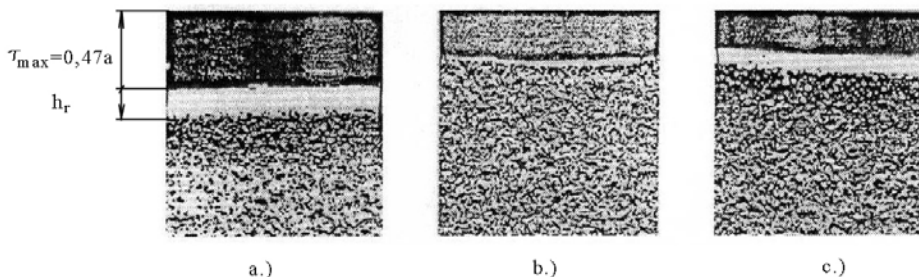


Figure 4. Change of the surface tensile stress in translational plain  
 a) dry process, b) MQL-lubrication, c) 5 v % emulsion

In the first stage of chip-removal the cooling, in the second stage the lubrication and in the third stage the detergent power has dominant effect. It to determine is not enough the amount of heat being formed the analyses that, it is also necessary to know which cutting element absorbs the heat flows. It is vital to consider the total amount of calculate heat flowing into the chip, which is the sum of about 50% of the heat forming in the cutting plane and about 60% of the heat forming between the chip and tool-face and about 25% of the heat which is formed from the rupture work. The amount of heat flowing into the tool is very little, that amount of heat is considerably less compared with the amount of heat, which remains in the workpiece or flows into the chip of the workpiece material

regardless and cutting factors. It is clear from the Fig.3 that the gross of heat about 60-80% is formed in the shear zone and 60-90% of the total heat is outgoing with the chip.

It can be seen in Fig.4., that the amount and depth of  $\tau_{max}$  as well as the width of lattice defect ( $h_r$ ) change the surface tensile stress. The workpiece surface according to fatigue life decreases with the increase of  $\tau_{max}$  and  $h_r$ .

The lattice defect can be reduced or can be eliminated by reducing the cutting force ( $F_c$ ). The methods of reducing the cutting force:

- reducing the chip area (A)
- increasing the cutting speed
- reducing the heat extraction regulated.

Friction therefore causes energy loss, compiled with easily separable energy dissipation in some sections of the process. It follows that at high temperature cutting guided instead of general cooling, which is unmanageable localized cooling has to be applied. Such cooling can be put into practice at atom or molecule level. In further development of this idea we studied the coefficients applied at the deduction of the Planck-rule for the absolute blackbody radiation that Einstein described.

The study of the energy introduced into the cut and the changes in consequence of that belongs to macrophysics, the frictional process - presenting the vital part of the cut – belongs to microphysics. Fig.5. shows the arrangement of macro- and microphysics in the science of physics.

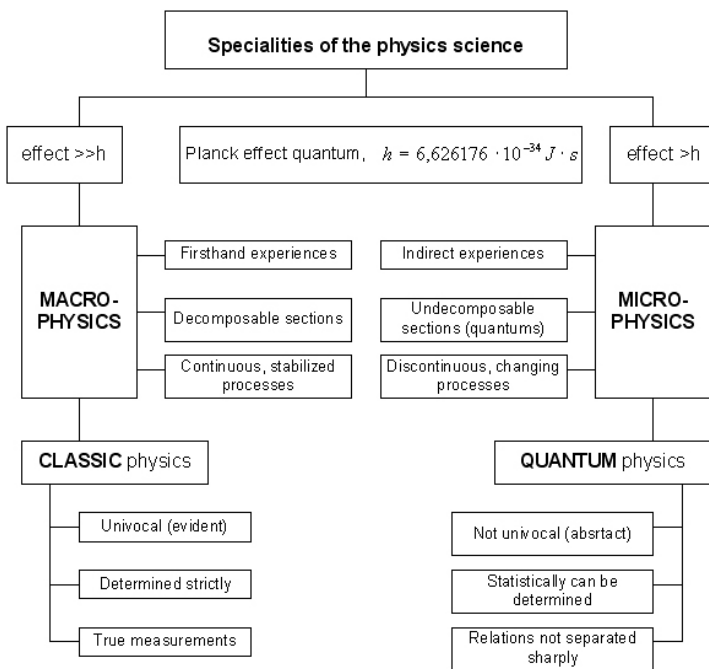
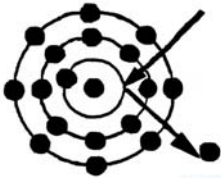


Figure 5. Specialities of the physics science

- The coefficients give the probability of three events that the atom or molecule:
- absorbs a photon from a ray of light (absorption) (Fig. 6.)
  - releases a photon upon the effect of incident light-ray (induced emission)
  - regardless whether or not light falls onto the atom, it emits a photon (spontaneous emission).



Electromagnetic waves

Visible light ( $\lambda = 10^{-6} m, f = 10^{14} - 10^{15} Hz$ )

Ultraviolet ( $\lambda = 10^{-6} - 10^{-8} m, f = 10^{15} - 10^{17} Hz$ )

X-ray ( $\lambda = 10^{-9} m, f = 10^{17} Hz$ )

Photon or photon effect

The photon energy:  $E = h \cdot f$

where:  $h$  – Planck constant ( $h = 6,626176 \cdot 10^{-34} J \cdot s$ )

$f$  – the photon frequency

Figure 6. Photon emitted by the effect of light (Csurgay, 1997)

In other words, in MQL-cooling the cooling effects accompanying the behaviour change of atoms and molecules following the impact of electromagnetic waves are used rather than the thermodynamic feature and kinetic energy of the material aggregation.

#### Conditions of the chipping

Cutting force can be measured during the cutting technology. The calculation method by which the important heat-energy can be obtained was worked out by Dr. István Valasek (1. table).

The calculations reveal that the power demand of part manufacturing is extremely high, in numbers  $E = 43$  GJ, which energy can meet 45 grey cast-iron, or tons of it is equal to one year power demand of two average households! In conclusion the power demand of part manufacturing is very high. I show the standard Ck60-steel specific energy consumption plotted against the change of chip thickness in Fig.7.

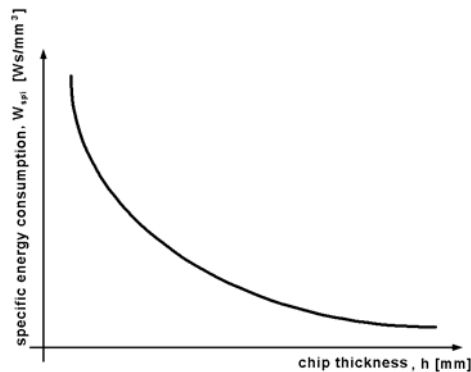
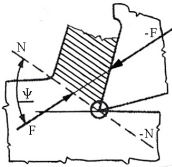
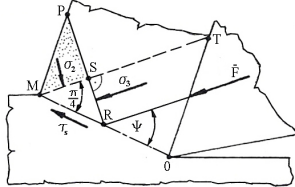
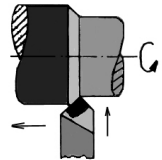
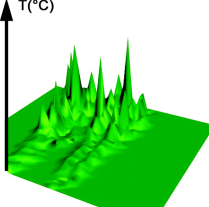
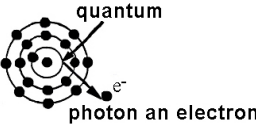
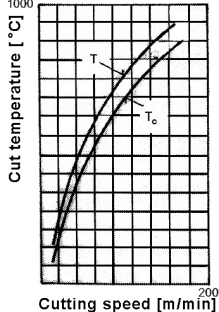


Figure 7. The specific energy-consumption at function of the chip thickness

Table. 1. Physical interpretation of the energy-process

1. Force, $F$ [N]	2. Specific cutting force, $k_c$ [N/mm <sup>2</sup> ]	3. Specific cut job, $W$ , [Ws/mm <sup>3</sup> ]	4. Energy	5. Conversion of energy	6. Heat energy, $E$ [J] Temperature, $T$ [°C]
					
<p>The chip-root is kept in balance by <math>F</math> forces equal in magnitude but opposite in direction from the tool-face and from the shear plane.</p>	<p>Cutting force effect on the theoretical chip area unit.</p>	<p>Work needed per unit volume to cut material.</p>	<p>Energy marks the capability of change in general meaning, and it marks the working capacity in physics. The energy of a certain physical system can be given with that work-quantity (<math>W</math>) by which it can be brought to this stage from some kind of initial stage.</p>	<p>Coefficients applied at the deduction of the Planck-rule describing the absolute blackbody by Einstein. They give the probability of that three events whether the atom or molecule:</p> <ul style="list-style-type: none"> <li>a) absorbs a photon from a ray of light (absorption)</li> <li>b) releases a photon upon the effect of incident light-ray (induced emission)</li> <li>c) regardless whether light falls onto the atom, it emits a photon (spontaneous emission).</li> </ul>	<p>The temperature is the amount of an objects heat energy capacity; the heating or cooling can be measured, and given by numerical value. The temperature is an intensive state-decider, it characterizes the macroscopic and microscopic condition of material simultaneously. It is a sensible thing on macroscopic level. Microscopically the objects temperature is directly proportional to the average kinetic energy of the particles comprising it.</p>
<p>Macrophysics</p>			<p>Microphysics</p>		

It is clear from the diagram that if the chip thickness increases then the specific energy consumption decreases during cutting.

The shear strength of the material can be also starting data determining the components of cutting force. Shows this Fig. 8.

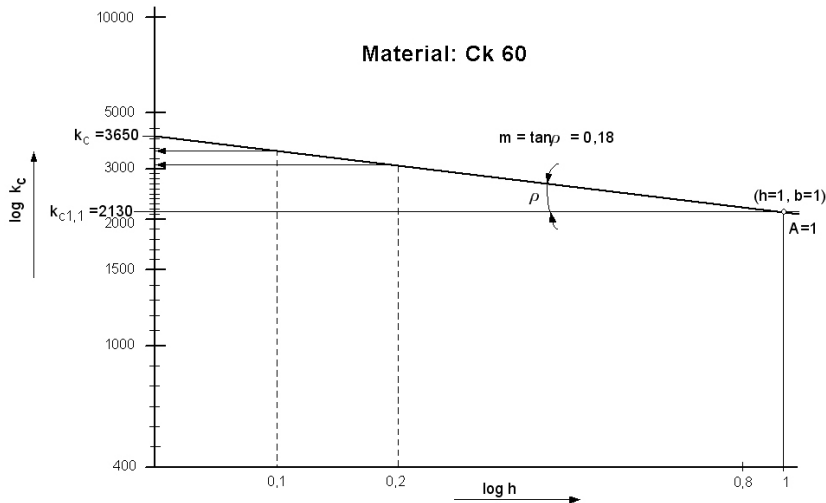


Figure 8. Definition of the  $k_{c,1,1}$  factor

It can be seen in Fig.8. that while the maximum value of forming during material testing is one unit, it is 3-4 times higher during cutting. Shear strength increases with the increase of the forming phase. So the shear strength of the material is always higher at cutting than at material testing and it changes as the function of relative deformation. It can be also established that the shear angle increases substantially with the increase of the strength, so the connection between shear strength and specific cutting force is not linear.

### Optimization of the chipping

The next question that emerges is: „How is it possible to make an advance?”

The development of present techniques would be the first alternative, where the automatization of machine-tools should be increased, multi-function coatings should be produced by developing a new generation of hard and tough tools, by developing colloid and bio-stable emulsions, in other words by increasing the efficiency of cutting and raising productivity. We must say NO to this alternative, because the items listed can be reached only with very high expenditures. The other alternative is searching new ways. including: adequate increase of the cutting speed  $400 < v_c < 1200$  m/min with renewed machine-tools, reduction of the chip area and cooling intensity (for example: partial and localized cooling by regulating the kinetic energy of molecules and quantum instead of using tons of emulsions).

Progressing further on the second alternative, it can be declared that the paradigm changing of cutting technologies have started.

The goals can be outlined as the following:

- increasing productivity
- eliminating lattice defects
- decreasing then eliminating the use of cooling lubricant
- decreasing losses
- minimizing environmental burden.

To fulfil the goals the followings are needed:

- $n = (8 - 12)10^4 \text{ min}^{-1}$  rev. machine-tools
- suitable tools
- chip area reduction
- modification of the kinetic energy of molecules and quantum
- substantially reducing the internal and external friction
- direct consequence of the changes.

There is a repeated contradiction in the experiments. Namely, the measured equilibrium temperature was  $\sim 300^\circ\text{C}$  lower at the thermal equilibrium than the one calculated for the orthogonal cut. The phenomenon was recurring, therefore physicists were drawn in to find out the cause of this abnormality. The physicists believe that a part of the environmental fluids (cooling lubricant and air) is ionized at the cutting temperature and pressure thus generating an electrical wind with a high cooling effect. The phenomenon was published in the international literature, and the Cooling-Lubrication Committee of Comecon took it into its working program. Five countries took part in the work of the Committee, Hungary was in charge of coordination. The Committee facts and data analysed the subject-matters being at disposal at that time, set the course of cutting development after further test- results. Fig. 9. displays the development conception.

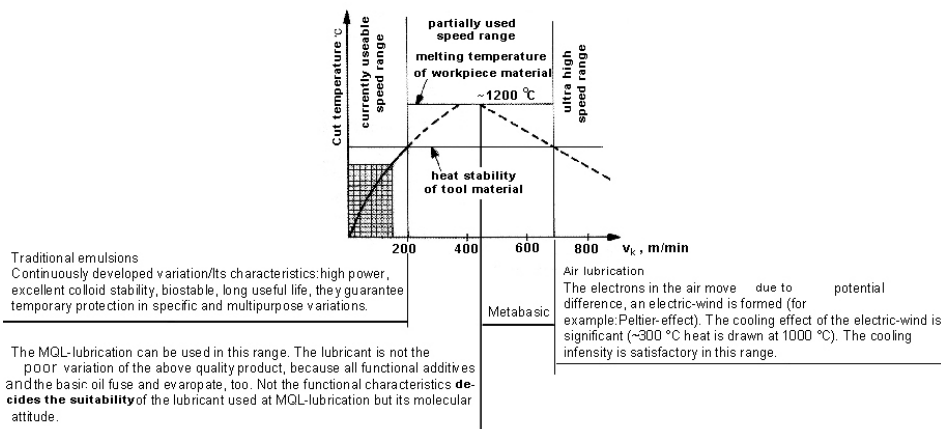


Figure 9. The cutting temperature (T) change as a function of cutting speed (v) in the case of steel workpiece and carbide-tool

The heat stability of the tool set limit to the increase of cutting speed. That hardness belonging to the tool critical temperature which is just enough for chip removal. If the tool material and/or its cladding makes the rise of cutting temperature possible with the increase of cutting speed, then a cutting speed ( $v \sim 400$  m/min) can be reached, at which the workpiece becomes soft in the shear plane, and melts at the contact point. When the workpiece melts, the cutting force reduces and that amount of heat part of the work needed for the absolute rupture also decreases, finally the cutting temperature from  $v \sim 450$  m/min cutting speed also starts decreasing. The tool can better endure that decreasing temperature, so there is no limit from the tool side for further increasing the cutting speed.

The possibility of further developments is limited by the available machine-tools, as the  $n = 60\,000 - 80\,000 \text{ min}^{-1}$  rev. needed can't be accomplished on them. It would be desirable, on the one hand, because the next optimal cutting point is, where the excess heat at chip removal does not exceed  $300^\circ\text{C}$ , which is transported safely by the electric wind. (Fülöp Lenard during the experimental test of photoelectric effect in 1899 proved that the particles leaving the illuminated metal surface were identical to electrons discovered by J. J. Thompson. In 1902 he verified by experiments that the energy of electrons did not depend on the intensity. According to Einstein the energy linearly depends on frequency, and the incline of graphs lines representing the linear dependence is the same for various metals.)

On the other hand, using high cutting speed results in high productivity so satisfactory cutting output can be reached by reduced chip area removal, too. By removing small chip area the surface fatigue of materials can be improved. Since at removing large chip area initial cracks are formed between material planes in that plane where the surface tensile stress and mainly tangential stress is maximum.

### *The research program*

Research program has been set up to reveal the MQL-lubrication process, by which we want to get answer for the following questions:

1. Results comparing dry- emulsive- and MQL-lubrication and their analyses.
2. The effects of additive, laser and visible light on MQL-lubrication.
3. The effect of viscosity on MQL-lubrication.
4. The effect of viscosity and laser on MQL-lubrication.
5. The effect of viscosity and visible light on MQL-lubrication.
6. The effects on the MQL-lubrication of further lubrication-characteristics, for example: structural group-composition, flash point, vapour pressure etc., different additives as for example: various fatty acids, alcohol ethoxyl-groups, lauryl alcohol.
7. Analysis and comparison of the effects of two types of typical synthetic oil containing (C,H and C,H,O):
  - with mineral-oil base lubricants



Table 2. During experiments used lubricants

Experimental code	ISO VG viscosity group	Type and character of the unguent
E1-A	ISO VG 32	complex doped mineral oil
E2-A	ISO VG 32	complex doped mineral oil
E3-S	ISO VG 32	complex doped synthetical oil
M1-32	ISO VG 32	aliphatic alcohol mixture
M2-2	ISO VG 2	C14 n-paraffin
M3-2	ISO VG 2	C14 n-paraffin + 8 v% lauryl alcohol
M4-5	ISO VG 5	mixed base mineral oil
M5-5	ISO VG 5	mixed base mineral oil + proper dopes
M6-15	ISO VG 15	mixed base mineral oil
M7-32	ISO VG 32	mixed base mineral oil
M8-32	ISO VG 32	poly- ( $\alpha$ ) - olefin
M9-46/68	ISO VG 46/68	B 01/40 poly-alkylene-glycol

### *The instruments of the experiment*

#### *Tool used for the experiment*

I have chosen „Sandvik” titanium-nitride coated (Mark: HC/TiN, DIN/ISO 513 - CNMG 1204 08 PF 4015) rotatable insert which I have fixed into 20x20 insert holder (PCLNR 2020K 12 ( $\gamma = -6^\circ$ ,  $\lambda_s = -6^\circ$ ,  $\kappa_r = 95^\circ$ )).

#### *The workpiece*

The workpiece quality: according to MSZEN 10084-1:2001 - A1:2001, 42CrMo4 (material No.: 1.7225) alloyed steel, belonging the temper-grade steel group, which is used for manufacturing heavy-duty automobile parts. Its C-content is higher than 0,2 % so its strength and toughness can be increased substantially by heat treatment. The dimensions of the workpiece:  $\varnothing 100 \times 1000$  mm (about: 61 kg/m).

#### *The machine tool*

I will carry out the experiments on the lathe-machine which is in the workshop of the Institute of Mechanical Engineering Technology, Faculty of Mechanical Engineering, Szent Istvan University. The type of the lathe machine is: C11A – single- spindle, manufactured in Bulgaria. I have chosen this type because the high revolution needed for my experiments can be set on this machine. Its characteristics:

- centre distance: 1550 mm
- centre height: 250 mm
- revolution-range: 16-2000  $\text{min}^{-1}$
- coefficient of rev. variation: 1,25
- morse: 5
- electric-motor rev.: 1440  $\text{min}^{-1}$

- electric-motor power: 15 kW
- pump power: 0,6 kW
- limit of machine-tool stiffness: 250 N/μm.

*System of minimal lubrication*

I use the lubricant feeder „Cobra 2000” of NOGA for applying the minimal lubricant.

*Measuring instruments*

- traditional micrometer (measuring range: 25 – 50mm, 50 - 75mm and 75-100mm)
- traditional caliper (1/20 – 150mm)
- metal microscope (Zeits Axi imager 1M, and Axiovision 4.7)
- WA33 (TYP PRLTA13) scale (accuracy: 0,001g) for measuring insert mass
- inductive odometer for measuring cutting force (typ: TR102)
- revolution counter for measuring revolution (own construction)
- measuring-data collector (spider8 controll)
- IGA 300 infra thermometer
- Mitutoyo SJ 201P diamond headed surface profilometer.

*Condition of experiments:* Normal climate DIN50014 and ISO554-1970

The aim of my tests is to establish measurable differences during experiments carried out with various cooling-lubricants. During the tests I change only the cooling-lubricants the other participants are unchanged (machine, tool, workpiece, technological parameters). I want to measure the back wear as a function of distance covered.

*Experimental limit:*

- VB back wear ( $VB_{max} = 200\mu m$ ),
- Pitting of main cutting edge/or tool point.

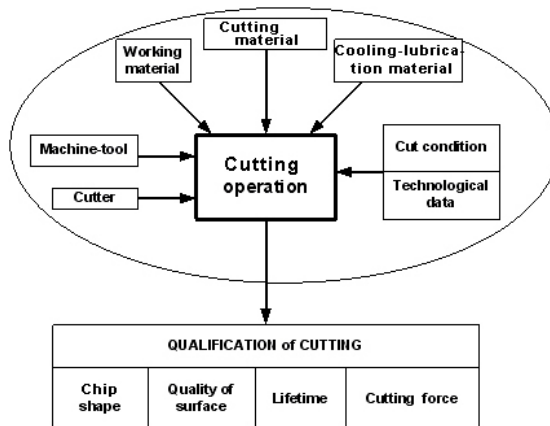


Figure 10. The characteristics measured at the tribological system of cutting

### Measured and calculated characteristics during experiments

The characteristics measured derive from the tribological model of cutting, as it is shown in Fig.10.:

The segment made from the machined material has to be evaluated in the  $\tau_{\max}$  plane.

### 3. Summary

The development of elements is not equal in the machine – cutting tool - cooling lubricant – workpiece systems, but one of the elements always enforces the development of the other system elements which result in the collective system development collectively. The goal of the present-work is to illustrate the uneconomic and environment pollution of lubrication technologies used until now. The development is imperative in this field. The minimal quantity lubricant (MQL) is one of the development trends (courses) immediate with which results can be got. Its further global advantage is the complete paradigm-shift in the mechanical engineering technology sometime in the future.

### References

- Bartz, W.J. és 70 co-authors: Kühlschmierstoffe und Zerspanung, Remingen-Malmsheim, expert-verlag 2000
- Csurgay, Á. – Simonyi, K.: Az információtechnika fizikai alapjai – Elektronfizika, Mérnöktovábbképző Intézet, Budapest, 1997.
- Kronenberg, M.: Grundzüge der Zerspanungslehre, Springer-Verlag, Berlin: 1954
- Lenard, P.: Über die lichtelektrische Wirkung. Ann. der Phys. 8 , 149-198 (1902)
- Valasek, I. – Tóth, I.: Megmunkálástribológia, Tribotechnik Kft, Budapest, 2003.
- Valasek I. – Kári-Horváth A.: Az üzemi emulziókezelési technológia felülvizsgálata és fejlesztési irányának meghatározása – Gépgyártás XLVII. Évfolyam, 2007. 5.szám (I.rész) pp 18-25
- Valasek I. – Pálffy A. – Kári-Horváth A.: Minimálkenésű (MMS) forgácsolási jellemzők meghatározása – Gépgyártás XLVII. Évfolyam, 2007. 2-3. szám, pp 47-56.

# **Impact of wire EDM on reciprocating sliding friction and wear response of WC based cemented carbides**

Koen BONNY, Patrick DE BAETS, Yeczain PEREZ,  
University Gent, Department of Mechanical Construction and Production  
Jef VLEUGELS, Omer VAN DER BIEST,  
Catholic University Leuven,  
Metallurgy and Materials Engineering Department  
Bert LAUWERS  
Catholic University Leuven Mechanical Engineering Department

## **Abstract**

Friction and wear characteristics of a number of WC based cemented carbides are compared in linearly reciprocating sliding experiments using a Plint TE77 tribometer. Flat samples of WC-Co and WC-Ni alloys with 6 up to 12 wt.% binder phase, carbide grain sizes ranging from 0.3 up to 2.2  $\mu\text{m}$  and various surface finish variants of wire electrical discharge machining (wire-EDM) or grinding have been tested against WC-6wt.%Co counter pins in unlubricated conditions under distinctive contact loads. The WC-Ni grade displayed superior wear resistance compared to the WC-Co grades. The surface modification due to EDM was evidenced to deteriorate the wear resistance of the cemented carbides. This finding could be linked to results of X-ray diffraction measurements of the residual stress level in the WC phase. Consecutive execution of gradually finer EDM regimes, however, enhances the wear performance considerably.

## **Keywords**

Friction, Wear, Tungsten Carbide, Electrical discharge machining

## **1. Introduction**

Based on economic reasons but especially today on the basis of ecological considerations as well, there is a rising need for an adequate limitation of wear and corrosion damage of machines and construction tools with attention to the efficient application of scarce materials and resources such as energy. In this way there is an obvious industrial demand for advanced materials to be applied under heavy tribological circumstances and preferably without lubrication as for instance for tools (chisels, cutting tools, metal forming dies, punches, etc.), various machine parts and in the fields of aerospace and automobile. WC based cemented carbides are widely used in engineering industries for their excellent mechanical properties and outstanding wear performance. Furthermore, they are suitable to be machined by electrical discharge machining (EDM) due to the binder phase which renders them sufficiently electrical conductive. More specifically, EDM has successfully

proven to be feasible for manufacturing WC-Co and WC-Ni alloys. One of the key advantages of EDM is the possibility of creating intricate shapes in a highly automated way, irrespective of strength or hardness of the base material. However, previous research investigations have already demonstrated the considerable impact of EDM parameters on surface quality, strength, hardness and fracture toughness, as well as on tribological characteristics.

This paper aims to elucidate the influence of EDM and particularly the impact of different EDM surface finish variants on friction and wear properties of a number of WC-Co and WC-Ni hardmetals, with 6 up to 12 wt.% binder phase and 0.3 up to 2.2  $\mu\text{m}$  carbide grain size, in oscillating sliding contact with WC-6wt.%Co cemented carbide.

Tribological characteristics of these grades against WC-6wt.%Co under distinctive normal contact loads were compared by performing dry linearly reciprocating sliding pin-on-plate experiments. Correlations between wear rate and friction on the one hand and contact force, sliding distance, binder phase, microstructure, surface conditions and residual surface stress in WC on the other hand were investigated.

## 2. Experimental

The chemical, physical, mechanical and microstructural properties of the WC-Co and WC-Ni alloys envisaged in this research are listed in Table 1.

The  $HV_{10}$  Vickers hardness was measured with an indentation load of 10 kg (Model FV-700, Future-Tech Corp., Tokyo, Japan). The fracture toughness  $K_{IC(30\text{kg})}$  was obtained by the Vickers indentation technique, based on crack length measurements of the radial crack pattern produced by Vickers  $HV_{30}$  indentations. The  $K_{IC}$  values were calculated according to the Shetty formula, (1):

$$K_{IC} = 0.0889 \cdot \sqrt{H_V} \cdot \left( \frac{P}{4l} \right) \quad (1)$$

with  $H_V$ , the Vickers hardness,  $P$ , the indentation load (N) and  $l$ , the total crack length (m), which is defined as the radial crack length ( $c$ ) minus half the indentation diagonal length ( $a$ ). The Young's modulus  $E$  was measured by the resonance frequency method on a Grindo-Sonic (J.W. Lemmens, Elektronika N.V. Leuven, Belgium), by means of the impulse excitation method (ASTM E 1876-99). The electrical resistivity was measured by a four terminal method on a Resistomat (TYP 2302 Burster, Gernsbach, Germany). The grain size distribution of the cemented carbides was acquired using computer image analysis software according to the linear intercept method. At least 1000 grains were measured for each grade. As can be derived from Table 1, the WC10Co grade exhibits the coarsest WC grain structure, with 50 % of the grains being smaller than 1.8  $\mu\text{m}$  and 95 % being smaller than 6.0  $\mu\text{m}$ . The WC10Co(Cr/V) grade has the finest microstructure, with 95 % of the grains smaller than 0.7  $\mu\text{m}$ .

Table. 1. Chemical, physical, mechanical and microstructure properties of WC-Co and WC-Ni grades

grade	WC10Co	WC12Co(V)	WC12Co(Cr)	WC10Co(Cr/V)	WC6Co(Cr/V)	WC8Ni(Cr)
binder content [wt%]	10	12	12	10	6	8
grain growth inhibitor	none	VC	Cr <sub>3</sub> C <sub>2</sub>	Cr <sub>3</sub> C <sub>2</sub> /VC	Cr <sub>3</sub> C <sub>2</sub> /VC	Cr <sub>3</sub> C <sub>2</sub>
Density [g/cm <sup>3</sup> ]	14.33	14.08	14.01	14.23	14.62	14.47
Thermal conductivity* [W.m <sup>-1</sup> .K <sup>-1</sup> ]	105	95	95	85	90	85
Vickers hardness HV <sub>10</sub> [kgf/mm <sup>2</sup> ]	1149± 10	1286± 8	1306± 5	1685± 38	1913± 13	1376±17
Fracture toughness K <sub>IC</sub> (30kg) [MPa.m <sup>1/2</sup> ]	> 15.5	15.4 ± 0.5	15.5 ± 0.6	9.7 ± 0.2	8.8 ± 0.2	10.6 ± 0.3
E-modulus [GPa]	578 ± 6	563± 2	546± 2	541± 4	609± 4	557± 3
Binder intercept length [μm]	0.9	0.4	0.4	0.1	0.2	0.3
WC mean grain size d <sub>av</sub> [μm]	2.2	0.9	0.9	0.3	0.6	0.8
WC grain size, d <sub>50</sub> [μm]	1.8	0.7	0.8	0.3	0.5	0.7
WC grain size, d <sub>95</sub> [μm]	6.0	1.8	2.1	0.7	1.2	1.8

\* data specified by manufacturer

The cemented carbides were machined and surface finished by grinding (JF415DS, Jung, Göppingen, Germany) with a diamond grinding wheel (type MD4075B55, Wendt Boart, Brussels, Belgium) or by wire-EDM on a ROBOFIL 2030SI (Charmilles Technologies, Switzerland) in de-ionized water (dielectric conductivity  $5 \mu\text{S}/\text{cm}$ ), with a CuZn37 wire electrode (diameter 0.25 mm, tensile strength 500 MPa). The wire-EDM process was performed using one rough material removal step with high spark thermal energy, i.e. E3, and subsequently several consecutive surface finishing steps, i.e. E8, E21 and E23, with globally decreasing energy input and pulse duration. For more details about generator settings for the EDM regimes as well as the corresponding  $R_a$  and  $R_t$  surface roughness, one is referred to our other publications. The surface finish variants of the investigated grades were characterized by scanning electron microscopy (SEM, XL30-FEG, FEI, Eindhoven) and surface profilometry (Somicronic® EMS Surfascan 3D, needle type ST305).

The tribological behavior of the WC-Co and WC-Ni alloys against WC-6wt.%Co pins in unlubricated conditions and an air-conditioned atmosphere of  $23 \pm 1 \text{ }^\circ\text{C}$  and  $60 \pm 1 \%$  relative humidity was evaluated using a Plint TE77 tribometer, in accordance with ASTM G133. The tested grades were flat specimens, whereas the pin tip displayed a diameter of 8.16 mm and  $R_a$  and  $R_t$  roughness of  $0.35 \mu\text{m}$  and  $2.68 \mu\text{m}$  respectively. The applied normal force ( $F_N$ ) and the concomitant tangential friction force ( $F_T$ ) as well as the penetration depth ( $\Delta d$ ) of each pin-on-flat sliding pair were recorded continuously using a load-cell, a piezoelectric transducer and an inductive displacement transducer respectively. The  $F_T/F_N$  forces ratio is defined as the coefficient of friction ( $\mu$ ), which can be differentiated in a static ( $\mu_{\text{stat}}$ ) and a dynamic ( $\mu_{\text{dyn}}$ ) component. For post-mortem assessment of the wear track topography, i.e. depth, length, width and volume, surface scanning equipment was used. Contact loads were varied from 15 N up to 35 N. The stroke length of the oscillating motion was 15 mm. A sliding velocity of 0.3 m/s was applied. The test duration was associated with a sliding distance of 10 km, allowing post-mortem wear volumes to be compared. Before each test, the specimens were cleaned ultrasonically with distilled water and acetone. Each experiment was performed using a new pin in order to achieve similar initial surface conditions.

### 3. Results and discussion

#### *Online friction and wear*

Typical and representative tribological data, obtained during real-time monitoring of friction and combined penetration depth for WC-Co and WC-Ni flat/ WC-6wt.%Co pin combinations are plotted in Fig. 1 as function of sliding distance, surface finish and imposed normal contact force. Each curve is an average of at least two wear experiments performed under identical conditions on samples of the same material. The error bars indicating the extent of the variations are excluded to improve the readability of the figure.

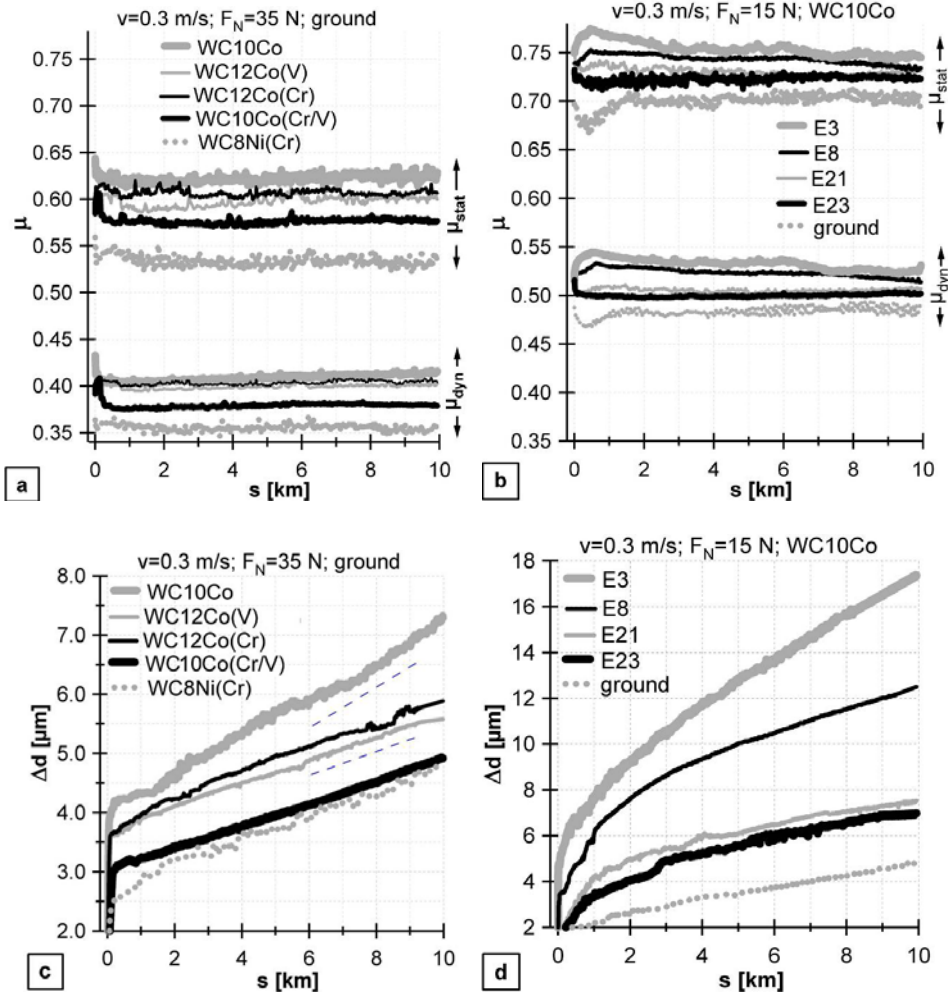


Figure 1.  $\mu_{stat}$  and  $\mu_{dyn}$  friction coefficient (a,b) and  $\Delta d$  penetration depth (c,d) as function of sliding distance and surface finish variants for WC-Co and WC-Ni grades sliding against WC-6wt.%Co at 0.3 m/s, under a contact load of 35 N (a,c) and 15 N (b,d)

In case of wear tests on ground samples using a 35 N contact load, the static and dynamic friction coefficient of the investigated tribopairs were measured to be in the range of 0.54–0.65 and 0.35–0.43 respectively, Fig. 1(a). In agreement with previous investigations, the dynamic and static component of friction display similar evolution as function of the sliding distance, however at a different level. Furthermore, the combined pin/plate penetration depth appears to remain below 8  $\mu\text{m}$  after a 10 km wear path, Fig. 1(c). Coefficient of friction as well as penetration depth are noticed to increase abruptly during the first meters of sliding, owing to the quickly growing contact surface area. After a running-in stage, a steady state regime is reached, in which the variations in the friction coefficient become marginal, Fig. 1(a), whereas the penetration depth increases at an almost

continuously reducing speed as function of the sliding distance, Fig. 1(c). Furthermore, the largest penetration depths are encountered with the WC10Co grade, whereas the lowest wear damage occurs with the WC8Ni(Cr) grade. This trend is commensurate with the respectively lower and higher friction level for these grades, and should be related to the mutual differences of WC grain size, binder phase and binder amount in the cemented carbides.

The surface finishing operation is found to have a considerable influence on friction and wear performance of the cemented carbides. The lowest friction coefficients are encountered with ground samples, whereas the wire-EDM'ed specimens with E3 surface finish exhibit the highest friction level, Fig. 1(b). This trend is also reflected in the penetration depth curves, Fig. 1(d). Moreover, both friction and wear are noticed to decrease with finer-executed EDM, up to values nearby to those recorded for the ground equivalents. The differences in friction and wear between wire-EDM'ed and ground samples are noticed to diminish with increasing sliding distance.

The initial sliding wear process is mainly caused by strong asperity interaction, i.e., fragmentation and deformation. As the sliding proceeds, the asperities are worn down, the initial surface roughness diminishes and the interlocking friction component decreases. The surface smoothing is confirmed by Table 2, which compares  $R_a$  and  $R_t$  roughness as function of sliding distance for a WC10Co grade with E3 surface finish, before and after wear testing. The surface roughness is obviously reduced during the sliding wear process. It is worth noting that similar trends in wear track surface roughness were observed for the other grades.

Table 2.  $R_a$  and  $R_t$  surface roughness for WC10Co grade with surface finish E3 after wear testing as function of sliding distance (s)

	$R_a$ [ $\mu\text{m}$ ]					$R_t$ [ $\mu\text{m}$ ]				
s [km]	0	0.1	1	4	10	0	0.1	1	4	10
roughness	2.08	0.12	0.081	0.072	0.071	15.18	1.66	1.10	1.03	1.02

The small fluctuations in the friction curves, especially during running-in wear and for the roughest EDM surface finish variant, are due to a continuous breaking and regeneration of micro junctions as a result of asperity interaction and should be related to the constantly changing degree of interlocking at the contact surface as well as to the removal of the thermally induced recast layer, exhibiting modified surface properties compared to the bulk material. Indeed, the wire-EDM induced heat affected zone (HAZ) was found to contain brittle tungsten subcarbide and eta-phase ( $\text{W}_3\text{Co}_3\text{C}$  and  $\text{W}_6\text{Co}_6\text{C}$ ) as well as surface cracks penetrating into the base material, Fig. 2, and/or thermal cracks of WC grains, both after rough and finer EDM steps. These already existing transgranular and/or intergranular cracks serve as notches for the (sub)surface material during the reciprocating sliding wear tests. Growth and propagation of these cracks increases the probability of grain fracture (see further, e.g. Fig. 6). In addition, depletion of binder and concomitant

loosening of WC grains after the EDM process was discovered, Fig. 2(b), deteriorating the strength properties at the surface. In agreement with Llanes et al., the soft top layer on the rough wire EDM'ed surface did not seem to reduce the friction coefficient.

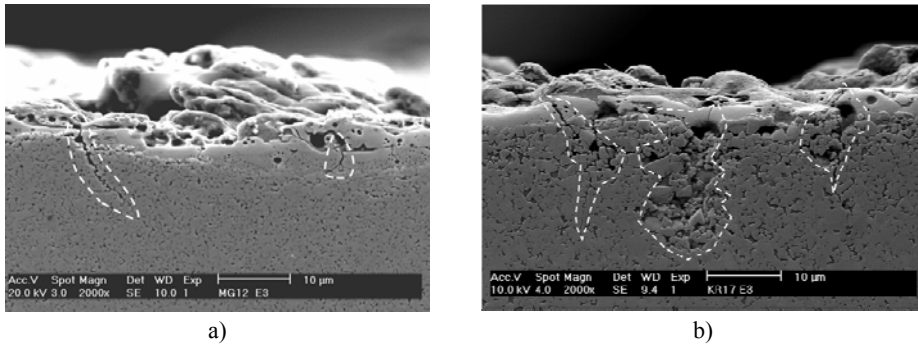


Figure 2. Cross-sectioned SEM micrographs in SE mode of wire-EDM'ed (E3 surface finish) WC-Co (a) and WC-Ni (b) alloys

The relatively small variation pattern in the coefficient of friction for both ground and wire-EDM samples points out the low incidence of adhesive wear by transfer of cobalt binder, probably occurring by mechanical interlocking of the soft binder phase of both contacting cemented carbides. The lowest friction levels are recorded for the WC8Ni(Cr) versus WC-6wt.%Co tribopairs.

Comparing Fig. 1(a) with 1(b) reveals that the friction coefficient decreases with higher normal contact load. An opposite correlation is observed between the penetration wear and the imposed normal contact load when comparing Figs. 1(c) and 1(d).

The differences in tribological properties between the distinctive surface finish variants should be correlated to the corresponding surface roughness and the occurrence of recast material and a heat affected zone after wire EDM, as shown in Fig. 2. Indeed, after rough EDM (surface finish E3), the cemented carbide is covered by recast material and contains an approximately 30 µm thick heat affected zone, which is obviously less wear resistant compared to the bulk material. The recast material is cut off by consecutive finer EDM steps, i.e., E8, E21 and E23, each leaving a gradually thinner HAZ, i.e., ca. 15 µm, 10 µm and 5 µm or less respectively, on the cemented carbide surface. Therefore, penetration depth exhibits the lowest values for the ground WC based alloys, on which no heat affected zone was induced, and displays the highest values for rough wire-EDM'ed WC based alloys, but decreases when the cemented carbide is surface finished up to a finer EDM variant.

The dependency of the coefficient of friction on the original surface roughness, originating from the investigated finishing regimes after wire-EDM and grinding, for a 4 km sliding distance is compared in Fig. 3(a) for the studied grades during

reciprocating sliding wear experiments using a 35 N contact load. Within the measured  $R_a$  and  $R_t$  range, both the static and dynamic coefficient of friction are noticed to decrease with enhanced surface finish refinement. Indeed, the initial wear process is mainly caused by strong asperity interaction, and thus, causing a higher friction for rougher surface finishes. A stronger correlation is noticed when the coefficient of friction for the cemented carbides after a 4 km sliding distance is plotted against thickness of the wire-EDM induced heat affected zone (HAZ), Fig. 3(b). It is clear that the ground samples, which do not have a HAZ, display the lowest friction level. It is worth noting that the thickness of the HAZ was obtained from cross-sectioned SEM views of wire-EDM'ed WC-Co and WC-Ni alloys, Fig. 2.

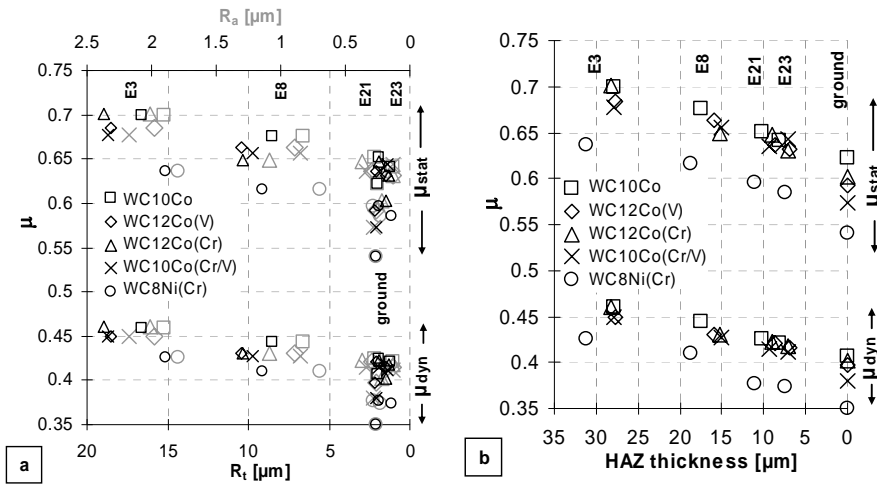


Figure 3. Steady state friction coefficient ( $\mu_{stat}$  and  $\mu_{dyn}$ ) against (a) surface roughness ( $R_a$  and  $R_t$ ) and (b) thickness of HAZ for WC-Co and WC-Ni alloys sliding against WC-6wt.%Co at 0.3 m/s under 35 N

#### Post mortem wear characteristics

In order to enable wear volumes to be compared, the sliding wear experiments were performed up to a total sliding distance of 10 km. From the obtained 3D wear track surface topographies of the WC-Co and WC-Ni grades, the corresponding wear track volumes ( $V_{wear}$ ) were derived. Based on these results, post-mortem volumetric wear rates ( $k_v$ ) were determined as the ratio of wear volume and the product of the applied normal force ( $F_N$ ) and sliding distance ( $s$ ), according to (2):

$$k_v = \frac{V_{WEAR}}{F_N \cdot s} \left[ \frac{mm^3}{N \cdot m} \right] \quad (2)$$

The post-mortem obtained wear track dimensions, together with the corresponding volumetric wear rates ( $k_v$ ), originating from sliding wear tests described in Fig. 1 using a 35 N contact load, a 0.3 m/s sliding velocity and a 10 km wear path are summarised in Table 3 for the studied WC-Co and WC-Ni alloys and surface finish variants. The volumetric wear rates are noticed to vary between  $1.9 \cdot 10^{-8}$  and  $4.5 \cdot 10^{-7} \text{ mm}^3 \cdot \text{N}^{-1} \cdot \text{m}^{-1}$ .

Under identical conditions of sliding distance, sliding speed and contact load, and consistent with the online recorded results shown in Fig. 1, the smallest depth and width of the wear scars are measured for the WC8Ni(Cr) alloy and ground surface finish, whereas the highest values are found with WC10Co specimens and E3 surface finish.

It should be noted that the wear depth for the WC-Co and WC-Ni versus WC-6wt.%Co combinations, after a 10 km sliding path using a 35 N contact load, ranges within or slightly exceeds the recast layer thickness for the E3 surface finish, and thus, in most cases, all traces of recast material should be removed. With decreasing recast thickness (regime E8), or amount of recast (regimes E21 and E23), however, the recast material was worn off more quickly.

Comparing the post-mortem, i.e., obtained by surface profilometry (see Table 3), with the online recorded, i.e. from the pin displacement (see Fig. 1), penetration depth after 10 km of sliding distance reveals small deviations. This is mostly attributed to the wear of the pin, which was not taken into account during post-mortem quantification.

The impact of surface roughness after grinding or wire-EDM on volumetric wear rate ( $k_v$ ), is demonstrated in Fig. 4(a) for the investigated WC-based alloys after reciprocative sliding wear experiments using a 35 N contact load and a 10 km sliding distance. Within the range of  $R_a$  and  $R_t$ , both the wear volume and wear rate are noticed to decrease with enhanced surface finish refinement. The grades with E3 surface finish exhibit the highest wear level, which improves drastically by the execution of gradually finer EDM finishing steps.

Not only surface roughness, but especially the thickness of the wire-EDM induced heat affected zone (HAZ) is noticed to influence the wear performance of the WC-Co and WC-Ni alloys, as illustrated by Fig. 4(b), in which wear volume and wear rate are plotted against HAZ thickness, obtained from cross-sectioned SEM views of wire-EDM<sup>3</sup>ed cemented carbides.

Indeed, the technology of wire EDM is in nature a thermal material removal process, occurring through melting and evaporation of the base material. Furthermore, wire EDM was found to induce a heat affected zone and a recast layer at the surface, in which resolidified molten material, voids, residual tensile surface stresses and (micro)cracks are generated. These phenomena lead to a considerable deterioration of surface quality and final properties such as strength.

Table. 3. Wear track dimensions, wear volume and volumetric wear rate for wire-EDM'ed and ground WC-Co and WC-Ni flats sliding against WC-6wt.%Co ( $v=0.3$  m/s,  $F_N = 35$  N,  $s=10$  km)

Grade	Surface finish variant	Width [mm]	Depth [ $\mu\text{m}$ ]	$V_{\text{wear}}(10\text{km})$ [ $10^{-3}$ mm <sup>3</sup> ]	$k_V$ (10km) [ $10^{-6}$ mm <sup>3</sup> ·N <sup>-1</sup> ·m <sup>-1</sup> ]
WC10Co	E3	1.10	24.3	156.3	0.447
	E8	1.05	21.3	124.3	0.304
	E21	1.00	13.2	52.6	0.150
	E23	0.95	10.1	31.7	0.091
	grinding	0.90	5.9	5.5	0.037
WC12Co(V)	E3	1.10	20.1	128.5	0.367
	E8	1.00	14.1	81.1	0.232
	E21	0.95	8.8	37.7	0.108
	E23	0.90	7.2	23.6	0.067
	grinding	0.80	4.8	3.9	0.026
WC12Co(Cr)	E3	1.10	19.6	122.3	0.349
	E8	1.00	12.5	69.4	0.198
	E21	0.95	8.0	35.4	0.101
	E23	0.90	7.1	22.52	0.064
	grinding	0.80	5.0	4.0	0.027
WC10Co(Cr/V)	E3	1.05	16.2	96.8	0.276
	E8	0.95	10.6	44.8	0.128
	E21	0.85	7.1	23.3	0.066
	E23	0.80	6.5	21.4	0.061
	grinding	0.70	4.4	3.2	0.022
WC8Ni(Cr)	E3	1.0	15.3	94.9	0.271
	E8	0.9	10.1	44.0	0.125
	E21	0.8	6.8	22.6	0.064
	E23	0.75	6.3	20.7	0.059
	grinding	0.70	4.1	3.0	0.019

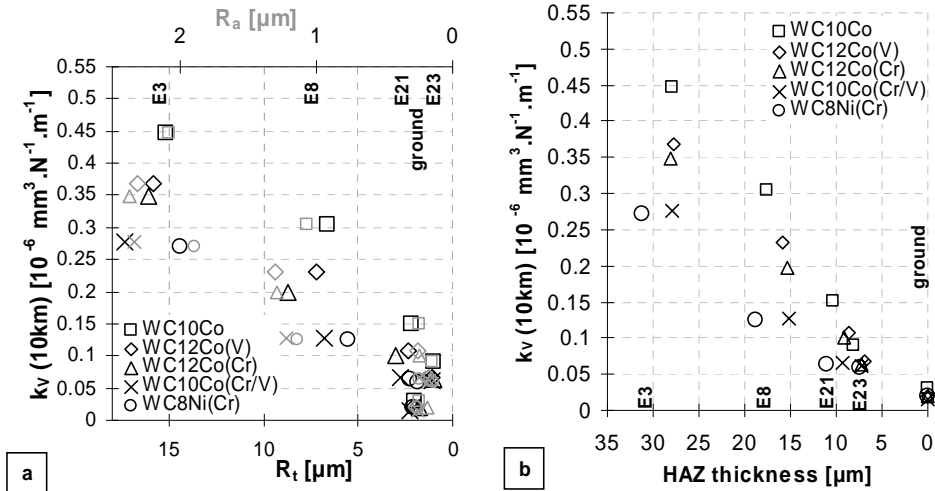


Figure 4. Wear rate versus (a) surface roughness ( $R_a$  and  $R_t$ ) and (b) thickness of HAZ for WC based alloys slid against WC-6wt.%Co at 0.3 m/s under 35 N

The inferior wear resistance of the heat affected material can be explained in terms of stress state modification. After cooling down the cemented carbide from sintering, the WC phase is in compression, whereas the binder phase is in tension, due to the higher thermal expansion coefficient of Co or Ni compared to WC. Contrary to the compressive stress state in the bulk material, the wire-EDM process was found to generate residual surface stresses which are tensile in nature.

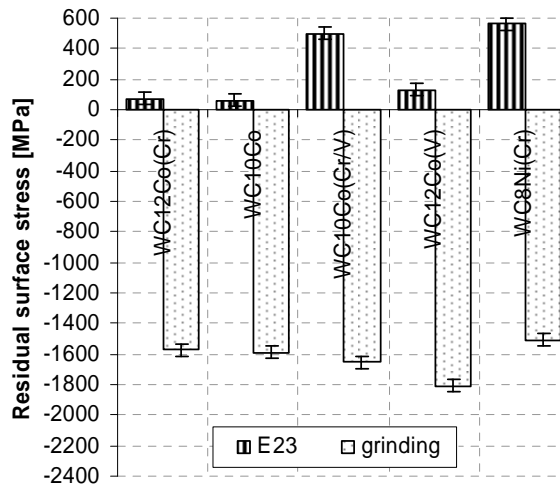


Figure 5. Surface residual stress in the WC phase of 2 cemented carbides after grinding and EDM finishing (regime E23): a + value indicates a tensile stress, whereas a - value represents a compressive stress

This is illustrated by Fig. 5, in which the surface residual stresses in the WC phase of the cemented carbides after grinding and the finest EDM finishing step E23 are compared. The measurements were executed by X-ray diffraction on a Siemens D500 XRD, using the  $d\text{-sin}2\psi$  method. The (300) WC peak, corresponding with a diffraction angle  $2\theta = 133.31^\circ$  was applied in order to acquire the residual stress. The  $\text{sin}2\psi$  range was varied from 0 to 0.6 in steps of 0.1, and the angle  $2\theta$  was varied between  $130^\circ$  and  $136^\circ$  at  $0.02^\circ/\text{steps}$  of 5 s.

It should be clear that a significant compressive stress occurs in the ground materials, owing to the mechanical impact during grinding, whereas a tensile stress is measured on the EDM surfaces, as a result of the thermal impact.

During the sliding wear experiments, the tangential stresses will build up with the residual tensile stresses in the wire-EDM surface, whereas the compressive stress state of ground surfaces more or less eliminates the tangential contact stress.

### *Wear surface analysis*

From the recorded tribological responses of the studied cemented carbides with distinctive surface finishing conditions, it can be inferred that the presence of recast layer primary determines the friction and wear characteristics. Once the WC-6wt.%Co pin has penetrated the recast layer, the wear behavior reaches a wear regime characteristic for the bulk material. The wear resistance of the recast material is substantially lower than that of the base material, as can be deduced from the much higher (initial) wear rate for the rough E3 surface finish compared to the ground surface finish.

The higher wear rate for the wire-EDM alloys can be explained in terms of surface roughness and thermally induced surface damage originating from the EDM process. Indeed, a higher surface roughness results in a higher abrasion level, owing to an increased ploughing component.

According to previous investigations on the friction and wear of cemented carbides, the general wear process was evidenced to occur by the accumulation of damage, fracture and removal of carbide grains. In this research, the occurring wear mechanisms were identified by SEM analysis on the wear scars.

The resulting scanning electron micrographs on the central part of wear scars on originally ground and wire-EDM'ed WC-Co and WC-Ni alloys after sliding wear experiments of 10 km at  $0.3 \text{ m}\cdot\text{s}^{-1}$  and under distinctive contact loads are presented in Figs. 6-8.

A first wear mechanism is illustrated in Fig. 6, which presents a cross-sectioned SEM view on the surface of wire EDM (regime E21) WC8Ni(Cr) after 10 km sliding at 0.3 m/s against WC-6wt.%Co under a 15 N normal contact force. The scanning electron micrograph clearly illustrates that, compared to the original surface finishing conditions, the wear track appears smoother, indicating that the surface of the cemented carbide was polished by the pin. This observation confirms the data given in Table 2, and, moreover, it allows distinguishing the wear track area from the original surface, and thus, the position of the wear track can be located for more detailed examination.

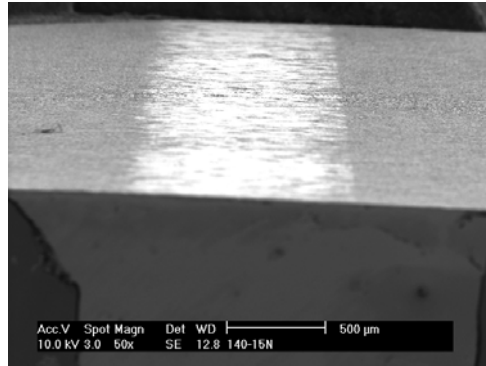


Figure 6. Cross-sectioned wear tracks of WC8Ni(Cr) with EDM finish E21, after 10 km sliding against WC-6wt.%Co at 0.3 m/s under 35 N

Besides the polishing effect, other wear mechanisms for the WC-Co and WC-Ni specimens could be identified as surface binder removal, WC grain cracking and WC grain pull out, Fig. 7. The relative contribution of these mechanisms is different and each of the observed wear mechanisms also occurs with modified relative importance for the distinctive EDM surface finish variants, owing to the different thermal impact of each EDM regime, such as Co binder depletion and pre-existing microcracks, Fig. 2.

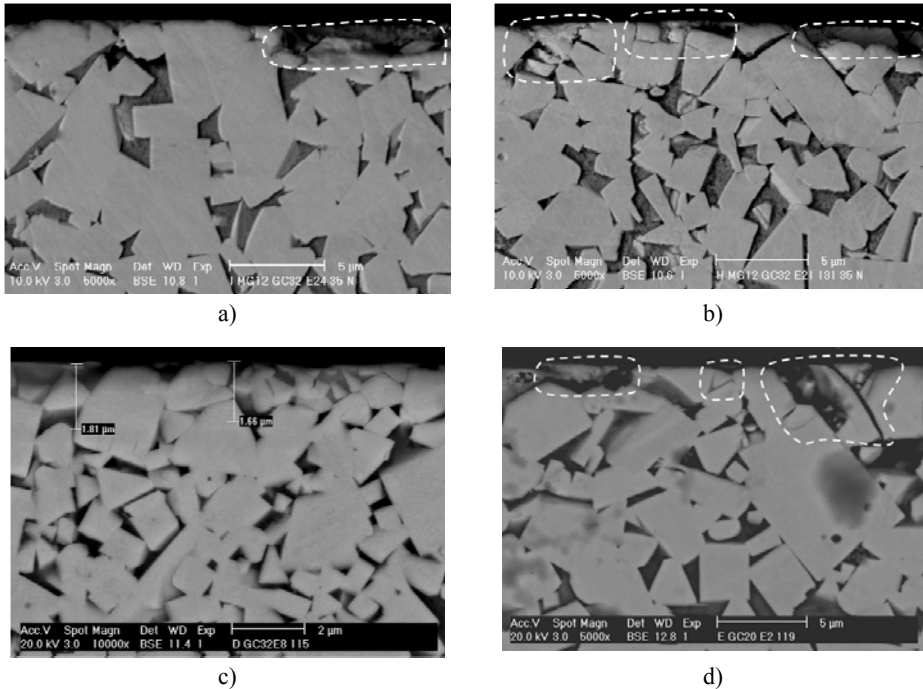


Figure 7. Cross-sectioned wear tracks of WC-Co after 10 km sliding against WC-6wt.%Co at 0.3 m/s under 35 N: (a) WC10Co E23, (b) WC10Co E21, (c) WC10Co E8 and (d) WC12Co(V) E3

The recast layer is noticed to be completely removed on both fine and rough EDM variants after sliding wear tests for 10 km under 35 N, contrary to equivalent wear tests with a 15 N contact load. However, small remainders of the wire-EDM induced heat affected zone, such as Co binder modification, are still visible on rough EDM surfaces, Fig. 7(c). A cross-sectioned view on the central part of the wear track on WC12Co(V) with E3 surface finish confirms the occurrence of several coexisting wear mechanisms, Fig. 7(d).

Similar observations are made in Fig. 8, which displays surface views in the central part of the wear tracks on WC10Co(Cr/V) grades, surface finished by EDM up to variants E3 and E21, after sliding 10 km against WC-6wt.%Co at 0.3 m/s under 35 N.

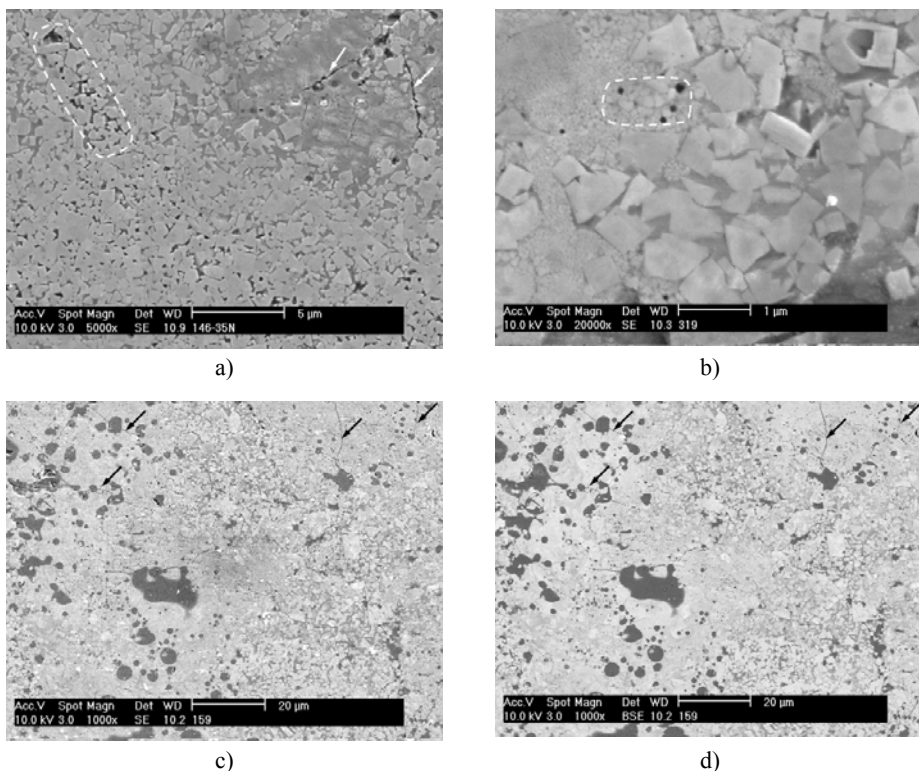


Figure 8. SEM top views of wear surfaces for WC10Co(Cr/V) grade with surface finish E21 (a) and E3 (b) and for WC12Co(Cr) with surface finish E3 (c,d) after 10 km sliding against WC-6wt.%Co at 0.3 m/s under 35 N

SEM analysis reveals the presence of surface cracks, Fig. 8(a). These surface cracks are induced by frictional stresses caused by the sliding contact, and are more likely to occur at a wire-EDM'ed surface compared to the bulk material. Indeed, pre-existing cracks on wire-EDM'ed cemented carbides, Fig. 2, were found to serve as notches for the (sub)surface material during reciprocal sliding. Surface cracks

could also be identified on the wear surface of WC10Co(Cr/V) with E3 surface finish, together with islandized, small remains of wire-EDM induced heat affected zone, Fig. 8(b). SEM analysis on worn surfaces on WC12Co(Cr) with E3 surface finish also reveals small amounts of recast material, Fig. 8(c,d), thus confirming that the HAZ has not been completely removed by the sliding wear experiments at 0.3 m/s under 35 N with a 10 km sliding distance. Furthermore, microcracks are noticed on the wear surface, as indicated by the arrows.

Based on the obtained wear data and SEM analysis on the wear surfaces of the WC-Co and WC-Ni grades, it can be inferred that the deteriorated wear resistance of wire-EDM specimens, compared to their ground equivalents, is attributed to the wire-EDM induced top layer.

#### 4. Conclusions

Dry reciprocating sliding experiments on WC-Co vs. WC-6wt.%Co and WC-Ni vs. WC-6wt.%Co combinations revealed that wire-EDM deteriorates the wear performance considerably, due to a thermally induced recast layer and residual tensile surface stresses in the WC grains, as evidenced by X-ray diffraction measurements. The surface roughness and the thickness of the recast layer, substantially less wear resistant compared to the bulk material, primary determine the (running-in) wear behavior. Consecutive execution of gradually finer EDM finishing regimes reduces the wear rate down to values nearby those for equivalent ground specimens. The volumetric wear rate for the studied cemented carbides after a wear test with a 10 km sliding distance, a 35 N contact load and a 0.3 m.s<sup>-1</sup> sliding speed, did not exceed 4.5·10<sup>-7</sup> mm<sup>3</sup>.N<sup>-1</sup>.m<sup>-1</sup>. Amongst the investigated grades, the most favorable tribological results were obtained for the WC-Ni grade, emphasizing the importance of further investigation in this direction.

#### 5. Acknowledgements

This work was co-financed with a research fellowship of the Flemish Institute for the promotion of Innovation by Science and Technology in industry (IWT) under project number GBOU-IWT-010071-SPARK and the Fund for Scientific Research Flanders (FWO) under project number G.0539.08. The authors gratefully recognize all support, scientific contributions and stimulating collaboration from the partners from Ghent University (UGent) and Catholic University of Leuven (K.U.Leuven). Special acknowledgement goes to CERATIZIT for supplying hardmetal grades and pins.

#### References

- J. Kozak, K.P. Rajurkar and N. Chandarana, Machining of low electrical conductive materials by wire electrical discharge machining (WEDM), J. Mater. Process. Tech. 149, 1-3, 2004, p. 266-271

- A.M. Gadalla and W. Tsai, Machining of WC-Co composites, *Mater. Manuf. Proc.* 4, 1989, p. 411-423
- A.M. Gadalla and W. Tsai, Electrical discharge machining of tungsten carbide-cobalt composites, *J. Amer. Ceram. Soc.* 72, 1989, p. 1396-1401
- B. Lauwers, W. Liu and W. Eeraerts, Influence of the composition of WC-based cermets on the manufacturability by Wire-EDM, *Transactions of the NAMRI/SME* 32, 2004, p. 407-414
- D. Jiang, G. Anné, J. Vleugels, K. Vanmeensel, W. Eeraerts, W. Liu, B. Lauwers and O. Van der Biest, Residual stress in hardmetals caused by grinding and EDM machining and its influence on flexural strength, Eds. G. Kneringer, P. Rödhammer and H. Wildner, *Powder Metallurgical High Performance Materials*, 16th Int. Plansee Seminar, Reutte, Austria, Vol. 2, 2005, p. 1075-1085
- B. Lauwers, J.-P. Kruth, W. Liu, W. Eeraerts, B. Schacht and P. Bleys, Investigation of material removal mechanisms in EDM of composite ceramic materials, *J. Mater. Process. Tech.* 146, 1-3, 2004, p. 347-352
- K. Bonny, P. De Baets, J. Vleugels, O. Van der Biest, B. Lauwers, W. Liu, EDM machinability and dry sliding friction of WC-Co cemented carbides, *International Journal of Manufacturing Research*, Vol. xx, Iss. x, 2009, p.
- K. Ishikawa, A. Iwabuchi and T. Shimizu, Influence of EDM on the wear characteristics of WC-Co cemented carbide, *J. Jpn. Soc. Tribol.* 48, 2003, p. 928-935
- L. Llanes, E. Idanez, E. Martinez, B. Casas and J. Esteve, Influence of electrical discharge machining on the sliding contact response of cemented carbides, *Int. J. Refr. Met. & Hard Mater.* 19, 2001, p. 35-40
- K. Bonny, P. De Baets, W. Ost, J. Vleugels, S. Huang, B. Lauwers, W. Liu, Influence of electrical discharge machining on the reciprocating sliding wear response of WC-Co cemented carbides, *Wear* 266, 1-2, 2009, p. 84-95
- K. Bonny, P. De Baets, J. Vleugels, O. Van Der Biest and B. Lauwers, Influence of surface finishing and binder phase on friction and wear of WC based hardmetals, *Materials Science Forum* 561-565, 2007, p. 2403-2406
- K. Bonny, P. De Baets, B. Lauwers, J. Vleugels and O. Van Der Biest, Influence of Electro-discharge machining, microstructural and mechanical properties on wear behavior of hardmetals, Eds. G. Kneringer, P. Rödhammer and H. Wildner, *Powder Metallurgical High Performance Materials*, 16th Int. Plansee Seminar, Reutte, Austria, Vol. 2, 2005, p. 863-877
- K. Bonny, P. De Baets, W. Ost, S. Huang, J. Vleugels, W. Liu, B. Lauwers, Influence of electrical discharge machining on the reciprocating sliding friction and wear response of WC-Co cemented carbides, *International Journal of Refractory Metals and Hard Materials* 27, 2, 2009, p. 350-359

- G.A. Garzino-Demo and F.L. Lama, The effect of surface finish of matching materials on friction and wear of uncoated and unlubricated sliding bodies, *Surface and Coatings Technology* 86-87, part 2, 1996, p. 603-609
- ASTM G133 - Standard test method for linearly reciprocating ball-on-flat sliding wear, In: *Annual book of ASTM standards*, 2002, vol 03.02, p. 558-565
- K. Bonny, P. De Baets, J. Vleugels, S. Huang, B. Lauwers, Dry Reciprocating Sliding Friction and Wear Response of WC-Ni Cemented Carbides, *Tribology Letters* 31, 3, 2008, p. 199-209
- K. Bonny, P. De Baets, B. Lauwers, J. Vleugels and O. Van Der Biest, Reciprocating friction and wear behavior of WC-Co based cemented carbides manufactured by electro-discharge machining, *Materials Science Forum* 561-565, 2007, p. 2025-2028
- K. Bonny, P. De Baets, J. Vleugels, S. Huang, B. Lauwers, Tribological Characteristics of WC-Ni and WC-Co Cemented Carbide in Dry Reciprocating Sliding Contact, *Tribology Transactions* 52, 4, 2009, p. 481-491
- K. Bonny, P. De Baets, J. Vleugels, S. Huang, O. Van der Biest, B. Lauwers, Impact of  $\text{Cr}_3\text{C}_2/\text{VC}$  addition on the dry sliding friction and wear response of WC-Co cemented carbides, *Wear*, DOI: 10.1016/j.wear.2009.06.013
- T. Yakou and T. Hasegawa, Relations between condition and electrically discharge machining and depth of surface crack in cemented carbides, *Trans. Japan Soc. Mec.* 61, 1995, p. 1192-1197
- R.S. Sayles, Basic principles of rough surface contact analysis using numerical methods, *Tribol Int.* 29, 8, 1996, p. 639-650
- A.A. Lubrecht and E. Ioannides, A fast solution of the dry contact problem and associated surface stress field using multilevel techniques, *ASME Journal of Tribology* 113, 1991, p. 128-133
- D.M. Bailey and R.S. Sayles, Effect of Roughness and Sliding Friction on Contact Stress, *ASME Journal of Tribology* 113, 1991, p. 729-738
- M.G. Gee, A. Gant and B. Roebuck, Wear mechanisms in abrasion and erosion of WC/Co and related hardmetals, *Wear* 263, spec. iss. 1-6, 2007, p. 137-148
- M.G. Gee, A. Gant, L.P. Byrne and B. Roebuck, Abrasion and reciprocating wear of hardmetals and ceramics, *NPL Report CMMT(A)*, Vol. 166, 1999
- J. Pirso, S. Letunovit and M. Viljus, Friction and wear behaviour of cemented carbides, *Wear* 257, 3-4, 2004, p. 257-265

# The praxeologic pattern for the innovation in the field of the industrial actuators

Vasile NASUI, Radu COTETIU, Adriana COTETIU  
North University of Baia Mare, Faculty of Engineering

## Abstract

The paper is going to originally develop the methodology in a close connection in the field of top products such as the industrial linear actuators. The research is focus to the development a praxeologic pattern using the general principles of the invention and of the management of technological innovation in the field of the industrial linear actuators by projection and creative techniques. The paper is trying to apply some points of view of praxeology in the optimization activity of the industrial electro mechanic linear actuators, which results in a reason by which some research problems are solving, planning an efficient work display. The paper proves that in order to obtain the best effect with a given effort you need a rationalization the action and through its good conceptual preparation on the basic of the principles offering by real practice of the efficacy.

## Keywords

linear actuators, praxeology, modelling

## 1. Introduction

The present day process of intense preoccupation for the improvement of the industrial orders, the achievement of an efficient pattern for the research of efficiency has got principal.

The exploitation of the mechanical technique system with implications on the studies viewing the factors that determine the efficiency pattern in the primordial sense. The management of technological innovation in the field of the industrial linear actuators is approached in many works, according to different principles for example, of dissipation of energy, of the degree of loading, of the empirical deduction or different simplified patterns not having a pattern according to the efficient principles.

Because in the model conditions as a rational activity viewing the way of doing it are only an application of the efficient technical principles in given conditions. Thus we justify the importance of praxeology for the management of technological innovation, knowing that this branch of science studies the general structure of the human action and of the conditions of their efficiency.

In the present day context, it `s not depriving of importance the idea that the technical optimum is the optimum of substance consumption must be followed

in a special way besides other principles which view systemically and globally the entire phenomenological process of the mechanical systems.

The increasing of the efficacy of the mechanic action system is explained, by applying the principles of the “well-done job” which result in principles extracted from the branches of management, energetic mechanic science, from the improvement not only of the science of the interactive organizations of the actuator systems.

The technical optimum is considered as a compromise of substantial combinations according to some optimization criteria, but in order to make it a real technical progress it has to contain structural modification by applying some praxeological principles.

The research has in view the establishment of an optimum solution according to the destination of the actuator using a great variety of solutions, starting from the simple recovering mechanisms of the mechanic, hydro, pneumo, electric types up to the macaroni recovering / regeneration systems of braking energy.

The use of new solutions, including the informatics technology and the applications of the proposed research is the answer to the challenges of the society of knowledge which targets the engineering solutions of controlling the movement through intelligent and efficient systems.

The proposed theme has a scientific importance because it approaches research in a top interdisciplinary domain which targets the energetic efficiency of mechanic systems and the protection of the environment. It targets the synthesis and the development of knowledge in order to generate new solutions of actuators having a structure with a combination of elements within an assemble, superior quality and on the basis of new principles using the way of deductive analytical logistics.

The conception research, of new types of actuators requires an interdisciplinary approach and a complex process of interference, of collaboration and coordination of scientific knowledge in the field of mechanical, informatics studies.

An actuator's function is to provide thrust and positioning in machines used for production or testing. One type is the electromechanical actuator, which converts the torque of an electric rotary motor into linear mechanical thrust (fig.1).

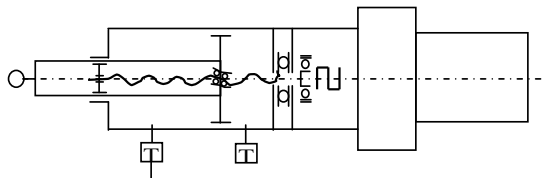


Figure 1. Linear electro-mechanic actuator

The linear actuator is composed of a motor turning a screw in which the nut on screw is not allowed to rotate. The conception of the system allows a high

degree of parameterizes and with very clear presentation in the representation of the knowledge being focused on a certain type of function.

The praxeologic pattern will be the following Table 1

Table 1. The praxeologic pattern

THE PRAXEOLOGIC PATTERN
<p>TOPIC / SUBJECT</p> <ul style="list-style-type: none"> <li>– efficiency of the human action logical optimization of the action;</li> <li>– instruction and education of the specialists;</li> <li>– „engineering of the well-dine thing”;</li> <li>– logics of the human action;</li> <li>– study of the general structure action;</li> <li>– achieve generalization on the basis of the data offered by real practice.</li> </ul>
<p>TECHNICAL PRINCIPLES</p> <ul style="list-style-type: none"> <li>– technical optimum: it’ the best organisation of the components;</li> <li>– principle of minimum resistance and minimum energy expenses;</li> <li>– the principle of the technical basis is to act with low effort;</li> <li>– the rationalization of the details in complex processes that add up considerably</li> </ul>
<p>PURPOSE OF THE MODELLING</p> <ul style="list-style-type: none"> <li>– construction of a set of technical general recommendations;</li> <li>– improvement of the dynamic of the technical progress in the studied field;</li> <li>– analytic description of the elements of the action and of their expression;</li> <li>– achievement of an interrogative space in view of the action optimisation</li> </ul>
<p>EFFECT OF THE MODELLING</p> <ul style="list-style-type: none"> <li>– clarifies the notions of efficient analysis by building up analytical definitions;</li> <li>– coordinates the problems by synthesis;</li> <li>– it improves the information regarding the technical qualities of the action;</li> <li>– it forms well–defined concept and systematic and systemic exposures;</li> <li>– it clarifies the approach by the formed algorithm conceptual device/apparatus</li> </ul>

This allows linear motion o the nut for the length of the screw. A position at some point along the screw is commanded by the user and the motor turns the screw until the nut reaches that position.

The way of functioning of the system has in view of a creative projection of new solutions of electro mechanic linear actuators using methods from the inventions.

## 2. The praxeologic principle of the management of technological innovation

As a general efficient realization in a mechanic system is the effect of the decreasing of the action efficiency and of the improving of the action over the objects is its counter factor which annihilates this effect. The alternation of the decreasing effect with its super -compensation by technical ingenuity leads to saving the resources. As a general principles is the principle of the least resistance and the one of the least expenses of mechanical work which applies to the mechanical systems, too.

The basic principle of technical logics always acts with the least relative effect. This underline the rob of the technical experience which can't be rationally described. This technical principle is that the technical loggias forces us to rationalize the details because once the activities and the processes increases, the utilization of the small advantages and the disappearance of the small dissipation of power is summed up in increasing big quantities.

To this, we can add the fact that while climb down the detail scale, the saving opportunities became more and more numerous on the conditions of continuous technical al self improvement. Another goal of the efficient pattern beside the building up of a set of recommendations and counter indications generally technical and the dynamic improvement of the scientific progress, there is also the analytic description of the elements of the action and that of different forms belonging to it.

The praxeology represent a science of improving the human action based practically exclusively on the logic's an engineer of the well-done job viewing pedagogically the instructions and the education of the professions.

Researching the most general conditions of the efficiency and the forms of improving the mechanic systems, the efficient pattern achieves the following:

- it classifies the that are used and the of the efficiency conditions contributing to the analytical definition;
- it coordinates the problems by creating systematic charts viewing the criteria systems for the improvement and for different possible details;
- it improves the observation and the previous information viewing the technical action qualities.

The efficient pattern of the management of technological innovation is useful in forming some well-qualified concepts, systematized exposures of some modalities to avoid the omission of important sides of some particular problems and to make easy the overall inclusion in a synthetic and synthetic way.

The pattern includes an appeal to the efficiency; it views not only the precision and economy, but also the way of approaching the problem by the formed conceptual apparatus, respectively the work schedule. From all the rationalizations, it results that the efficient praxeologic pattern is an acknowledgement of action that try on the basic of the data offered by real practice to achieve some generalizations.

The application of the points of view of praxeology in the research activity of the action efficiency as a predominantly mentally activity has a result a rationalization by which these research problem is solved. By applying this rationalization to the research problems linked to the improvement of the mechanic efficiency it result that this can be defined as a process of improvement of the functions basis, techniques, resources and human factors.

This leads in first place to a functional concept starting with the basic principle forward the details. As a general conclusion of evaluation of the action efficiency we should up in mind that all the mechanic systems function in the best way possible, but according to some criteria taking into consideration the working conditions

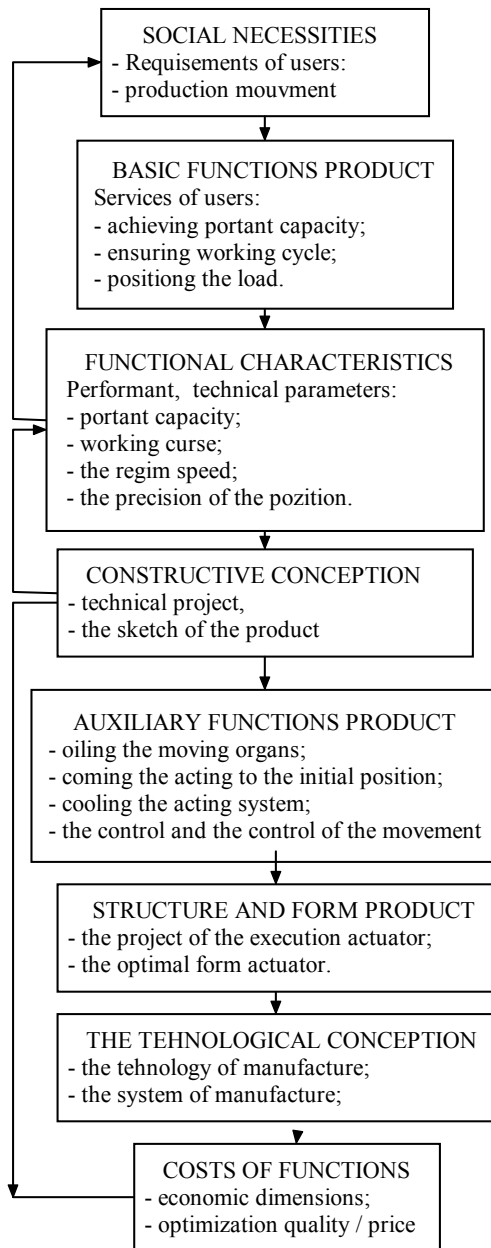


Figure 2. The concept of the actuator after the analysis of value

Indicator of quality of the mechanic system, the efficacy can be put down under the form of an extreme criterion of maximum as a constructive condition of any system with different utilization's and this is  $\eta = \max.$  or a function condition.

The selection of the extremes comes progressively on new sequences and within the context, we propose a new approaching way in the optimal selection on the basic of a pattern of mechanic system of structural phenomenological type which has as a basic, both the structural and tribological improvement.

The quality mark of on optimization operation is represented directly by  $\delta_z$ , which is used when the extreme sense moves the initial value  $z_1$  and the one  $z_2$

$$\delta_z = z_2 - z_1 \tag{1}$$

The fact of  $\delta_z$  expresses the constructive and functional imperfection is more than an attribute to the system. Among the best selection terrible, new criteria are introduced; they are linked to the informational aspects, achieving this big efficiency of the improving process. The conception and its manufacture assisted on the computer has as application field the assembly of the process of developing new products, covering the conception aspects, manufacture and the link between them.

The worldwide industrial contact, starting from the types of product, the ways and types of production and manufacture, determines a certain typology and organization of the manufacture whose model develops nowadays towards the fractal virtual / competing / extended manufacture, where the development is achieved on the principles of integrated technology using the advances informatics technology.

In the concrete case of manufacturing of the actuators the information flux and of materials the fractualisation of the manufacture is direct no go between passing directly from the suppleness to the action areas by the organization of a system of data management (fig.3)

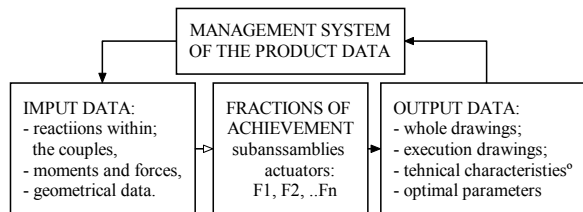


Figure 3. The fraction of the production of the actuators

Using new smart programs of projection the method of the value analysis has as an objective the optimization of the report between the value of use and the cost price of the product.

According to this, the product as physical structure is the material support of some functions which offer it value of use for a user; there is no interest in the product itself but in the functions of the product, respectively in the services which this can offer him.

In the analysis of the value the performances express the level of achieving of some functions objectively measurable (their technical dimensions) and the costs of manufacture is reported to the functions of the product and not to their physical components.

It results that the analysis the value as technique of reducing costs and of qualitative improvement of the products, has the fundamental characteristic of functional analysis.

Theoretically, the approach of the concept and the design of the actuator after the analysis of value are taking place according to Figure 3 in which:

1. Testing at the user of the reconsidered parameters in view of ensuring optimal dimensions;
2. Reconsidering the parameters in comparison to the limits imposed by the adopted constructive conception;
3. Reconsidering the initial conception in comparison to the costs of the functions for the economic efficiency.

### 3. Summary and conclusions

The approached praxeologic pattern is used in forming clear concept, a systematic exposure of the ways to avoid the omission of some sides of particular problems and to make easier the comprehension as a whole in a synthetic and systematic way.

This pattern includes an appeal to efficiency has in view not only precision and saving but also the way we approach the problem by the formed conceptual apparatus, the working algorithm.

Out of the reasoning results that the praxeologic pattern is knowledge of the actions performed which try offered data on the real practice to achieve some generalization and to increase their efficiency optimization modelling is not just an application of the technical - praxiological principles under concrete conditions this justifying the use of praxeology on optimization because this branch science studies the general structure of the human conditions and the conditions of their efficiency.

The applicative and experimental researches viewed the practical checking and the making up of the theoretical patterns used in the output and also convergences to the ways of approaching the problems to reality. The applicative and experimental researches viewed the practical checking and the making up of the theoretical patterns used in the output and also convergences to the ways of approaching the problems to reality.

The work deals with the assimilation of some modern systems of action of linear electro mechanic actuator type used to machine-tools from intelligent systems of production and to the ecologic industrial tools on the basis of some invention patent which should replace the classical ones, consumer energy, immediate use as acting mechanisms of the tubs and obstacle on the hydro-technical arrangements.

The work integrates itself into the present day researches in the field of the development of the modern mechanic transmissions making contributions in their optimal design.

Continuing the research will be done by the implementation of the active and pro-active actions, bringing the formation of the staff in the context of a data base and a pattern of good practice.

The implementation of a net of creative projection, using the methodology of the competitive engineering has in view the development of these products with the active participation of the beneficiary.

#### 4. Acknowledgment

The experimental researches of the linear electro mechanic actuator are the outcome of the researches done by the Laboratory of The Basis of Experimental Research of the North University of Baia Mare, Engineering Faculty.

#### References

- Askin, R., and Strandridge, C., *Modelling and Simulation of Manufacturing Systems*, John Wiley & Sons Inc, SUA.,
- Banks, J. (2001) *Discrete Event System Simulation*, Prentice Hall Inc. SUA.
- Borangiu, Th.. (2003) *Advanced Robot Motion Control*. Editura AGIR. Editura Academiei Romane.
- Chrzsosolouris, G. (2006) *Manufacturing Sytems: Theory of Practice*. Springer Edition.
- Cotetiu, R., Kuric, I., Marcincin, J.N., Ungureanu, N. (2005) *New Trends in Mechanical Design and Technology*. Editura Risoprint, Cluj-Napoca.
- Gillinch, G. R., (2003) *Dinamica masinilor. Modelarea sistemelor tehnice*. Editura AGIR.
- Hennet, J.C. (1997) *Concept set outils por les systemes de production*. Editions Cepadues, Toulouse
- Kuric, I., Marcincin, J.N., Cotetiu, R., Ungureanu, N.S. (2007) *Development of Progresive Technologies. Computer Support for Progressive Technologies*. International DAAAM, Vienna.
- Mohora, C., Cotet, E. and Patrascu, G. (2001) *Simularea sistemelor de productie*. Editura Academiei Române.
- Montgomery, D.C., (1996) *Design of Analysis of Experiments*, 4<sup>th</sup> Edition, John Wiley & Sons, New-York,

---

Năsui, V., (2006) *Actuatori liniari electromecanici*. Editura RISOPRINT Cluj Napoca.

Năsui, V., (1996) *Optimizarea randamentului mecanic*, Editura Universității de Nord Baia-Mare.

Popa, A., (2000) *Controlul digital al sistemelor mecatronice*. Editura Orizonturi Universitare Timisoara.

Popa, I:F. and Duta; L, (2007) *Sisteme flexibile de fabricatie*. Editura AGIR, Bucuresti.

\*\*\* *Aircraft Engineering and Aero-space Technology*. MCB University Press, 70, nr. 4, pp. 259–264, 1998.

# Machining questions of engineering ceramics (Zirconium-dioxide ZrO<sub>2</sub>)

Gellért FLEDRICH, István PÁLINKÁS  
Szent Istvan University, Faculty of Mechanical Engineering

## Abstract

The up-to-date engineering ceramics are rivals of other up-to-date constructional materials at most applications. During developing up-to-date engineering ceramics as a consequence of competition beside developing their material structure it is important to discover the technological conditions more thoroughly and more wide-ranging. To fill this requirement we determine cutting data for machining zirconium-dioxide in our research work.

## Keywords

partly stabilized, „t-m” transformation, micro-crack, hard turning.

## 1. Introduction

The up-to-date engineering ceramics fill important part in many fields of advanced technologies. The engineering practice gets such modern structural materials through them which preserve their outstanding mechanical, thermal, chemical and other properties during extreme conditions unlike till now. The properties of ceramics are decided basically by their chemical compositions and micro-structures. However several results have been achieved so far during research work and development, but in the technological practice couldn't be got such chemical, mechanical, thermal, tribological properties deduced theoretically from the chemical, boucling- and phase relation of special ceramic materials. Considering that the mechanical properties of zirconium-dioxide are most favourable to machine it with tuning I deal further with this in more detailed form.

Zirconium-dioxide was already used as refractory material at the end of 19<sup>th</sup> century. As structural material it is used more and more since 1975. As a functional material it is used most frequently as oxygen-sensor as well as oxygen-ion conductor because of its strong connecting capability with oxygen. During mechanical application the volume change is used taking place during from tetragonal into monoclinal phase transformation.

## 2. Crystal structure, phase transformation

The ZrO<sub>2</sub> has got three crystal structures. The pure ZrO<sub>2</sub> is in monoclinal (m) state at room temperature. It takes on tetragonal (t) structure if  $T \sim 1170^{\circ}\text{C}$ . From here it

becomes cubic © latticework at  $T \sim 2370^{\circ}C$  ( $CaF_2$ -structure). The void spaces forming at high temperature can be traced back to spaces of hydrogen net.

The monoclinal state is Beddeleyit in the nature. In the technical application standpoint the PSZ (Partially Stabilized Zirconia) and the TZP (Tetragonal Zirconia Polycrystals) are important in particular. I deal further with the PSZ – Zirconium dioxide in more detail. The phase transformation can be well perceived in Figure 1. Beside this it can be well discernible that the heating and cooling curves are similar to the iron martensitic transformation unambiguously.

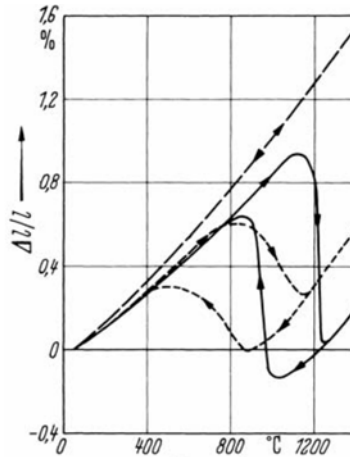


Figure 1. Dilatometric curve in the function of temperature according to Cutris (1947). Continuous line: pure  $ZrO_2$ ; short dash line: 5% Mol CaO alloy; long dash line: 19,8% Mol CaO.

The partially stabilization with calcium is used long. However important technical possibilities can be reached by MgO alloy building, because by this stabilization can be reached at lower temperature.

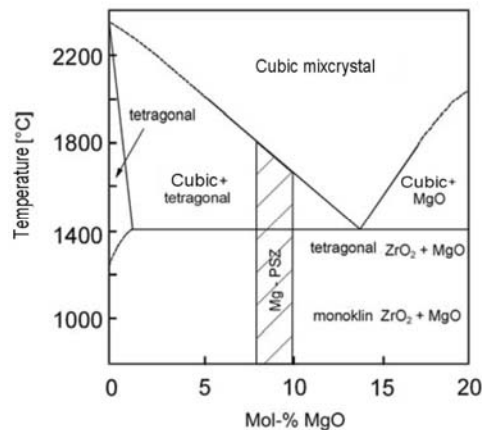


Figure 2.  $ZrO_2$  transformation system in the  $ZrO_2$ -MgO alloy. (Grain, C, F, 1967)

The optimum stabilization takes place at 8-10% MgO content. In the material sintered at the tetragonal ZrO<sub>2</sub> grains the tetragonal-monoclinal transformation can be achieved. They are at metastabil state at room temperature. In case of mechanical load pulling stress develops, a critical value of which the phase transformation takes place: monoclinal grains are formed with greater volume and almost „close” the crack propagation. The tetragonal- monoclinal transformation is without diffusion similarly to martensitic phase transformation in steels knows long, it is a structure transformation without composition change.

This property is responsible of zirconium-dioxide ceramics for long range resistance against load.

### 3. Mechanical properties

In case of zirconium-dioxide materials the mechanical properties determine the dimensions of the error, the structure and the phase transformation deriving from transformation effect. Inasmuch the „t → m” phase transformation takes place only at high mechanical stress, the breaking strength will be lower and in such a case the strength can be determined on the basis of critical dimension of error. If the transformation (t → m) threshold is low the atomic movements start earlier. Then the aim is to reach higher breaking strength.

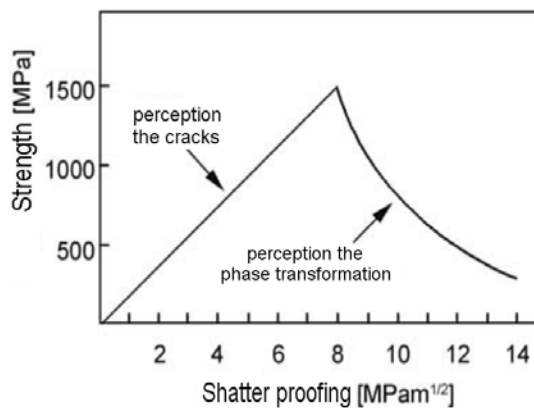


Figure 3. The relation of strength and shatter proofing in case of phase transformation ceramics.

The result of phase transformation can be seen in Figure 4. Though the ceramic examined is Al<sub>2</sub>O<sub>3</sub> alloyed with ZrO<sub>2</sub>, but it is interesting, it can be seen the ZrO<sub>2</sub> phase transformation closed the crack propagation.

Important mechanical properties, first of all ZrO<sub>2</sub> based engineering ceramics can be seen in Table 1.

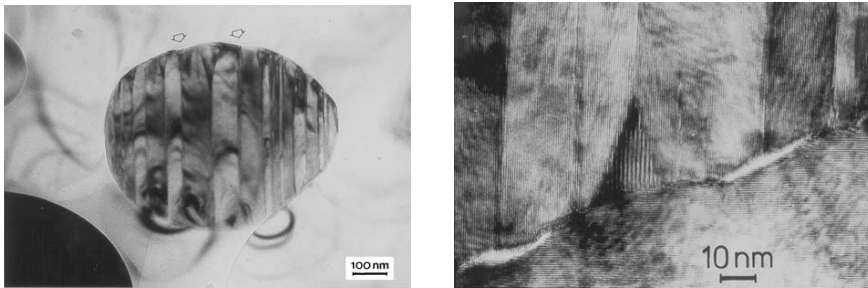


Figure 4. High resolution SEM-exposure of monoclinal double-twin formed at micro-crack. (Max Planck Institut für Metallforschung, Stuttgart)

Table 1. Important mechanical properties of various alloyed ZrO<sub>2</sub>.

		Mg-PSZ	3Y-TZP	12Ce-TZP	ZTA 16% Al <sub>2</sub> O <sub>3</sub>
Strength *	MPa	400-80	800-1600	500-800	580-800... 1200
Fracture strength	MPam <sup>1/2</sup>	7-15	5-6	10-17	8-10...15
Young modulus ( E )	GPa	200	210	80-110	350-380
Hardness	HV <sub>0.5</sub> GPa	7-17	12-13		16-18

\* Measuring bending with 4 dots

#### 4. Some questions of final machining of ceramics.

The zirconium-dioxide ceramic provides wide-ranging application possibilities because of its good strength and toughness properties. For example it is important element of textile industry and the iron-steel production. It is often used at bearing and sealing systems in the mechanical engineering. In such cases the machining after sintering gets an important role.

Now days the grinding and hiving are the wide-spread machining generally after sintering. The material removal is small quantity is case of such machining. The micro-cracks forming can be seen in Figure 5. taking place by the cutting grain.

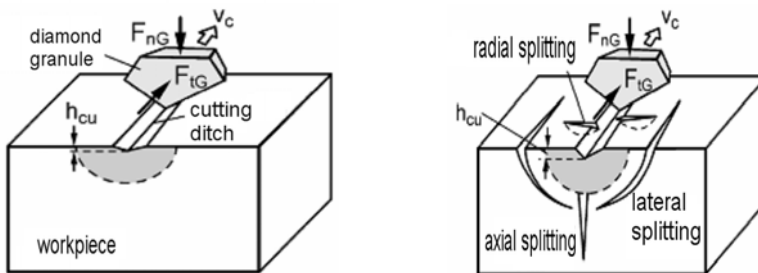


Figure 5. Theoretical possibility of micro-crack forming during cutting one grinding grain (Source: Lawn, Marshall, Evans)

The surface quality is positively influenced by grinding tools with fine grain ceramic bonding during machining of ceramics. The smaller grain size reduces

the chip volume removed, the cutting force respectively as well as the surface pressure also reduces. The power demand of cutting increased despite of these deriving from the number of micro-cracks reduces and so the possibility of breaking-out elementary particles also reduces. The so-called fine hard turning of hard, tough material arises for a long time as possible replacing the grinding. In addition to the proper tool materials developed for this the machine-tools also had to be developed.

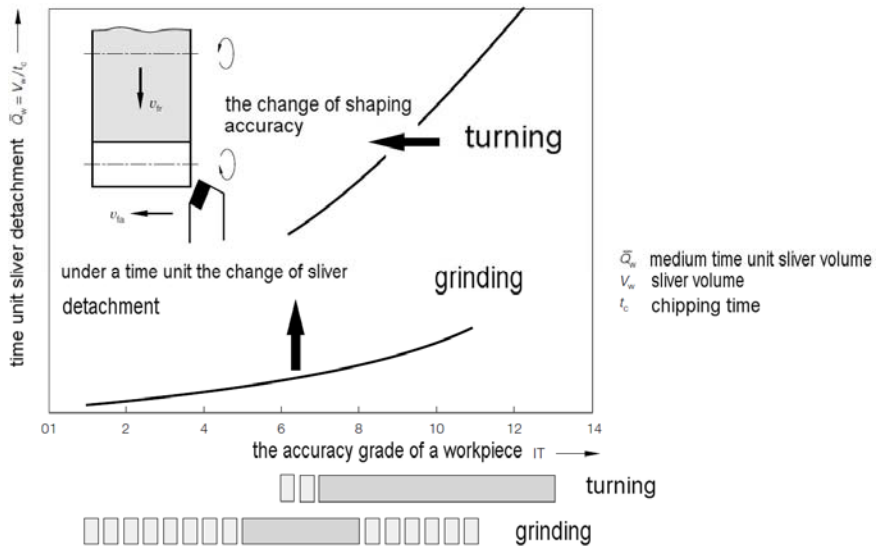


Figure 6. The chip amount removed during time unit in function of the machining accuracy in case of turning and grinding (Fritz and his fellow.)

In the Figure 6. can be seen that the amount of chip removed during time unit is significantly greater in case of turning. Considering the accuracy classes of range is just the dimension range the moving, wearing and sliding elements of machine parts. Deriving from this it would be important developing a more economical and more productive machining.

### 5. Conclusion

The application of the technical ceramics between extreme relations appears as an increasingly bigger claim. The extraordinary characteristics presuppose special shaping. Nowadays the shaping procedures (onto final work) following the sintering are squeezed between narrow bars. The production of semi-finished products similar to the structural substance can be imagined only after the development of sliver detachment methods with bigger efficiency. We make

researches concerning the chipping at our institute. The above ones make the turning as big substance detachment opportunity, possible with nowadays modern tool substance. Our examinations concerning the turning deal with the possible cutting tools, the cutting strengths, the effects of their changes on the components.

## References

- A. H. Fritz, G. Schulze (Hrsg.) (2007):Fertigungstechnik. 8. Aufl *Springer Verlag, Berlin* 279. old.
- Curtis, C.E. (1947): Development of zirconia resistant to thermal shock. *J. Am. Ceram. Soc.* 30 180-196.
- H. Salmang, H. Scholze (2007): Keramik, *Springer Verlag, Berlin*
- Swain, M.V.; Rose, L.R.F. (1986): Strength Limitations of Transformation-Toughened Zirconia Alloys. *J. Am. Ceram. Soc.* 69 511-518
- Mészáros I., Szepesi D. (2006): Edzett acélok nagy pontosságú megmunkálása IV. *Gépgyártás XLVI. évf. 4. sz.* 29-33 old.
- Szépölgyi J. (1994): Korszerű műszaki kerámiák, *Magyar Tudomány*, 4. sz. 7-13 old.

# **The effects of humidity on surface resistance of magnesium catalyzed cast polyamide 6**

Mátyás ANDÓ, Gábor KALÁCSKA,  
Szent Istvan University, Faculty of Mechanical Engineering  
Tibor CZIGÁNY  
Budapest University of Technology and Economics

## **Abstract**

The magnesium catalyzed polyamide 6 can absorb the humidity of air. Due to this the surface resistance, i.e. the antistatic characteristic changes. In our material developing program a special grades were produced, which have appropriate antistatic characteristics under dry conditions, too. With graphite additive having conductive characteristics it could be reached that the surface resistance of new material did not depend on moisture content. It was found also that surface resistance – in general – can change with order of magnitude within few hours after production.

## **Keywords**

cast polyamide 6, humidity, surface resistance,

## **1. Introduction**

In the industrial and agricultural machines, plastic parts are used in several cases. It is known that plastics due to their good insulating characteristics are able to be charged, which increases the pollution. With antistatic parts this effect can be avoided, moreover, it provides more advantages during the operation. Antistatic plastics are not charged, therefore discharge will not develop (e.g. by accident a person to earth it), and sparks will not emerge (which may cause in special cases an explosion or blast eg. in agriculture the phenomenon of powder blast). Other advantages of antistatic or electrically conductive plastic parts are the easier and cost saving storage and material handling and maintenance orders.

As a part of the present material developing process, cast PA 6 with antistatic characteristics were produced. The humidity absorption of the base matrix has an effect on the grade of the antistatics, therefore the experiments on humidity effects are necessary.

## **2. Characteristics of base matrix**

The material is produced by Quattroplast Kft, under the name DOCAMID 6G-H. This material can not be compared directly to other polyamide 6 products in the

world because of the magnesium catalyser used for the production. In general, polyamide 6 (PA6) type plastics are made with polycondensation, but for casting purposes the ring opening polymerization is used. The advantage of the latter is the fact that the chain formation takes place without water in a few minutes, which enables a faster production contrary to the conventional polycondensation technology. For starting the ring opening polymerization, usually natrium catalyser is used, but by the present material magnesium catalyser was used. The characteristics of DOCAMID 6G-H is summarized in table 1.

Separate examinations were made to explore the humidity content of the base matrix as different machine parts made of polyamides that were able to absorb the humidity content of the air. The absorption follows the law of diffusion. The outer surface layer is able to bound humidity fast, but this humidity content reaches the lower layer very slowly. On figure 1 the humidity absorption of samples, soaked in 20°C water, is shown in the function of time.

Table 1. Characteristics of DOCAMID 6G-H base matrix

Density	1,15 g/cm <sup>3</sup>
Tensile strenght	85 MPa
Elongation at break	60%
Elastic modulus	3300 MPa
Charpy impact strength	>8 kJ/m <sup>2</sup>
Shore D hardness	83
Volume resistance	10 <sup>15</sup> Ω·cm
Surface resistance	10 <sup>13</sup> Ω
Heat Distortion Temperature (HDT)	95°C

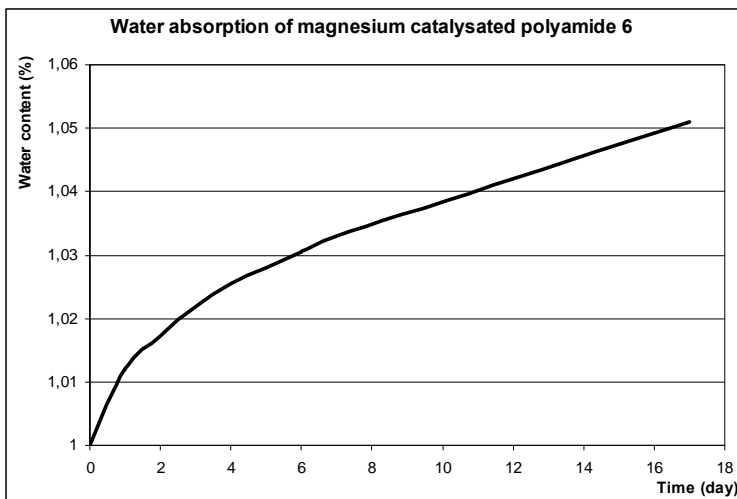


Figure 1. Water absorption of magnesium catalyzed polyamide 6

It can be seen on the figure that after 17 days the samples still not reached the impregnation level, only the speed of absorption became constant (0,2 %/day $\approx$ 0,02 g/day). This experiment proves also the slow impregnation process, though machine parts usually do not cope with water for such a long time. However they cope with the humidity of air, therefore it is reasonable to take the possible impregnation into consideration. Impregnation due to air humidity content means an even slower process.

There is a need to deal with humidity absorption due to other reasons of design, too. Humidity causes the change of dimensions of the polyamide parts and mechanical properties, too.

### 3. Surface resistance measurement

Among electrical tests the surface resistance measurement is widely used to check the antistatic characteristics of the materials. Surface resistance measurement is standardized. Now the standard called „IEC 60093 Methods of Test for Volume Resistivity and Surface Resistivity of Solid Electrical Insulating Materials” and published in 1980 is in use.

For the research the GIGALAB Digital Mega-Ohmmeter, produced by ITECO, was used. The diameter of the used rubber electrodes were  $\varnothing 63$  mm, their width were 4 mm. For the measurement 100 V potential was used, which means a measurement range of  $10^5 - 2 \cdot 10^{11} \Omega$ . This range is just appropriate for antistatic measurements, as above  $10^{12} \Omega$  the polymers are insulators, below  $10^6 \Omega$  the polymers are conductive. During the research the required antistatics was defined in  $10^9 \Omega$  surface resistance. The measurement accuracy in this range was in  $\pm 5 \%$ . The measurement settings can be seen on figure 2 (the distance maker should be taken away after the setting of the two electrodes).

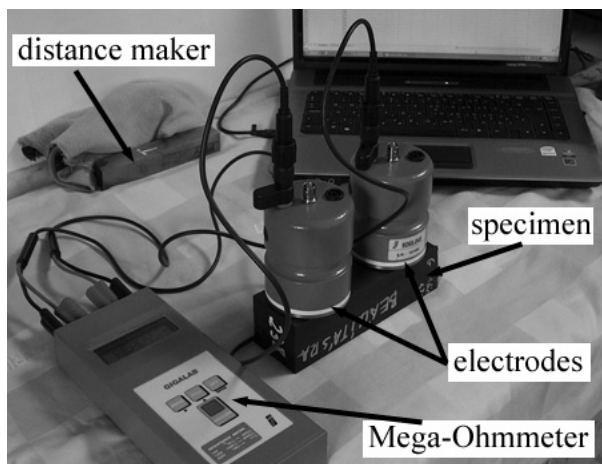


Figure 2. Setting of surface resistance measurement

#### 4. The surface resistance in time

The working conditions of different machines are often changed. These changes can have an influence on parts, therefore on plastic parts as well. Therefore the change of surface resistance was examined in time. During the experiment that outstanding case was taken, when the absolutely dry sample was put into water. The results are shown in table 2.

Table 2. Surface resistance change of originally dry sample put into water in the function of time

Conditioning	0 hour	24 hours	48 hours	72 hours	96 hours	120 hours
Surface resistance ( $\Omega$ )	$7.58 \cdot 10^{10}$	$5.8 \cdot 10^7$	$3.96 \cdot 10^7$	$3.92 \cdot 10^7$	$3.33 \cdot 10^7$	$3.35 \cdot 10^7$

It can be seen that surface resistance changes basically during the first 24 hours. This means that the value of surface resistance reacts fast to the modified conditions. The more humid air is able to change the antistatic characteristics of the dry material in a few hours. The experienced material behaviour suggests to select the proper antistatic characteristics valid under dry conditions as well.

#### 5. Effects of humidity content on surface resistance

For reaching antistatic characteristics the applied additives in base PA 6 matrix enhance the existing humidity effects. The surface resistance is decreased furthermore. On figure 3 the behaviour of TA52 composites (material softening additive) can be seen. Three main stages are compared: dry, normal (RH 50%) and wet (saturated in water) samples.

In present case the additive can not absorb humidity just the base matrix. In case of sample containing 10 % additive, depending on the stages, the surface resistance changes between  $10^{11}$  and  $10^7 \Omega$ . This means that the originally good insulator ( $10^{13} \Omega$ ) plastic, depending on the surroundings, can have worse or even better antistatic characteristics. However in case of 20 % additive, independently from surroundings, the antistatic characteristics are good (below  $10^9 \Omega$ ).

The independence of polyamide parts from the environment has several advantages, e.g. no need for conditioning, or the maintenance can be held in regular periods (e.g. the stuck contamination is not changing according to the environment).

In figure 3 it also can be seen that the surface resistance of normal samples (RH 50%) are between the wet and dry samples' values but are closer to the dry ones. The working condition of cast polyamide parts is usually air (not water), that's why the dry and normal stage curves are suggested to be taken into account during design with cast polyamide parts.

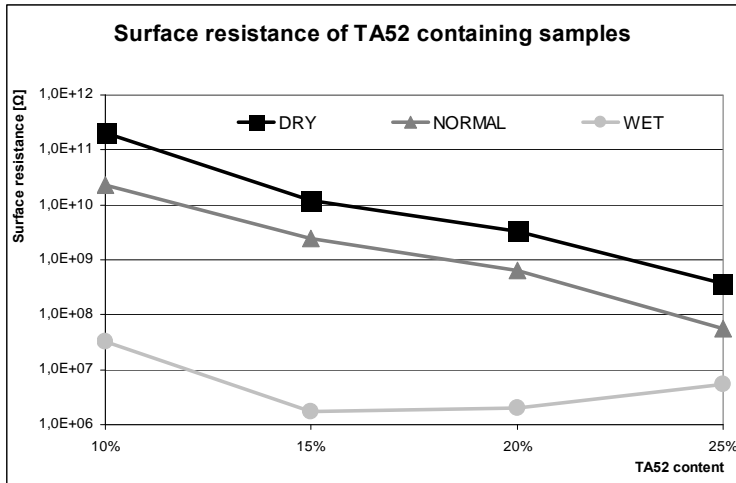


Figure 3. Surface resistance of PA6 composites in different stages

### 6. Effects of humidity content on the under-surface layers

In case of cut of the given polyamide 6 part, the humidity content and the resistivity will be different. The humidity content of the deeper or under-surface layers are important during machining. Due to the slow impregnation process lower humidity content is expected, i.e. their surface resistance is going to be higher. For testing this, a sample with 1% graphite content was examined conditioned in RH50%. The surface resistance of the layers was examined.

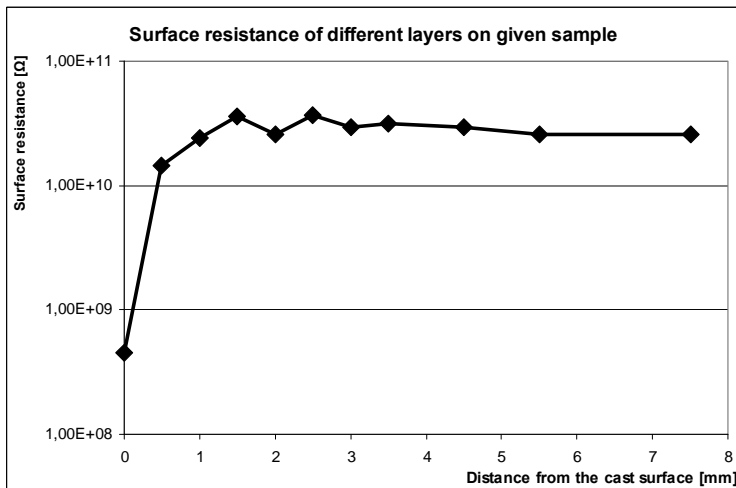


Figure 4. Surface resistance of different layers on given sample.

On figure 4 it can be seen that in the near-surface zone (original cast surface) the humidity content results smaller surface resistance that it was found for dry material (eg. after removing 2.5 mm). From the experiments it was found that 5 months conditioning is enough for humidity to diffuse into 0.5 mm depth. The measurements show that in layers deeper than 1 mm the sample is nearly dry. Further resistance values are influenced only by the distribution of additives. However these variations are negligible. On the basis of these it can be stated that after sudden material detachments dry condition surface resistance can be expected, though the new surface can become to the state of humid surface resistance in 24 hours.

## 7. Summary

There is an increasing need for using antistatic polyamide 6 versions. Those materials react fast to the environmental effects, i.e. their surface resistance (antistatics) can change significantly. For stable working performance of natural cast polyamide 6 material, which is generally used as an isolator material, the needed surface resistance should be taken as the possible most wet condition sample having lowered resistance. In case of antistatic composite version of cast PA 6 the dry sample's value should be taken into consideration as a critical values. The different composites have different sensitivity to the humidity, but the dry ones have higher surface resistivity.

## References

- Gächter R., Müller H.: *Műanyagadalékok zsebkönyve*, 1989 Budapest Műszaki Könyvkiadó
- Kalácska G.: *Műszaki polimerek és kompozitok a gépészmérnöki gyakorlatban*, 2007 Gödöllő 3C-Grafika Kft.
- Macskási L.: *Műanyagok előállításának kémiai és műveleti alapjai*, 1996 Budapest Abigél Bt.
- Novák I., Krupa I.: *Electro-conductive resins filled with graphite for casting applications*, 2007 *European Polymer Journal*, 40 (7) 1417-1422

# **Influence of secondary electro-conductive phases on the friction and wear response of ZrO<sub>2</sub>-based composites**

Koen BONNY, Patrick DE BAETS, Yeczain PEREZ,  
University Gent, Department of Mechanical Construction and Production  
Jef VLEUGELS, Omer VAN DER BIEST,  
Catholic University Leuven,  
Metallurgy and Materials Engineering Department  
Bert LAUWERS  
Catholic University Leuven, Mechanical Engineering Department

## **Abstract**

ZrO<sub>2</sub>-40vol.%WC, ZrO<sub>2</sub>-40vol.%TiCN and ZrO<sub>2</sub>-40vol.%TiN composite flats were surface finished by wire-EDM, grinding and polishing. Their reciprocative dry sliding friction and wear behavior against WC-6wt.%Co cemented carbide pins was compared using a Plint TE77 tribometer. The worn surfaces and wear debris of the ZrO<sub>2</sub>-based composite grades were characterized by scanning electron microscopy (SEM), energy dispersive X-ray analysis (EDX) and surface topography. Correlations between wear volume, wear rate and coefficient of friction on the one hand and material properties on the other hand were determined. Based on the experimental results, a strong dependence of tribological characteristics on the secondary electro-conductive phase as well as on surface finishing conditions was evinced.

## **Keywords**

zirconia composite, wire-EDM, surface roughness, reciprocative sliding, friction, wear, pin-on-plate

## **1. Introduction**

ZrO<sub>2</sub> ceramics have been indicated as very strong and tough oxides owing to the stress-induced phase transformation from tetragonal to monoclinic zirconia. Combined with the low density, the excellent chemical inertness and the capacity to preserve the mechanical properties in a wide range of temperatures has brought zirconia ceramics to the front end material to meet a large number of industrial applications in the fields of automobile, manufacturing and cutting tools punches and biomedical applications.

The incorporation of hard phases such as WC, TiCN or TiN into a ZrO<sub>2</sub> matrix not only improves the hardness, but also reduces the electrical resistivity, making these composites suitable for electrical discharge machining (EDM).

This material removal method allows very complex shapes to be produced full automatically and with high accuracy and irrespective of the hardness of the material because no mechanical contact is involved in this process.

This paper focuses on laboratory-made yttria-stabilized ZrO<sub>2</sub>-based composites with 40 vol.% of TiN, TiC<sub>0.5</sub>N<sub>0.5</sub> or WC addition. These composites have already proven their feasibility for electrical discharge machining (EDM) in de-ionized water. Flat specimens were machined and surface finished by wire-EDM, grinding and polishing. The tribological behavior was investigated in dry sliding friction experiments on a pin-on-plate testing rig. Wear surfaces were examined by SEM analysis in order to identify the occurring wear mechanisms. Correlations between wear volume and coefficient of friction on the one hand and surface conditions and material parameters on the other hand were investigated.

## 2. Experimental

The zirconia composites were obtained by hot pressing of yttria-stabilised ZrO<sub>2</sub> powder mixtures with 40 vol. % of WC, TiC<sub>0.5</sub>N<sub>0.5</sub> or TiN phase. More information on the processing and characterisation of the ZrO<sub>2</sub> composites is given elsewhere. Mechanical, physical and microstructural features are listed in Table I.

Table 1: Physical, mechanical and microstructural properties of ZrO<sub>2</sub>-based composites

Composite grade	A	B	C
Secondary Phase*	WC (20 nm)	TiCN (3-5 μm)	TiN (0.8-1.2 μm)
E [GPa]	328±4	284±3	274±2
HV <sub>10</sub> [kgf/mm <sup>2</sup> ]	1691±8	1422±10	1370±7
K <sub>IC</sub> [MPa.m <sup>1/2</sup> ]	8.5±0.4	7.0±0.2	5.6±0.1
Density [g/cm <sup>3</sup> ]	9.80	5.76	5.81
ρ [10 <sup>-6</sup> Ω.m]	4.3	17.0	4.6
d <sub>av</sub> average grain size [μm]	0.25	0.37	0.38
d <sub>50</sub> grain size [μm]	0.11	0.22	0.24
d <sub>90</sub> grain size [μm]	0.54	0.84	0.86

\* number indicates crystal size of secondary phase powders

It is worth noting that all reported values are the average of at least five measurements. The composites cover a wide range of material properties. The ZrO<sub>2</sub>-WC composites combine excellent hardness and toughness. The ZrO<sub>2</sub>-TiN composite displays the lowest hardness and E-modulus but intermediate toughness. The finest grain size distribution of the secondary phase is

encountered with ZrO<sub>2</sub>-WC, with 90 % of the grains being smaller than 0.54 μm. Representative scanning electron micrographs of the different composites are shown in Fig. 1.

The regarded zirconia composite grades were surface finished by wire-EDM or by grinding and polishing, ultimately with diamond paste, up to optical finish. The wire-EDM was executed on a ROBOFIL 2000 (Charmilles Technologies, Switzerland) in deionized water (dielectric conductivity 11 μS/cm), using a CuZn37 wire electrode with a diameter of 0.25 mm and a tensile strength of 500 MPa. One rough EDM step followed by several consecutive finishing cuts with gradually lower energy input and shorter energy pulse duration were performed to reduce the surface roughness below 1 μm R<sub>a</sub>. The device settings for the different wire-EDM steps are described in previous investigation. The grinding operations were performed on a JF415DS (Jung, Göppingen, Germany) with a diamond grinding wheel (type MD4075B55, Wendt Boart, Brussels, Belgium).

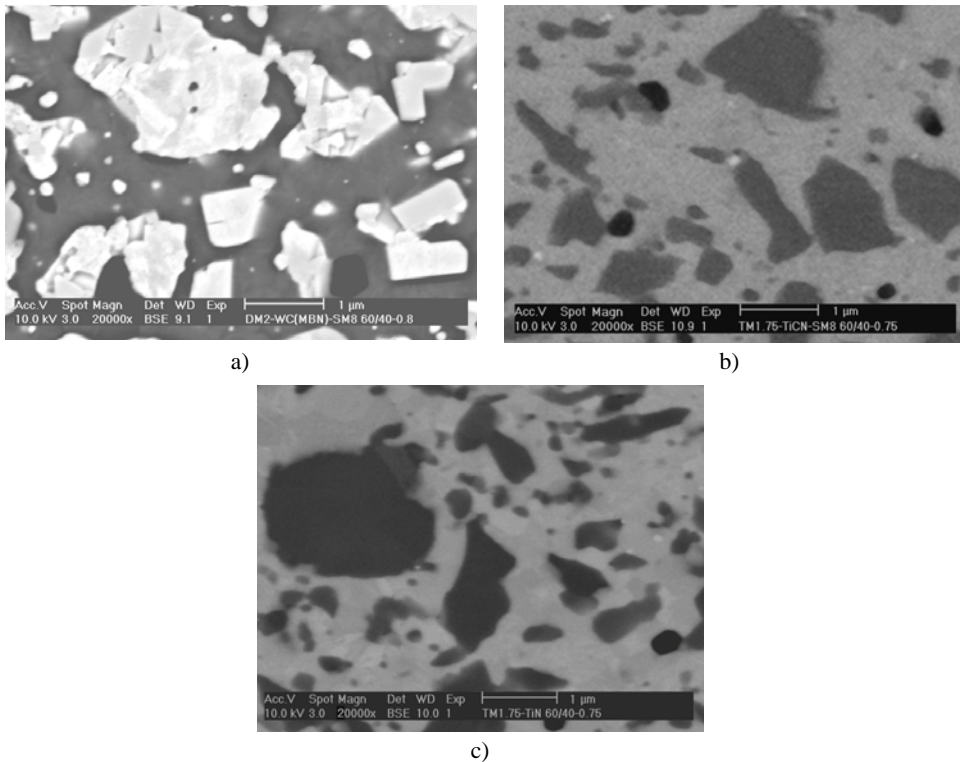


Figure 1. Microstructure of ZrO<sub>2</sub> composites with 40 vol.% (a) WC (bright phase), (b) TiCN (dark phase) or (c) TiN (dark phase)

The R<sub>a</sub> and R<sub>t</sub> surface roughness for the studied ZrO<sub>2</sub>-based composite grades with three surface finish variants are summarized in Table 2. It is worth noting that the data in Table II are obtained in accordance with the ISO 4288 standard

and they represent the average values of at least five roughness measurements. The lowest  $R_a$  and  $R_t$  level is encountered with polished plate specimens, whereas the wire-EDM'ed ZrO<sub>2</sub>-based grades exhibit the highest surface roughness.

Table 2:  $R_a$  and  $R_t$  surface roughness for wire-EDM'ed, ground and polished ZrO<sub>2</sub>-based composites

Surface roughness	Finishing operation	Grade A	Grade C	Grade E
$R_a$ [ $\mu\text{m}$ ]	wire-EDM	0.87	0.70	0.65
	grinding	0.09	0.06	0.18
	polishing	0.008	0.007	0.009
$R_t$ [ $\mu\text{m}$ ]	wire-EDM	7.39	6.37	5.16
	grinding	0.60	0.50	1.42
	polishing	0.07	0.04	0.08

The tribological behavior of wire-EDM'ed zirconia composites was evaluated using a high frequency Plint TE77 tribometer, in which WC-6wt.%Co cemented carbide pins were oscillated against zirconia composite counter plates in air-conditioned atmosphere at 23 °C and 60 % relative humidity, in conformity with the linearly reciprocating pin-on-flat sliding wear test principle described in ASTM G133. The pin material (CERATIZIT grade MG12 with 6 wt. % Co) displays a hardness  $HV_{10}$  of 1913 kgf/mm<sup>2</sup>, a fracture toughness of 9.3 MPa·m<sup>1/2</sup> and an E-modulus of 609 GPa. The radius and the  $R_a$  and  $R_t$  surface roughness of the pin hemisphere were determined to be 4.08 mm, 0.35  $\mu\text{m}$  and 2.68  $\mu\text{m}$  respectively. Contact forces of 15 N up to 35 N were applied, with a 0.3 m/s sliding velocity and a 15 mm stroke length. The test duration was associated with a sliding distance of 10 km.

The imposed normal force ( $F_N$ ) and the concomitant tangential friction force ( $F_T$ ) were recorded continuously as function of sliding distance (s), respectively by means of a load-cell and a piezoelectric transducer. The  $F_T/F_N$  forces ratio is defined as the coefficient of friction ( $\mu$ ), which can be differentiated in a static ( $\mu_{\text{stat}}$ ) and a dynamic ( $\mu_{\text{dyn}}$ ) component. Simultaneously, the combined wear depth ( $\Delta d$ ), resulting from the pin penetrating the counter plate, was acquired by an inductive displacement transducer. The experiments were executed up to a sliding distance of 10 km in order to allow post-mortem wear volumes to be compared. Each test was repeated at least three times under identical conditions. Before testing, both pin and plate specimens were rinsed ultrasonically in distilled water with a detergent solution (2% Tickopur R33, 50 °C, 15 minutes) and immersed in acetone and cleansed in cold distilled water. For each wear test, a new WC-6wt.%Co pin was used in order to approximate equal initial pin surface conditions. The wear tracks were examined using scanning electron microscopy (SEM, XL-30 FEG, FEI, Philips) and energy dispersive X-ray

spectroscopy (EDS). The generated wear was quantified volumetrically by surface scanning equipment (Somicronic EMS Surfscan 3D, type SM3, needle type ST305).

### 3. Results and discussion

#### Friction and penetration depth

Typical and representative tribological data obtained during real-time monitoring of friction coefficient and combined penetration depth for wire-EDM ZrO<sub>2</sub>-based composite flats/ WC-6wt.%Co pin combinations sliding at 0.3 m/s under a 15 N contact load are presented in Fig. 2. Each curve is an average of at least three wear experiments performed under identical conditions. Error bars indicating the extent of the variations were excluded in order to make the figures better readable.

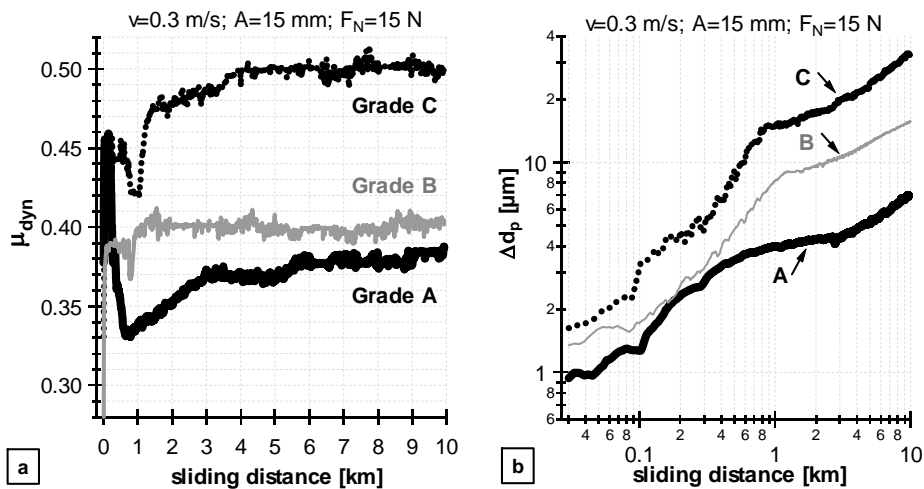


Figure 2. Dynamic friction coefficient (a) and penetration depth (b) for wire-EDM'ed ZrO<sub>2</sub>-based composites sliding against WC-6wt.%Co pins at 0.3 m/s using a 15 N normal contact force

The dynamic friction coefficient of all tribopairs was measured to be in the range of 0.33-0.52, Fig. 2(a). It should be noted that the static friction coefficient varied similarly as function of the sliding distance, but at a higher level, compared to the dynamic friction coefficient. The friction coefficient is noticed to increase abruptly during the first meters of sliding and then gradually ascends further during the growing pin on plate contact surface and the concomitant removal of the recast surface layer. After a running-in stage, the friction coefficient drops down shortly and rises again above its prior level. Beyond a sliding distance of 4 km, the variations in the friction force curve appear to be marginal.

The temporary drop down followed by a steep increase in friction coefficient corresponding to a sliding distance of approximately 1 km has not been fully elucidated and probably represents an edge phenomenon, but could also be due to changes in the sliding contact surface as a result of the removal of the wire-EDM induced recast layer. The fluctuations in the friction curves, both during and after the running-in stage, are due to a continuous breaking and regeneration of micro junctions as a result of asperity interaction and should be related to the constantly changing degree of adhesion between the contact surfaces.

In agreement with previous investigation, the effect of the secondary phase on friction is quite pronounced, Fig. 2(a). The lowest friction level is encountered with the ZrO<sub>2</sub>-WC composite, whereas the ZrO<sub>2</sub>-TiN specimens exhibit the highest coefficient of friction.

The strong influence of the nature of the secondary phase on friction characteristics is also reflected in the online measured penetration depth of the investigated tribopairs, in full agreement with previous research. As can be seen in Fig. 2(b), the wear depth is found to be largest for the ZrO<sub>2</sub>-TiN composite and lowest for the ZrO<sub>2</sub>-WC.

In all cases, the penetration wear is noticed to increase abruptly during the first meters of sliding and then gradually ascends further with growing pin on plate contact surface. During the first 100 meters of sliding, the penetration depth remains below 3 μm, but then rapidly rises. At this point, the influence of the secondary phase material on the wear resistance of the zirconia composites becomes more pronounced. After this initial stage, corresponding to a sliding distance of about 1 km, wear depth increases at an approximately constant rate. Grossly, it can be stated that wear depth varies exponentially as function of sliding distance, and thus, the sliding wear process presumably reaches an equilibrium situation.

#### *Wear volume*

In order to examine the reciprocating sliding wear behavior, research was mainly focused on analysis of wear characteristics in the equilibrium wear regime. Wear experiments were carried out under the condition of a constant total sliding distance of 10 km. From the 3D wear track surface topographies of the ZrO<sub>2</sub>-based composites, the corresponding wear track volumes ( $V_{wear}$ ) were extracted. Based on the obtained wear volume, a volumetric wear rate ( $k_v$ ) was derived from (1):

$$k_v = \frac{V_{WEAR}}{F_N \cdot s} \left[ \frac{mm^3}{N \cdot m} \right] \quad (1)$$

where  $F_N$  represents the imposed normal contact force while  $s$  stands for sliding distance. Some numerical data are presented in Table III, in which post-mortem wear track dimensions, wear volumes and volumetric wear rates  $k_v$  (10 km) for

the ZrO<sub>2</sub>-based composites are compared when a 15 N contact load was applied. Under identical conditions of sliding distance and sliding speed, the smallest depth and width of the wear scars were measured for the ZrO<sub>2</sub>-WC, whereas the highest values occurred for the ZrO<sub>2</sub>-TiN composite. These findings fully confirm the observations made in Fig. 2. The sequence of ZrO<sub>2</sub>-WC, ZrO<sub>2</sub>-TiCN and ZrO<sub>2</sub>-TiN for the relative wear quantification ranking was also found in previous investigations.

*Table 3. Wear track dimensions and volumetric wear rates for ZrO<sub>2</sub> grades slid against WC-6wt.%Co pins (s=10 km, F<sub>N</sub>=15 N)*

Wear quantification	Grade A	Grade B	Grade C
Width [mm]	1.05	1.15	1.55
Depth [μm]	4.8	12.8	29.6
V <sub>wear</sub> (10km) [10 <sup>-3</sup> mm <sup>3</sup> ]	8.9	92.3	320
k <sub>v</sub> (10km) [10 <sup>-6</sup> .mm <sup>3</sup> .N <sup>-1</sup> .m <sup>-1</sup> ]	0.058	0.62	2.13

Comparing the post-mortem obtained results with the online measured vertical displacement reveals small deviations in wear depth values. This is partly attributed to the wear of the pin, which was not taken into account during post-mortem quantification. However, the correspondence between real-time monitoring and post-mortem quantification is quite acceptable. Hence, it may be inferred that the online wear monitoring technique yields a reliable sliding wear prediction for the tribocouples investigated.

#### *Impact of surface finish*

Friction and vertical displacement curves versus sliding distance for WC-6wt.%Co pins sliding at 0.3 m/s under a 15 N contact load against ZrO<sub>2</sub>-TiN composite flats with wire-EDM'ed, polished or ground surface finish are plotted in Fig. 3. Within the full sliding wear path range the effect of the surface finishing operation on the coefficient of friction is quite pronounced, Fig. 3(a).

The lowest friction level is encountered with the ground ZrO<sub>2</sub>-TiN samples, whereas the wire-EDM'ed ZrO<sub>2</sub>-TiN equivalent exhibits the highest friction level. A similar trend is observed for the penetration depth curves, Fig. 3(b).

Already during the first sliding meters wear depth turns out to exhibit higher values for the wire-EDM'ed ZrO<sub>2</sub>-TiN samples compared to their ground and polished equivalents. The considerable higher initial wear loss for wire-EDM'ed ZrO<sub>2</sub>-TiN composites should be attributed to a combination of (i) higher initial surface roughness, (ii) the relatively higher ease of removal of the recast layer induced by the wire-EDM process, and (iii) the higher friction coefficient.

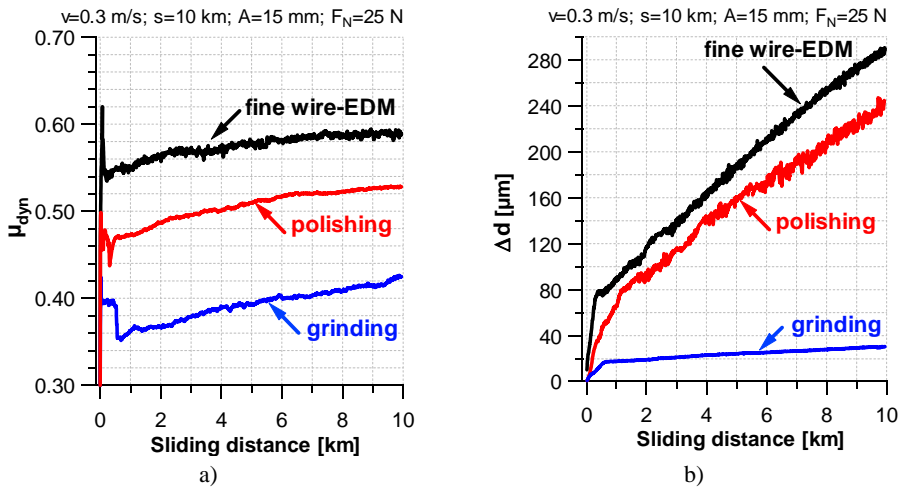


Figure 3. Dynamic friction coefficient (a) and penetration depth (b) for WC-6wt.%Co pins sliding at 0.3 m/s using a 25 N normal contact force against ZrO<sub>2</sub>-TiN with different initial surface finishes

### Wear surface analysis

Comparison of the friction and wear responses of the zirconia-based composites has demonstrated that the wear characteristics are affected considerably by the secondary phase material and the involved wear mechanisms. The occurring wear mechanisms were identified by scanning electron microscopy.

After each sliding wear test the generated wear debris particles were collected for microscopic examination. The wear debris was mainly located in the outer extensions of the wear track but occasionally also inside, along and adjacent to the wear scars. Scanning electron micrographs in SE mode of the wear debris particles derived from ZrO<sub>2</sub>-based composites slid against WC-6wt.%Co pins at a 10 Hz oscillating frequency under 15 N contact load are presented in Fig. 4.

The debris from the ZrO<sub>2</sub>-WC composite is relatively strongly agglomerated and mainly occurring as chunks, Fig. 4(a). Atomic number contrast, i.e. backscattered electron, micrographs reveal the presence of a small amount of remaining bright WC particles in a darker atomic number contrast W-Zr-O-Al matrix. However, the WC particles in the debris are substantially smaller than in the original composite material.

SEM micrographs of wear debris originating from wire-EDM ZrO<sub>2</sub>-TiCN grade B composite slid against WC-6wt.%Co pins at 10 Hz and 15 N are shown in Fig. 4(b). The wear debris is significantly less agglomerated compared to the ZrO<sub>2</sub>-WC composite. No phases could be differentiated in the debris by means of backscattered electron images, indicating that the original ZrO<sub>2</sub> and TiCN phases are integrated in the debris material, which contains Zr, Ti, Al and O. The nature of the debris particles is nanometric.

The optical appearance of the wear tracks was smooth, indicating that the surface of the composite was polished as a result of the sliding contact with the

WC-6wt.%Co pin. The smoothening is confirmed by R<sub>a</sub>- and R<sub>t</sub> measurements before and after wear testing. The normal roughness profile of a ZrO<sub>2</sub>-TiN composite within the wear track yields average R<sub>a</sub>- and R<sub>t</sub>-values of 0.015 μm and 0.11 μm respectively, which is quite below the original surface roughness after wire-EDM (see Table II).

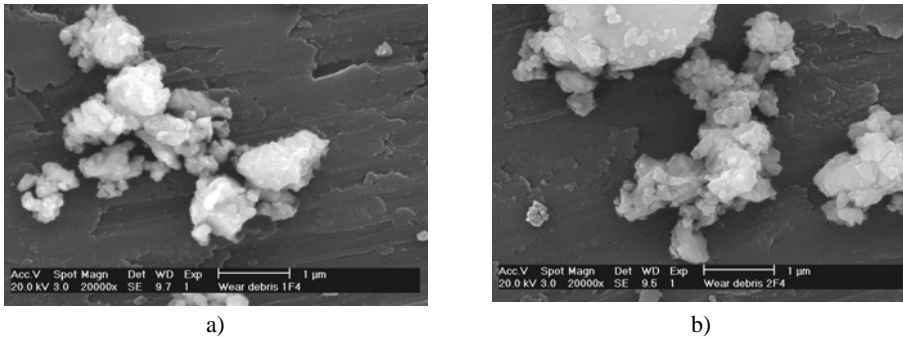


Figure 4. SEM micrographs of wear debris originating from (a) ZrO<sub>2</sub>-WC and (b) ZrO<sub>2</sub>-TiCN slid for 10 km at 0.3 m/s under a 15 N contact load against WC-6wt.%Co

Top view SEM micrographs of the worn surfaces of ZrO<sub>2</sub>-based composites with wire-EDM surface finish after sliding for 10 km at 10 Hz under a 15 N normal contact force against WC-6wt.%Co cemented carbide pins are presented in Fig. 5.

For the ZrO<sub>2</sub>-TiCN wear surface, abrasive ploughing grooves parallel to the sliding direction of the pin are observed, Fig. 5(a). The microstructure in the wear scar corresponds to the microstructure of the base material, i.e. the grain size of the TiCN phase is not changed due to the sliding of the pin. Furthermore, a small amount of wear debris can be observed, locally covering the wear track surface. The bright particles could be identified as WC phase, originating from the WC-6wt.%Co pin.

SEM analysis on the worn ZrO<sub>2</sub>-TiN composite surface after comparable reciprocating sliding wear testing reveals the formation of wear debris layer on the wear surface, Fig. 5(b). Moreover, microcracks are observed in the debris film, Fig. 5(c). The microcracking in the debris layer leads to localised spalling and delamination. At the moment that the debris film in the wear track spalls off, the base material becomes visible. In the delaminated debris layer areas, a fractured pristine composite surface is observed, Fig. 5(b), indicating that the adhesion strength of the debris layer to the substrate can be quite high. Removal of the material might be due to initiation and subsequent propagation of surface cracks.

The formation of wear debris layer, microcracks in the debris layer and delamination were encountered as well for the ZrO<sub>2</sub>-WC flat /WC-6wt.%Co pin sliding combinations, Fig. 5(d). The microcracks in the debris layer are induced

by tangential stresses due to the reciprocal sliding movement of the pin on the composite surface. As indicated elsewhere, this stress development can cause the tetragonal ZrO<sub>2</sub> phase to transform to monoclinic ZrO<sub>2</sub>. However, the occurrence of this t-m phase transformation of ZrO<sub>2</sub> could not be evidenced in the present investigation.

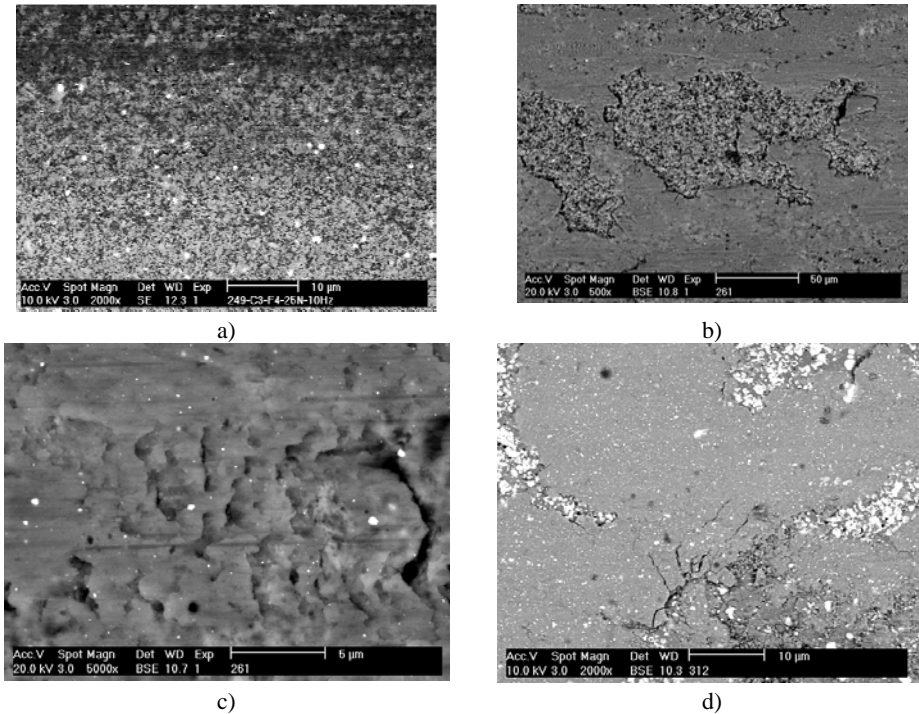


Figure 5. SEM surface views in the center of the wear track of wire-EDM'ed zirconia composites after sliding 10 km at 0.3 m/s under a 25 N contact load: (a) ZrO<sub>2</sub>-TiCN grade B; (b,c) ZrO<sub>2</sub>-TiN grade C; (d) ZrO<sub>2</sub>-WC grade A

#### 4. Conclusions

Amongst the ZrO<sub>2</sub>-based composites, ZrO<sub>2</sub>-WC exhibited the best performance in mechanical properties. The impact of the secondary phase was reflected as well in the dry reciprocating friction and wear behavior against WC-6wt.%Co cemented carbide. The most favorable tribological results were obtained for ZrO<sub>2</sub>-WC compared to ZrO<sub>2</sub>-TiN and ZrO<sub>2</sub>-TiCN composites with equal volumetric secondary phase content. The secondary phase material governs the observed wear mechanisms, which were identified as polishing, micro-abrasion, spalling and delamination, as well as the formation of a wear debris layer, to which ZrO<sub>2</sub>-TiCN was observed to be least prone. A higher contact pressure was found to result in increasing wear and increasing coefficient of friction.

## 5. Acknowledgements

This work was co-financed with a research fellowship of the Flemish Institute for the promotion of Innovation by Science and Technology in industry (IWT) under project number GBOU-IWT-010071-SPARK and the Fund for Scientific Research Flanders (FWO) under project number G.0539.08. The authors gratefully recognize all support and scientific contributions from the investigation partners from Ghent University (UGent) and Catholic University of Leuven (K.U.Leuven). A special appreciation goes to CERATIZIT for supplying the cemented carbide pins.

## References

- R. H. J. Hannink P.M. Kelly, B.C. Muddle, Transformation toughening in zirconia-containing ceramics, *Journal of the American Ceramic Society* 83[3], p. 461-487, (2000)
- M.H. Bocanegra-Bernal and S.D. De La Torre, Phase transitions in zirconium dioxide and related materials for high performance engineering ceramics, *Journal of Materials Science* 37[23], p. 4947-4971, (2002)
- M. Woydt, New directions in tribology: Materials-based concepts for an oil-free engine, p. 459-468, London: Mechanical Engineering Publications Ltd, (1997)
- C.Z. Huang, L. Zhang, L. He, H. L. Liu, J. Sun, B. Fang, Z. Q. Li, X. Ai, A study on the development of a composite ceramic tool ZrO<sub>2</sub>/(W, Ti)C and its cutting performance, *Journal of Materials Processing Technology* 129[1-3], p. 349-353, (2002)
- V. Sergo, V. Lughì, G. Pezzotti, E. Lucchini, S. Meriani, N. Muraki, G. Katagiri, S. Lo Casto, T. Nishida, The effect of wear on the tetragonal-to-monoclinic transformation and the residual stress distribution in zirconia-toughened alumina cutting tools, *Wear* 214[2], p. 264-270, (1998)
- M.H. Myint, Fuh JYH, Wong YS, Lu L, Chen ZD, Choy CM, Evaluation of wear mechanisms of Y-TZP and tungsten carbide punches, *Journal of Materials Processing Technology* 140[1-3 spec.], p. 460-464, (2003)
- W. Burger, H.G. Richter, C. Piconi, R. Vatteroni, A. Cittadini, M. Boccalari, New Y-TZP powders for medical grade zirconia, *Journal of Materials Science: Materials in Medicine* 8[2] pp.113-118, (1997)
- Y.Morita, K. Nakata, K. Ikeuchi, Wear properties of zirconia/alumina combination for joint prostheses, *Wear* 254[1-2], p. 147-153, (2003)
- M. Arin, G. Goller, J. Vleugels, K. Vanmeensel, Production and characterization of ZrO<sub>2</sub> ceramics and composites to be used for hip prosthesis, *Journal of Materials Science* 43[5], p. 1599-1611, (2008)

- J. Vleugels and O. Van der Biest, Development and characterization of Y<sub>2</sub>O<sub>3</sub>-stabilized ZrO<sub>2</sub> (Y-TZP) composites with TiB<sub>2</sub>, TiN, TiC and TiC<sub>0.5</sub>N<sub>0.5</sub>, *Journal of the American Ceramic Society* 82[10], p. 2717-2720, (1999)
- G. Anné, S. Put, K. Vanmeensel, D. Jiang, J. Vleugels, O. Van der Biest, Hard, tough and strong ZrO<sub>2</sub>-WC composites from nanosized powders, *Journal of the European Ceramic Society* 25[1], p. 55-63, (2005)
- D. Jiang, O. Van der Biest, J. Vleugels, ZrO<sub>2</sub>-WC nanocomposites with superior properties, *Journal of the European Ceramic Society* 27[2-3], p. 1247-1251, (2007)
- D. Jiang, S. Salehi, K. Vanmeensel, J. Vleugels, O. Van der Biest, Development and characterization of ZrO<sub>2</sub>-TiC<sub>0.5</sub>N<sub>0.5</sub> nanocomposites, *Proceedings 9th Conference & Exhibition of the European Ceramic Society*, Slovenia, p. 19-23, (2005)
- E. Barbier and F. Thevenot, Titanium carbonitride-zirconia composites: Formation and characterization, *Journal of the European Ceramic Society* 8[5], p. 263-269, (1991)
- S. Salehi, O. Van der Biest, J. Vleugels, Electrically conductive ZrO<sub>2</sub>-TiN composites, *Journal of the European Ceramic Society* 26[15], pp.3173-3179, (2006)
- J. Kozak, K.P. Rajurkar, N. Chandarana, Machining of low electrical conductive materials by wire electrical discharge machining (WEDM), *Journal of Materials Processing Technology* 149[1-3], p. 266-271, (2004)
- B. Lauwers, J.-P. Kruth, W. Liu, W. Eeraerts, B. Schacht, P. Bleys, Investigation of material removal mechanisms in EDM of composite ceramic materials, *Journal of Materials Processing Technology* 146[1-3], p. 347-352, (2004)
- B. Lauwers, W. Liu, J.P. Kruth, J. Vleugels, D. Jiang, O. Van der Biest, Wire EDM machining of Si<sub>3</sub>N<sub>4</sub>-, ZrO<sub>2</sub>- and Al<sub>2</sub>O<sub>3</sub>-based ceramics, *International Journal of Electrical Machining* 10, p. 33-37 (2005)
- B. Lauwers, K. Brans, W. Liu, J. Vleugels, S. Salehi, K. Vanmeensel, Influence of the type and grain size of the electro-conductive phase on the Wire-EDM performance of ZrO<sub>2</sub> ceramic composites, *CIRP Annals - Manufacturing Technology* 57[1], p. 191-194 (2008)
- K. Bonny, P. De Baets, J. Vleugels, A. Salehi, O. Van der Biest, B. Lauwers, W. Liu, Influence of secondary electro-conductive phases on the electrical discharge machinability and frictional behavior of ZrO<sub>2</sub>-based ceramic composites, *Journal of Materials Processing Technology* 208[1-3], p. 423-430, (2008)
- K. Bonny, P. De Baets, J. Vleugels, A. Salehi, B. Lauwers, W. Liu, EDM machinability and frictional behaviour of ZrO<sub>2</sub>-TiCN composites,

- International Journal of Machining and Machinability of Materials* 3[3-4], p. 226-240, (2008)
- K. Bonny, P. De Baets, J. Vleugels, A. Salehi, O. Van der Biest, B. Lauwers, W. Liu, EDM machinability and frictional behavior of ZrO<sub>2</sub>-WC composites, *International Journal of Advanced Manufacturing Technology*, DOI: 10.1007/s00170-008-1551-0
- S. Jahanmir, Friction and wear of ceramics, *Tribology International* 28[6], p. 421-427, (1995) Friction and wear of ceramics
- K. Bonny, P. De Baets, J. Vleugels, A. Salehi, B. Lauwers, W. Liu, Reciprocative sliding wear of ZrO<sub>2</sub>-TiCN composites against WC-Co cemented carbide, *Wear* 265[11-12], p. 1767-1775, (2008)
- K. Bonny, P. De Baets, J. Vleugels, A. Salehi, O. Van der Biest, B. Lauwers, W. Liu, Influence of electrical discharge machining on tribological behavior of ZrO<sub>2</sub>-TiN composites, *Wear* 265[11-12], p. 1884–1892, (2008)
- K. Bonny, P. De Baets, J. Vleugels, A. Salehi, O. Van Der Biest, B. Lauwers, W. Liu, Sliding wear of electro-conductive ZrO<sub>2</sub>-WC composites against WC-Co cemented carbide, *Tribology Letters* 30[3], p. 191-198, (2008)
- K. Bonny, P. De Baets, J. Vleugels, O. Van der Biest, A. Salehi, W. Liu, B. Lauwers, Reciprocating sliding friction and wear behavior of Electrical Discharge Machined Zirconia-based Composites against WC-Co Cemented Carbide, *International Journal of Refractory Metals and Hard Materials* 27, p. 449-457, (2009)
- K. Bonny, P. De Baets, W. Ost, Y. Perez, J. Vleugels, O. Van der Biest, W. Liu, B. Lauwers, Influence of secondary phases on the tribological response of electro-discharge machined Zirconia-based composites against WC-Co cemented carbide, *Wear*, DOI: 10.1016/j.wear.2009.03.046
- E.T. Fischer, P.M. Anderson, S. Jahanmir, Influence of fracture toughness on the wear resistance of yttria-doped zirconium oxide, *Journal of the American Ceramic Society* 72[2]: 254-257 (1989)
- R.C. Garvie, R.H. Hannink, R.T. Pascoe, Ceramic steel?, *Nature* 258, p. 703-704, (1975)
- M. Terheci, J. Nanos, H. Giannakoudaris, S. Abanteriba, Tribological behavior of yttria-stabilised zirconia under dry sliding conditions when tested against itself and grey automotive cast iron, *Wear* 201[1-2], p. 26-37, (1996)

## The current stage of the cutting process simulation

Mircea LOBONȚIU, Alina Bianca (POP) BONȚIU, Gheorghe Ioan POP  
North University of Baia Mare, Faculty of Engineering

### Abstract

The paper's attempt is to highlight the usefulness of simulation processes using the modern cutting processes with finite element simulation. The first part of the paper is a summary of the current methods used in the simulation of cutting processes using finite element analysis and the second part contains an example of cutting simulation.

### Keywords

simulation, FEM, cutting

### 1. The current stage of the cutting process simulation

As it is known, in the cutting processes are always involved two components, namely the workpiece and the tool. In the literature, the cutting process is defined as the process of cutting - deformation, separation and removal of excess material – such as chips.

From a continuum mechanics point of view, suitable constitutive or governing equations that can describe this phenomenon are needed to predict chip flow, cutting forces, cutting temperature, tool wear, etc. However, the solutions of displacement or velocity, stress, strain and temperature fields in metal cutting processes have not easily been obtained since large deformations and temperature rise lead to highly nonlinear and time dependent mechanics of the process.

Modelling and simulation of machining processes is a critical step in the realization of high quality machined parts. To precisely simulate the machining operations, accurate models of cutting tools used in the machining processes are required.

The advancements in the domain of Computer Aided Design (CAD) allow a designer to specify the cutting tool surfaces in terms of bi-parametric surface patches. Using such an approach, one may develop the comprehensive three-dimensional (3D) surface based definitions of the cutting tools.

The surface model of a cutting tool can be converted into a solid model and may further be used for the Finite Element based on engineering analysis, stress analysis and simulation of the cutting process; besides the precise grinding / sharpening of cutting tool surfaces.

A computational approach using the finite element method soon became a mainstream for the analysis of machining after it has been developed. Because, it provides a nearly exact displacement and/or velocity field depending on the assumptions made while building the model for orthogonal metal cutting operation.

In finite element simulation of large deformation solid mechanics processes, two numerical formulations have been extensively used; the Lagrangian formulation and the Eulerian formulation.

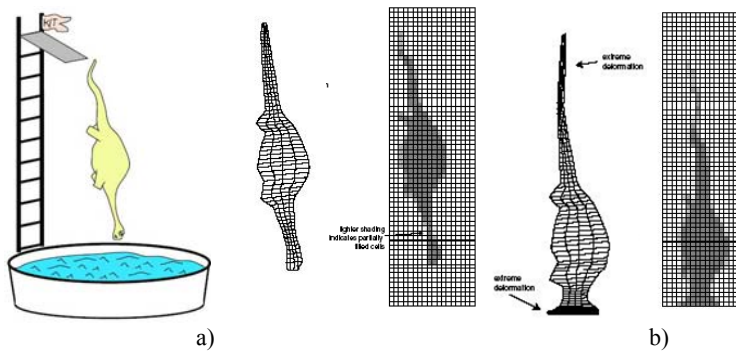


Figure 1. Numerical models (a) Lagrangian (b) Eulerian

In the former approach, the finite element mesh is attached to the material and follows its deformation, whereas in the latter, the mesh is fixed in space while the material flows through the mesh. The Lagrangian approach is largely used in solid mechanics applications and is particularly suitable for cases in which unconstrained flow occurs over free boundaries, because the mesh closely represents material boundaries.

The Lagrangian formulation is easy to implement, efficient and fast converging, especially when the strains are relatively small. However, difficulties arise when this approach is used for problems involving large deformation, nonlinear boundary conditions that change in the course of deformation, and when element distortion and mesh entanglement are critical factors in the analysis. In addition, load fluctuation often occurs if boundary conditions change in the course of deformation.

Eulerian approaches, tracking volumes rather than material particles, did not have the burden of remeshing distorted meshes (Strenkowski and Athavale, 1997). However, steady state free-surface tracking algorithms were necessary and relied on assumptions such as uniform chip thickness, not allowing the modelling of milling processes or segmented chip formation.

As M.S. Gadala is saying in the paper „On the mesh motion for ALE modelling of metal forming processes”, it may be concluded that neither Lagrangian nor Eulerian approaches alone are well-suited for modelling

deformation processes involving both large deformation and unconstrained flow of material.

In fact, the strong point of each method is the weakness of the other, and the two methods complement each other in this respect. The application of Arbitrary Lagrangian–Eulerian (ALE) formulation in metal-forming operations is born out of the need for an approach that can combine the advantages of both methods while avoiding their drawbacks. In an ALE analysis, the FE mesh is neither attached to the material nor fixed in space, but each degree of freedom of the system may be assigned an arbitrary motion independent of the material deformation.

Therefore, ALE is a general formulation that may reduce to Eulerian or Lagrangian formulations as special cases. This provides a powerful tool for modelling processes where large and highly localized deformation of material occurs, and significant unconstrained flows of material on free boundaries are evident.

## 2. The cutting process simulation using the finite element analysis

To achieve this simulation we have used DEFORM 2D application, which, next with other FEA applications, allows the use of the Lagrangian method to simulate the cutting process.

We decide to use this method because in this simulation we follow the strain and temperature distribution at the tool tip.

In this paper we have used the turning process for simulation. In the literature, in some points of view, the turning process is frequently studied, but in the present work we chose to study a particular case, in which all the following parameters are the same in all situations:

- Tool material – Tungsten Carbide (WC);
- Workpiece material - 15CrNi6;
- Cutting speed 100 [m/min];
- Cutting depth 0,5 [mm];
- Feed 0,1 [mm/rev];
- Ambient temperature 20 [°C];
- Shear friction factor 0,6.

As it is known, the tool tip radius influence the surface condition, in terms of the cutting depth, the workpiece rotation speed and the tool feed. Another very important influence on the surface state has the tool geometry modification, due to temperature and forces occurred during cutting.

In this tool tip radius influence analysis on the cutting parameters, we considered three different radii, while the other geometric parameters of the tool remained unchanged (Figure 2).

Figure 3 shows the results obtained from cutting simulation, wherefrom result that the increasing of nose radius lead to an increase of tensions in the cutting area up to a value of approximately 860 MPa at the same processing conditions.

However, the values of cutting forces occurred in cutting were higher at larger radii (Figure 4).

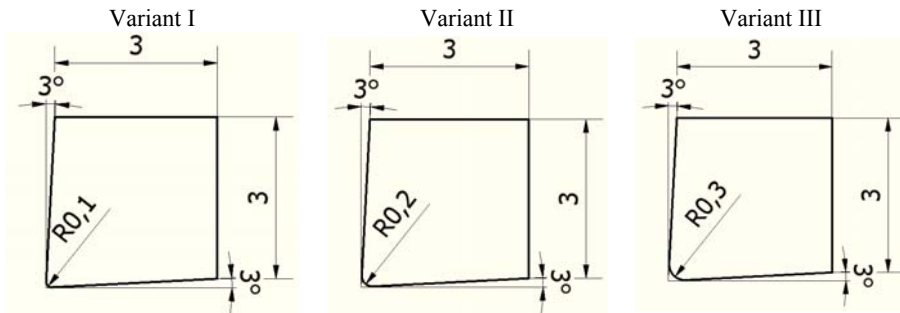


Figure 2. Tool geometry. Variable radius

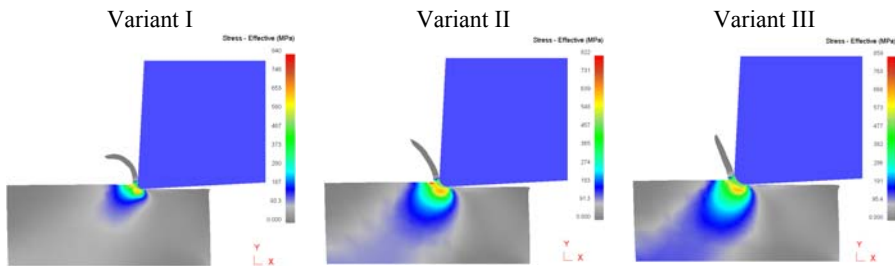


Figure 3. The stress distribution on the cutting area

The tip radius increase also influences the chips formation in terms of thickness, which leads to some different chips form.

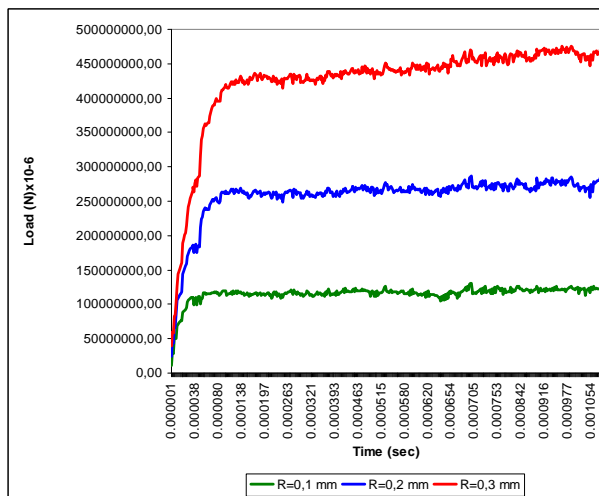


Figure 4. The tool tip radius influence on the cutting forces by X direction

The stress distribution in the workpiece is directly influenced by the geometric shape of the tool tip.

Thereby increasing the tool tip radius, the stress distribution is a radial one, on a larger area of workpiece, reason for which the chips deformation is smaller.

For a small radius of the tool tip we get a sudden cutting forces increase at the cutting beginning, than the forces maintaining a value of around 122 N. Increasing the radius, the forces values are increasing too, and their maintaining is more difficult.

In figure 5 are presented the results obtained from temperature distribution simulation in the cutting area after the tip radius is modified. It can be observed a temperature increase to a value of about 372°C to 465°C (Figure 5).

The temperature distribution is directly influenced by the tool tip geometry, and this influences the generated chips temperature.

For a smaller radius we obtain a temperature distribution on the smaller chip surface, which leads to a more pronounced deformation of the chip.

For a greater radius we obtain a temperature distribution on the bigger chip surface. Thus, besides the tool geometric shape which tends to compress the material, the temperature favours this too.

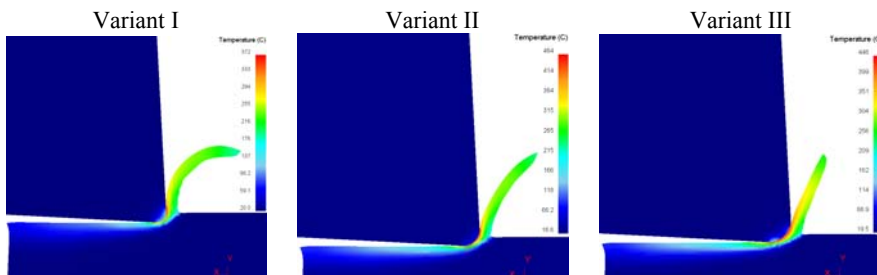


Figure 5. Temperature distribution in the cutting area

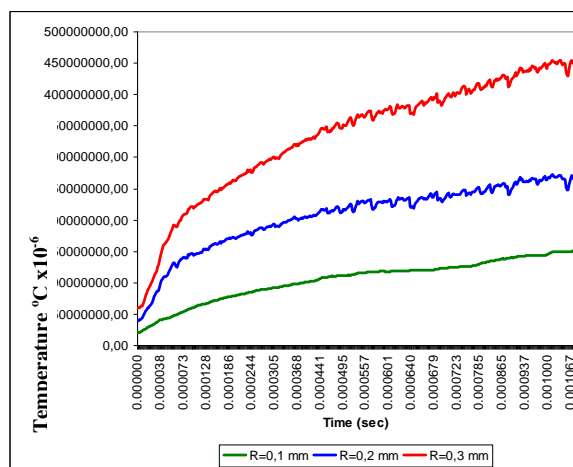


Figure 6. Tool tip radius influence on the temperature in the cutting area

Figure 6 shows the range of temperature values occurring during the cutting process for the three studied variants.

It can be seen that for radii of 0.2 and 0.3 mm, the temperature oscillations are similar to the same time intervals, only that range of temperature is higher. Well for such a growth range of 0.1 mm for  $R = 0.2$  mm we have an increased temperature of 14.8% and, the increase of radius with 0.2 mm for  $R = 0.3$  mm, we have an increase temperature of 18,4%.

### 3. Conclusions

Following the variation analysis of the tool tip radius, in the paper are presented findings related to the workpiece and tool temperature, the chips geometry and the stress distribution.

The chip deformation style is also influenced by the tool tip changes, which presents the cutting processes analysis perspective using DEFORM 2D software.

This study presents the analysis perspective of the influence of tool geometric parameters on the surface quality and for the entire cutting process.

### References

- Benson, D., J., An efficient, accurate, simple ALE method for nonlinear finite element programs, *Comput. Methods Appl. Mech. Eng.* 72 (1989) 305–350.
- Cheng, J., Kikuchi, N., A mesh re-zoning technique for finite element simulations of metal forming process, *Int. J. Numer. Methods Eng.* 23 (1986) 219–288.
- Gadala, M., S., Movahhedy, M., R., Wang, J., On the mesh motion for ALE modeling of metal forming processes, *Finite Elem. Anal. Des.* 38 (2002) 435–459.
- Gadala, M., S., Wang, J., Simulation of metal forming processes with finite element method, *Int. J. Numer. Meth. Eng.* 44 (1999) 1397–1428.
- Haber, R., B., A mixed Eulerian–Lagrangian displacement model for large deformation analysis in solid mechanics, *Comput. Methods Appl. Mech. Eng.* 43 (1984) 277–292.
- Marusich, T., D. and Ortiz, M., Modeling and Simulation of High-Speed Machining, *Int. J. Num. Meth. Eng* 38 (1995), 3675-94.
- Obikawa, T., Sasahara, H., Shirakashi, T. and USUI, E., Application of Computational Machining Method to Discontinuous Chip Formation, *Journal of Manufacturing Science and Engineering*, 119 (1997), 667-674.
- Obikawa, T. and Usui, E., Computational Machining of Titanium Alloy-Finite Element Modeling and a Few Results, *Journal of Manufacturing Science and Engineering*, 118 (1996).

---

Pop, GH., I, Bonțiu (Pop) Alina Bianca, *CAD and FEA optimization of ADIPUR Equipment*, Erin, Ostrava 2009.

Wang, J., Gadala, M., S., Formulation and survey of ALE method in nonlinear solid mechanics, *Finite Element, Anal. Des.* 24 (1997) 253–269.

Zienkiewicz, Z., C., Flow formulation for numerical solution of forming processes, in: Pitmann et al. (Eds.), *Numerical Analysis of Forming Processes*, Wiley, New York, 1984.

\*\*\*Deform 2D, Help.

# Hot-dip galvanizing: further challenges

László SZABADI, Lajos PÉK

Szent Istvan University, Faculty of Mechanical Engineering

## Abstract

Among the various surface protection processes the coating has an important role with metals and within this the hot-dip galvanizing, which classic application field is the atmospheric load. This technology permanently developed known from the 18<sup>th</sup> century is widely used in Europe for protecting metal construction surfaces. The hot-dip galvanizing technology also spreads in Hungary but it doesn't reach the European application proportion. Nowadays new expectation arises with new applications: wear resistance in sliding applications. We launched an experimental research to study the wear resistance of different layers. This article gives a brief review about the historical background and the base stage of our measurements.

## Keywords

hot-dip galvanizing, corrosion, steel surfaces, layers

## 1. Introduction

The wear – and – tear of metal constructions is caused by the fatigue and the friction, the wear caused by friction and first of all the corrosion. The metal constructions without protected surface get ruined sooner or later as a result of surrounding agents first of all of the air oxygen and moisture content further more because of impurities (gases, dust, soot, etc).

If an iron or steel surface is left without protection, then first reddish-brown spots appear later larger and larger similar consistent surfaces.

Porous, lamellar structure formation covers the whole surface slowly. This process continues till the whole structure doesn't change to such formation. This formation is the rust, the process is the corrosion.

The iron without protection loses about 0,1 mm from its thickness yearly because of atmospheric effects.

The corroding processes take place by chemical electrochemical ways and in many cases mechanical effects take also part in these. The corrosion – the returning of the metals to the lowest energy level – is perhaps the sole true feature of the majority of iron – and iron based alloys. The inclination to corrosion of the metals is so great that without protecting their surfaces the structures are generally not capable perform their long – lasting function.

Reducing the losses for protecting the metal constructions various processes have been developed which are called comprehensively surface – protection. The corrosion follows is any case, it is not yet all the same how fast it takes place.

## 2. Layers for surface protections

The task of corrosion protection – that can be temporary or permanent depending on the required time of protection – influencing, reducing by active or passive way the corrosion speed. By active way with proper forming the construction from the corrosion protection point of view, as for with surface protecting process by developing surface coating resisting against load, securing passive protection. Among the various surface protection processes the coating has an important role with metals and within this the hot-dip galvanizing, which classic application field is the atmospheric load. This technology permanently developed known from the 18<sup>th</sup> century (fig.1.) is widely used in Europe for protecting metal construction surfaces.

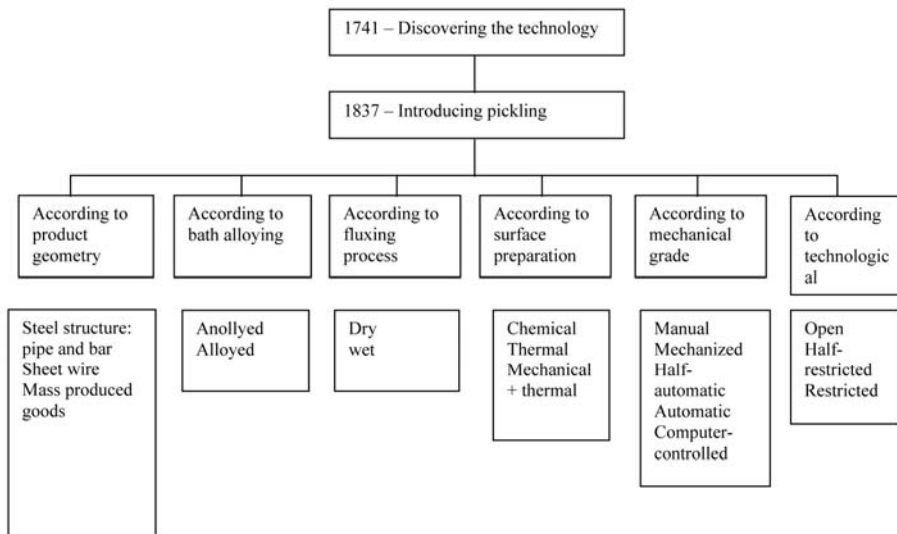


Figure 1. Developments directions of hot-dip galvanizing

The hot-dip galvanizing technology also spreads in Hungary but it doesn't reach the European application proportion. The cause of this can be the higher cost comparing with the traditional surface protection processes but what is compensated with longer scale service-life and that fact in opposition to painting giving porous surface, this technology doesn't require permanent service and restoring expenditure. The peculiarity of the galvanizing technology is that

forming the protecting layer against corrosion by mainly so – called „dry” process is carried out. On the steel surface to be coated surface preparation that is after grease extraction securing specified cleanliness stage, after prickling, flux treatment and drying zinc coating is formed containing multilayer by dipping into 445-460<sup>0</sup>C zinc-bath, linking with diffusion alloy layers and in optimum case containing pure zinc top layer.

The traditional dipping galvanizing basically forms the layer securing resistance against corrosion as a result of thermodiffusion process. During the period in the melt two – way diffusion process starts on the boundary surface of the melt and of the metal to be coated. The Fe-atoms of the steel structure diffuse to the direction of the melt, the Zn-atoms of melt diffuse to the direction of the structure surface. During the period of dipping into the zinc – melt the iron and the zinc react with each other and iron-zinc alloy layers are forming. After lifting out from the melt pure zinc layer is deposited onto the alloy, which corresponds to the bath of zinc – melt concerning its composition. After the chemical transformation there is no need generally for further protection of the steel because of the forming coating on the surface.

The strongly adhesive lowest „gamma” layer touching the surface to be coated at normal structure zinc-layer is 1-2 μm thick, surmount hard brittle „delta” layer thickness is 30-40 μm. To this layer connects the similarly hard, brittle 20-30 μm thick „zeta” layer. Over this layer is that one which sticks to the alloy layers only at taking out the part. This 8-12 μm thick tough „eta” layer composition is equal with the zinc-melt. (fig.2.)

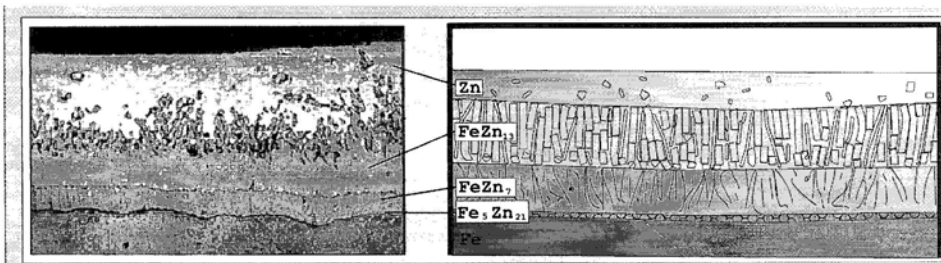


Figure 2. Layer structure

Basic zinc carbonate layers form on the surface galvanized because of oxidation processes. These top layers are those which really take over the corrosion protection. This protective layer is the so – called „zinc-patina” which forms on the surface after hot-dip galvanizing. After the resistant air tint has formed the zinc corrosion speed reduces. The mass of the protective air tint decreases very slowly in consequence of the air adulterants and moisture content respectively by mechanical effects and is re-produced from the zinc-base according to the thermodynamic equilibrium conditions, while by such measure also decreases the zinc coating. This process is very slow apart from a few

exceptions because of the excellent, long – lasting corrosion resistance of zinc-layers can be attributed to this process. The layer loss – that is the general decrease of zinc coating – changes depending on the corrosion load. It is 0,1µm/year at low corrosion load (for example at inner spaces) 4,0-8,0 µm/year at outer industrial atmosphere. The zinc corrosion – rates are lower at 2 µm/year in most European countries. Decade old durable corrosion protection can be estimated because zinc-coating having more than 80 µm thickness. In this case if longer protective length of time is desired or the painting has aesthetic part, then the zinc – coating can be painted, that is can be combined with other coatings. This process (hot-dip galvanizing + painting) is called Duplex process. So the zinc – coating is protected against weather conditions. The service – life of the coat of paint is longer over the zinc – layer because in case of possible scratches or smaller damage of the coat of paint the zinc-layer prevents with great capability of resistance that these damages can form the starting places of corrosion. The paint protects the zinc-coating, the zinc-coating however prevents the under-rusting of the coat of paint.

The length of time zinc-coating protective effects depends on the type and intensity of the coating thickness, depends on the corroding factors helping the corrosion (for example air pollution) and on the additional loads (for example erosion effects because of dust and sand in the air.)

## References

- Antal Árpád: Tüzhorgonyzás Kiadvány Magyar Tüzhorgonyzók Szövetsége. Dunaújváros
- Szabó Andrea – Dénes Éva: A felület érdességének és a fürdő alumínium tartalmának hatása a kialakult horganybevonat tulajdonságaira. *Anyagok világa*. II. évfolyam 2. szám. 2001.
- Antal Árpád: A horganybevonatok atmoszférikus ellenállása kiváló. *Tüzhorgonyzás szakfolyóirat*. V. évfolyam 1. szám. 2006.
- Antal Árpád: A tüzhorgonyzás technológiája II. *Tüzhorgonyzás Szakfolyóirat*. II. évfolyam. 1. szám. 2003.
- Gecsei G. – Kaczander K.: *Acéltermékek tüzhorgonyzása*. Műszaki Könyvkiadó Budapest. 1986.
- Antal Árpád: A tüzhorgonyzási technológia rövid története. *Tüzhorgonyzás Szakfolyóirat*. I. évfolyam. 1. szám. 2002.
- Ipari járdarács. Gyártmánykatalógus. NAGÉV. 2007.

# **Cutting engineering ceramics with normal edge tool (lathe machining of zirconium dioxide)**

Gellért FLEDRICH, Károly PETRÓCZKI

Szent Istvan University, Faculty of Mechanical Engineering

## **Abstract**

During improvement of the technology the demand of special serviceable high temperature, high-strength materials e.g. zirconium dioxide is increasing now. The mechanical working after sinter is confined to grinding and honing. Our research work deals with a better possibility of material removal. A special measuring system was elaborated for this purpose. The article summarizes briefly the main questions of the topic and next the main parts of the measuring system is presented.

## **Keywords**

engineering ceramics, phase transition, strain gage, measuring system

## **1. Introduction**

Last few decades material research in engineering ceramics gave the possibility new unthinkable before mechanical applications. Instead of the foregoing rigid ceramics the new advanced and better resistant against mechanical load so called tough ceramics has appeared. These are so called engineering ceramics. For example nowadays several parts of the car are made from ceramics from engine sleeves to the break parts. The advantageous behaviour comes from more uniform micro structure ceramics as before. As the structure of the material is more homogeneous the probability of the evolution of local stress centre is decreasing.

## **2. Engineering Ceramics (zirconium dioxide)**

Investigations show, that the phase transitions in ceramics coexists with volume change and can be generated by mechanical load. For example in case of zirconium dioxide during mechanical applications in phase transition from tetragonal into monoclinal the generated volume change is applied.

The partially stabilized PSZ (Partially Stabilized Zirconia) and the tetragonal polycrystalline zirconium oxide TZP (Tetragonal Zirconia Polycrystals) are important in aspect of technical application. First of all the paper deals with the ZrO<sub>2</sub> machining, which is partially stabilized by MgO.

The influence of the phase transitions to the micro cracks were investigated by many researchers. The results show, that the optimal stabilization occurs at the 8-10 % MgO content. In the sintered material in case of tetragonal  $ZrO_2$  grains tetragonal – monoclinal change can be generated. At room temperature they are in metastable state.

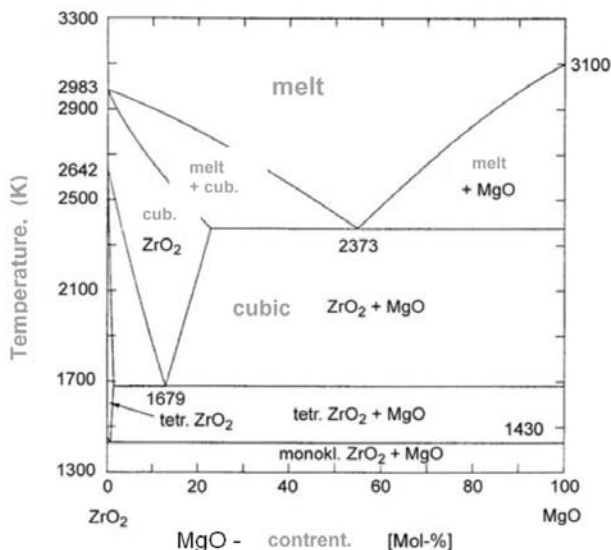


Figure 1. The quasi binary constitutional diagram of  $ZrO_2 - MgO$

Local tension stress occurs in case of mechanical load at a micro crack and at its corner in the material and at a critical value the phase transition can intervene: higher volume monocline grain is generated and so it blocks the way of crack (Fig. 2.). The tetragonal – monoclinal structural change is a diffusion and content alteration free change similar to the well known martensitic phase transition in steel. This behaviour of the zirconium dioxide ceramics gives the long term resistance against the mechanical load.

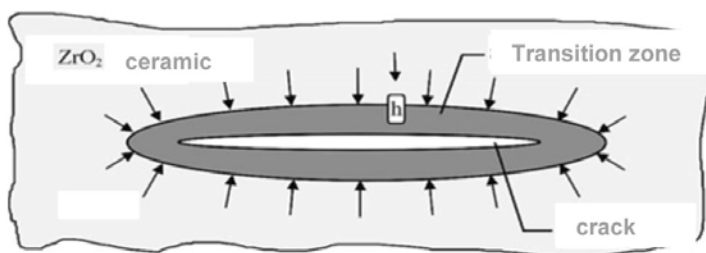


Figure 2. The prevention of a micro crack propagation with phase transition

The mechanical characteristics of the engineering ceramics can be improved with other technology beside the methods of reducing the micro crack as was mentioned before.

During sintering a contraction process occurs and this has to be considered. So the technological accuracy  $\pm 0,5-1,5$  % in case of component manufacturing. Many times this accuracy isn't acceptable (i.e. bearings, etc...) and additional machining is necessary. To this time the grinding and honing was the only possibility to machining. Nowadays regarding to the new possibilities the research works are toward to the new, productive and cheaper technology and one of the new possibility is the lathing. Next the measuring system for this purpose is presented.

### 3. Two-component Measuring System

Special self designed and manufactured axial and tangential component cutting force measuring tool holder with strain gages was applied during measurements. In this configuration the feeding direction ( $F_f$ ) and the cutting direction ( $F_c$ ) force can be measured by the measuring tool holder (Fig. 3.).

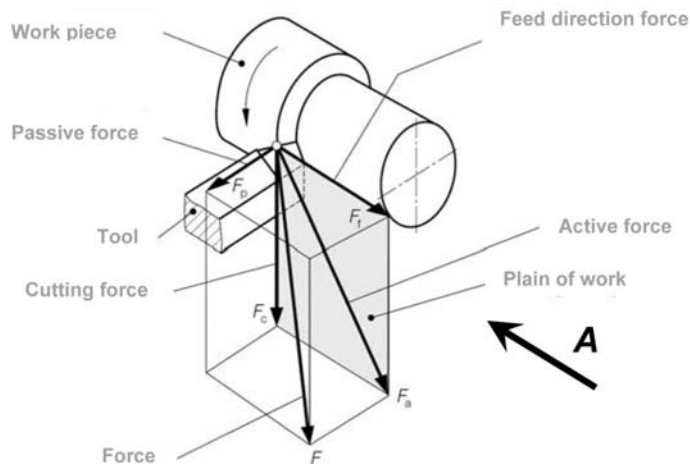


Figure 3. Components of cutting force (ISO 3002/4, DIN 6584)

The operation of the two component force transducer is the following (Fig. 4.). The  $B_{c11}$  and  $B_{c12}$  strain gage half bridge output voltage is proportional with the bending moment in plane  $S_1$  caused by the force  $F_c$ . Similarly  $B_{c21}$  and  $B_{c22}$  strain gage half bridge output voltage is proportional with the bending moment in plane  $S_2$  caused by the force  $F_c$ , too. If two half bridges are completed each other to full bridge so, that the output voltages can subtract, than the full bridge output voltage depends on the subtraction of two bending moment i.e. ( $F_c * k$ ).

As the  $k$  factor is constant, that's why the output voltage is proportional with the  $F_c$  and it doesn't depend on the loading point. Similarly the measurement of the force  $F_f$  with strain gages  $B_{f11}$ ,  $B_{f12}$ ,  $B_{f21}$ ,  $B_{f22}$  are the same.

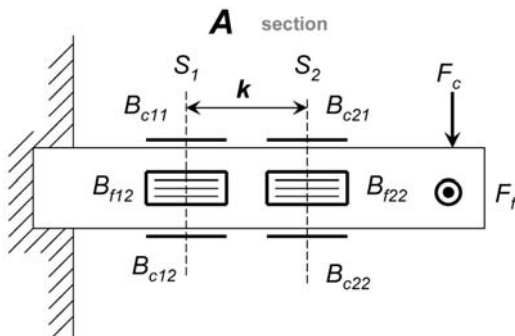


Figure 4. The scheme of the measuring tool holder

The type of the KYOWA made foil strain gage is KFG-1-120-C1-11. The main parameters of the strain gages are the following: measuring length of the strain gage: 1 mm, the carrier dimension: 4,8 mm x 2,4 mm, resistance: 120  $\Omega$ , the gage factor: 2,1. The strain gages are self-compensated to steel and the full bridge configuration is temperature compensated alone, so the temperature coefficient of the transducer is very good.

The calibration of the force transducer can be realised with standard weight or with a calibrated force transducer. During the calibration process the sensitivity of the transducer vs. acting force position must be checked.

The measurements were done by Hottinger Baldwin Messtechnik GmbH (HBM) made „Spider8” PC measurement electronics (Fig. 5). The measuring system is capable to carry out the measuring job very much. The execution of measurement and data processing was done by „HBM CATMAN Professional” software.

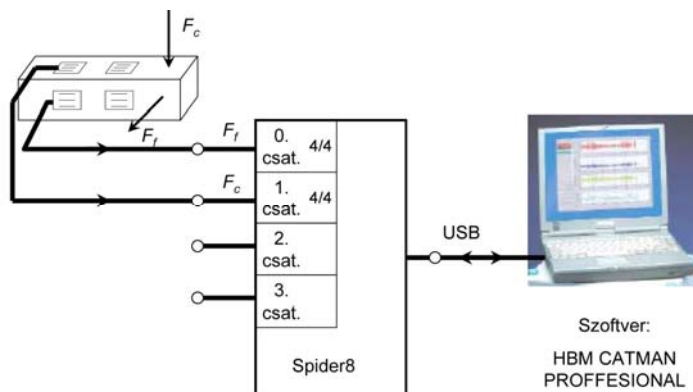


Figure 5. Block diagram of the measuring system

#### 4. Conclusions

The great demand has been increased very much for special properties and even conformable of environmental regulations engineering ceramics. After sintering the dimensional accuracy of the manufactured parts are  $\pm 0.5-1.5$  %. So many times very hard ( $\sim 1200-4000$  Vickers) surfaces must be machined. Semi manufactured articles can be manufactured only with technology of higher degree of material removal. Remarkable problem is the micro cracks formation during hard state machining. The proper machining and the proper material selection are the possibilities to reduce it. Two component force measuring method likely gives the possibility to discover the correlation between the cutting force and micro cracks.

#### References

- H. Salmang, H. Scholze (2007): *Keramik*, Springer Verlag, Berlin
- Szépölgyi J. (1994): Korszerű műszaki kerámiák, *Magyar Tudomány*, 4. sz. 7-13 old.

# Online monitoring of polymer matrix composites

Quintelier JAN

University College Ghent, Department of Mechanics

Ost WOUTER, Patrick DE BAETS

University Gent, Department of Mechanical Construction and Production

## Abstract

Polymer matrix composites are widely used as bearing materials for heavy load applications. Still fundamental knowledge about the wear mechanisms of these materials and the evolution in time of these mechanisms is lacking. Currently these mechanisms are only analyzed by post mortem analysis. The Laboratory Soete, based on the well-known pin-on-disc test rig, has developed a new test-setup. Instead of the standard composite specimen and steel disc, a rotating composite disc and steel pin is used to be able to have a visible composite wear track. Standard wear and friction measurements will be further combined with vibration measurements. The vibration measurements give valuable information about the pin-disc contact. The combination of all these measurements should yield valuable information on the active wear mechanisms, the occurrence of fiber and matrix fracture, fiber pull out, generated frictional heat, formation mechanisms of wear particles, and the interaction between all these effects.

## Keywords

Large Wear, Tribology, Composites, Pin-on-disc

## 1. Introduction

The study of wear of polymers in general and polymer based composites in particular is finding increasing citations in literature due to the availability of wider choice of materials, ease of manufacturing, good strength, and light weight. An area in which their use has been found to be very effective is the situations involving sliding contact wear. The polymer-based materials are preferred in recent years over metal-based counterparts in view of their low coefficient of friction and ability to sustain high loads. This has given an impetus to industrial production of the materials, as for instance in the production of composite bearing components used in automobile industries such as gears, cams, wheels, etc. The introduction of fibers as reinforcing agents in polyester based polymer materials widens the scope for structural application in view of their processing useful properties. However, the deployment of these materials as components for use in actual service requires good understanding of the processing related structure and its influence on wear.

Techniques for wear analysis are acoustic emission, particle analysis, SEM, ... Most of these techniques are post mortem analyzing techniques. Due to differences between the static and kinetic coefficient of friction, restarting a tribological test means changing the original parameters of the material, resulting in possible differences in wear behavior of the two materials.

## 2. Experimental

The test rig is a classical pin-on-disc with composite disc and steel pin. A camera was placed on the test rig to take pictures online. The pin is constructed to contain most of the additional sensors (acoustic emission, 3D accelerometer, strain gauges and thermo couples). The pin, made of steel, with a length of 35mm is hollow at the top, because measuring bending of the pin with strain gauges requires a sufficient strain in the steel pin. Two flat parallel faces close to the contacting surface are places for the accelerometer and the acoustic emission sensor. Thermo couples can be placed all over the pin geometry. A ball, from a ball deep groove ball bearing ( $\varnothing 8$  mm) forms the mating surface, or the top of the pin.

Characteristics of this test rig are: relative velocities from 10 till 100 mm/s, a possible normal load up to 1000 N, an online camera and the possibility to place additional sensors on the pin for further research. For the measurement of the wear depth of the wear track, a contactless proximitor is used, providing an estimate of the evolution of the wear depth with time.

## 3. Test material

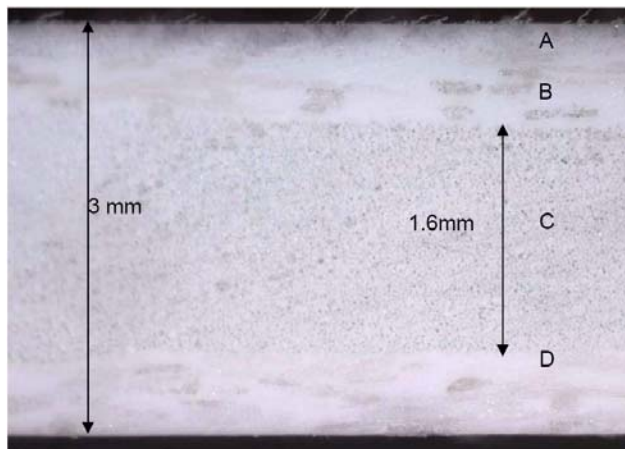


Figure 1. Transverse section of the composite material, with A: a surface mat, B and D the non-woven and C the zone with unidirectional fibers

The material used is a low profile, flame retardant polyester grade, reinforced with glass fibers. The plate was pultruded, indicating a constant fiber orientation

in the zone C (see Fig. 2). The pultruded profile exists of 4 layers: a surfacing mat (A) (~0.1-0.2mm), a non-woven (B) (~ 0.55 mm), continuous glass fibers (C) (~ 1.6 mm) and a non-woven (D). This means that the orientation of the fibers will play an important extra factor in the wear mechanisms due to the orientation. The discs were cut out by water jet process from the pultruded plate.

#### 4. Results

Results of online measurement techniques are given in Figs. 2 and 3. Fig. 2 deals with the FFT analysis of the vibration measurements. These were measured in the frictional direction. Due to the FFT-spectra, related to the number of the current round a variation in time can be noticed. The first graph is the FFT at the beginning of the test. Here a point contact between pin and disc existed because there is still no wear. Even after 100 rounds the wear is of this kind that only small wear particles are removed and the total contact area can still be defined as a point contact.

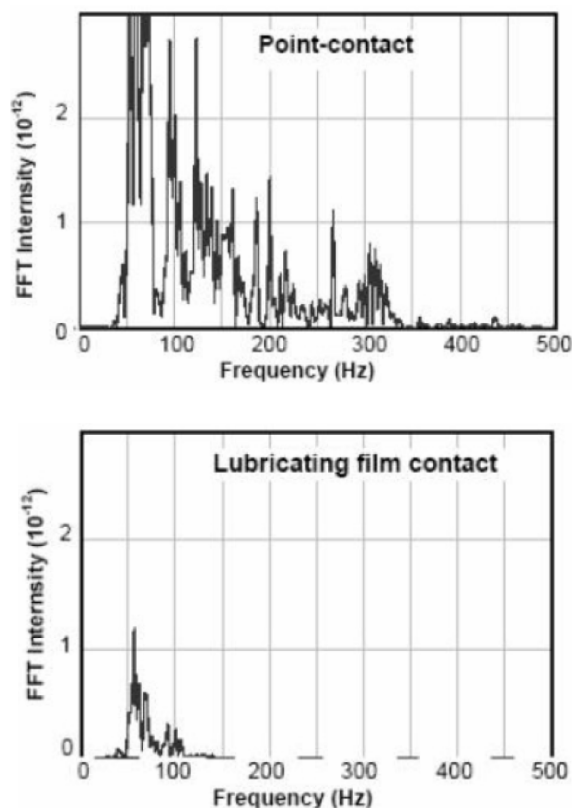


Figure 2. Vibrations on a pin-on-disc tribotester, depending on the state of the wear track

The second part of the disc was after 5,600 rounds. This intensity of the FFT is much lower due to several coinciding events. First of all the contact area between pin and disc has grown. There is now some elliptical contact as discussed in. Also the formation of a thin polymer film could be noticed into the wear track. This thin polymer film then plays the role of a solid lubricant. The pin top then contacts pure polymer film which exists from different particles agglomerating due to the applied pressure of the pin. The sliding of the pin into the wear track is then governed by sliding on a more fluid film than the original surface. Later on, after the unidirectional fibers are reached, the polymer film gets removed. The glass fibers in the bulk result in a more rigid backing than the polymer. The FFT intensity then gives higher values again, only now even a difference between the different fiber orientations can be noticed. Parallel fiber orientation results in a smoother frictional behavior and thus lower amplitude of sliding. The perpendicular orientation, where the pin needs to jump over the fibers (hardly any polymer between the fibers) higher amplitudes is seen.

Fig. 3 gives some basic results of the AE testing. The AE sensor is placed on the pin, and the transfer of signals between the composite surface and the sensor has to travel through a lot of material contacts (composite – steel ball – steel pin – glue – sensor), so it was expected that the signals detected on the sensor had a low energy and got mostly lost during all materials crossed. The results on the contrary were very reliable, and could be compared to the material structure.

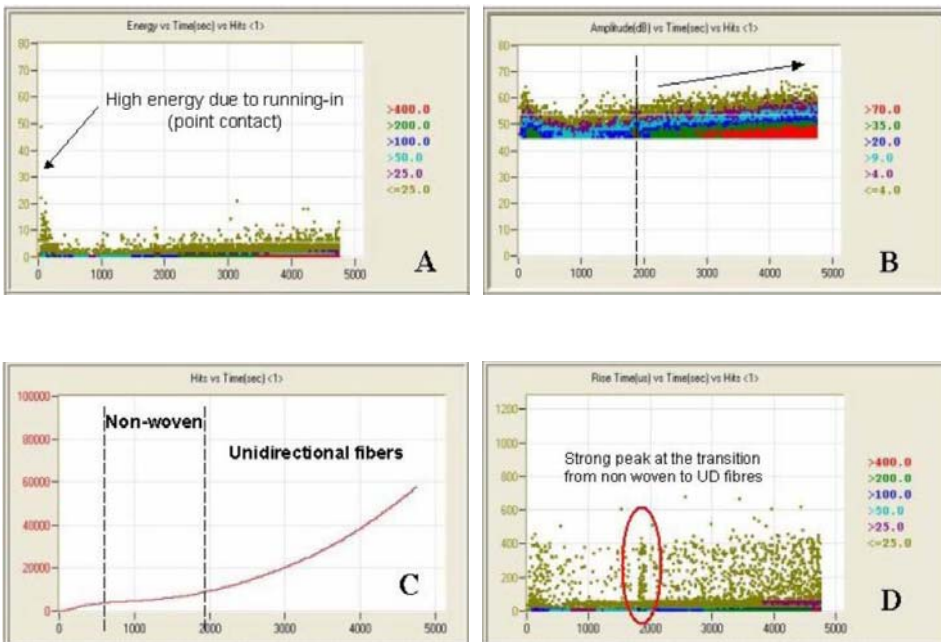


Figure 3. Overview of a test at 20 N, 128 mm/s, A: energy vs time, B: amplitude vs time, C: hits vs time, D: rise time vs time

Fig. 3 A gives the energy of the measured signals in function of the time. As one can see, high energy signals in the beginning, which are due to the running-in, the start of the wearing were the pin is forced to penetrate into the composite surface. Near the end of the testing the energy also rises, due to more fiber breaking when the unidirectional fibers are reached. Fig. 3 C gives a perfect relation between the 'hits' counted on the sensor and the material structure. The top layer, without glass fibers does not give many hits because no glass fibers are broken and the only hits come from possible matrix cracking and wear. The polyester fibers are plastically deformed before they break releasing low energy signals. In the non-woven section, the number of hits rises. Now glass fiber fragments are available in the contact surface and can break. Still the number of hits is not increasing spectacular. This is due to the fact that the glass fibers are short fibers and these can be pulled out. Pull out of fibers has a different energy contact than fiber breaking. After reaching the unidirectional fibers in the bulk the increase in hits is exponential. The increase is due to the large number of fiber breaking. When the fibers are laying perpendicular to the direction of movement the pin breaks those fibers to pass, which results in more hits but also in a rise of the coefficient of friction. In the parallel case with lower coefficient of friction, the fibers can be pressed aside until all matrix material is removed. This results in a glass-steel contact, which then determines the coefficient of friction. The breaking of the fibers is now more related to the shear forces, but the final state of the broken fiber looks the same as for the perpendicular case, so the same signals are noticed, only some times later if one is concerned about one specific layer.

In Fig. 3 D the rise time is given in function of the time. The rise time is the time needed for a signal to reach its maximum amplitude. One can notice that there is at the border of the non-woven and the unidirectional fibers a larger amount of signals with different rise times. This is due to a possible polymer layer in between.

In Fig. 3 B, where the maximum amplitude of the signals is given in function of time and in function of the number of hits, a rise in amplitude with test duration can be noticed. This is due to more fiber breaking when the pin is in contact with the unidirectional fibers. Also the number of hits with low amplitude is rising, which is due to the large increase in measured hits, and more and more fiber breaking.

## 5. Conclusions

On line monitoring of the wear of polymer matrix composites gives a lot of extra information about the wear track. Possible conclusions about the current state of the wear track, the possible mechanisms and the influence of the fibers can be visualized. Although these results are very promising, post mortem analysis still gives extra information, and is still needed to explain the measured results.

Vibration analysis gives information about the current state of the contact between pin and disc, it reveals the formation of a polymer film, and indicates the wear of the pin resulting is a higher contact area.

Acoustic emission gives structure related results in a basic set up different behaviour in time can be explained by the possible wear mechanisms and their signal content.

## References

- S.K. Biswas and K. Vijayan, *Wear*, Vol. 158 (1992), pp. 193-211
- S. Huguet, N. Godin, R. Gaertner, L. Salmon and D. Villard, *Composites Science and Technology*, Vol. 62 (2002), 1433-1444
- M.Q. Zhang, Z.P. Lu, K. Friedrich, *Trib. Int.* Vol. 30, No.2 (1997) pp. 87-102
- J. Quintelier, P. De Baets, J. Degrieck, A. Ledda, W. Phillips, H. Sol and D. Van Hemelrijck: *Mater. Sci. Forum*, Vol. 475-479 (2005), pp 1083-1086
- Quintelier, P. Samyn, L. De Doncker, P. De Baets, D. Van Hemelrijck, H.Sol, *Journal of Adhesion*, Vol. 82(11) (2006), pp. 1033-1060

# Design of electro-rheological flow control valve

László FÖLDI, László JÁNOSI

Szent Istvan University, Faculty of Mechanical Engineering

## Abstract

Use of intelligent materials has been a more widespread technology in the last ten years in the area of research and development of mechatronic equipments. It's main reason is that some problems of the utilization needed such a solution, which couldn't be solved only with new materials produced by material texture modification. In this case, materials must be applied, that changes dynamically its own properties according to the varied ambient parameters. One group of these materials is electro-rheologic (ER) liquids that change their shear strength according to the electric field. The main aim of this work is the modification of basic properties of this kind of liquids and specification of its utilization possibilities in mechatronic systems such as hydraulic control equipments. Mathematical model as well as its numerical solution of a flow control valve (ER valve) as an appropriate element of Hydraulic systems has been prepared during this work. Function tests of this unit have been carried out by computer aided simulation of the above mentioned mathematical model.

## Keywords

electro-rheological, valve

## 1. Introduction

The ER phenomenon as a material model is described by the Bingham model related to ER liquids, which is based on the mathematical model describing the non-newton liquids. The Bingham model is a complex viscoplastic rheological model. As a material model it can be divided into an ideally ductile an ideally viscous member. (Fig. 1 )

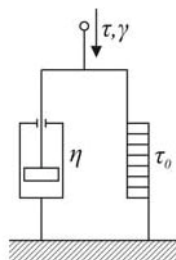


Figure 1. The Bingham model

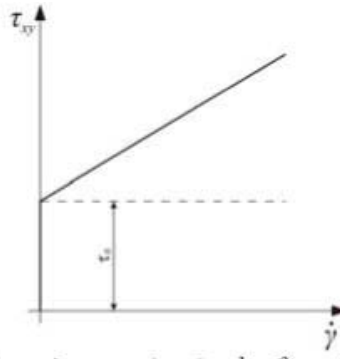


Figure 2. The shearing tension in the function of shearing gradient

### Research Objectives

The aim of testing of the flow properties of the ER liquids is to establish a model, which can be generally applied of testing the behaviours of ER liquids made of different materials considering the phisycal data of the applied materials. By computer simulation the parameters of this mathematical model can be determined, which can be generated by minimum search. As the first step of the model identification the approximate search of the minimum of the established target fuction is accomplished by genetic algorithm, then the refinement of the result with the known numerical methods. During my further researches I would like to examine the possibility of usability various plants as ER liquids as well as the conductance of plant oils.

## 2. The application of the flow regulator

During the further material and application tests it is practical to use a device which has application possibilities too. In this consideration for further investigations we need the design of a hydraulic ER valve, which can be operated built in hydraulic circuits.

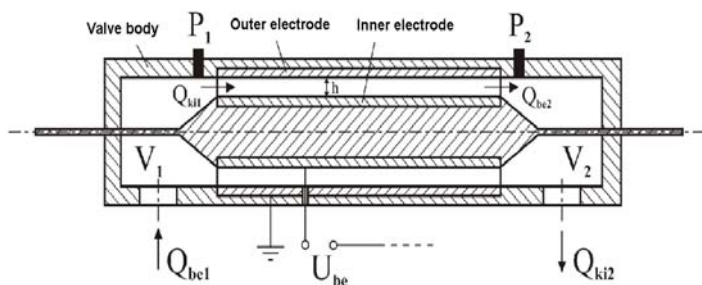


Figure 3. The ER valve

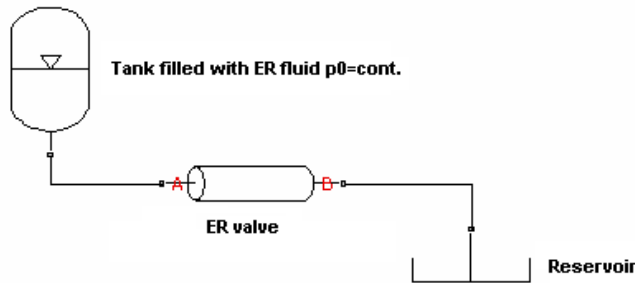


Figure 4. The conceptual diagram of simulation

*The Numerical Solution of the Applied Mathematical Model*

The solution of the mathematical model of the ER valve was accomplished by MATLAB with block-oriented method, using Kelvin-Thompson return-circuit principle.

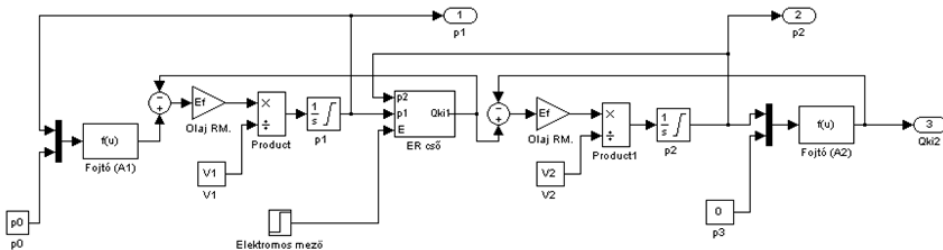


Figure 5. The block diagram of simulation

With this method the volume, which was evolved by the constant pressure difference, put on the ER valve can be measured. In this layout the the liquid volume can be controlled by electric field strength. With this we can create a hydraulic valve, which without moving parts, can be controlled by the application of electric field. It can be seen from the measurement data of the professional literature, that for the evolution of the effect it is enough (2-10) ms, which is a much smaller value, that the indication time of the proportional valves applied nowadays.

**3. The results of operation of the model**

In Chart 6 at making the simulation results we applied 6 bar inlet pressure.

As it seems on the figure 6. the flow is 42 l/min up to 20 ms, then by switching 2 kV/mm electric field the streaming flow decreases to 18 l/min in 40ms.

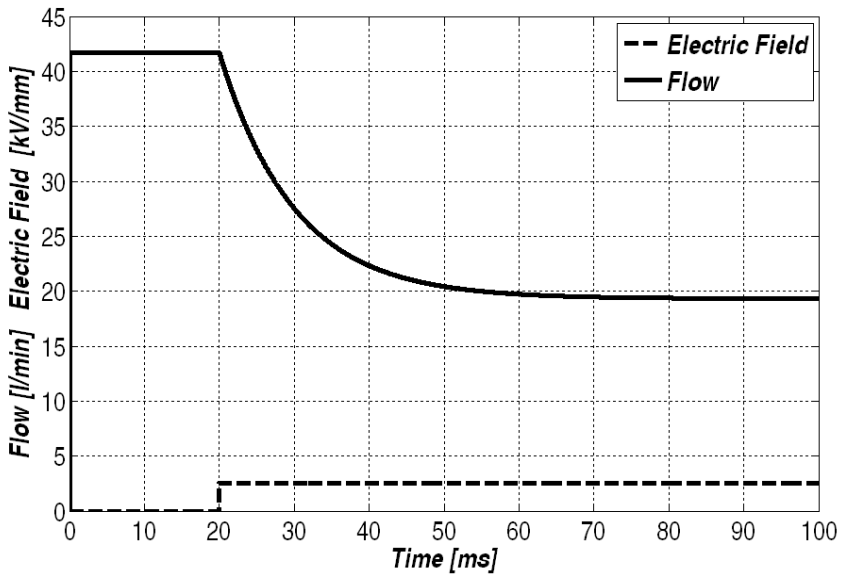


Figure 6.

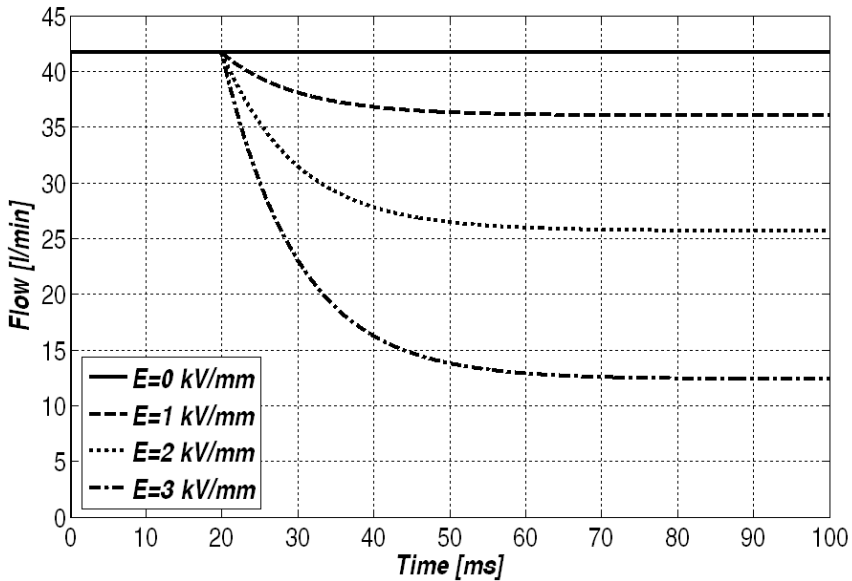


Figure 7.

At the simulation in the figure 7. constant 6 bar inlet pressure ( $p_0$ ) was used. It is shown that how the flow changes at various size electric field.

The expectable behaviour of the flow control valve at different tank pressure and electric field

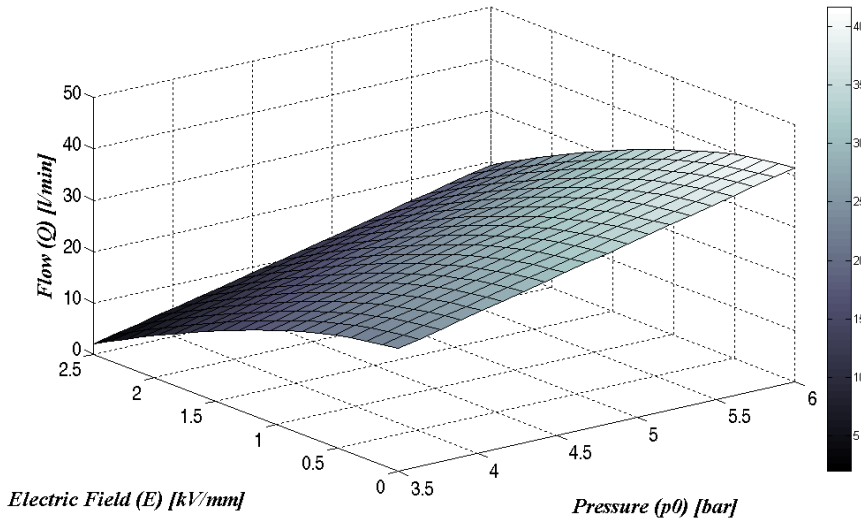


Figure 8.

At these simulation the effect of the changes in the input pressure ( $p_0$ ) and the electric field ( $E$ ) on the flow ( $Q$ ) is represented.

## References

- Csizmadia B. – Nándori E. (szerk.): Modellalkotás, Nemzeti Tankönyvkiadó, Budapest, 2003.
- Dr. Farkas I.: Számítógépes szimuláció. Gödöllő, 1999.
- H.-G. Lee – S.-B. Choi: Dynamic properties of an ER fluid shear and flow modes, In: Materials and Design, 2002., XXIII. évf.
- Rácz, P. – Szüle, Zs.: Mérési módszer a talajlazítás mértékének kimutatására az elektromos vezetőképesség segítségével. In: Gép, 2007. LVIII. évf. 4. sz., pp. 54 – 57.
- Sárközi E.- Dr. Jánosi L. (2006): Különböző repcefajtákból nyert növényi olaj vizsgálata hajtóanyag alkalmazási szempontból, Gép 2006. Különszám
- Valasek I. – Auer J. (szerk.): Kenőanyagok és vizsgálataik, Tribotechnik Kft., Budapest, 2003

# The role of the tool path orientations in ball nose end milling

Marius COSMA, Lucian BUTNAR, Vlad DICIUC, Sever POP  
North University of Baia Mare, Faculty of Engineering

## Abstract

This study describes an experimental analysis of the influence of tool path orientations on the surface topography and vibrations level, in three axes ball nose end milling of  $45^{\circ}$  inclined surfaces. The ball nose end milling has very complex machining mechanism, because the cutting edge is determined on spherical surface and the result of milling is roughness of surface that is an uncut strip created between the two cylindrical cutting passes. The tool path orientations are determined by feed and stepover directions on the inclined workpiece surface and have a big influence on the surface quality and chatter stability of dynamic milling system. The aim of present study is to investigate finish milling on a  $45^{\circ}$  inclined workpiece surface with a view of roughness and vibrations in order to identify the best tool path orientation. This experimental study confirms geometric model of ball nose end milling and establish a few recommendations when finish milling at an inclined workpiece on three-axes milling centre.

## Keywords

tool, path, ball nose end mill, roughness, vibrations

## 1. Introduction

Complex surface machining by milling, is characterized by high production rates, high dimensional and geometrical shape accuracy and roughness of surface and the development of cutting tools, provide a very competitive alternative to grinding and electrical discharge machining (EDM). Complex curved surfaces (sculptured surfaces) are encountered in many objects such as small batch components, automotive parts, aircraft components, turbine blades, injection moulds and dies, electrodes for electrical discharge machining etc.

In 3-axes ball nose end milling, a possibility to avoid cutting at tool tip that is moving in a linear motion and the cutting speed is zero, is to assure for workpiece surface a minimal inclination angle, between tool axis and surface normal.

The cutter path orientation is crucial in achieving desired machined surface and without considering the impact of cutting edge with undeformed chip in

different path strategy with adequate consideration of the chip area variation, cutting forces, temperature and vibration analysis, the result can lead to cutter failure and therefore lead to unnecessary waste of time, cost and poor surface quality. The tool path orientations are determined by feed and according as stepover direction, the ball nose end milling can be (Fig.1):

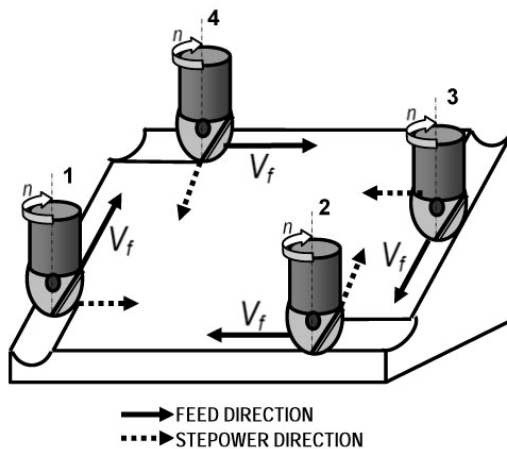


Figure 1. Tool path orientations (1-vertical upward; 2-horizontal upward; 3-vertical downward; 4-horizontal downward)

Another application parameter of importance is to use of down milling tool paths as much as possible when the cutting edge goes into cut at maximum chip thickness. Up milling can be favourable when having old manual milling machines with large play in the lead feed screw, because a counter pressure is created which stabilizes the machining.

In generally, upward milling has a cutting process at more favourable cutting speed (the effective diameter is bigger) that in downward (Fig. 2), but edge cut entrance and chip area transition is important for a good cutting process (Fig. 3).

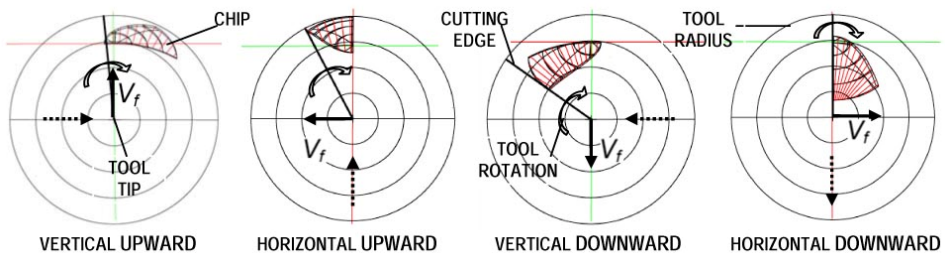


Figure 2. Relative positions between tool and chip (45° inclined workpiece surface)

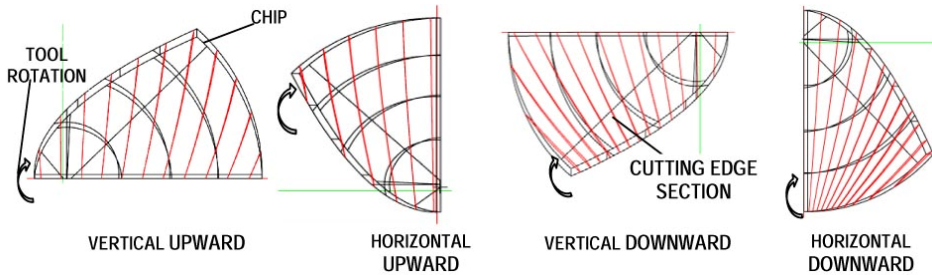


Figure 3. Different entrance of cutting edge in undeformed chip ( $45^{\circ}$  inclined workpiece surface)

Frequently, manual polishing operations are necessary due to the machining surface and for reduce the polishing time and cost, appropriate tool path strategy should be selected to improve the dimensional accuracy, the surface roughness and minimal vibrations characteristics. The aim of present study is to investigate finish milling on a  $45^{\circ}$  inclined workpiece surface with a view of roughness and vibrations in order to identify the best tool path orientation.

## 2. Experimental procedure

### Tooling and workpiece

In this experiment, a new solid carbide ball nose end mill type TORNADO SECO Tools, cod JH 720 was used, with 4-flute, 8 mm diameter and 100 mm length. Workpiece configuration presented in Figure 4, made from general use steel OL 52 type, STAS 500/1-80, with a nominal composition of 0.20% C, 1.6% Mn, 0.05% Si, 0.05% P, 0.05% S and Fe balance was used in the experimental work.

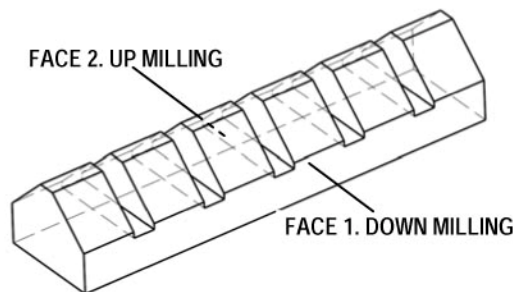


Figure 4. Workpiece with  $45^{\circ}$  inclined surfaces

The cutting experiment were carried out on a workpiece with two faces  $45^{\circ}$  angle inclined (Face 1 down milling and Face 2. up milling) and each face was separated in six little surfaces for different tool path orientations (Fig. 5). The

first digit represents the face and the second digit represents the tool path strategy as follow: 1-vertical upward; 2-horizontal upward; 3-vertical downward; 4-horizontal downward; 5-vertical zigzag and 6-horizontal zigzag (the arrows significations are presented in figure 1).

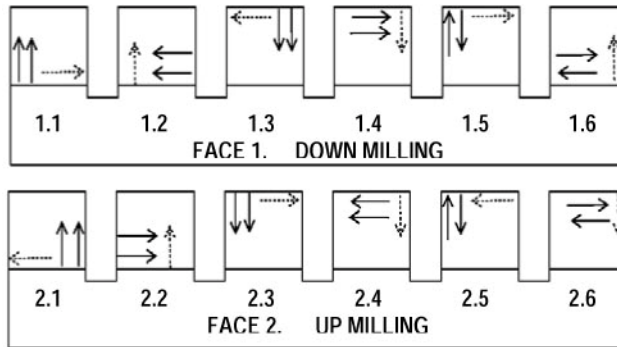


Figure 5. Tool path orientations scheme on workpiece

#### Experimental equipment and setup

The cutting tests were performed on a vertical CNC 3-axes milling machine Microcut Challenger 2412 with a continuous variable speed up to 10 000 rpm and a maximum spindle power of 25 kW (Fig. 6). To avoid tool holder collision with the workpiece fixture, a tool overhang of 45 mm was employed throughout the tests and the cutter were checked prior to machining, to ensure run out up to 0.01 mm. Surface images were performed on a microscope with magnification up to 20X equipped with high resolution digital camera and surface roughness measurement with Multi-parameter Surface Roughness Measuring Instrument LINKS Model 2222.

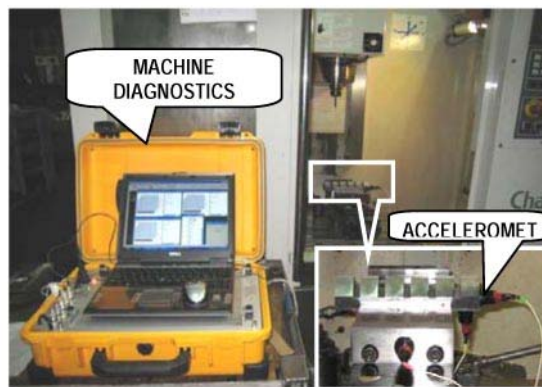


Figure 6. Vibrations equipment on milling centre

Cutting dynamic measurement was carried out using Brüel & Kjær equipment, Portable Machine Diagnostic Toolbox type 9727 (Fig. 6, Fig. 7 ), with three unidirectional piezoelectric accelerometers 2, model ENDEVCO type 752A12, fixed with magnetic fixtures on workpiece 1 on each CNC reference milling centre axes (X, Y, Z), signal analyzer 3 and PC laptop 4.

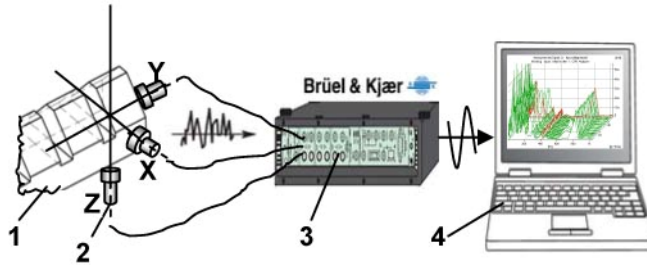


Figure 7. Scheme of dynamic measurement

*Cutting and measurement conditions employed*

The effect of using different cutter path orientations in finish milling was investigated in relation with chip formation, surface roughness and cutting vibrations. The workpiece was fixed in a rigid machine vice and all surface machining were conducted in dry cutting, with addition high pressure air blast delivered through a nozzle, directed at the cutting area. The axial depth  $a_p$  and radial depth  $a_e$  of cut used were 0.2 mm and they were ensured that it was aligned on normal  $N-N$ , respectively along the workpiece surface, illustrated in figure 8 for horizontal upward milling.

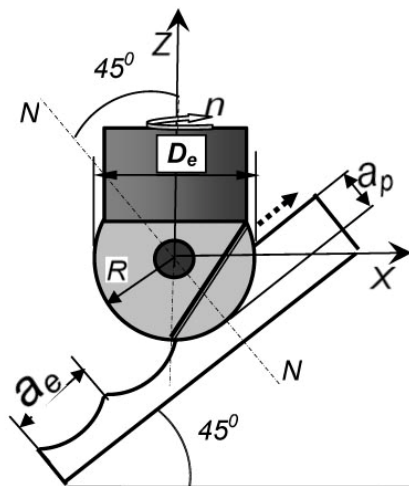


Figure 8. Horizontal upward milling

The cutting speed used was 100 m/min instead to avoid that the tooth passing frequency not exceed the natural frequency of the system. In respect with effective diameter  $D_e$  the tool rotation was  $n=6000$  rpm, and the feed per tooth 0.1 mm/tooth. In summary:

– cutting speed	(m/min)	110
– spindle speed	(rpm)	6000
– feed per tooth	(mm/tooth)	0.03
– axial depth of cut	(mm)	0.2
– radial depth of cut	(mm)	0.2
– tool ball nose radius	(mm)	8
– tooth number		4
– tool overhang length	(mm)	45

### 3. Experimental results and discussions

#### *Surface topography and roughness*

Finishing operation, where a small radius ball nose end mill at minimum radii demands is used to generate the complete desired surface, results in a surface with a large number of uncut strips (scallops) and for remove these scallops, if surface roughness require, is necessary benchwork, that consist in manual grinding and hand polishing (super-finishing) which give a satisfying surface accuracy, but it always has a negative impact on the dimensional and geometrical accuracy.

Surface quality as a result of ball nose end milling is determined by topography and can be evaluated using different parameters. Theoretically, it is the best to calculate ten points for the height of irregularities,  $R_z$ , but this parameter is not usually mentioned in a technical drawing. This function fulfils the arithmetical mean deviation of the profile  $R_a$ , which is used in this experiment, measured in longitudinal direction (feed direction) and transversal direction (stepover direction). Surfaces topography are presented in figure 9 for face 1 of workpiece (down milling) and in figure 10 for face 2 (up milling).

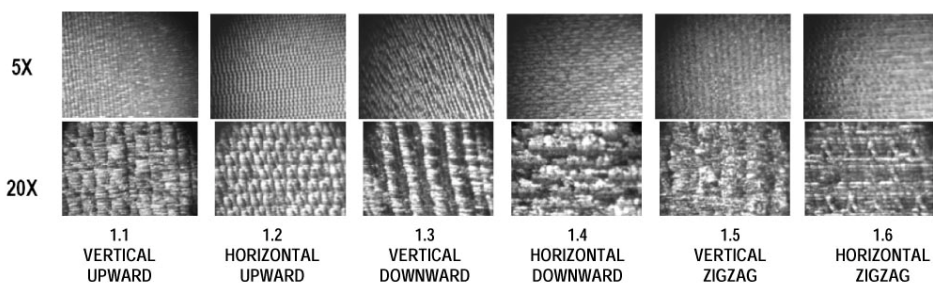


Figure 9. Surfaces topography (down milling)

Figure 9 and 10 details the big differences aspects of faces topography in accord with different tool path orientations, using the same cutting conditions. Comparison in terms of regularly scallops resulting after cutting process, horizontal upward orientation achieved the best cutting conditions, which are in accord with edge cut entrance and chip area transition (Fig. 3) to the high chip thickness and small area. In opposite situation, horizontal downward orientation achieved the worst surface topography, with irregular scallops and many scratches because the edge cut entrance in undeformed chip is to the small chip thickness and very large contact between cutting edge and machined surface. Using zigzag tool paths result the worst topography in vertical or horizontal orientations.

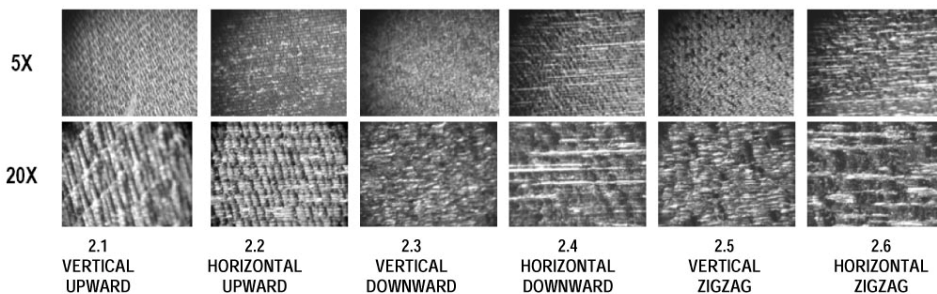


Figure 10. Surfaces topography (up milling)

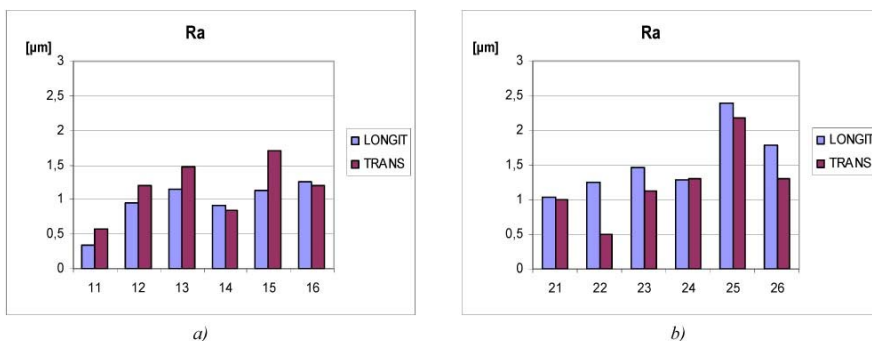


Figure 11. Comparison of Ra parameter value for various tool path orientations

The average mean surface roughness  $Ra$ , adopted to determine the longitudinal and transversal workpiece roughness, was measured for a sampling length of 4.0 mm and cut-off length of 0.8 mm, and represented in figure 11 a) for face 1 (down milling) and figure 11 b) for face 2 (up milling). The result clearly illustrate in graphics that using a vertical upward orientation (surfaces 11, 21) gave the lowest surface roughness and in generally lowest values for down milling. The biggest values are results for zigzag tool path (surfaces 15, 25) and especially in vertical orientations.

### *Dynamic of cutting and vibrations*

Ball nose end mills generate complex chip geometry and non-uniform thickness distribution along the cutting edge and work contact zone (Fig. 3), creating cutting forces in three Cartesian directions. The cutting force is proportional to the chip thickness and may excite the machine tool system and presence of chatter leads to poor surface finish, chipping of the tool and large dynamic loads on the spindle and table structure. Most of the research focuses on chatter stability in milling and presented analytical prediction but study about vibrations level in respect to cutting path are scant. Therefore, a detailed knowledge on the evaluation of vibrations in different cutter path strategies for finish milling is essential.

Cutting vibrations measurement were carried out using scheme from figure 7, where the dynamic signal was analyzed and stored for each tool path strategy for 50 seconds of machining. Data analysis was performed using special software *PULSE LabShop Version 10.3* in CPB mod analyzer (frequency / time / amplitude of vibration speed Fig. 12).

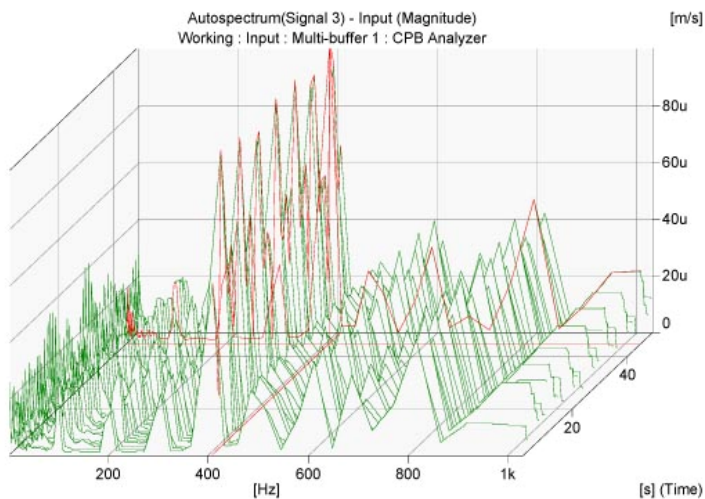


Figure 12. CPB diagram (horizontal zigzag 2.6 for Z axis)

The software has a facility to study different frequency band slice on a CPB diagram and see the amplitude of vibrations in time domain (Fig. 13). The dynamic signal is periodically, carried to the rotating tool (6000 rpm) and tooth number (4), resulting a fundamental frequency  $f=400$  Hz for study. Results of measurement are represented in figure 14.

The level vibrations is in generally higher for up milling (Fig. 14, b) and especially for zigzag tool path, result in correspondence with surface roughness (Fig. 11, b). The milling process has good cutting conditions (low vibration level) for vertical upward and horizontal upward (surfaces 11, 12).



Figure 13. Slice on fundamental harmonic 400 Hz (horizontal zigzag surface 2.6 for Z axis)

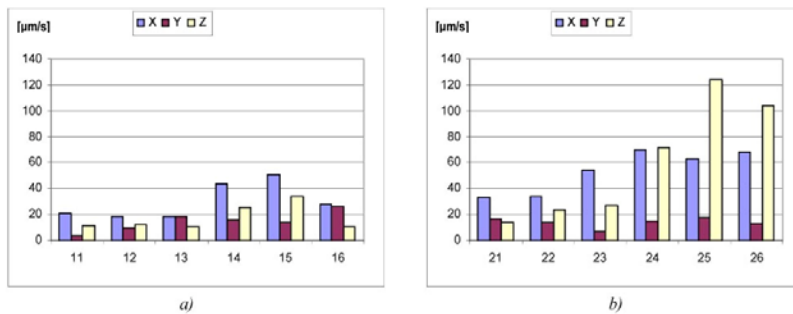


Figure 14. Comparison of speed vibrations value for various tool path orientations

#### 4. Conclusions

This experimental study confirms geometric model of ball nose end milling and following conclusions have been derived, when finish milling at an inclined workpiece angle of  $45^{\circ}$ :

- using a vertical upward tool paths, gave the lowest roughness and vibrations;
- the worst surface and high vibrations level was obtained using zigzag tool path;
- avoid as much as possible downward tool path when the effective cutting edge is near to the tip tool and cutting speed is reduced to low effective diameter;
- down milling is more favourable process that up milling in all tool path strategies.

#### References

- Cosma, M.: Considerations Concerning the Milling of Complex Curved Surfaces Using Ball Nose End Mills. Inter ING 2005, Petru Maior University of Tg. Mureș, 2005, ISBN 973-7794-41-9, pp. 91-96.
- Toh, C.K.: Cutter Path Orientations When High-Speed Finish Milling Inclined Hardened Steel. The International Journal of Advanced Manufacturing Technology, Vol. 27 No. 5-6, 2005, pp. 473-480.

- Generating Mechanism of Ball End Mill Based on Deflection by FEM. JSME International Journal, Series C, Vol. 47, No. 1, 2004, pp. 8-13.
- Cosma, M.: Geometric Method of Undeformed Chip Study in Ball Nose End Milling. Scientific Buletin, Serie C, Vol. XX, North University of Baia Mare, 2006, ISSN 1224-3264, pp. 49-54.
- Cosma, M.: Horizontal Path Strategy For 3D-CAD Analysis of Chip Area in 3-Axes Ball Nose End Milling. 7th INTERNATIONAL MULTIDISCIPLINARY CONFERENCE North University of Baia Mare, Scientific Buletin Serie C, Vol. XXI, Romania, 2007, ISSN-1224-3264, pp. 115-120.
- Pay, E. – Cosma, M., Vertical Path Strategy For 3D-CAD Analysis of Chip Area in 3-Axes Ball Nose End Milling. 7th INTERNATIONAL MULTIDISCIPLINARY CONFERENCE, North University of Baia Mare, Scientific Buletin Serie C, Vol. XXI, Romania, 2007, ISSN-1224-3264, pp. 585-590.
- Budak, E. – Altintas, Y.: Analytical Prediction of Chatter Stability Conditions for Multi-Degree of Systems in Milling. ASME Journal of Dynamic Systems, Measurement and Control, vol. 120, 1998, pp. 22-30.
- Abrari, F. – Elbestawi, M.A. – Spence, A.D.: On the Dynamics of Ball End Milling: Modeling of Cutting Forces and Stability Analysis. International Journal of Machine Tools and Manufacture, vol. 38, No. 3, 1998, pp. 215-237.
- Altintas, Y. – Shamoto, E. – Lee, P.A. – Budak, E.: Analytical Prediction of Stability Lobes in Ball End Milling. ASME Journal of Manufacturing Science and Engineering vol. 121, 1999, pp. 586-592.

# Loading simulations of nanotube networks

Ibolya ZSOLDOS

Szent Istvan University, Faculty of Mechanical Engineering

## Abstract

A modification is suggested to the Brenner potential cut-off function in order to compute atomic forces of carbon nanostructures in a more realistic way and giving a possibility to fit the atomic forces to experimental data. With the modified Brenner potential the loading diagram and the tensile strength were determined for an example of the carbon nanotube networks. According to these new computational results carbon nanotube networks can be the materials which inherit the extremely high strength of the graphite sheet and they bring this property in all directions of the 3D space (not only in 1 direction as the nanotubes).

## Keywords

nanotube, network, simulation

## 1. Introduction

The  $sp^2$  carbon-carbon bond in a graphite layer is the strongest of all chemical bonds in solids. Theoretical strength values of the graphene were determined as  $\sigma_C \cong 0.316 \text{ TPa}$  derived from the Young's modulus and  $\sigma_T \cong 0.14\text{--}0.177 \text{ TPa}$  derived from the work of fracture. This theoretical strength is important because it is the maximum theoretical strength for all solids.

The carbon nanotubes could be the materials which approach the theoretical strength of the graphene. Direct mechanical measurements of the tensile strength were carried out on multiwalled carbon nanotubes (MWCNC) and on single wall carbon nanotube (SWCNT) ropes. To determine the tensile strength a theoretical way was carried out by molecular mechanical calculations using different energetic potential functions. Different types of SWCNT-s were studied using primarily the empirical Brenner potential. For the same purpose the Tersoff and the Morse potential were used, as well. Recently the finite deformation shell theory was developed for theoretical studies of carbon nanotubes. This continuum theory is based on use interatomic potential, as well, and can be the next generation of theoretical methods to determine mechanical properties.

Accordingly, today the straight carbon nanotubes are the strongest materials. Nevertheless they show this property only in one direction. Their extremely high strength can be led by nanotube junctions into different directions of the three-

dimensional (3D) space. The significance of nanotube junctions was first discovered in their electronic properties. For example a heterogeneous junction built from a zig-zag and an armchair tube behaves like a rectifying diode with nonlinear transport characteristics. The Current-Voltage characteristics of a Y junction are measured, as well, and we may hope that the molecular transistor will be found in the group of the Y junctions. In our earlier research work we have defined a set of nanotube junctions built from armchair and zigzag type straight tubes. We have shown that any number of tubes having an optional diameter can be connected in a junction and we have developed a method to construct their models as well. Our system is created in such a way that if a tube of a given type is taken out from the junction, it can always be replaced with a contrary type one. This property can be interesting in electric applications. Later we have presented that nanotubes of any chirality can be connected in a junction. Nanotube junctions consisting of more than 3 tubes were observed in various experiments.

From different nanotube junctions different nanotube networks can be built. The basic types of regular networks are named as supersquare (the network constructed from X junctions), supergraphene (the honeycomblike network constructed from Y junctions), supercubic (the network constructed from junctions having 6 perpendicular tubes) and superdiamond (the network constructed from tetrahedral junctions). Several mechanical properties (Young's modulus, bulk modulus and deformation mechanisms) were determined for supersquares and supergraphenes. Special fractal networks, so-called supercarbon nanotubes based on the nanotube structures were defined. Others prognosticate a successful future for the random nanotube networks, although these networks have not contained junctions so far, only disordered tubes as dropping pickup sticks. They could be the most stable and the strongest electric conductors having almost zero failure probability. Researchers hope a new and cheap technology for their manufacturing will be found shortly. Several research institutes in the world prepare them today in plastic impregnated technology.

The goal of this work was to develop a method in order to calculate the loading diagram and the tensile strength of nanotube networks.

## 2. Computational method

To determine the loading diagram and the tensile strength, atomic forces are needed to compute. The atomic forces can be calculated from a derived energetic potential function. For this purpose we have chosen the empirical Brenner potential which is generally used in molecular mechanics and molecular dynamic studies not only in carbon nanostructures but in hydrocarbon structures, as well.

Brenner developed the interatomic potential for carbon as

$$V(r) = V_R(r) - \bar{B}_{ij} V_A(r_{ij}) \quad (1)$$

for atoms  $i$  and  $j$ , where  $r=r_{ij}$  is the distance between atoms  $i$  and  $j$ .  $V_R$  and  $V_A$  are the repulsive and attractive terms given by

$$V_R = \frac{D_e}{S-1} e^{-\sqrt{2S}\beta(r-R)} f_{ij}(r_{ij}) \quad (2)$$

$$V_A = \frac{D_e S}{S-1} e^{-\sqrt{2/S}\beta(r-R)} f_{ij}(r_{ij}) \quad (3)$$

The so-called cut-off function  $f_{ij}(r_{ij})$ , which restricts the pair potential to the nearest neighbours, is given by

$$f_{ij}(r_{ij}) = \begin{cases} 1, & r_{ij} < R_1 \\ \left[ 1 + \cos\left(\frac{r_{ij} - R_1}{R_2 - R_1} \pi\right) \right] / 2, & R_1 \leq r_{ij} \leq R_2 \\ 0, & r_{ij} > R_2 \end{cases} \quad (4)$$

The parameter  $B_{ij}$  in Eq. (1) represents a multibody coupling between the bond from atoms  $i$  and  $j$  and the local environment of atom  $i$ , and is given by

$$B_{ij} = \left[ 1 + \sum_{k(\neq i, j)} G(\theta_{ijk}) f_{ik}(r_{ik}) \right]^{-\delta} \quad (5)$$

where  $\theta_{ijk}$  is the angle between bonds  $i-j$  and  $i-k$ , and the function  $G$  is given by

$$G(\Theta) = a_0 \left[ 1 + \frac{c_0^2}{d_0^2} - \frac{c_0^2}{d_0^2 + (1 + \cos \Theta)^2} \right] \quad (6)$$

For atoms  $i$  and  $j$  that have a different local environment, Brenner suggested the replacement of the coefficient  $B_{ij}$  in Eq. (1) by

$$\bar{B}_{ij} = (B_{ij} + B_{ji}) / 2 \quad (7)$$

In accord with our experience more authors have noticed that the cut-off function affects the computation of the atomic forces very strongly. It introduces a dramatic increase in the interatomic force at  $r= R_1$  (like a camelback on the force curve), which rises sharply with a peak at around 30% strain, Fig. 1.b. To avoid this problem Shenderova *et. al.* shifted the cut-off function to larger strains

so that it occurs after the inflexion point in the interatomic potential. Belytschko *et. al.* have found that the cut-off function affects strongly even when it is shifted to 100% strain. Duan *et. al.* assumed the cut-off function equal to 1 to avoid the dramatic increase in the interatomic force. Mylvaganam *et. al.* defined the changes of the slope on the interatomic force as different stages of the stress-strain curve.

Table 1.

Nanotube structure	$\sigma_T$ (GPa)	method
SWCNT ropes	13-50	loading experiment
MWCNT	11-63	loading experiment
MWCNT	150	loading experiment
(5,5) nanotube	123	calculated with Morse potential
(9,0) nanotube	94	
(12,12) nanotube	112	calculated with Morse potential calculated with Morse potential calculated with Morse potential calculated with Morse potential calculated with Brenner potential
(16,8) nanotube	106	
(12,4) nanotube	98	
(20,0) nanotube	93	
(20,0) nanotube	110	
(10,0) nanotube	105.38	calculated with Morse potential calculated with Brenner potential calculated with Morse potential calculated with Brenner potential
(10,0) nanotube	99.89	
(10,1) nanotube	106.09	
(10,1) nanotube	100.46	
(10,3) nanotube	110.21	
(10,3) nanotube	102.59	
(10,5) nanotube	116.83	
(10,5) nanotube	104.20	
(10,7) nanotube	124.09	
(10,7) nanotube	104.93	
(10,9) nanotube	130.93	
(10,9) nanotube	105.64	
(10,10) nanotube	134.01	
(10,10) nanotube	111.93	
(10,10) nanotube	1357	calculated with Brenner potential
(17,0) nanotube	754	
(14,14) nanotube	250*	calculated with Brenner potential
(24,0) nanotube	125*	
(6,6) nanotube	152.3	calculated with Tersoff potential
(8,3) nanotube	107.6	
(10,0) nanotube	92.5	
(5,5) nanotube	1700-1800*	calculated with Brenner potential
(9,0) nanotube	1400*	
(10,10) nanotube	1700-1800*	
(17,0) nanotube	1400*	
(15,15) nanotube	1700-1800*	
(26,0) nanotube	1400*	

\*The value is read from the loading diagram.

Beside the above mentioned problem there are uncertainties in the measured and calculated strength values of carbon nanotubes, as well. In Table 1 we summarized the tensile strength values found in the literature. The values are rather different.

The reasons for the differences are partly because of the differences in the structures and partly because  $\sigma_T$  is not defined the in same way by the authors.

To compute atomic forces in a more realistic way we suggest a modification in the cut-off function in the formulas of the Brenner potential. Figure 1 shows the effect of the cut-off function on the energetic potential and on the atomic force curve in the case of only one chemical bond of the graphite sheet. The cut-off function ( $f_{ij}$ ) is a monotonously decreasing curve, it decreases from 1 to 0 between the distances of  $R_1$  and  $R_2$ , Fig.1.a. If we omit it from Brenner's formulas, the energetic potential approaches zero in the infinite, but if we do not leave it out, the curve approaches zero at  $R_2$ , Fig.1.b. The effect is stronger on the atomic force function: the curve computed with the cut-off function is basically other than the one without the cut-off function, Fig.1.b. Beside this there is a break point on the force curve, as well.

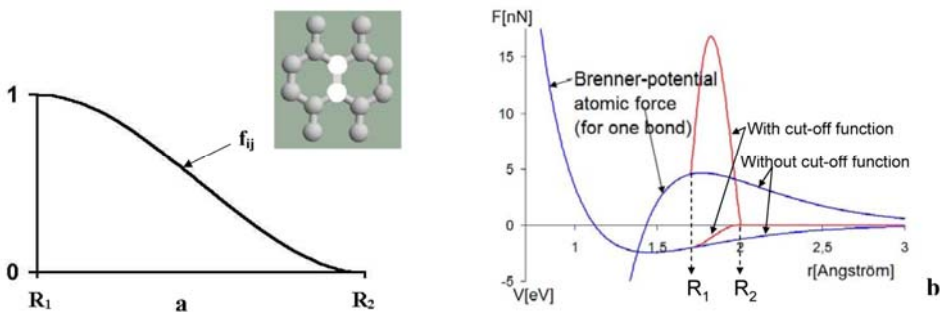


Figure 1. The cut-off function (a) and its effect on the energetic potential and on the atomic force curve (b) in the case of only one chemical bond of the graphite sheet

It is obvious that there is a large set of functions which keep the property of the original cut-off function: they decrease monotonously from 1 to 0 between  $R_1$  and  $R_2$ , Fig.2.a. Consequently if we use the elements of this set like cut-off function to compute the energetic potential and the atomic forces we can define a curve set for both of them, Fig.2.b. It is important to mention that a small change in the energetic potential curve between  $R_1$  and  $R_2$  means a large change in its derived function, in the atomic force curve. We suggest choosing the cut-off function from the function set in such a way that we fit the force curve to experimental results if it is possible. Beside this we suggest putting the value of  $R_1$  to the minimum place of the energetic curve to avoid the breakpoint of the functions.

To describe the curve set of the cut-off function mathematically we used polynoms in two different intervals defined by

$$f_{ij}(r) = \begin{cases} f_1(r), & R_1 \leq r \leq R_T \\ f_2(r), & R_T < r \leq R_2 \end{cases} \quad (8)$$

where

$$f_1(r) = a_0 + a_1r + a_2r^2 + a_3r^3 + a_4r^4 \text{ and } f_2(r) = b_0 + b_1r + b_2r^2 + b_3r^3.$$

The selection is favourable because polynoms are derived very easily. The two different intervals between  $R_1$  and  $R_2$  are separated by the inflexion point of the curve having coordinates of  $R_T$  and  $f_T$  which will be the free parameters for the fitting, Figure 3.

The conditions to fit the curves at  $R_1$ ,  $R_2$  and  $R_T$  determine nine different linear equations as

$$f_1(R_1) = 1 \quad (9)$$

$$f_1'(R_1) = d \quad (10)$$

$$f_1(R_T) = f_T \quad (11)$$

$$f_1'(R_T) = f_2'(R_T) \quad (12)$$

$$f_1''(R_T) = 0 \quad (13)$$

$$f_2(R_T) = f_T \quad (14)$$

$$f_2(R_2) = 0 \quad (15)$$

$$f_2'(R_2) = 0 \quad (16)$$

$$f_2''(R_T) = 0 \quad (17)$$

The role of the 'd' parameter in Eq. (10) is to fit the force curve at  $R_1$  to avoid the breakpoint if  $R_1$  is not chosen to the minimum place of the energetic potential. Since we put  $R_1$  to the minimum place,  $d=0$  in our calculations detailed in the Section 2.

The free parameters of  $R_T$  and  $f_T$  are intended to fit the potential function to experimental data. The tensile strength ( $\sigma_T$ ) of several MWNTs is known from experiments today (see Table 1) and we will use one of these data for the fitting later (last paragraph of this chapter). We mention here that although the cut-off function as a cosine function (as it was used by Brenner originally) is more realistic in physics, it is not able to fit the function because of the absence of free parameters.

We used a cubic and a fourth-degree polynom to solve the equation system (9)-(17).

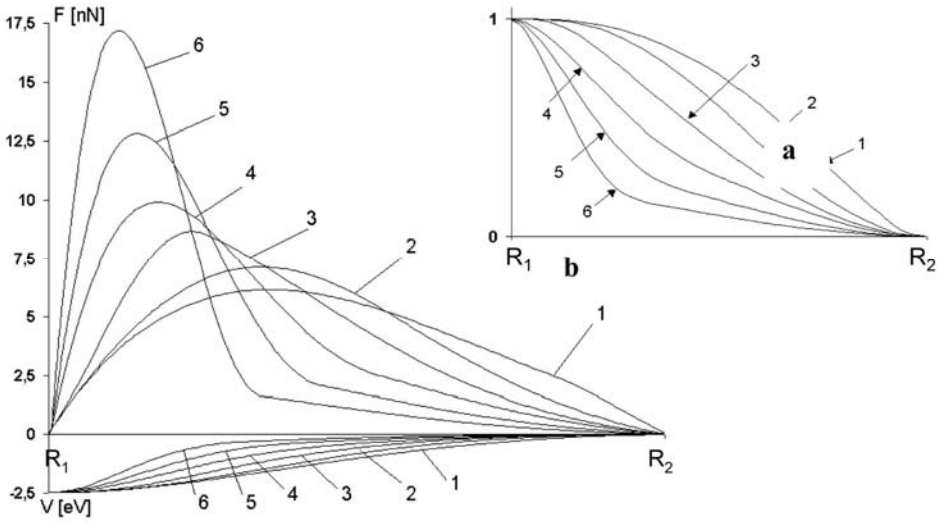


Figure 2. a) a set of the cut-off functions, b) The energetic potential (lower half of the diagram) and the atomic forces (upper half of the diagram) computed with (6) different elements of the cut-off function set (for only 1 chemical bond of the graphite sheet).

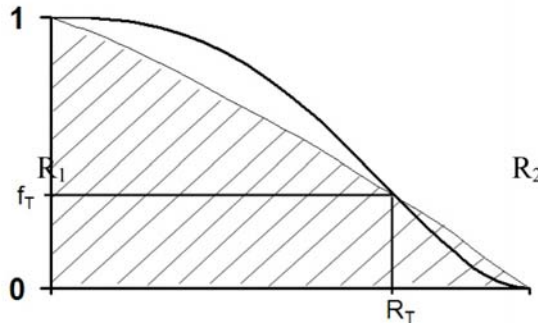


Figure 3. The coordinates of the inflexion point R<sub>T</sub> and f<sub>T</sub> which will be the free parameters

In Eq. (19)-(25) we show the solution of the nine equations for the coefficients of the polynoms. The recursive formulas can be used in computer codes very easily:

$$b_3 = \frac{f_T}{2(R_2 - R_T)^3} \quad (19)$$

$$a_4 = \frac{3f_T - 3 - d(R_T - R_1) + 6b_3(R_2 - R_T)^2(R_T - R_1)}{(R_T - R_1)^4} \quad (20)$$

$$a_3 = \frac{4a_3 [R_T^3 - R_1^3 - 3R_T^2 (R_T - R_1)] + 3b_3 (R_2 - R_T)^2 + d}{3(R_T - R_1)^2} \quad (21)$$

$$b_2 = -3b_3 R_T \quad (22)$$

$$a_2 = -3a_3 R_T - 6a_4 R_T^2 \quad (23)$$

$$a_1 = d - 2a_2 R_1 - 3a_3 R_1^2 - 4a_4 R_1^3 \quad (24)$$

$$b_1 = d - 2b_2 R_2 - 3b_3 R_2^2 \quad (25)$$

$$a_0 = 1 - a_1 R_1 - a_2 R_1^2 - a_3 R_1^3 - a_4 R_1^4 \quad (26)$$

The mathematical description of the curve set is not so easy. There are too many conditions (Eq. (9)-(17)) and the solution for them is generally only partial. For example, let us regard the solution for an interval of  $R_1=0.145\text{nm}$  and  $R_2=0.2\text{nm}$  (this value was used everywhere in the literature). In this case we can choose values for  $f_T$  and  $R_T$  only inside a part of the rectangle defined by  $(R_1, R_2)$  and  $(0,1)$  shown as the hatched area in Fig. 3. If the inflexion point is beyond this area, the monotonously decreasing property is not realized. However the hatched area was enough to find the most applicable curve from the function set.

We fitted our parameters to experimental data calculated for one chemical bond. For this purpose we have chosen Demczyk's et.al. measurement on multiwalled nanotubes because the measured structure can be derived from their paper. They observed a tensile force of  $18\mu\text{N}$  on a tube having a diameter of  $12.5\text{nm}$ , the type of the tube is not known. If we assume that the tube was a zigzag type tube, then the outer tube has to have a  $(160,0)$  structure. The distance of the parallel tubes has to be minimum  $0.34\text{nm}$  which is the interlayer graphite distance, accordingly the inner tubes have to have  $(150,0)$ ,  $(140,0)$ ,  $(130,0)$ , ...,  $(10,0)$  structures. It means that  $160+150+140+\dots+10=1360$  bonds being parallel with the loading direction have to be broken together, so the tensile force is  $18\mu\text{N}/1360=13.23\text{nN}$  for one bond. If we assume that the tube was an armchair type tube, then the outer tube has to have a  $(92,92)$  structure. The distance of the parallel tubes has to be minimum  $0.34\text{nm}$  which is the interlayer graphite distance, accordingly the inner tubes have to have  $(86,86)$ ,  $(80,80)$ ,  $(74,74)$ , ...,  $(8,8)$  structures. It means that  $2(92+86+80+\dots+6)=1500$  bonds have to be broken together, the angle between the bonds and the loading direction is  $30^\circ$  at the beginning of the loading. Considering that the angle has to be a bit smaller at the tensile force, the tensile force has to be a bit smaller than  $18\mu\text{N}/1500/\cos 30^\circ=13.86\text{nN}$  for one bond. To fit the maximum atomic force we have chosen  $13.3\text{nN}$ .

The strain value of the maximum force cannot be known in Demczyk's et.al. paper therefore we tried to compute without this.

In a special iteration procedure we varied the value of  $R_T$  between  $R_1$  and  $R_2$  beside this we varied the value of  $f_T$  between 0 and 1. It is obvious that for every value of  $R_T$  we can find a value of  $f_T$  so that the maximum force is the same, because we do not know the place of the maximum force. In this work we selected 4 characteristic  $(R_T, f_T)$  pairs in order to compute forces. The  $(R_T, f_T)$  pairs with the corresponding atomic force and the energetic potential curves can be seen in Fig. 4. We mention again that in the case of a very small change in the energetic potential (see the fitted energetic functions in the lower part of the diagram) there is a large change in the atomic force function (see the fitted force functions in the upper part of the diagram: the change here is only in the place of the maximum force).

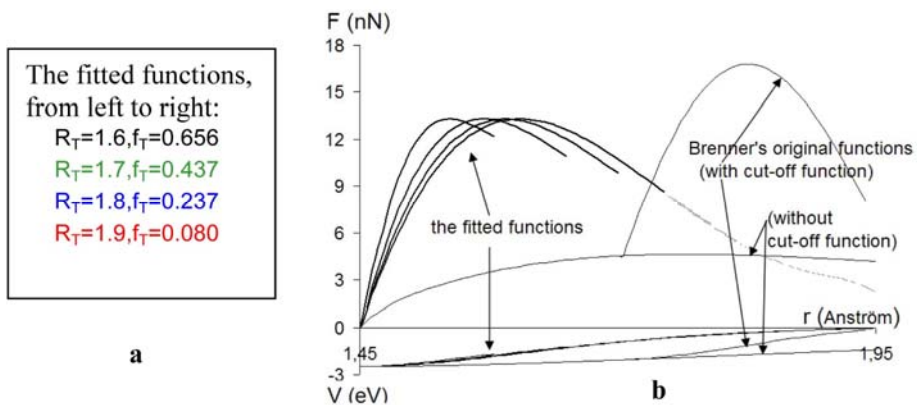


Figure 4.  $(f_T, R_T)$  pairs (a) and the corresponding atomic force ( $F$  in nN-s, upper part) and the energetic potential curves ( $V$  in eV-s, lower part) fitted to experimental data (b)

The maximum force on the fitted functions is smaller than the maximum one on the Brenner's original function, Fig. 4.b, although we do not know how realistic our assumption is for the structure of the MWCNT in Demczyk's et.al. experiment. The places of the maximum force, the tensile strain (6-12%) on the fitted functions are smaller than it is on Brenner's function (30%), as well, because we have shifted  $R_1$  to the place of the minimum energy. For the tensile strain there are experimental results, as well: Yu et. al. measured about 5% on SWCNT ropes and about 10-12% on MWCNT, but we do not know it from Demczyk's et.al. paper. If there will be other or more accurate experimental data for the strain, it could be needed to fit the functions again and maybe to change  $R_1$  and/or  $R_2$ . We notice that there can be smaller changes in the slope on the descending branch of the fitted atomic force curve in several cases (e.g. the dotted line in Fig. 4.b), but this part of the atomic force function and that of any loading diagram is not important in engineering aspect.

In the end we mention that the values of  $R_1$  and  $R_2$  affect the maximum atomic force very strongly. Agrawal et. al. showed differences in the loading

diagram of nanotubes if  $R_1$  is varied between 1.6 and 1.7. In our calculation  $R_1$  equals to the equilibrium atomic distance in unloaded state to avoid the break point on the atomic force curve. The physical mean of a slope-change on the curve is not known.  $R_2$  is the same as Brenner's original value.

For the energetic potential we used the second set of parameters provided by Brenner adopted here as follows:

$$D_e=0.9612\text{nN nm}, S=1.22, \beta=21\text{nm}^{-1}, R=0.139, \delta=0.5, a_0=0.00020813, c_0=330, \\ d_0=3.5, R_1=0.17\text{nm}, R_2=0.2\text{nm}.$$

This set corresponds to the equilibrium bond length  $r_0=0.145\text{nm}$ .

In order to compare our method with other works (see in Table 1), we have calculated the tensile strength of a zigzag (10,0) and an armchair (10,10) tube in the case of the four selected  $(R_T, f_T)$  pairs. In these calculations we have divided the maximum force calculated from the loading process (parallel with the tube axis) by the cross section of the tubes given by  $D\pi t$  where  $D$  is the diameter of the tube and  $t=0.34\text{nm}$  is the interlayer graphite distance. We have found that the tensile strength of the (10,0) tube is 156GPa for all the four  $(R_T, f_T)$  pairs and the corresponding strain is between 5 and 13%, the tensile strength of the (10,10) tube is 178GPa for all the four  $(R_T, f_T)$  pairs and the interval of the corresponding strain is a bit greater than it is for the (10,0) tube. The order of magnitude of these values is the same as more other published results. Our  $\sigma_r$  values are greater than Duan's et. al. and Belytschko's et. al. results where the cut-off function is omitted from the calculations, and smaller than Agrawal's et. al. results where the second generation of the Brenner potential was applied. The tendency that an armchair type tube is stronger than a zigzag type tube is similar in our calculation to the one Duan's et.al. work, where the chirality dependence of nanotubes was studied.

### 3. Calculated results

The aim of this work was to determine the strength properties of carbon nanotube networks. A super-diamond structure consisting of (3,3) nanotubes was selected for our computation. In Figure 5 we can see the 1186 atom initial unit cell of 39.94 Angström. During our calculations we kept periodic boundary condition.

The loading simulation was carried out by elongating the structure in very small steps. After each step we computed the new equilibrium positions of the carbon atoms. We noticed for the equilibrium coordinates that any cut-off functions of our set gave the same result as the original one. Namely the modified cut-off function does not change the minimum place of the energetic potential. In Figure 6 the three snapshots of the simulation show the structure after 28%, 40% and 55% elongation. It can be seen that the structure starts to break at the straight tubes and not at the junctions.

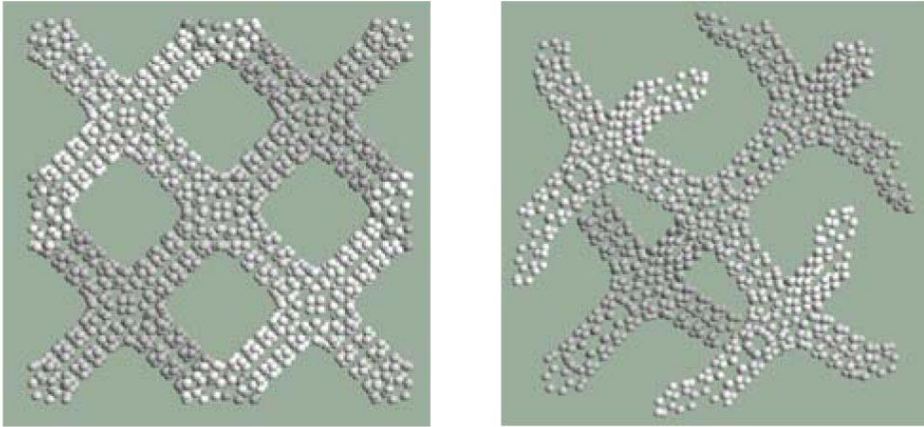


Figure 5. Different views of the unit cell of the selected network

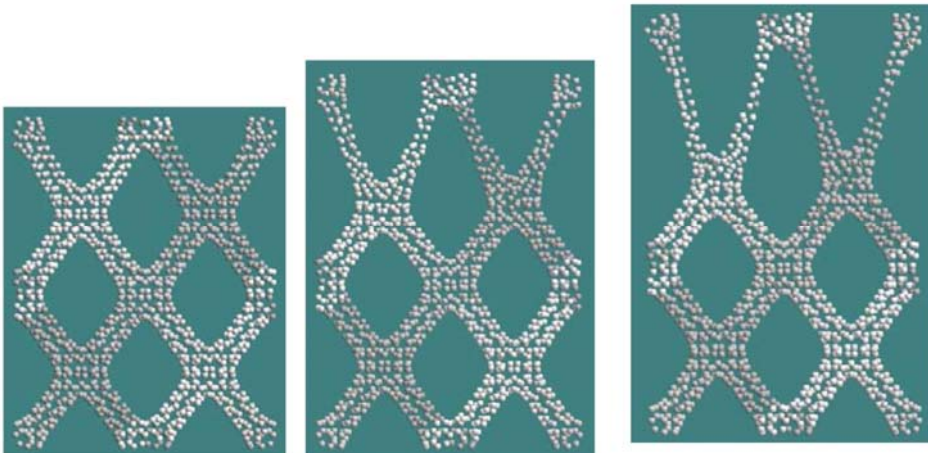


Figure 6. The structure after 28, 40 and 55% elongation

In the end we calculated the loading diagrams using the 4 selected  $(R_T, f_T)$  pairs to compute atomic forces detailed in the Section 1. To determine the tensile strength we divided the maximum force by the cross section of the unit cell. We carried out the computations for two main directions, Fig. 7 b. The loading diagram and the calculated tensile strength for the direction being perpendicular to the faces of the unit cell (Dir. 1) can be seen in Figure 7 a. If the loading direction is parallel with the tube axes (Dir. 2), the value of the tensile strength was a bit smaller: 20.2, 20.7, 21.1 and 21.4 GPa for the selected  $(R_T, f_T)$  pairs of (1.6, 0.656), (1.7, 0.437), (1.8, 0.237), (1.9, 0.080), respectively.

Thus the tensile strength is between 24.3 and 25.1 GPa and the corresponding strain is between 20% and 50% for the direction which is perpendicular to the faces of the unit cell. Similarly, the tensile strength is between 20.2 and 21.4

GPa and the corresponding strain is between 20% and 50% for the direction which is parallel with the tube axes. To sum up the difference in the tensile strength between our network and the single nanotubes is less than one order of magnitude, and we mention beside the above that our example is not the densest network.

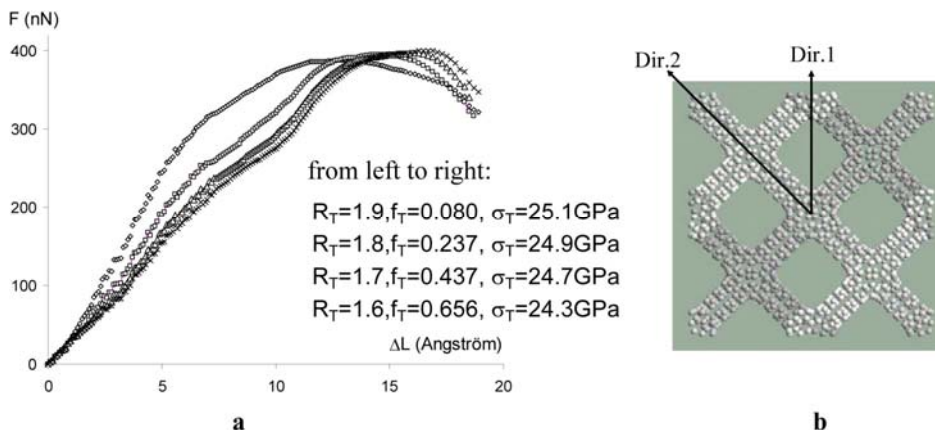


Figure 7. The loading diagrams and the tensile strength (a) for the first loading direction (b)

#### 4. Conclusions

As the cut-off function of our modified Brenner-potential was fitted to experimental loading data it can be applied in a more realistic way in order to compute the loading simulations and characteristic forces of various carbon nanostructures.

Carbon nanotube networks can be the materials which inherit the extremely high strength of the graphite sheet and they bring this property in all directions of the 3D space (not only in 1 direction as the nanotubes).

#### 5. Acknowledgement

This work was supported by OTKA grants K 73776 in Hungary.

#### References

- Demczyk BG, Wang YM, Cumings J, Hetman M, Han W, Zettl A, Ritchie RO. Direct mechanical measurement of the tensile strength and elastic modulus of multiwalled carbon nanotubes. *Mater. Sci. and Eng. A* 2002;334:173-178.
- Coulson CA. *Valence*. Oxford University Press 1952; Oxford

- Kelley BT. *Physics of Graphite*. Applied Science 1981; London
- Polanyi M. *Uber die Natur des Zerreissvorganges*. *Z. Phys.* 1921;7:323-327.
- Orowan E. *Fracture and strength of solids*. *Rep. Prog. Phys.* 1949;12:185-232.
- Yu MF, Lourie O, Dyer MJ, Moloni K, Kelly TE, Ruoff RS. *Strength and breaking mechanism of multiwalled carbon nanotubes under tensile load*. *Science* 2000;287:637-640.
- Yu MF, Files BS, Arepalli S, Ruoff R. *Tensile loading of ropes of single nanotubes and their mechanical properties*. *Phys. Rev. Lett.* 2000;84:5552-5555.
- Fu CX, Chen YF, Jiao JW. *Molecular dynamics simulation of the test of single-walled carbon nanotubes under tensile loading*. *Sci. in China E* 2008;50:7-17.
- Mylvaganam K, Zhang LC. *Important issues in a molecular dynamics simulation for characterising the mechanical properties of carbon nanotubes*. *Carbon* 2004;42:2025-2032.
- Agrawal PM, Sudalayandi BS, Raff LM, Komanduri R. *Molecular dynamic (MD) simulations of the dependence of C-C bond lengths and bond angles on the tensile strain in single-wall carbon nanotubes (SWCNT)*. *Comput. Mater. Sci* 2008;41:450-456.
- Duan WH, Wang Q, Liew KM, He XQ. *Molecular mechanics modelling of carbon nanotube fracture*. *Carbon* 2007;45:1769-1776.
- Belytschko T, Xiao SP, Schatz GC, Ruoff R. *Atomistic simulations of nanotube fracture*. *Phys. Rev. B* 2002;65:235430-1-8.
- Jeng YR, Tsai PC, Fang TH. *Effects of temperature and vacancy defects on tensile deformation of single-walled carbon nanotubes*. *J. of Phys. and Chemistry of Solids*, 2004;65:1849-1856.
- Meo M, Rossi M. *Tensile failure prediction of single wall carbon nanotube*. *Engineering Fracture Mechanics* 2006;73:2589-2599.
- Wu J, Hwang K.C, Huang Y, *An atomistic-based finite-deformation shell theory for single-wall carbon nanotubes*, *Journal of the Mechanics and Physics of Solids*, 2008;56(1):279-292.
- Yao Z, Postma HWCh, Balents L, Dekker C. *Carbon nanotube intramolecular junctions*. *Nature* 1999;402:273-276.
- Bandaru PR, Daraio C, Jin S, Rao AM. *Novel electrical switching behaviour and logic in carbon nanotube Y junctions*. *Nature Materials* 2005;4:663-666.
- Zsoldos I, Kakuk G, Reti T, Szasz A. *Geometric construction of carbon nanotube junctions*. *Modelling Simul. Mater. Sci. Eng.* 2004;12:1-16.
- Laszlo I. *Construction of atomic arrangement for carbon nanotube junctions*. *Phys. Stat. Sol.* 2007;244:4265-4268.

- Ting JM, Li TP, Chang CC. Carbon nanotubes with 2D and 3D multiple junctions. *Carbon* 2004;42:2997-3002.
- Romo-Herrera JM, Terrones M, Terrones H, Dag S, Meunier V. Covalent 2D and 3D networks from 1D nanostructures: Designing new materials. *Nanoletters* 2007;7:570-576.
- Graner G. Carbon nanonets spark new electronics. *Scientific American* 2007;5:58-65.
- Coluci VR, Dantas SO, Jorio A, Galvao DS. Mechanical properties of carbon nanotube networks by molecular mechanics and impact molecular dynamics calculation. *Phys. Rev. B* 2007;75:075417-1-7.
- Coluci VR, Galvao DS, Jorio A. Geometric and electronic structure of carbon nanotube networks: 'super'-carbon nanotubes. *Nanotechnology* 2006;17:617-621.
- Brenner DW. Empirical potential for hydrocarbons for use in simulating the chemical vapor deposition of diamond films. *Phys. Rev. B* 1990;42:9458-9471,.
- Brenner DW, Shenderova OA, Harrison JA, Stuart SJ, Ni B, Sinnott SB. A second- generation reactive empirical bond order (REBO) potential energy expression for hydrocarbons. *J.of Phys.* 2002;14:783-802.
- Shenderova OA, Brenner DW, Omeltchenko A, Su X, Yang LH. Atomistic modeling of the polycrystalline diamond. *Phys. Rev. B* 2000;61:3877-3888.
- Yakobson BI, Samsonidze G, Samsonidze GG. Atomistic theory of mechanical relaxation in fullerene nanotubes. *Carbon* 2000;38:1675-1680.

# **Abrasive Wear of Different Polymer/Steel Gear Pairs**

Gábor KALÁCSKA

Szent Istvan University, Faculty of Mechanical Engineering

Ottó EBERST, Sever POP

North University of Baia Mare, Faculty of Engineering

Patrick DE BAETS

University Gent, Department of Mechanical Construction and Production

## **Abstract**

Research was performed on the friction, wear and efficiency of plastic gears made of modern engineering polymers and their composites both in a clean environment (adhesive sliding surfaces) and in an environment contaminated with solid particles and dust (abrasive), with no lubrication at all. The purpose is to give a general view about the results of abrasive wear tests including seven soil types as abrasive media. At the first stage of the research silicious sand was applied between the meshing gears and the wear of plastic and steel gears was evaluated and analyzed from the point of different material properties (elongation at break, hardness, yield stress, modulus of elasticity) and its combinations. The different correlations between the experienced wear and material features are also introduced. At the second stage of the project the abrasive sand was replaced with different physical soil types. The abrasive wear of gears is plotted in the function of soil types. The results highlight on the considerable role of physical soil types on abrasive wear resistance and the conclusions contain the detailed wear resistance. The results offer a new tribology database for the operation and maintenance of agricultural machines with the opportunity of a better material selection according to the dominant soil type. This can finally result longer lifetime and higher reliability of wearing plastic/steel parts.

## **Keywords**

agricultural machines, gears, tribology, abrasive wear

## **1. Introduction**

In the agriculture the plastics are well-known. From the sixties polymers are considered to be up-to-date materials regarding light weight, corrosion resistance, easy to machine and install. At early stages plastics were used mainly as foil houses, tubes, water distribution and pipe units. The main focus went on PS, PVC and PP materials (Edmister 1966) (Szabó 1974) (Placz 1978) (Horánszky 1979).

A decade later with arising engineering polymers a new field of applications was invented. Parts of some agricultural implements for hard agricultural conditions can be made of some plastic types. The loading capacity and adhesive and abrasive wear resistance became more and more important (Vámos 1983). The seventies and eighties were addressed to the gradual development of polymer machine elements in agricultural machines. The main focus went with different polyamide types: PA 6, PA 11, PA 12 (Kragelszkij V. 1987) (Antal M. 1989) (Yamaguchi I. 1990).

Gears are essential parts of machines from the point of view of dynamics and engineering. The research program dealt with key effects of further drive developments: the macro- mezo- and micro-surface tribological phenomena of gear mesh. These are essential to be known for the reliable operation of the machines. Friction and wear are critical from the point of efficiency and lifetime of gear units. Till the end of nineties in the literature there were no general information about plastic/steel gear mesh, even no tribological information about new engineering polymer and composite gears. The research team started to clarify the mentioned lack of engineering knowledge and this article is focused on the abrasive wear.

Concerning our global tribological approach to the topic the right place of abrasive testing is shown in *Table 2*. Among many other test categories the abrasive research of model gears means only one category in system theory. Some of our earlier results were published in several articles (Kalácska 2001, 2002, Zsidai 2002, 2003, DeBaets 2002, 2004).

### *Objective*

Breakdowns of agricultural machines frequently occur because of the abrasion due to soil, sand and other mineral-based small and very hard particles acting on the working surfaces. Abrasion occurs if the contacting interface between two surfaces has interlocking of an inclined or curved contact, ploughing takes place in sliding. As a result of ploughing, a certain volume of surface material is removed and an abrasive groove is formed on the weaker surface (*Figure 1*). This type of wear is called abrasion (Bushan 2001).

Soil as an abrasive media means a large category. From the point of caused wear on working surfaces the physical soil types are essential and have to be clarified (Barczy 1997, 2003, 2005). According to the recommendations seven different physical soil types were selected (Birkás 2006, Prokisch 2007) as abrasive media for further laboratory wear tests. The whole soil abrasive media project with polymer/steel gear pairs was built on reference measurements conducted with sand test gears.

Steps of the research, where the main focus is the abrasive wear, was as follows:

- reference sand test with different polymer/steel gear pairs
- abrasive measurements with seven soil types and different polymer/steel gear pairs
- comparison of wear results between the test systems

- comparison of wear resistance of polymer/steel gear pairs in the function of soil types
- recommendations for material selection for design and reconstruction during maintenance knowing the dominant working conditions, the given soil type as essential abrasive media

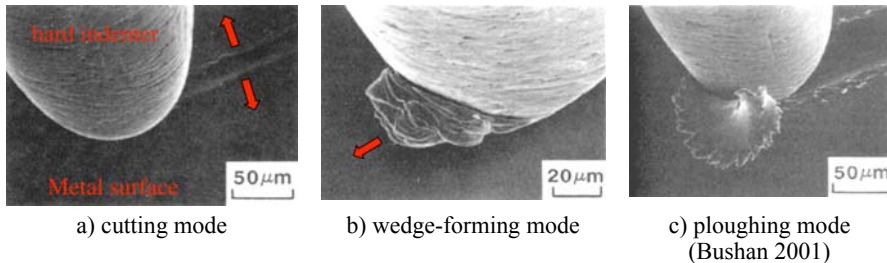


Figure 1. Three different modes of abrasive wear of metal observed by Scanning Electron Microscope (Bushan: Modern Tribology Handbook)

### Working conditions in field

At first the real operation of the dominant wear mechanism of sliding polymer/steel surfaces, e.g. gears and slide bearings of harvesters had to be clarified. Formerly extensive studies were done in this field during the development of ply-wood bearings of John Deere, New Holland and Claas harvester machines in the eighties and nineties (Beer 1995, Pellényi 1997). One of the main conclusions was that beside the surface stochastic fatigue process the ratio between adhesive and abrasive wear mechanism varies in the function of the dust distribution (depending on the height above the ground level (Figure 2)). Other output of the studies was that abrasive effect is dominant beside the adhesion and fatigue regarding the quick and aggressive surface deterioration, thus, abrasive wear process had to be clarified and optimized in the wear system.

Typical harvesters (Figure 2) have many plastic/steel gear pairs in the new constructions that really urge the detailed knowledge of different polymer/steel gear wear under different urgent conditions. Beside gear applications in agricultural machines the increasing role of moving and wearing plastic elements were emphasized by Szendrő et al (2005) and Tiba (2006).

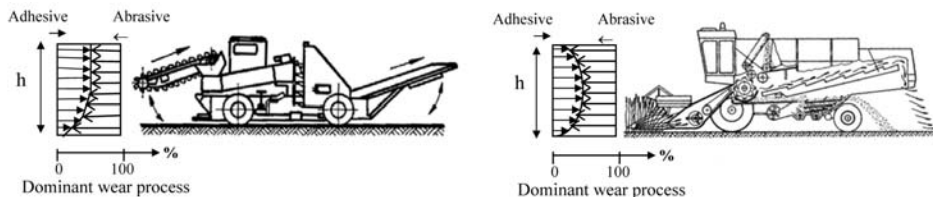


Figure 2. Ratio between adhesive and abrasive effects in the function of dust distribution (height above ground level)

## 2. Materials and Methods

### *Tested involute spur gears*

Only generally available plastics have been used for manufacturing the tested spur-gears and other test specimens. These plastics are widely known all over the world: on the basis of sale records of semi-finished plastic products (rods, tubes, plates, etc.) in the Central European region and according to reports of buyers it is supposed that approximately 90 % of industrial plastics used for manufacturing polymer gears have been selected. For the measurement of machine elements gears were manufactured with the Fellow's machining technology (*Figure 3*). The material of the driven gear was made of S355 steel, the quality of the tooth surface in its initial condition was Ra 2.5  $\mu\text{m}$ . Further data: drive ratio 1:1, module  $m = 1,25$  mm, pitch diameter  $D = 45$  mm, number of teeth  $z = 36$ , load carrying tooth width  $b = 16$  mm.



*Figure 3.* Gears (according to Fellow's technology) with the reference abrasive media (siliceous sand)

The following polymers (*Figure*) were used for the reference measurements:

- PA 6G Na: cast polyamide 6 (PA6G), Na catalytic
- PA6 Mg: cast polyamide 6 (PA6G), Mg catalytic
- PETP TX: PETP/PTFE composite
- GF30: extruded polyamide 66 composite with 30% glass fibre reinforcement
- POM-C: polyoximethylene co-polymer.

The main technical properties of the polymers are listed in *Table 1*, based on catalogues supplied by the manufacturers (Quattroplast, 2007):

*Table 1.* Material properties

Polymers	Elongation at break (%)	Modulus of elasticity, E (MPa)	Hardness, HR M	Yield stress, (MPa)	(H/E)x10 ratio
PA6-Mg	40	3000	86	85	0,287
Pa6-Na	25	3300	88	80	0,277
PA66GF-30	7	5200	98	185	0,188
POM-C	30	3000	86	70	0,287
PETP TX	8	3200	94	75	0,294

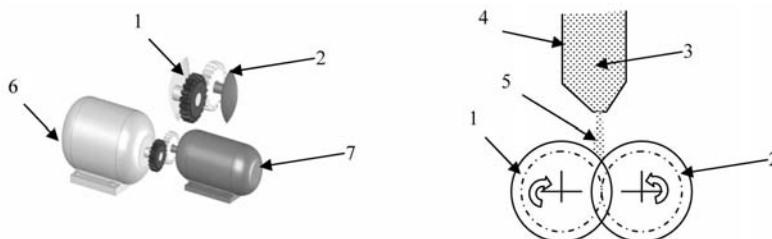
### *Test system and conditions*

Among the applied test systems shown in table 2. the abrasive measurements are highlighted. The system approach of a certain tribological problem was studied 20 years ago (Czichos H. 1987) (Valasek I. 2002) in accordance with the DIN 50320 standard. Furthermore the DIN 50322 specified the wear test categories that can be a good base to classify our test categories, too. These testing categories are shown in *Table 2*.

Conditions of the abrasive gear tests:

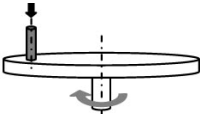
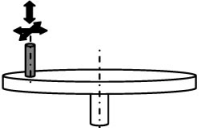
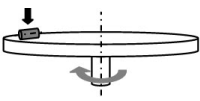
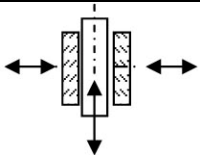
- abrasive media: siliceous sand (*Figure 3*) for reference tests and selected soil types
- particle size: < 200  $\mu\text{m}$  (two times screening, with first and second screening the gap clearance was 500  $\mu\text{m}$  and 200  $\mu\text{m}$ , respectively)
- operational time in abrasive test: 60 minutes/gear pair
- temperature: + 22 °C
- for each measurement a new steel gear was used
- the sand could flow out from the sand holder via the outlet port with diameter  $\text{\O}1,5$  mm at central position above the rotating gears (flow-speed 10 ml/min)
- the classified sand was used only once for measurements and the detached polymer and metal particles were observed after the test
- at the beginning of the test a ten minute long running-in period was applied without abrasive particles, this was followed by 60 minutes normal operational test
- gear weight was determined by „Balanta Sibiu” analytic balance, with 0,1 mg accuracy
- multi-teeth measure was executed by a gear tooth micrometer with 0,01 mm accuracy
- siliceous sand having plastic and steel particles was observed by a „Zeiss Amplival Universal” microscope (magnification 40), teeth surfaces by a „Zeiss Binocular” microscope (magnification 5)
- after the measurements the abrasive medium was mixed with glycerol and placed onto the glass of the microscope for the evaluation.

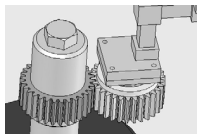
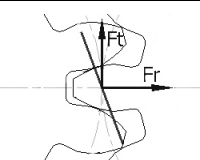
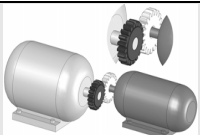
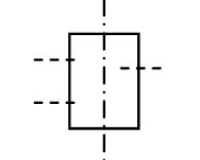
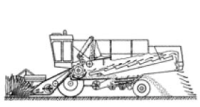
According to the internationally accepted method the controlled even flow of abrasive media contaminates the mating gear teeth surfaces. During the test period a preliminary set speed and torque is transmitted. The weight of the gears is measured before and after the wear tests. *Figure 4* shows the scheme of abrasive gear test method.



*Figure. 4.* Gear test in abrasive flow 1- polymer driving gear, 2- driven steel gear, 3- sand as abrasive media, 4- hopper, 5- sand flow, 6- driving motor, 7- braking motor

Table 1. Test systems

DIN 50322 test category	Correlation to the working gears	Definition	Characteristics	Model	Environment Clean (Adhesive)	Environment Abrasive	Remark
VI.	•	Static pin-on-disc	<ul style="list-style-type: none"> <li>• Polymer pin, rotating steel disc</li> <li>• Static and constant load, speed and ambient temperature</li> <li>• Friction and wear</li> </ul>		X	-	<ul style="list-style-type: none"> <li>• Small-scale measurements</li> <li>• <b>Carried out</b></li> </ul>
VI.	•	Dynamic pin-on-plate	<ul style="list-style-type: none"> <li>• Polymer pin, steel plate</li> <li>• Dynamic load, speed</li> <li>• Friction, wear and improved deformation effect</li> </ul>		X	-	<ul style="list-style-type: none"> <li>• Small-scale measurements</li> <li>• <b>Carried out</b></li> </ul>
VI.	•	Cylinder-on-disc	<ul style="list-style-type: none"> <li>• Polymer cylinder, rotating steel disc</li> <li>• Static and constant load, speed and ambient temperature</li> <li>• Friction and wear</li> </ul>		X	X	<ul style="list-style-type: none"> <li>• Small-scale measurements</li> <li>• Counterformal contact approaching teeth connection</li> <li>• <b>Carried out</b></li> </ul>
V.	•	Plate-on-plate	<ul style="list-style-type: none"> <li>• Dynamic</li> <li>• Overload behaviour</li> <li>• Role of dimensions (stress distribution, edge effects, heat partition and conductivity ...etc.)</li> </ul>		X	-	<ul style="list-style-type: none"> <li>• Large-scale measurements</li> <li>• Effects of edges, size and heat conductivity</li> <li>• <b>Carried out</b></li> </ul>

IV.	●	Gear-gear	<ul style="list-style-type: none"> <li>• Friction tests,</li> <li>• Real gears, polymer-steel pairs</li> <li>• Constant torque, low load level, low speed regime</li> <li>• Combination of rolling-sliding contact</li> </ul>		X	-	<ul style="list-style-type: none"> <li>• Efficiency, friction energy loss</li> <li>• <b>Carried out</b></li> </ul>
IV.	●	Teeth-pairs	<ul style="list-style-type: none"> <li>• Friction tests,</li> <li>• Real teeth, polymer-steel pairs</li> <li>• Friction control on the connection line</li> </ul>		X	-	<ul style="list-style-type: none"> <li>• Model of the dynamic friction phenomena on the teeth surfaces</li> <li>• Clarified dynamic friction on teeth surface</li> <li>• <b>Carried out</b></li> </ul>
III.	●	Gear-drive test	<ul style="list-style-type: none"> <li>• Wear tests</li> <li>• Polymer - steel gear pairs</li> <li>• Highly loaded drive, constant torque</li> <li>• High speed</li> </ul>		X	X	<ul style="list-style-type: none"> <li>• Wear resistance</li> <li>• Wear in the function of material properties</li> <li>• <b>Carried out</b></li> </ul>
II.	●	Epicyclical gear	<ul style="list-style-type: none"> <li>• Real construction with polymer – steel gears</li> <li>• „Closed box” test</li> <li>• Dry and oil lubricated drive tests</li> <li>• High load</li> </ul>		X	X	<ul style="list-style-type: none"> <li>• Friction losses,</li> <li>• Efficiency</li> <li>• <b>In progress</b></li> </ul>
I. /theoretical target of modelling/	●	Harvester cutting board, polymer gear drive	<ul style="list-style-type: none"> <li>• Running field test</li> <li>• Wear control of original constructions</li> </ul>			X	<ul style="list-style-type: none"> <li>• Dynamic effects</li> <li>• Wear in abrasive environment</li> <li>• Changing abrasive condition</li> <li>• <b>In progress</b></li> </ul>

The maximum allowed output to be transmitted by polymer spur-gears according to the Lewis formula (DeBruyne 1999 and Eberst 2005):

$$P = \frac{m \cdot y \cdot b \cdot d \cdot n \cdot f_1 \cdot f_2 \cdot \sigma}{6 \cdot 10^6} \quad [\text{kW}] \quad (1)$$

where:

m = module, mm

y = tooth form factor

b = load carrying tooth width, mm

d = pitch circle diameter, mm = m · z

z = number of teeth

n = speed, rpm

$f_1$  = speed factor =  $\frac{0,75}{1 + v} + 0,25$

v = circumferential speed of the gear at the pitch circle, m/s

$\sigma$  = allowable stress on the root of the tooth, N/mm<sup>2</sup>

$f_2$  = operating conditions factor

Under conditions set for the experiment 830 watt output was transmitted, which means a slight overload from the point of mechanical load carrying capacity of each selected polymer gear. Practical experiences proved that the mechanical overload acts on the surfaces causing increased wear. The slight mechanical overload with increasing wear perform region III. in *Figure 5*. In the tribology literature that region is called transition between moderate (II. and IV. in *Figure 5*) and severe wear.

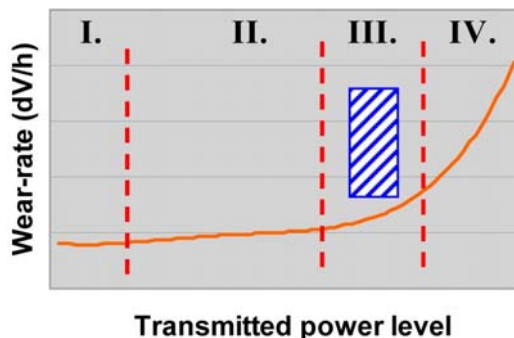


*Figure 5.* Theoretical approach to the overload regime (III.) of the tests

### *Soils for the tests*

The sites for taking soil samples were chosen according to the basic principles of soil mapping. The soil sampling was carried out with the Pürckhauer auger technique. The Pürckhauer auger is a steel tube, 1 m in length, its diameter is

between 1 and 3 cm, half or a third of the length of which is open, with a solid steel head at one end, with a hole drilled. The auger is driven into the soil by a plastic hammer and after a few rotations it is pulled out of the soil, containing a soil profile. The auger is made of a very strong and resilient alloy and its hardness makes it easy to take samples from very compact or heavy clayey soils or soils containing stones. Another benefit of the technique is that it enables studies of soil type, thickness of layers, colour, physical type, carbonate, pH value and moisture without excessively disturbing soil structures, and it has proven to be suitable for roughly distinguishing and separating soil patches. The description of the auger and the identification of the soil types are based on the work of Stefanovits (1999) and Szodfridt (1994). After the profile description, disturbed soil samples were taken from the designated layer.

The selected and tested soils used as abrasive material can be seen in *Table 3*.

*Table 3. Selected soils*

Nr.	Soil type	colour	Texture (symbol)	CaCO <sub>3</sub>
1.	wind-blown sandy soil	sand yellow	sand (H)	+
2.	humic sand soil	light brown	loamy sand (HV)	+
3.	brown soil, Ramann-type brown forest soil	rust-brown	loamy sand (AH)	0
4.	lime coated chernozem	brown, mixed, increasingly light in colour	loam (V)	++
5.	chernozem-brown forest soil	light brown	Loamy (AV)	+++
6.	erubase soil	black	Loam (A)	0
7.	gravelly skeletal soil	yellowish -reddish	small pebble, sand (KH)	+

### 3. Results and Discussion

#### *Abrasive wear with silicious sand*

Wear volume in mass was measured and expressed in % comparing to the original mass of the gear teeth mass. The plotted wear volumes are averaged from five different test runs.

Under abrasive conditions the trend of wear resistance of polymer gear materials is shown in *Figure 6*. Apart from favourable values obtained by cast polyamide 6 materials, the PETP/PTFE composite also showed good durability in the tested system. Relative high wear was experienced at the POM-C and the reinforced polyamide 66. In comparison to plastic gears, the wear on steel gears running in pair with the polyamide ones shows a reverse trend. Increasing wear on plastics is causing a slight decrease in wear on steel, with the exception of the cast polyamide 6 with Mg catalyst. Specifications of materials can explain these phenomena only partially, since higher plasticity causes higher embedding

capacity on the plastic surface, which increases abrasion on the metal surface. It is interesting to note, that in the clean (adhesion) tests the highest wear on steel gears was generated by the reinforced polyamide 66 material (Pa 66 GF30). However, in abrasion tests the lowest level of wear on steel gears was measured with using the same material (PA 66 GF30).

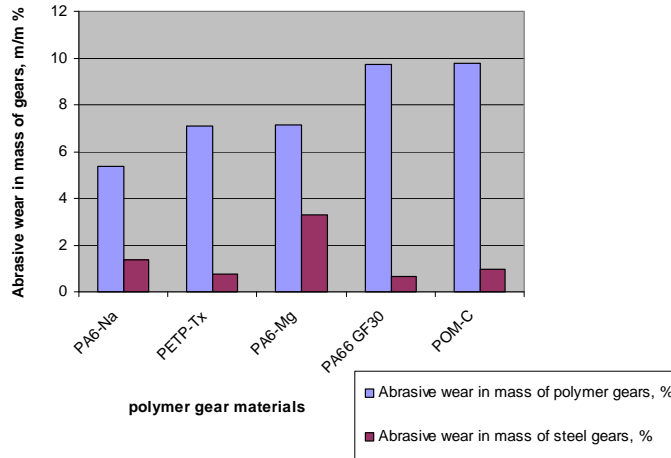


Figure 6. Abrasive wear in mass of polymer and mating steel gears, %  $t=60$  minutes,  $n=1330$  1/min,  $M=6.1$  Nm, abrasive material: siliceous sand,  $T=22^{\circ}\text{C}$

*Effects of the elongation at break of polymer materials on the abrasive wear behaviour of plastic gears.*

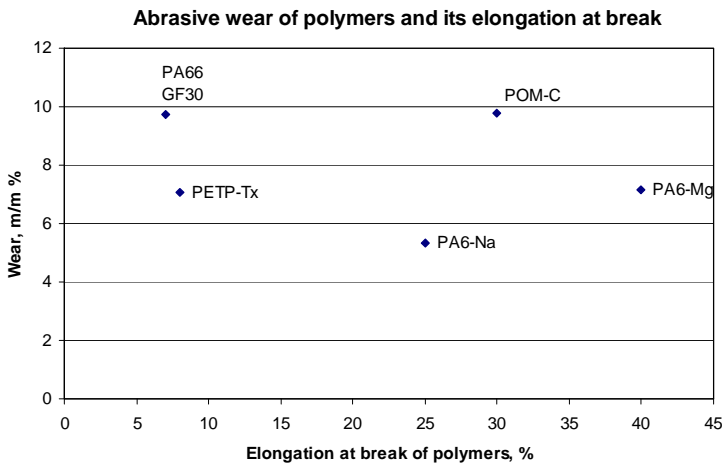


Figure 7. Abrasive wear in mass (%) of polymer gears in the function of the elongation at break of polymer materials, ( $A$ , %),  $t=60$  minutes,  $n=1330$  1/min,  $M=6.1$  Nm, abrasive material: siliceous sand,  $T=22^{\circ}\text{C}$

There is a loose link between elongation at break of engineering plastics and abrasive wear on plastic gears, with the exception of „POM-C” and „Pa 66 GF30” (fig.7.). It is obvious that glass fibre content strongly reduces the elongation of PA 66, and in case of POM-C the co-polymer molecular chain structure differs from the other materials. Regardless PA 66 GF30 and POM-C a linear correlation with negative gradient could be plotted for PETP-TX, PA 6-Na and PA6-Mg. That means materials with lower elongation at break - more rigid materials - suffered a bit higher abrasive wear.

*Effects of the modulus of elasticity of polymer materials on the abrasive wear behaviour of plastic gears.*

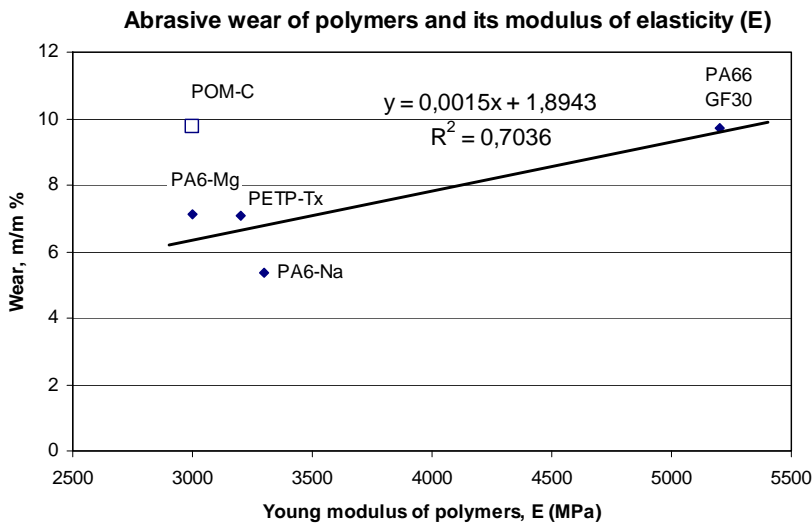


Figure 8. Abrasive wear in mass (%) of polymer gears in the function of the modulus of elasticity of polymer materials, (E, MPa), t=60 minutes, n= 1330 1/min, M= 6.1 Nm, abrasive material: siliceous sand, T= 22°C

In the tested system linear correlation can be drawn between abrasive wear of polymer gears and E modulus of the materials. The only exception is POM-C with co-polymer structure. The increasing modulus of elasticity slightly increased the abrasive wear. (fig. 8).

*Effects of the hardness of polymer materials on the abrasive wear behaviour of plastic gears.*

The comparison of surface hardness of polymer gears with abrasion wear results indicates that the increasing hardness increased the wear, too, instead of trends accepted generally for steels. (fig. 9.). POM-C is also exception and not comparable directly with the other homo-polymers.

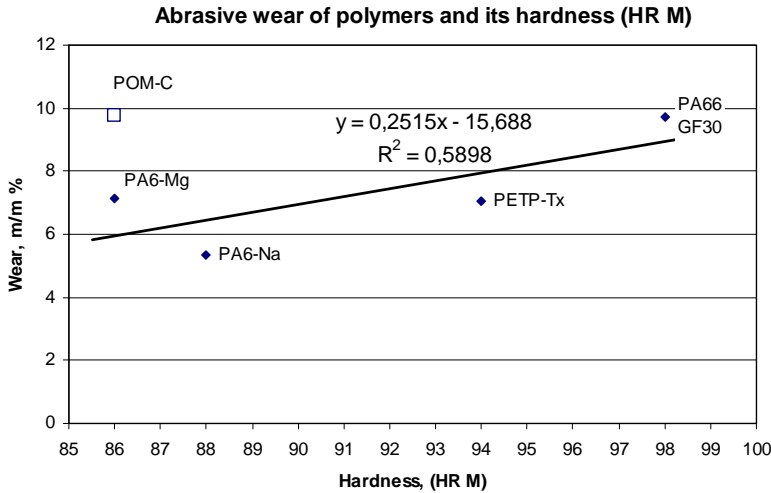


Figure.9. Wear in mass (%) of polymer gears in the function of the hardness of polymer materials (HRM) t=60 minutes, n= 1330 1/min, M= 6.1 Nm, siliceous sand abrasive, T= 22°C

*Effects of the yield stress of polymer materials on the abrasive wear behaviour of plastic gears.*

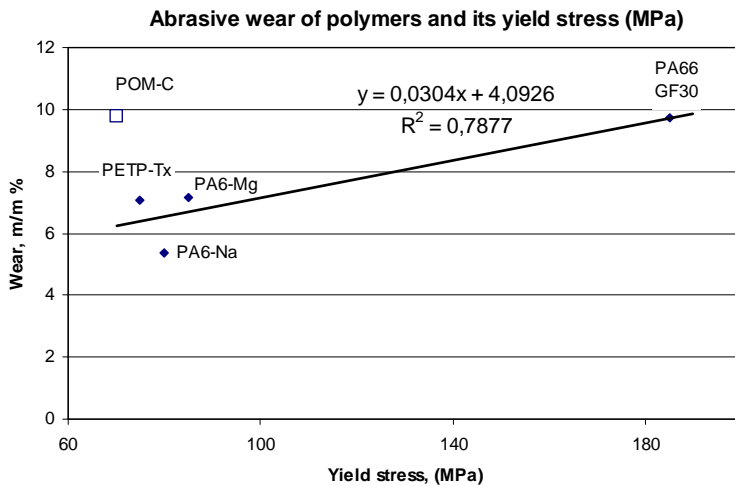


Figure.10. Wear in mass (%) of polymer gears in the function of the yield stress of polymer materials (Re) t=60 minutes, n= 1330 1/min, M= 6.1 Nm, siliceous sand abrasive, T= 22°C

Regarding the yield stress of materials and the measured wear similar behaviour to hardness can be stated. Increasing yield stress slightly increased the wear, too. POM-C is also exception and not comparable directly with the other homo-polymers. (fig.10.). It is important to emphasize the range of yield stress

in our case because very low stress values result no real abrasion resistance (common plastics like PVC, PP) proved by engineering practice.

The „ $K=(Re \times HR) / (E \times A)$ ” factor of polymer materials on the abrasive wear behaviour of plastic gears.

Among the possible combinations of material properties the "K" material factor of polymers with no dimension can be expressed. The experienced abrasive wear can be evaluated with K values, too. (fig.11.)

$$K = \frac{[Yield\ stress(MPa)] \cdot [Hardness, HRM]}{[Modulus\ of\ elasticity, E(MPa)] \cdot [Elongation\ at\ break, A]} \quad (2)$$

Results of the tested system indicate (Fig. 11.) that, with regard to the described abrasion of polymer-steel pairs of gears, the wear of polymer gears is in linear correlation with the "K" factor calculated from the specifications of the material in question and showing relatively good R<sup>2</sup>. Higher "K" factors cause slight increase in the abrasion wear on polymers. POM-C was found to be exception, which could not be treated as other polyamides (PA) or polyethylene-terephthalate (PETP), as indicated by the previous figures as well. Despite its relatively low "K" factor, POM-C caused unfavourable abrasion wear.

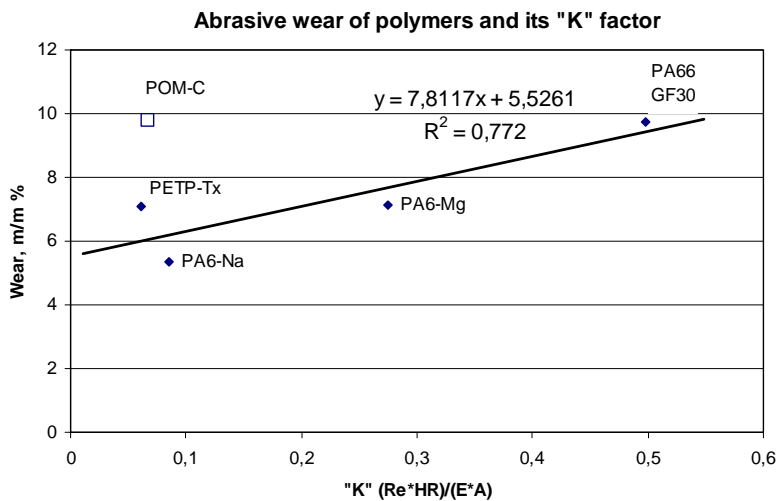


Figure.11. Abrasive wear in mass (%) of polymer gears in the function of "K=(Re\*HR)/(E\*A)" material factor t=60 minutes, n= 1330 1/min, M= 6.1 Nm, siliceous sand abrasive, T= 22°C

*Wear evaluation from the point of H/E ratio of polymers*

H/E ratio expresses the opposite trend to “K” factor H/E is often used features in tribology to evaluate the wear or friction. Linear regression with negative

gradient is shown in *fig.12*. Increasing H/E ratio decreases the abrasive wear. POM-C is exception again.

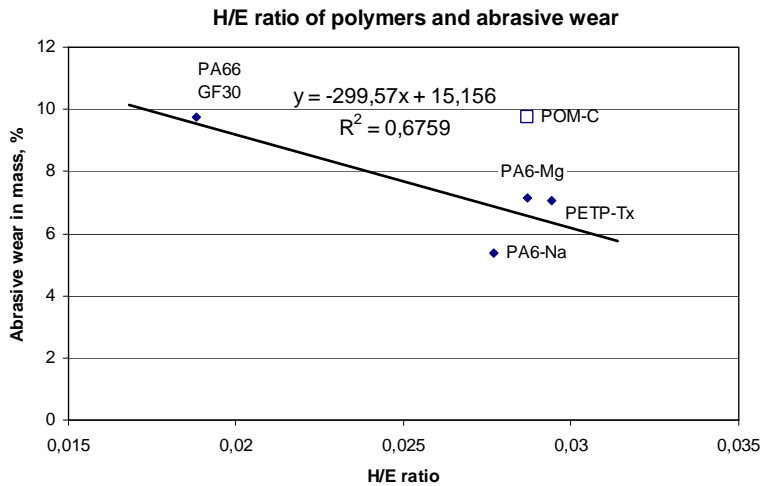


Figure.12. Abrasive wear in mass (%) of polymer gears in the function of H/E ratio  
 t=60 minutes, n= 1330 1/min, M= 6.1 Nm, siliceous sand abrasive, T= 22°C

Concerning the brief summary in *table 4*. we can see that some of the material properties showed connection (linear regression) with the measured wear. In each case the POM-C was not comparable as co-polymer to the behaviour of homo-polymers. Ranking the correlations to the wear the yield stress was found the best (*table 4*).

Table 4. Evaluation of correlations

Correlation to:	Abrasive wear of polymer gears
Elongation at break of polymers	1
Modulus of elasticity of polymers	2
Hardness of polymer	2
Yield stress of polymers	3
"K=(Re*HR)/(E*A)" material factor	3
H/E ratio	2

0: no clear correlation found, 1: weak connection, difficult to state a function,  
 2: acceptable correlation, 3: Clear trend, easy to describe the connection

*Results of abrasive wear tests with different soils*

Figures 13 to 16 show the measured wear loss of the polymer gear teeth mass under different soil abrasive materials. The columns show the difference after 1 and 2 hour operation. Additional engineering polymers were involved at this stage of the project into the measurements to study the role of the reinforcing materials, as follows:

- PA 6 GOL: cast polyamide 6, oil filled composite version
- PETP: natural PETP
- PA 66E: extruded natural PA 66
- PA 6 Mo: cast polyamide 6, filled with MoS<sub>2</sub>

Therefore the effect of oil and MoS<sub>2</sub> in cast PA 6 and the effect of PTFE in PETP base can be studied.

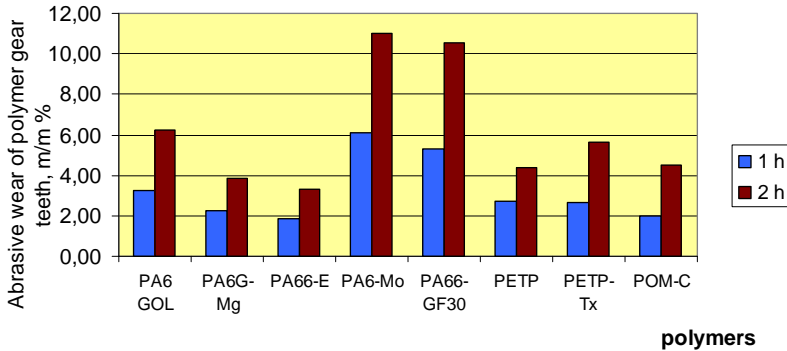


Figure 13. Abrasive wear of polymer gear teeth in mass%, with loamy sand (AH) abrasive material, after 1 h and 2 h operation

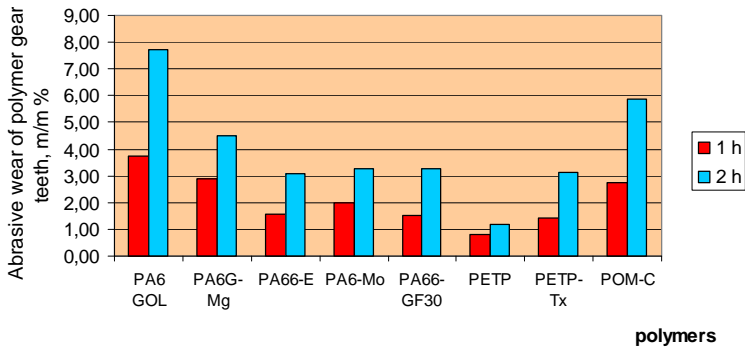


Figure 14. Abrasive wear of polymer gear teeth in mass%, with loamy sand (AV) abrasive material, after 1 h and 2 h running

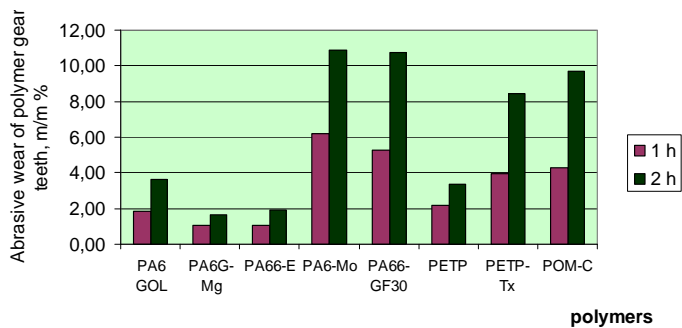


Figure 15. Abrasive wear of polymer gear teeth in mass%, with sand with small pebbles (KH), after 1 h and 2 h running

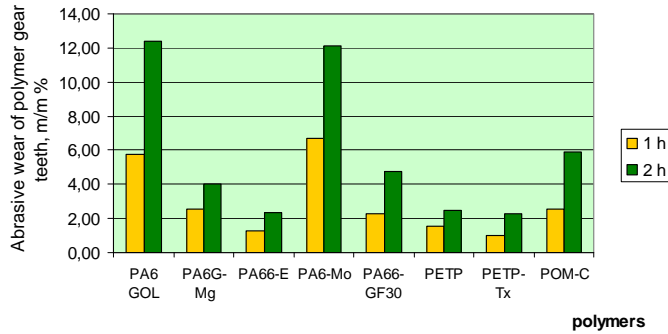
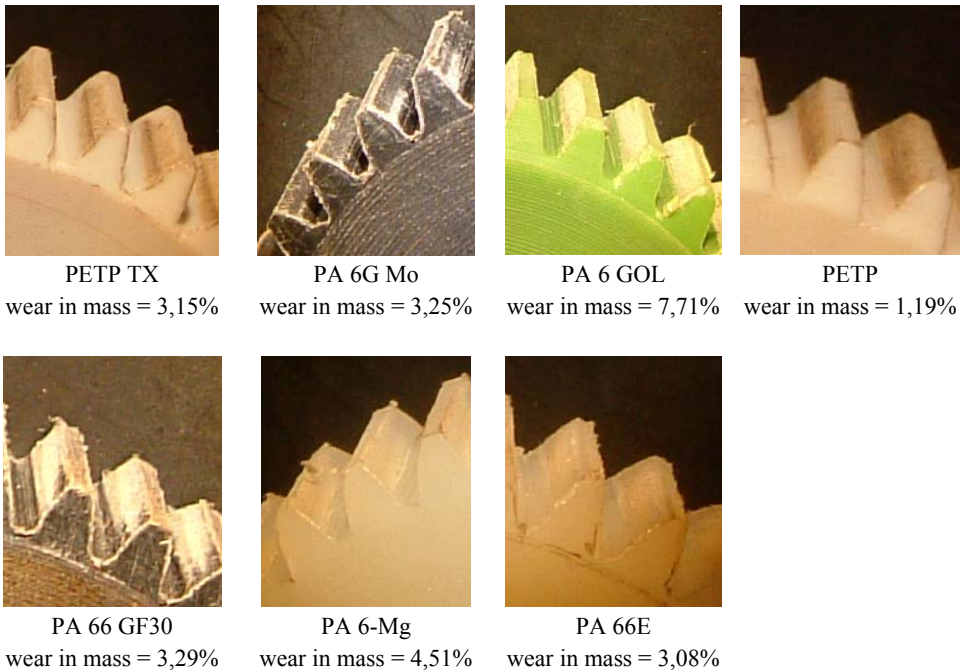


Figure 16. Abrasive wear of polymer gear teeth in mass%, with loam (A) abrasive material, after 1 h and 2 h running

Table 5. shows the worn surfaces after 2 hours running in case of loamy abrasive material(AV)

Table 5. The worn gear teeth surfaces with loamy abrasive material



#### 4. Conclusions

The abrasive role of soil particles can establish a new maintenance strategy due to specific wear-resistance ranking of structural materials in the function of

dominant soil types. The local soil features can be taken into account for material selection during machine repair. At present research the sand (H) and loam (A) caused very high wear values (10 – 12% ) with certain polymers, but regarding an average behaviour loamy sand (VH) and small pebble sand resulted high wear. Among the polymers extreme wear values (low and high wear loss, 2% and 12%) were found with sand (H) and loam (A). The most even wear was experienced with loamy (AV) media. The magnesium catalytic cast polyamide 6 (PA 6 G Mg) as strategic engineering polymer for agricultural machines performed quite well comparing to the composites and PETP versions. The low wear volumes of PA 6-Mg highlights the role of mechanical properties of engineering polymers especially toughness and strain ability of the materials have to be examined in the future.

- Laboratory testing with siliceous sand gives rough estimation of abrasive wear resistance comparing to the rank with a certain soil type.
- The real abrasive wear resistance in a geographical region can be determined according to the soil type (abrasive media).
- Polyamide 6 materials provided large spread according to the reinforcing materials. Comparing to the natural version the composites with internal oil and MoS<sub>2</sub> resulted weaker wear resistance. The internal oil lubrication version of polyamides was found the worst.
- Regarding PETP and PETP/PTFE composite material, the natural PETP performed better. The PTFE particles in the base material matrix reduced the abrasion resistance.
- Comparing the natural and glass fibre reinforced PA 66 it can be stated that the glass fibre content strongly reduced the abrasion resistance of the material.
- Natural polyamide 6 is better in abrasive systems than POM C, which is preferred material in clean environments and for machining purposes.

Finally the experienced abrasive wear resistance ranking put into the *table 6*. Ranking is shown in lines for a certain polymer material against different abrasive media. The lowest value „1” means the first position having lowest wear with a certain abrasive media. The highest ranking value „8” means the top wear with a certain abrasive media. The last column of *table 6* expresses the average ranking for a given polymer taking the 8 abrasive media into account.

The statements of this article are based on a normal and moderate overload running of gear pairs as it was shown in „2.2. Test system and conditions”. It is important to note that in case of gear drives running under the risk of stochastic overload, guidelines of material selection may change. The behaviour of materials under overload can be mapped out with experiments conducted on test bench. As far as safety is concerned, it is important to know whether a polymer gear will be deformed with higher wear, will be smeared or will break rigidly under overload.

Also important to highlight that the functions between material properties and the experienced abrasive wear are valid within the testing range of our selected engineering polymer properties and can not be converted directly to the commodity plastics family having totally different material properties and structures.

Table 6: relative ranking of wear resistance

Polymers	Siliceous sand	Soil types (symbol)							Average score
		V	AH	Small pebble, sand (KH)	Sand (H)	Loamy (AV)	Loamy sand (VH)	Loam (A)	
PA6-Na	1	-	-	-	-	-	-	-	
PETP	-	1	4	3	4	1	1	3	2
PETP TX	2	8	5	5	5	3	2	1	4,14
PA6-Mg	3	5	2	2	6	6	3	4	4
PA6 GOL	-	6	6	4	7	8	5	8	6,28
PA6 Mo	-	4	8	8	3	4	7	7	5,8
PA 66E	-	3	1	1	2	2	4	2	2,14
PA 66 GF30	4	7	7	7	8	5	8	5	6,71
POM-C	5	2	3	6	1	7	6	6	4,42

1: lowest abrasive wear of polymer gear (best wear resistance)

8: highest abrasive wear of polymer gear (worst wear resistance)

## 5. Acknowledgement

The project was supported by Hungarian (OTKA, OMFB Tét), Belgian and Romanian research funds. Special thanks to the member of the research team for their hard work (research team: O.Eberst, M. Kozma, L. Zsidai, P. DeBaets, W. Ost, R. Cotetiu, R. Keresztes, S. Pop, R. Lefánti, L. Szabó, G. Gódor, M. Andó)

## Reference

- Edmister T- Fouss I. (1966): Drainage with plastic materials in the United States. *Materia Plastica ed Elastomeri*. 32./3)
- Szabó A. (1974): Soil improvement with polymer foams (in Hungarian). *Mezőgazdasági Technika*. 3.
- Placz Gy. (1978): Polymer products of TVK for the agriculture . (in Hungarian). *Műanyag és Gumi*. 15./2.
- Horánszky Zs.- Szabó A.- Turi I. (1979): Plastics in the agriculture (in Hungarian). *Műszaki Könyvkiadó*.
- Vámos E. (1983): Tribology handbook Friction wear and lubrication of machines and machine elements. (in Hungarian). *Műszaki Könyvkiadó*.
- Kragelszkij V.- Mihin N. (1987): Friction and wear calculation of machine structures. (in Hungarian). *Műszaki Könyvkiadó*.

- Antal M. (1989): Engineering application of plastics. I. II. (in Hungarian). *Gépipari Tudományos Egyesület. Kiadványszerkesztési és Műszaki iroda.*
- Yamaguchi I. (1990): Tribology of plastic materials. *Tribology series 16.* Elsevier. Amsterdam.
- Kalácska G.- Zsidai L.- Kozma M.- DeBaets P.- Vercammen K. (2002): Tribology research of engineering plastics by different tests. *Bulletin of the Szent István University. Gödöllő 2001-2002.* p 119-127
- G. Kalácska, P. De Baets. (202): Tribological research of up-to-date, environment-friendly self-lubricating materials: correlation between large scale and small scale tribotesting *Int. Conf. On Machinery*, May. 2002, Budapest (Hungary) p.194-199
- L. Zsidai, G. Kalácska, K. Vercammen, K. Van Acker, P. De Baets. (2002): The different tribological behaviour of polymers on DLN coating and steel surface. *Insycont 2002*, Int. Congress On Tribology, Krakow (Poland). *Tribologia nr.6/2002* (186), p 1737-1750
- L. Zsidai, P. De Baets, P. Samyn, G. Kalacska, A.P. Van Peteghem, F. Van Parys (2002): The tribological behaviour of engineering plastics during sliding friction investigated with small-scale specimens. *WEAR 253* 673-688
- G. Kalacska, R. Keresztes, L. Zsidai (2002): Self-lubricating polyamides. *Intertribo. Stara Lesna.* p. 194-198
- L. Zsidai, E. Kislinder, P. DeBaets, M. Kozma, G. Kalacska, P. Samyn (2002.): Tribological properties of PA, POM, and PETP polymers by different tribological systems. *Intertribo Stara Lesna.* p. 255-258
- P.Debaets- F.VanParys- G.Kalacska (2002): The friction and wear of different polymers under high load conditions. = *Synthetic lubrication*, Vol 18, , p.109-118.
- G. Kalacska, R. Keresztes, P. Debaets (2003):. Dynamic tribological testing of polymers. ICCE10. (*Tenth annual international conference on composite/nano engineering*) New Orleans, p. 293-295.
- De Baets, Kalácska- et. al. (2004): Friction and Thermal Effects of Engineering Plastics Sliding Against Steel and DLN-Coated Counterfaces. = *Tribology Letters 17* (2). Plenum Publishing Corporation.. p. 269 – 288.
- Bharat Bushan (2001): Modern Tribology Handbook. Vol I. & II: *CRC Press LLC.* New York.
- Barczy A. – Kupi K. – Tirczka I. (1997): Basics for farming and plant cultivation for Hungarian regions (In: Ángyán J. - Menyhért Z. (ed.): Flexible plant cultivation and rational environment management. (in Hungarian). *Mezőgazdasági Szaktudás Kiadó, Bp.*, p. 414 and p. 217-260.

- Barczi A. – Centeri Cs. (2005): Trends of erosion and deflation in Hungary. (In: Stefanovits
- P. – Micheli E. (ed.) (2005): Significance of soils in XXI. Century. (in Hungarian) *MTA Társadalomkutató központ*, Budapest, p. 403. and p. 221-244.
- Barczi A. – Füleky Gy. – Gentischer P. – Néráth M. (1999): Basics of soil science for agricultural utility of Tihany region. (in Hungarian). *Növénytermelés*. Tom. 48., No. 3., p. 301-310.
- Birkás M., Dexter, A. R., Kalmár, T. Bottlik, L. (2006): Soil quality – soil condition – production stability. *Cereal Research Comm.* 34. 1. 135-138.
- J. Prokisch – D. Hovánszki – É. Széles – B. Kovács – Z. Györi (2007): Inhomogeneity of the agricultural soils in Hungary. *Cereal Research Communications*, Vol. 35, No. 2 pp 957-960
- Beer, Gy., Kalácska, G., Pellényi, L. (1995): Wear resistance tests of farm-machines materials. (in Hungarian). *Járművek és Mezőgazdasági Gépek*. Budapest, 1995/2/64-67p.
- Pellényi Lajos (1997): Tribological and mechanical parameters of up-to-date, self-lubricated plywood-bearings of farm machines. *PhD dissertation. GATE* Gödöllő, 1997
- Szendró P., Nagy J., Vincze Gy. (2005): Analyses of Chopping Cylinder Drive Torque Components. *Progress in Agricultural Engineering*. Akadémiai kiadó, Budapest. p. 33-56.
- Tiba Zs. (2006): Bending and Torsional Vibrations of Long Cardan Drives. *Progress in Agricultural Engineering*. Akadémiai kiadó, Budapest. p. 1-34. Material properties and delivery program. *Quattroplast Ltd.* Hungary. 2004.
- Czichos H. (1987): Tribology- A System Approach to the Science and Technology of Friction, Lubrication and Wear. *Elsevier*, Amsterdam.
- Valasek I. (2002): Tribológia. Vol. 1. *Tribotechnik Kft.* Budapest.
- Freddy DeBruyne (1999): Technical manual of semi-finished engineering polymers. DSM EPP, Tielt. Belgium.
- Eberst Otto (2005): Abrasive wear of engineering polymers. *PhD thesis. Universitatea De Nord, Baia Mare.*
- Stefanovits, P., Filep, Gy. and Füleky, Gy. (1999): Soil Science. (in Hungarian). *Mezőgazda kiadó*, Budapest
- Szodfridt I. (1994): Study of productive lands in forestry. (in Hungarian). *Mezőgazda Kiadó*, Budapest

# **Analysis of the make-up and break-out behaviour of API line pipe threaded connections**

Jeroen VAN WITTENBERGHE, Patrick DE BAETS, Wim DE WAELE  
University Gent, Department of Mechanical Construction and Production

## **Abstract**

In this study a series finite element analyses on API Line Pipe conical threaded pipe connections is carried out to quantify the influence of connection's geometry and contact properties on the stress distribution resulting from make-up and the load distribution over the threads when an external load is applied. In the assembled pipes, small sliding of the thread contact surfaces is still possible due to elastic deformation under external loads. To validate the results of the finite element analyses and to obtain a value for the coefficient of friction for the thread surfaces, experimental make-up and break-out tests were carried out. In an additional fatigue test, the sliding of the threads caused fretting fatigue damage.

## **Keywords**

threaded connection, finite element analysis, coefficient of friction, experimental testing

## **1. Introduction**

Threaded pipe connections are used in the oil and gas industry as an easy-to-assemble alternative for welding and in applications where pipes should be frequently coupled and uncoupled. They consist of a male and a female part called respectively 'pin' and 'box'. To maintain a sealed and secure connection while being subjected to external variable loads, threaded connections are commonly preloaded. To be able to introduce the preload, conical threaded connections are being used. The assembly of the connections is referred to as 'make-up' and disassembling as 'break-out'. The applied make-up torque is an important parameter and should be controlled accurately to obtain a good connection. However even with the same make-up torque, the connection's behaviour changes with varying surface properties of the threads and the global geometry of the connection. The combination of the make-up torque together with external loads and the geometry of the threads results in a complex stress distribution over the connection. Local stress concentrations at the thread roots can initiate fatigue cracks, in time causing the connection to fail. According to Griffin et al (2004) the highest stress concentration under axial load can be

expected at the last engaged thread (LET) of the pin. Newport and Glinka (1991) showed that this is because the load is distributed unevenly over the threads of the connection and the thread carrying the highest load is the LET of the pin. In order to improve the strength of a threaded connection, these stress concentrations and the load distribution over the threads should be studied. Both global and local connection parameters can have an influence on the load and stress distribution over the connection. It is known from Newport and Glinka (1991) that the thread type has an influence on the stress concentration factor in the root of the threads since a thread acts like a notch and has a stress raising effect on the local stress. Assanelli et al (1997) showed that the load distribution over the threads can be changed by altering the taper angle of the pin or box, creating a small mismatch.

Despite the make-up torque, small sliding of the thread contact surfaces is still possible due to elastic deformation under external loads. This means, the contact zones of the threads will change under load, which complicates the analysis of the couplings. In the present study it was found that the contact behaviour of the mating surfaces of the connection and in particular the coefficient of friction (COF), has a significant influence on this sliding. A series of finite element analyses was carried out on a model of an API Line Pipe connection to quantify the influence of the coefficient of friction and the number of make-up turns. To validate the presented results make-up tests and a fatigue test were carried out.

## 2. Numerical modelling

### *Finite element model*

In the present study 2D axisymmetric finite element analyses (FEA) were carried out using the software package ABAQUS<sup>®</sup>. Using 2D axisymmetric models for the analysis of threaded connections is common practice, since they produce accurate results with a reduced calculation time (Zhong, 2007). The model consists of an API Line Pipe threaded connection with a nominal size of 4" according to API 5B (1996). The pipe body has an outside diameter of 114.3 mm and wall thickness of 6 mm, the box has a length of 114.3 mm and an outside diameter 132.1 mm. An elastic-plastic material model for API Grade B steel is used, which has a minimum yield strength of 241 MPa and minimum tensile strength of 413 MPa according to the API 5L specifications (2000). In the elastic region a Young's modulus of 208 GPa and Poisson coefficient of 0.3 is used.

Part of the model of the API Line Pipe connection is shown in Fig. 1. The model consists of a section of the pin and a section of a half box. The body of the pin extends over a length of 100 mm to the left to exclude boundary effects (not shown in the figure). Fig. 1. also shows the resulting von Mises stresses from an analysis of the standard API Line Pipe connection. The analysis is carried out in two steps. During the first step, the make-up is modelled by applying an initial overlap between the male and female part of the connection

and then bringing them into contact. The size of the overlap corresponds to the specified number of make-up turns. In the pin the make-up causes a compressive hoop stress which can be very high and even exceed the material's yield strength. Once the make-up step is completed, an additional external axial tensile stress is applied at the left end of the pin. The pull-out strength of this type of connection is 373 kN (Clinedinst, 1976), which corresponds to a uniform axial tensile stress of 183 MPa in the pipe body. Since the modelling of thread pull-out is not of interest and usage factor of 0.72 is common practice for pipelines (Bay, 2003), a maximum applied tensile stress of 150 MPa was chosen. This is higher than the normal maximum service stress of 132 MPa, but lower than the pull-out stress.

As can be seen in Fig. 1 the highest stress appears in the LET of the pin as can be expected from Griffin et al (2004). This will also be the region where a fatigue crack is most likely to initiate.

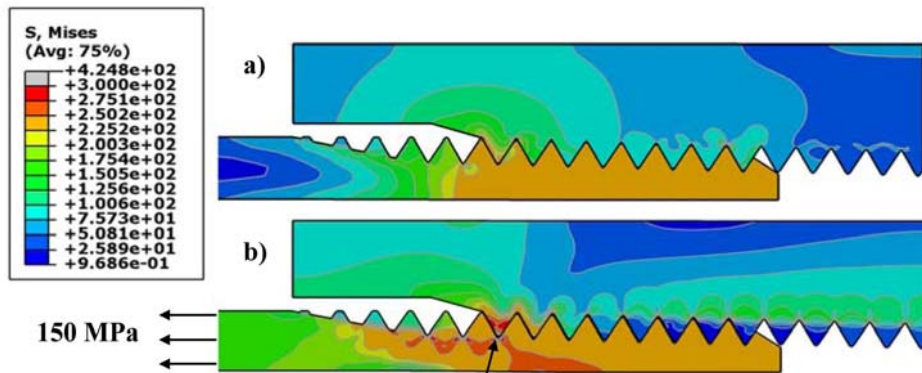


Figure 1. Von Mises stress distribution a) at make-up; b) with an external axial tensile stress of 150 MPa

#### *Influence of the coefficient of friction*

Once a certain external tensile stress is exceeded, the threads will start to slide over each other creating an opening between the threads. This means the gas or liquid inside the pipes will find their way out through the helical path created by the thread opening. It is obvious that such a leak is undesirable. From Fig 2 it can be seen that the opening is highly dependent on the coefficient of friction  $\mu$  between the threads. The opening is defined as the perpendicular distance between the thread flanks, and varies between 0.03 mm when  $\mu = 0.16$  and 0.41 mm for the frictionless situation, at an external tensile stress of 150 MPa. The opening increases slowly from 0 to a value of approximately 0.025 mm, and when a certain limit stress  $S_L$  is reached, the threads start to slide and the opening increases significantly. It can be seen from the graph that the limit stress increases with increasing COF and that paths of the opening during sliding are

parallel for the different COF's. Based on the simulations, an empirical correlation was found for the limit stress  $S_L$  and the opening  $O$ :

$$S_L = 124 + \mu \cdot 169 \text{ [MPa]} \tag{1}$$

$$O = 0.014 ( S - S_L ) + 0.025 \text{ [mm]} \text{ for } S > S_L \tag{2}$$

With  $S$  the externally applied tensile stress in the pin body. If during fatigue loading, the maximum cyclic stress exceeds the limit stress, there is a possibility for fretting fatigue cracks to initiate from the threads contact surface. It can be concluded that accurate knowledge of the coefficient of friction is necessary to perform correct finite element analysis. Since values of the coefficient of friction between 0.06 and 0.15 can be found in literature, more precise values should be obtained experimentally. Further values for the coefficient of friction were obtained through experimental make-up tests.

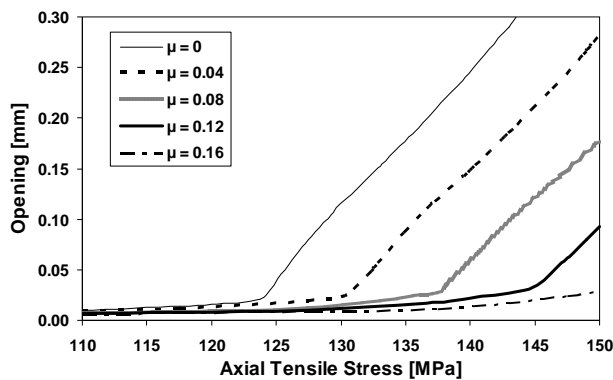


Figure 2. Influence of the coefficient of friction on the thread opening

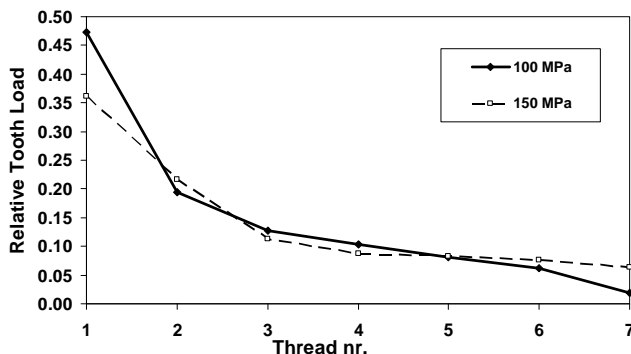


Figure 3. Load distribution over the threads as a percentage of the total load.

### Load distribution over the threads

When the threads start to slide, the contacting surface between the threads will decrease, increasing the resulting contact pressure. The load distribution over the threads, however, is not affected by this pressure change and is the same for the different COF's. The load distributions for an external tensile stress of 100 MPa and 150 MPa as a percentage of the total load is given in Fig. 3. Thread nr. 1 corresponds to the LET of the pin. Note that at an external stress of 100 MPa the LET carries 47% of the total load. With a higher external stress applied, the LET will start to bend, transmitting part of its load to the other threads. This way the tooth load decreases to 36% at a tensile stress of 150 MPa.

### Number of make-up turns

According to the API 5B specifications (1996), the connection should be made up in such a way that the end of the box recess (unthreaded part at the left side of the box in Fig. 1) coincides with the plane of the vanishing point of the thread runout of the pin. Depending on the tolerances this corresponds to between 1 and 3 make-up turns. As will be shown further in this paper, the number of make-up turns to be used in the models should be lower than the specified number since a certain rotation is necessary to settle the connection. For this reason the number of make-up turns was varied from 0.25 to 3 (see Fig 4). The tooth load at the LET of the pin with an external stress of 150 MPa does not change significantly with the number of make-up turns. For an external tensile stress of 100 MPa, the tooth load at the LET of the pin increases linearly from 47% to 53% for 1 to 3 make-up turns, but for a lower number of make-up turns the tooth load moves to the values obtained for the higher stress of 150 MPa. The thread opening decreases with increasing number of make-up turns, but saturates for 1.75 make-up turns or more. This is because the engaged body of the pin yields completely and plastic deformation appears for 1.75 make-up turns or more.

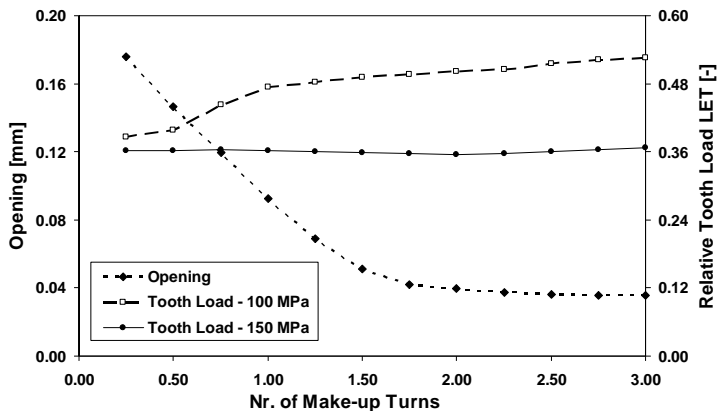


Figure 4. Influence of make up turns on thread opening and relative tooth load on the LET of the pin ( $\mu = 0.12$ )

### 3. Experimental validation

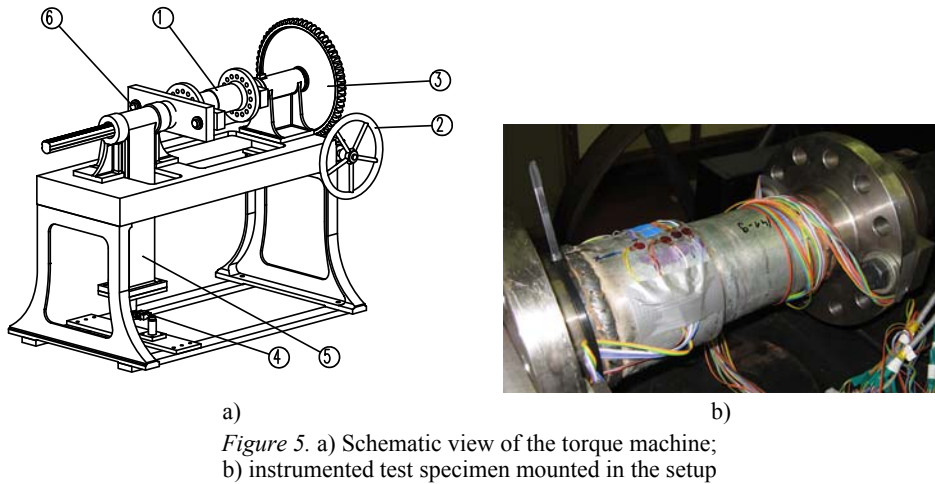
To validate the modelling of the make-up and to obtain a value for the COF between the threads the make-up of the connection was performed on a torque machine. Additionally a fatigue test was carried out on a four-point bending fatigue test setup using a coupled pipeline segment with a total length of 3 m.

#### *Make-up tests*

During the make-up it is necessary to accurately control the rotation and to measure the resulting torque. In order to do this, a setup was made by modifying an old torque machine. The new setup is presented in Fig. 5a. The test specimen (1), consisting of a pin and box, is mounted in the torque machine by the use of flanges that are welded to pin and box. Drive wheel (2) rotates a worm which drives the gear (3). This causes the pin of the test specimen (1) to rotate with respect to the stationary box. The resulting torque is transmitted to the lever arm (5) which is connected to the loadcell (4). The measured load multiplied by the length of the lever arm (1.00 m) equals the acting torque. To allow an axial motion during make-up, a linear guiding system (6) is present. The torque machine has a capacity of 2500 Nm, and the maximum test specimen length is 400 mm. Two torque tests were performed, the resulting torque-turn graph of one of the tests is shown in Fig.6. The number of rotations was put to zero at the point where the torque started to increase, the so-called ‘hand-tight’ situation. The total number of make-up turns is 1.09 which lays within the area of the specified 1 to 3 make-up turns according to API 5B (1996). The measured make-up torque was 1401 Nm, which conforms API 5C3 (1989), that specifies the make-up torque should be between 850 Nm and 1430 Nm. From the torque-turn data, a coefficient of friction  $\mu$  can be calculated. This is done by finding the best fit between the experimental data and the analytically calculated torque  $T$  given by equation (3).

$$T = \int \mu \cdot p \cdot r \cdot dA \quad (3)$$

With  $p$  the local contact pressure between pin and box,  $r$  the pin radius at the interface (at the pitch line of the threads) and  $A$  the contact surface. For the two torque tests a value of  $\mu = 0.11$  and  $\mu = 0.15$  was found. As can be seen in Fig. 6, the torque increases first to a value of about 50 Nm and stays constant for about 0.35 rotations. This is because all connections have some geometrical deviations and the connection needs to settle before the threads of pin and box are completely in contact with each other. Once the threads are fully contacting, the torque builds up, following the path of the linear fit. The linear fit becomes zero at a value of 0.42 rotations, so from this point of view, the number of final make-up turns is only  $1.09 - 0.42 = 0.67$ . This shifted value should be used as input for the finite element models since there is a perfect match between the geometry of pin and box in the models. In a previous study of Assanelli et al (1997) an analogue shift was observed for an API 8-round threaded connection.



In Fig. 5b it can be seen that strain gauges were attached to the test specimens to measure strains during make-up. They were attached at different locations over the outside wall of the box and the inside wall of the pin. The measured strain values at the final torque of 1401 Nm were compared to the modelled strains. As input for the finite element model, a COF of 0.13, 0.67 make-up turns and the measured value for the taper difference was used. The results are shown in Fig.7a for axial strain  $E_{xx}$  and in Fig. 7b for hoop strain  $E_{zz}$ . The distance is measured along the pipe axis, starting from the vanishing point of the thread runout of the pin. The RMS deviation between the measured and simulated values was  $117 \mu\epsilon$ . When the number of make-up turns was changed to 0.60, the RMS deviation even decreased to  $80 \mu\epsilon$ . This situation would correspond to an experimental number of make-up turns of 1.02 and a torque of 1200 Nm. These values are still within the API specifications.

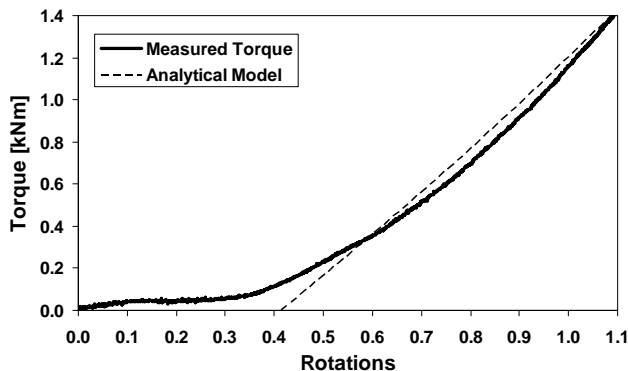


Figure 6. Torque vs. number of turns

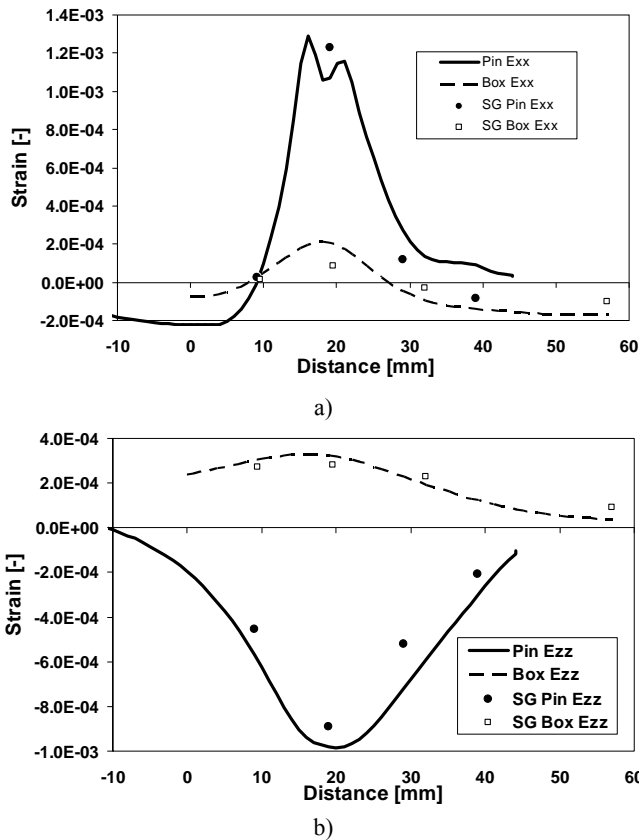


Figure 7. a) Axial strain  $E_{xx}$ : calculated (lines) vs. measured by strain gauges SG (points) b) Hoop strain  $E_{zz}$ : calculated (lines) vs. measured by strain gauges SG (points)

### Fatigue Test

On a four-point bending setup, a fatigue test was carried out on coupled pipeline segments with a 4" API Line Pipe connection and a total length of 3 m. The applied stress amplitude at the outside wall of the pin was 75 MPa with an R-factor of 0.1 ( $S_{max} = 167$  MPa,  $S_{min} = 17$  MPa) and was fluctuated at a frequency of 1 Hz. From the analysis of the measured data it was found that a crack started to grow from the last engaged thread of the pin (indicated by the arrow in Fig. 8a) after 18620 cycles. At 20350 cycles, the test was stopped and the connection uncoupled. The grease that was used during assembly had turned black, which is an indication of fretting corrosion. Fretting corrosion could be expected since the maximum applied stress of 167 MPa exceeds the limit stress  $S_L = 146$  MPa which is found by substituting the value of  $\mu = 0.13$  in equation (1). Detailed examination of the fracture surface showed that the crack initiated in the root of the LET of the pin (see detail in Fig. 8b), which is the location with the highest stress concentration in the finite element model.



Figure 8. a) Fatigue crack emanating from LET pin, b) detail of the root of the LET of the pin.

#### 4. Conclusions

A 2D axisymmetric finite element model of an API Line Pipe threaded connection has been presented. It was used to simulate and analyse the behaviour of this coupling type. Complementary experimental tests have been carried out as a validation. Following conclusions can be made:

- Both the make-up of the connection as the behaviour of the threads under load is influenced by the coefficient of friction between the threads.
- A value for the coefficient of friction was determined based on make-up experiments. Strains measured during the make-up tests were in good agreement with the values obtained with the model.
- Small sliding of the thread contact surfaces appears under external loads, the magnitude of this sliding depends significantly on the coefficient of friction and the number of make-up turns. Under fatigue loads, this sliding can cause fretting fatigue.
- The number of make-up turns given in the API specifications should not be used as such for input in finite element models.
- During the fatigue test a crack emanated from the root of the LET of the pin, which is the region with the highest stress in the finite element model.

#### 5. Nomenclature

- $E_{xx}, E_{zz}$  axial and hoop strain -
- $O$  thread opening mm
- $S$  stress MPa
- $S_L$  limit stress MPa
- $T$  torque Nm
- $\mu$  coefficient of friction -

## 6. Acknowledgements

The authors would like to acknowledge the financial support of the BOF fund (B/04939) of the Ghent University-UGent and of the FWO Vlaanderen (3G022806).

## References

- API Specification 5B (1996), Specification for Threading, Gauging and Thread Inspection of Casing, Tubing and Line Pipe Threads (U.S. Customary Units), American Petroleum Institute, fourteenth edition.
- API Bulletin 5C3 (1989), Bulletin on Formulas and Calculations for Casing, Tubing, Drill Pipe and Line Pipe Properties, American Petroleum Institute, fifth edition.
- API Specification 5L (2000), Specification for Line Pipe, American Petroleum Institute, forty-second edition.
- Assanelli, A.P., Xu, Q., Benedetto, F., Johnson, D.H., Dvorkin, E.N. (1997), Numerical/experimental analysis of an API 8-round connection. *Journal of Energy Resources Technology-Transactions of the ASME*. 119(2), pp. 81–88.
- Bay, Y. (2003), Elsevier Ocean Engineering Book Series, Volume 3: Pipelines and Risers, (Bhattacharyya, R. and Mc Cormick, M.E.), Elsevier Science Ltd., Oxford, U.K.
- Clinedinst, W.O. (1976), Joint Strength Formulas for API Threaded Line Pipe, API Circular PS-1533.
- Griffin, R.C., Kamruzzaman, S., Strickler, R.D. (2004), Casing Drilling Drill Collars Eliminate Downhole Failures. *Offshore Technology Conference*, 3–6 May 2004, Houston, Texas, USA.
- Newport, A. and Glinka, G. (1991), Concentration of Cyclic Stresses in Preloaded Threaded Connections. *Journal of Engineering Mechanics-ASCE*, 117(6), pp. 1257–1273.
- Zhong, A. (2007), Thread Connection Response to Critical Pressures, *Abaqus Users' Conference*, May 2007, pp. 690–706, Paris, France.

# Strength analysis of the frame of filter machine

István OLDAL, László SZENTESI

Szent Istvan University, Faculty of Mechanical Engineering

## Abstract

Manufacturing of a new type of filter machine is started in Hungary last year. Functional design was done before so main data are available. But strength analysis is also required to design a new filter machine construction. Strength analysis contains analysis of rack and loaded elements. Analysis of main frame elements is showed in this work. Procedure covers from determination of loads to evaluation of results.

## Keywords

filtering, strength analysis, rack and loaded element

## 1. Introduction

Result of designing data for strength analysis is available. Frame of filter machine is important part of complex. First loads have to be calculated from weight data.

Data for calculation:

Applied material in all cases: S355 C

Yield strength: 355 N/mm<sup>2</sup>

Young modulus: 210.000 N/mm<sup>2</sup>

Shear modulus: 80.000 N/mm<sup>2</sup>

Quality of welding: 1st class specification of manufacturer

Reduction factor of welding: 0.9

Minimal safety factor at critical points: 1.2

Calculated mass data:

Head plate: 3300 kg

End plate: 3100 kg

Press plate: 2900 kg

Side beam: 1250 kg/pc

Filter sheets: 900 kg

Hydraulic cylinder: 1250 kg/pc

Container: 2500 kg

Electric system: 1500 kg

Hydraulic supply: 500 kg

Valves, pipes: 1200 kg

Container: 300 kg  
 Other equipments: 2000 kg

## 2. Strength analysis

### *Loads of frame*

Fourth corner of frame are legs as constraints. End plate loads A45 area head plate loads A50 area can be seen fig. 1.

Bigger beams are 400x150x6.3 closed cross sections. Smaller beams are 140x140x6.3 closed cross sections. On geometric model shells are in the middle of walls.

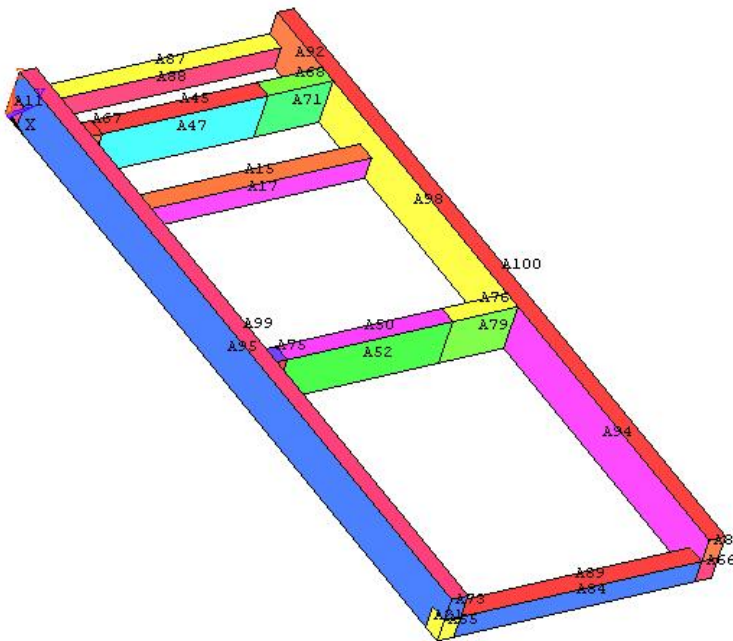


Figure 1. Geometric model of frame

Load on end plate is sum of next loads:

- weight of end plate: 30411N
- half weight of press plate: 14224,5N
- half weight of side beam: 6131,25N
- 20% of filter weight: 1765,8N
- weight of hydraulic cylinders: 24525N

$$F_{end} = 30411 + 14224,5 + 6131,25 + 1765,8 + 24525 = 77057,55N \quad (1)$$

Load on head plate is sum of next loads:

- weight of head plate: 32373N
- half weight of press plate: 14224,5N
- half weight of side beam: 6131,25N
- 80% of filter weight: 7063,2N
- weight of pipes: 11772N

$$F_{head} = 32373 + 14224,5 + 6131,25 + 7063,2 + 11772 = 71563,95N \quad (2)$$

*FEM model of frame*

Frame made of closed cross sections. FEM model is built of SHELL elements in order to calculate all stresses and critical point. In case of design for allowable stress equivalent stress is below yield strength so material model is linear elastic.

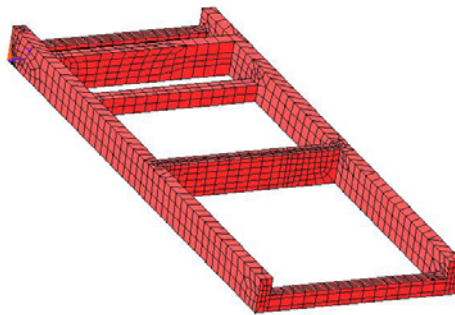


Figure 2. FEM mesh of frame

*Results for frame*

Equivalent stresses (von Mises) from FEM modelling are can be seen on Fig. 3.

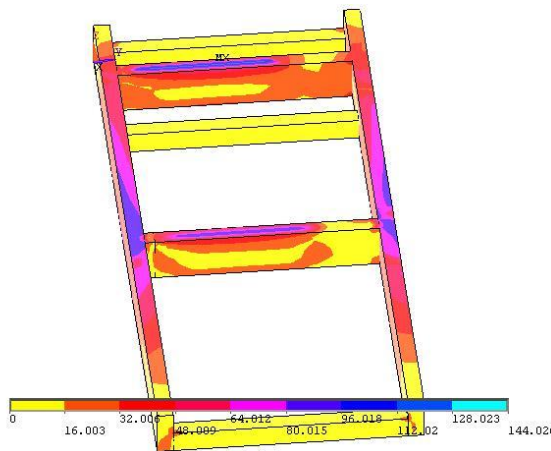


Figure 3. Equivalent stress on frame (MPa unit)

Maximal equivalent stress is 144MPa in critical point.  
Safety factor in this point:

$$n = \frac{355}{144.026} = 2.46 \quad (3)$$

Factor is higher than 1.2 so frame is adequate.

Reaction forces in supports: 52561N, 47441N, 23367N, 23079N.

#### *Loads of leg*

Loads of four legs are different. Maximal loads in critical leg:

- Maximal force from frame: 52561N
- 25% of container weight: 6131.25N
- 25% of electric system: 3678.75N
- 25% of another container: 735.75N
- 25% of other equipments: 4905N

$$F_{leg} = 52561 + 6131.25 + 3678.75 + 735.75 + 4905 = 68011.75N \quad (4)$$

Vertical part of leg is made of 150x150x10 horizontal part of leg is made of 180x140x8 closed cross section. FEM model of legs are SHELL elements in centre plane of plates. Geometric model can be seen in Fig. 4.

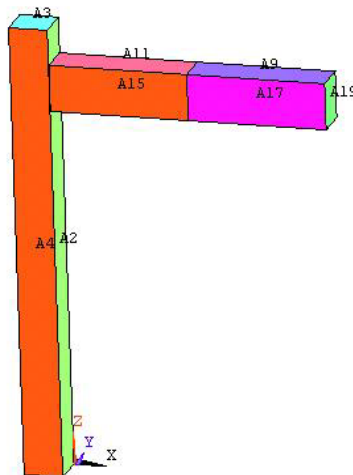


Figure 4. Geometric model of leg

#### *FEM model of leg*

Frame made of closed cross sections. FEM model is built of SHELL elements in order to calculate all stresses and critical point. In case of design for allowable stress equivalent stress is below yield strength so material model is linear elastic.

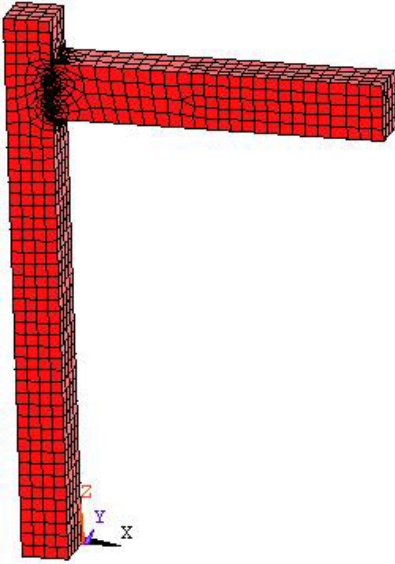


Figure 5. FEM mesh of leg

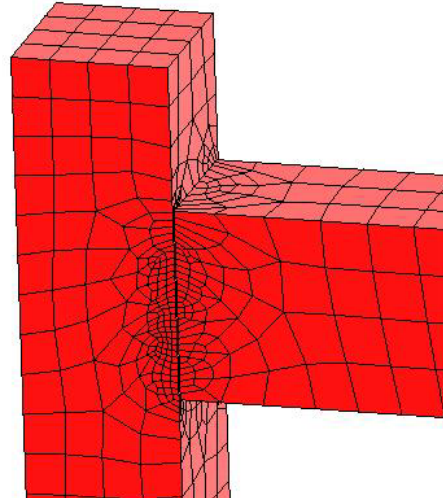


Figure 6. FEM mesh of critical part of leg

Load of leg acts on underside supports act on horizontal areas. Effect of front leg is modelled on A19 area as symmetry condition. (Fig. 4.)

*Results for leg*

Calculated equivalent stresses can be seen on Fig. 7. and 8.

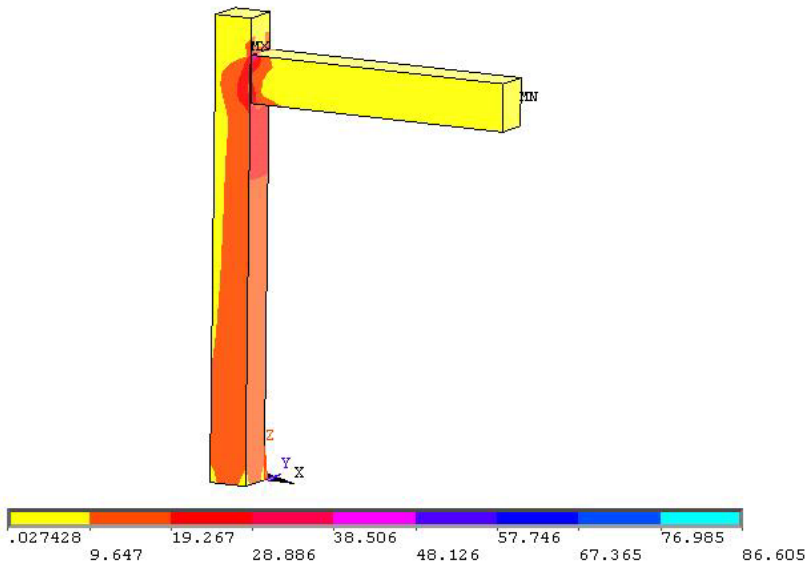


Figure 7. Equivalent stresses in leg (MPa unit)

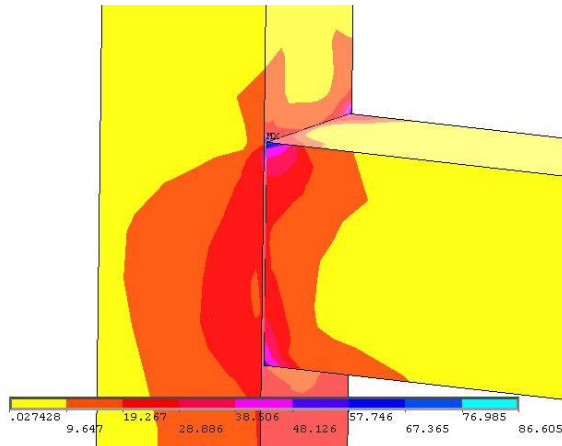


Figure 8. Equivalent stresses in critical part (MPa unit)

Maximal equivalent stress in critical point is 86.6MPa. This point is in welded area so yield stress has to be reduced with 0.9 factor.

Safety factor in critical point:

$$n = \frac{355 \cdot 0.9}{86.605} = 3.69 \quad (5)$$

Factor is higher than 1.2 so frame is adequate. This factor is valid to horizontal position of container. That has to be taken into consideration when legs positions are adjusted.

### 3. Summary

Frame of filter machine suits the requirements. Filter machine is safe. Other loaded elements of machine have to be analyzed but safe of machine isn't reduced by fault of these elements. It is required only for good working. After manufactured of filter machine a loading analysis is required

### References

- MSZ ENV 1991-1
- MSZ ENV 1991-2-1
- MSZ ENV 1991-2-4
- EN 10219-1: 2006
- EN 10219-2: 2006

# The effect of the punch clearance on the punched surface

Lucian BUTNAR, Marius COSMA, Otto EBERST,  
North University of Baia Mare, Faculty of Engineering  
Gellért FLEDRICH  
Szent Istvan University, Faculty of Mechanical Engineering

## Abstract

The surface quality manufactured by punching is influenced by a series of factories from which a major importance has the clearance between the punch and the active plate. The clearance magnitude and its departure from the optimum determine high variations of the dimensional and form precision and also of punched surface roughness. The paper approaches theoretical and experimental aspects concerning the relation between the punch clearance and the punched surface quality.

## Keywords

punching, clearance, surface quality

## 1. Introduction

The principal factors that influence the punched surface quality are:

- size of punch-active plate clearance;
- wear state of cutting edges: punch and active plate;
- punch and active plate processed precision;
- stamp engineering;
- type and state of press that activates the stamp;
- punch – active plate friction level;
- punched material structure, proprieties and thickness.

Of these, the most important factor is the clearance that influences the roughness as the stamped surface precision. The designing, engineering and assembling of stamp pursue the reach of an optimum clearance. The optimum clearance is the bilateral clearance between the active elements. Its size depends just of:

- mechanical characteristics of punched material;
- the  $g$  thickness of metal sheet - semi-product.

The clearance determination is from the table or by calculation with the following relations:

$$j_o = 2(g - h_f) \cdot tg \alpha_0; \quad (1)$$

or

$$j_o = K_1 g^2 + K_2 g, \tag{2}$$

where  $\alpha_0$  is the angle of fissure propagation,  $K_1, K_2$  are the coefficients depending of quality and mechanical proprieties of material.

The smooth zone size  $h_f$  from the stamped surface and also the smooth zone percentage (ratio  $h_f/g$ ) represent two indicators of punched surface quality – figure 1.

$$h_f = g - \frac{j_o}{2tg\alpha_0}, \tag{3}$$

$$h_f = -\frac{K_1}{2tg\alpha_0} \cdot g^2 - \left(\frac{K_2}{2tg\alpha_0} - 1\right) \cdot g. \tag{4}$$

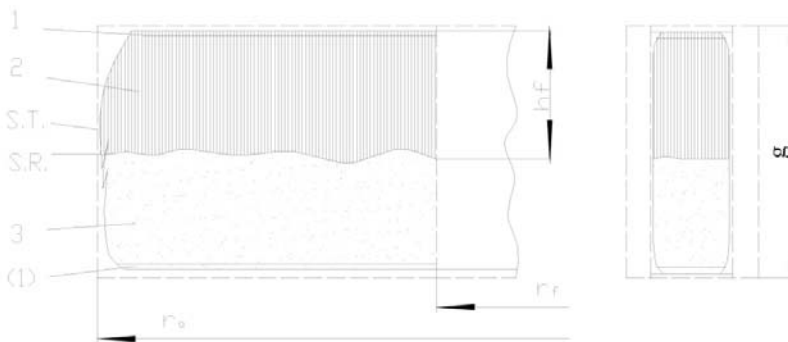


Figure 1. The stamped surface: 1 – the elastic tensions zone; 2 – the plastic tensions zone (smooth zone); 3 – the shearing zone; S.T. – theoretical surface; S.R. real surface.

## 2. Clearance influence on the stamped surface quality

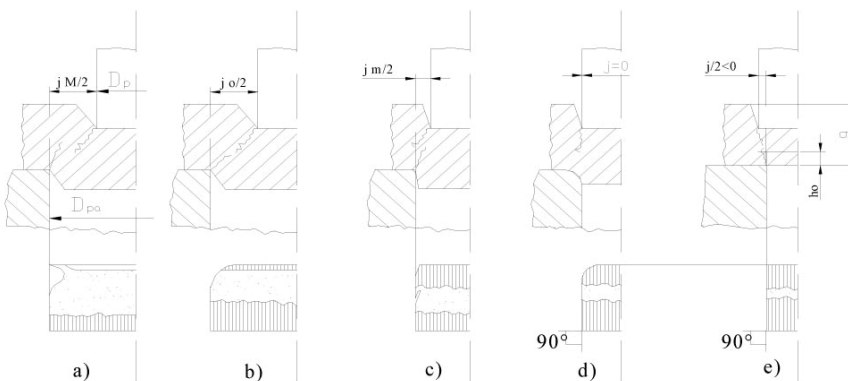


Figure 2. Clearance value influence on the stamped surface: a) high clearance; b) optimum clearance; c) low clearance; d) null clearance; e) negative clearance.

The repercussions of clearance deviation from the optimum clearance on the stamped surface are present in figure 2.

The a, b, c cases represent the ordinary punching and the d, e cases represent the high precision punching.

*The high clearances* make metallic addition, high roughness surface, where the smooth zone percentage is low and the perpendicular deviation is high.

*The optimum or the next optimum clearance* conduces to a common propagation surface of fissures  $\alpha_0$ , improves the cutting condition, reduces the medium roughness, enlarges the smooth zone percentage and reduces the perpendicular deviation. The medium roughness surface obtained is  $R_a = 3,2 \dots 1,6 \mu\text{m}$  thru the ordinary punching and  $R_a = 0,8 \dots 0,2 \mu\text{m}$  thru the high precision punching.

*A lower clearance as the optimum* can extend the smooth zone  $h_f$  but on cut surface appear frequently superposed of material sheets.

*The null and negative clearances* from the high precision punching correlate with adequate active element geometry and stamp engineering improve the cut surface quality and its perpendicularity. The plastic zone extends almost on the whole section.

The stamp clearance deviation is produced by a wrong design, an imprecise execution or by the cutting edge wearing of active elements. The deviation worsens the stamped surface. For example, for a steel piece with thrust resistance  $R_m < 500 \text{ N/mm}^2$ , thickness 10 mm, with an optimum clearance  $j_{\text{opt}} = 1,5 \text{ mm}$ , and a deviation of effective clearance  $-40\%$  to  $40\%$ , the results are represented in table 1 and the variation chart  $h_f = h_f(\Delta j)$ , in figure 3.

*Table 1.*

Soft steel $R < 500 \text{ N/mm}^2$									
Thickness $g[\text{mm}]$	10	10	10	10	10	10	10	10	10
Optimum clearance $j[\text{mm}]$	1.5	1.5	1.5	1.5	1.5	1.5	1.5	1.5	1.5
Effective clearance deviation $\Delta j[\%]$	-40	-30	-20	-10	0	10	20	30	40
Effective clearance $j[\text{mm}]$	0.9	1.05	1.2	1.35	1.5	1.65	1.8	1.95	2.1
Optimum plastic zone $h_{f0}/g[\%]$	28.57	28.57	28.57	28.57	28.57	28.57	28.57	28.57	28.57
Effective plastic zone $h_f/g[\%]$	57.14	50	42.85	35.71	28.57	21.43	14.28	7.14	18E-15
Plastic zone variation $\Delta h_f/g[\%]$	28.57	21.43	14.28	7.14	0	7.14	-14.28	-21.42	-28.57

We can see, a continue linear decrease of the stamped surface quality  $h_f$  [mm] simultaneous with growing of clearance deviation from the optimum.

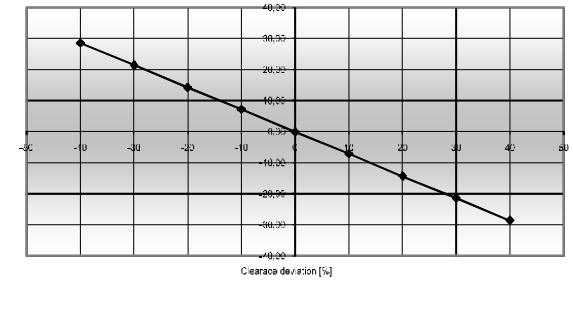


Figure 3. The clearance variation theoretical influence on smooth zone percentage  $h_f/g$ [%].

The higher clearances as the optimum with 10% worse the surface quality and reduce the smooth zone with about 7%.

Lower clearances as the optimum with about 5-10% produce superposed of material sheets.

### 3. Experimental researches of the clearance influence on the stamped surface quality.

The experimental researches were made in S.C. Matrix S.A. Baia Mare using a stamp for metallic sheet with  $g = 10$  mm – figure 4. There were executed six punches with different dimensions that gave different clearances, higher and lower as the optimum  $j_{opt} = 1,5$  mm.

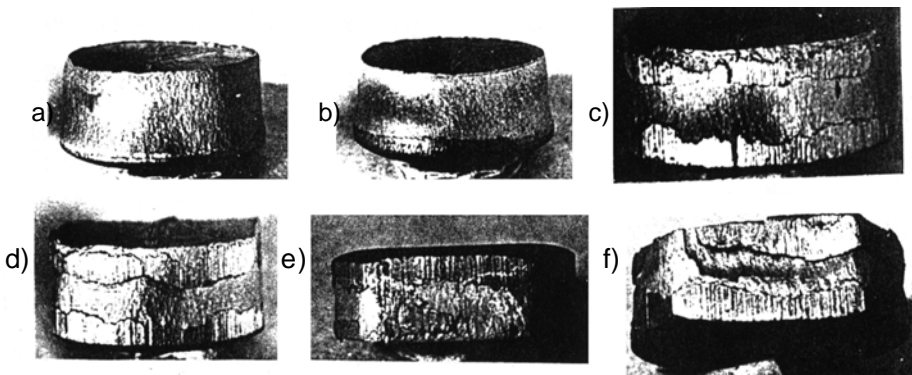


Figure 4. The stamped piece surface: a)  $j > j_{opt}$ ; b)  $j = j_{opt}$ ; c)  $j < j_{opt}$ ; d)  $j \ll j_{opt}$ ; e) un-uniform clearance; f) superposed of material sheets  $j < j_{opt}$ .

For each experiment, the active elements had un-wear edges cleaned as the semi-product with technical alcohol.

It was measured the smooth zone  $h_f$  with the meter ZKM 05-250D.

The results are presented in table 2 and the clearance variation influence on smooth zone percentage  $h_f/g$  [%] in figure 5.

Table 2.

Thickness $g$ [mm]	Effective clearance $j$ [mm]	Optimum clearance $j_o$ [mm]	Clearance variation $joc \Delta j$ [mm]	Plastic zone $hf/g$ [%]
10	2.12	1.5	0.62	12.27
10	1.90	1.5	0.40	19.55
10	1.72	1.5	0.22	24.47
10	1.50	1.5	0.00	27.63
10	1.32	1.5	-0.18	37.12
10	1.10	1.5	-0.40	40.88

In optimum clearance stamping, the smooth zone percentage  $h_f/g$  is 27,63 % next to the theoretic value 28,57%.

#### 4. Conclusions

The clearance deviation from the optimum produces a quality surface variation next to the theoretical. So, lower clearances with 0,4 mm extend the smooth zone to about 40% from stamped surface. Higher clearances with 0,62 mm reduce the smooth

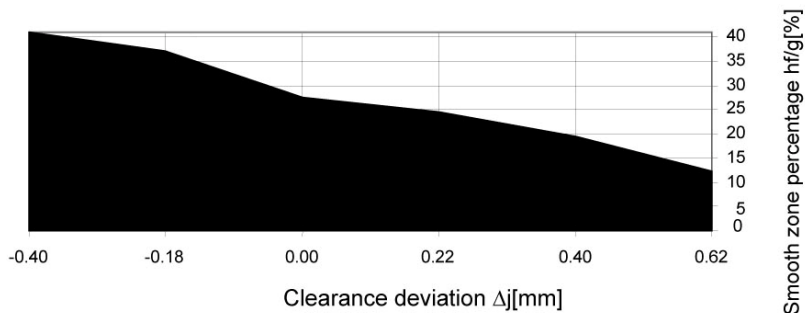


Figure 5. The clearance variation experimental influence on smooth zone percentage  $hf/g$  [%].

zone to 12%. But the lower clearances produce superposed of sheet material; appear important deviations of smoothness and material wrenches. In the high clearance, the stamped surface has a pronounced frustum configuration.

---

## **References**

- Butnar., L., Contribuții asupra fabricării roților dințate prin deformare plastică.  
Teza de doctorat, Universitatea Tehnică Cluj - Napoca, 2002.
- Iliescu, C., Tehnologia debitării, decupării și perforării de precizie. București,  
Editura Tehnică, 1980.

# The optimal milling energy in a planetary ball mill

Gyula KAKUK, Ibolya ZSOLDOS, István OLDAL,

Szent Istvan University, Faculty of Mechanical Engineering

Ágnes CSANÁDY

Bay Zoltán Foundation, Institute of Materials Science and Technology

## Abstract

*Further improving the previous models describing the operation of planetary ball mills the study determines the impact energy transmitted towards the material during the milling and the milling power. It points out relationship between the ratio between the angular velocity of the sun disk and the vials, and the geometrical parameters of the mill. By exploring the relationship between the model created for the milling process taking place in the planetary ball mill and the milling parameters depending on the mill, and using the calculations executed, data more authentic than previous ones can be obtained on the energy transferred to the mill product during the milling process, and on the efficiency of milling. This information provide a more plannable mechanical milling for researchers decomposing materials in planetary mills, and for specialists dealing with the improvement and application of these technologies.*

## Keywords

high-energy planetary ball milling, energy transfer,

## 1. Introduction

Nowadays, there are several possible solutions for producing nano-structure materials using conventional and/or newly developed technologies of material science. During these processes the size, structure, composition, and morphological characteristics of „grains” and/or “phases” can be altered with the aimed selection of technological parameters. Possible ways of production include mechanical milling having been applied for decades in the production of powder materials. The improvement results of different type mills (e.g. the possibility of higher energy input) have made it possible by now to produce nano-crystalline powders by mechanical milling. However, it is inevitable to have adjustability more accurate then before, for purposive milling and the quality insurance of products intended to be produced by milling.

During the milling process carried out in the planetary mill, the impact velocity and the angle of impact has a significant effect on the energy transferred to the powder particles to be milled by the flying ball. Consequently, the movement and impact of the balls are important factors, on the inspection of which thorough mathematical studies have been carried out.

According to Lü and Lai the greater the angular velocity of the sun disk, the greater the increase in the impact velocity as the detachment velocity of the balls increases and the flying time shortens. This impact velocity is an important parameter, which determines what energy acts upon the powder particles during the mechanical milling.

Besides and before Lü and Lai, several authors and studies had already dealt with determining the energy transferred by the balls to the material to be milled.

The study of Burgio et al. has been considered initial basis for many when determining the impact velocity of the ball and the energy transferred to the powder. Analyzing the above studies it can be stated that when determining the detachment angle and the detachment velocity they do not take into consideration forces resulting from *relative movements* (e.g. Coriolis force). Impact energy is described as the difference between the kinetic energy calculated for the moment of detachment of the ball and the velocity of the ball after the impact. No information is given on determining the location of the impact. Although, they give data of exact (measured) speed and detachment angle for a certain setup of mill type Pulverisette P5 and different ball sizes, but they provide no calculated impact energy.

P. Le Brun et al. published another relationship on determining the detachment angle of the milling ball, and they highlight the importance of the of the speed rate (ratio) between the sun disk and the vial, which influences the trajectory of the balls, and even the amplitude and ratio of the impact and friction energy which can be transferred to the material to be milled. In their study, Abdellaoui and Gaffet present the change in impact energy and power related to the angular velocity of the sun disk primarily in connection with planetary mills types G5 and G7 (but also for other milling devices), however, they do not give their calculation relationships. In another study relying upon the work of the above mentioned Burgio et al. they present calculation correlations for determining the impact energy, but no information is found on the location of the impact, furthermore, they do not take forces resulting from relative movements into consideration either in their calculations. Magini et al. give a simplified correlation for determining impact energy in their study, and they focus on inspecting the collision between the ball and the material to be milled. Iasonna and co. Magini in one of their studies examined energy transfer and power consumption during the milling process. They measured electric and mechanical power consumption on a Fritsch P5 milling device. During milling Fe-Zr powder they examined the influence of the number and size of balls, and that of the quantity of powder filled-in on the power consumption. Rojac et al. prepared the so-called milling map of a  $\text{NaNbO}_3$  ceramic-oxide system. Every point of the milling map indicates a certain state of the mechanochemical reaction. From the milling map the experimental states, e.g. milling parameters can be determined in order to achieve the intended end-product. For the calculation of impact energy values used for the milling maps, the equations of Burgio were used with minor alterations.

Several researchers have already dealt with modelling processes taking place in the planetary ball mill (Fritsch P4) used during our work, however, literature

dealing with the relationship between the milling parameters regulating the process and the energy transferred to the material to be milled is incomplete. Taking this fact into consideration, it is reasonable to further clarify processes taking place in the planetary ball mill, and a more accurate exploration of the influence of milling parameters.

## 2. Kinetic modelling of a planetary ball mill

The description of forces acting on the milling ball in the planetary ball mill is based on the study of Lu and Lai written in 1998. After a verification the calculation mentioned can be used as an initial point for the model intended to be established. A part of this description should be outlaid in point 2.1. in order to understand the whole model. From chapter 2.2. the further construction details of the model introduced by Lü and Lai will be described. The kinetic modelling of the mechanical milling process of the planetary ball mill was started with the following statements and simplifying assumptions:

- a) the milling ball can detach from the wall of the vial, when the force acting upon it, pointing towards the radius of the vial is zero,
- b) the new junction point of the ball and the vial acts as a point of impact, disregarding the elastic impact of the ball,
- c) there is no relative movement (sliding) between the ball and the wall of the vial before the point of detachment,
- d) the resistance of the medium within the vial is neglected,
- e) gravitation acting on the ball ( perpendicular to the plain inspected ) is disregarded,
- f) any rotation of the ball is disregarded,
- g) only ball-wall collisions are taken into consideration, ball-ball collisions are not.

Modelling steps are as follows:

- Description of motion and force conditions
- Determining the detachment angle
- Determining the detachment velocity
- Determining the impact point
- Determining the impact velocity
- Determining the impact energy and power
- Recording planetary ball mill working curves.

### *Planetary ball mill motion and force conditions*

The vial within a ball mill carries out planetary motion. The two (or in some cases four) vials with radius  $r_v$  are located on the sun disk at a constant distance of  $r_p$  from point O, around which they rotate with an angle velocity  $\omega_p$ , as it is shown on Figure 1. The centre point of the vials is point  $O_1$ , and they rotate with an angular velocity  $\omega_v$  around their own axes, in the opposite direction against rotation  $\omega_p$ . In the mathematical equation below, the expressions “absolute” and „relative” relate to the parameters, which were determined according to the

XOY absolute and xO<sub>1</sub>y relative co-ordinate systems. Consequently, the motion of the ball with a mass  $m_b$  along the wall of the vial can be presented as follows.

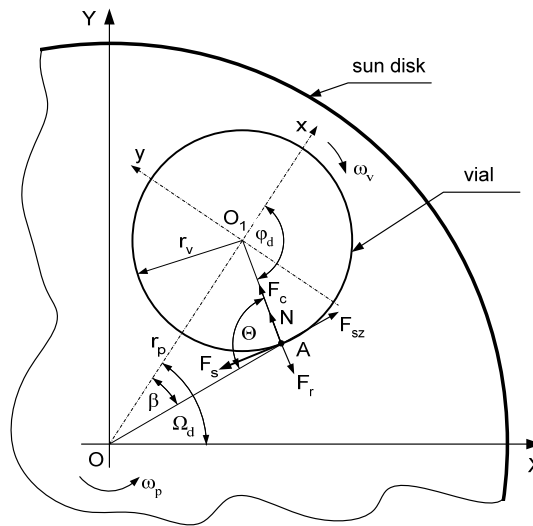


Figure 1. Force and motion conditions in a planetary ball mill

Forces acting upon the ball in the vial are the transporting force, relative force, which act from the centre of the sun disk and from the centre of the vial, marked  $F_{sz}$  and  $F_r$ . Constraining forces are  $N$  and  $F_s$ , normal and friction force, which result from the interaction of the ball and the vial, and the force  $F_c$  resulting from the Coriolis effect, and the force of gravity. Applying the D’Alembert principle the balls can be described using statical equilibrium equations, if the accelerations are taken into calculation as inertia forces, which are equal to the product of the mass of the ball and the acceleration values. Consequently, the force acting outwards from  $O$  is transporting force, the force acting outwards from  $O_1$  is relative force, and the Coriolis force acting towards  $O_1$  can be stated as follows:

$$\vec{F}_{sz} = -m_b \cdot \vec{a}_{sz} \tag{2.1}$$

$$\vec{F}_r = -m_b \cdot \vec{a}_r \tag{2.2}$$

$$\vec{F}_c = -m_b \cdot \vec{a}_c \tag{2.3}$$

where  $m_b$  is the mass of the ball,  $a_{sz}$ ,  $a_r$  and  $a_c$  are the transportation acceleration from  $O$ , relative acceleration from  $O_1$ , and the Coriolis acceleration. Acceleration values can be stated as follows:

$$\vec{a}_{sz} = \vec{\omega}_p \times \vec{v}_p \quad (2.4)$$

$$a_{sz} = \overline{OA} \cdot \omega_p^2 = \frac{r_p + r_v \cdot \cos\varphi_d}{\cos\beta} \cdot \omega_p^2 \quad (2.5)$$

$$\vec{a}_r = \vec{\omega}_v \times \vec{v}_v \quad (2.6)$$

$$a_r = r_v \cdot \omega_v^2 \quad (2.7)$$

and

$$\vec{a}_c = 2 \vec{\omega}_p \times \vec{v}_v \quad (2.8)$$

$$a_c = 2 \cdot \omega_p \cdot \omega_v \cdot r_v \quad (2.9)$$

The resultant of forces within the system can be stated according to Figure 1:

$$\vec{\Sigma F} = m_b \cdot (\vec{a}_{sz} + \vec{a}_r + \vec{a}_c) \quad (2.10)$$

$$N = F_r - F_c - F_{sz} \cdot \cos(\pi - \theta) \quad (2.11)$$

where  $N$  is the normal force acting upon the surface of the vial, which is the inertia force resulting from the acceleration of the ball.

Using equations 2.5, 2.7, and 2.9 the forces can be stated as:

$$\begin{aligned} F_{sz} \cdot \cos(\pi - \theta) &= m_b \cdot a_{sz} \cdot \cos(\pi - \theta) = \\ &= m_b \cdot \omega_p^2 \cdot \frac{r_p + r_v \cdot \cos\varphi_d}{\cos\beta} \cdot \cos(\pi - \theta) \end{aligned} \quad (2.12)$$

$$F_r = m_b \cdot r_v \cdot \omega_v^2 \quad (2.13)$$

$$F_c = 2 \cdot m_b \cdot \omega_p \cdot \omega_v \cdot r_v \quad (2.14)$$

### *Determining the detachment angle of the milling ball*

Let's suppose that when  $N=0$  the ball detaches from the surface of the vial wall. This crucial condition can be stated as follows:

$$N = 0 \quad (2.15)$$

$$\begin{aligned} m_b \cdot \omega_p^2 \cdot \frac{r_p + r_v \cdot \cos \varphi_d}{\cos \beta} \cdot \cos(\pi - \theta) + 2 \cdot m_b \cdot r_v \cdot \omega_p \cdot \omega_v &= \\ &= m_b \cdot r_v \cdot \omega_v^2 \end{aligned} \quad (2.16)$$

where  $\varphi_d$  is the angle of detachment of the ball from the wall of the vial, Figure 1.

Let the relationship (ratio) between the angular velocity of the vial and the sun disk will be as follows:

$$i = \frac{\omega_v}{\omega_p} \quad (2.17)$$

Settling equation 2.16 and after carrying out the appropriate modifications, and using equation 2.17 the angle of detachment of the ball from the wall of the vial can be determined.

If the sun disk rotates anticlockwise while the vial rotates clockwise, the angle of detachment will be as below:

$$\varphi_d = \arccos\left(-\frac{r_v \cdot (1-i)^2}{r_p}\right) \quad (2.18)$$

#### *The influence of the ratio (i) on the angle of detachment and on the ball trajectory*

The detachment and impact positions depend on the size of the vial ( $r_v$ ), the position of the vial on the sun disk ( $r_p$ ), and the rate of the angular velocity, that is the ratio ( $i$ ). When  $r_v$  and  $r_p$  are fixed, detachment depends on only  $i$ , therefore it seems to be reasonable to determine those ratio values, under, between, and above which the milling ball runs on a different trajectory.

The determination of the limits of the ratio was started from relationship 2.18. Inspecting the relationship it can easily be understood that the angle of detachment can only be interpreted between +1 and -1, that is the solution of the inequations

$$-\frac{r_v}{r_p} \cdot (1-i)^2 \geq -1, \quad (2.19)$$

and

$$-\frac{r_v}{r_p} \cdot (1-i)^2 \leq 1 \quad (2.20)$$

provide the values of  $i_{limit}$  and  $i_{critical}$  by fixed geometrical parameters ( $r_p, r_v$ ).

Inequation 2.20 is valid in case of any arbitrarily chosen speed ratio and geometrical characteristics due to the negative sign before the fraction  $\frac{r_v}{r_p}$ .

Results of the inequation 2.19 provide the limit values of the ratio, which will be as follows without the steps of deduction:

$$i_{limit} = 1 - \sqrt{\frac{r_p}{r_v}} \leq i \leq 1 + \sqrt{\frac{r_p}{r_v}} = i_{kritikus} \quad (2.21)$$

From relationships 2.17 and 2.21 it can be stated that in case of using the construction of a given mill ( $r_p$ ) and a given vial ( $r_v$ ), the rotary speed of the sun disk ( $\omega_p$ ) and the vials ( $\omega_v$ ) should be set in a way that the condition 2.21 is met, in order to achieve the greatest possible impact energy and the best possible milling power, as the ball detaches from the wall of the vial at this point. If this condition is met, that is  $i_{limit} \leq i \leq i_{critical}$ , then milling will be implemented according to the impact and friction method, when the kinetic energy transmitted by the milling balls to the powder is the greatest possible.

As a function of  $i_{limit}$  and  $i_{critical}$ , the trajectory of the balls determines three operational modes, the existence of which has already been verified by experiments of Brun et al. [P.Le Brun, et al. 1993.]:

- chaotic mode (if  $i < i_{limit}$ )
- impact and friction mode (if  $i_{limit} \leq i \leq i_{critical}$ )
- pure friction mode (if  $i > i_{critical}$ ).

### Impact and friction mode

In this mode, as indicated by Figure 2, the trajectory of the ball is described very well by the principles of dynamics. Energy can be divided into two components at the moment of the impact. Namely, to the normal component, which results in the increase of the effective impact energy transferred to the powder particles, and to the tangential component, which may occur as friction energy.

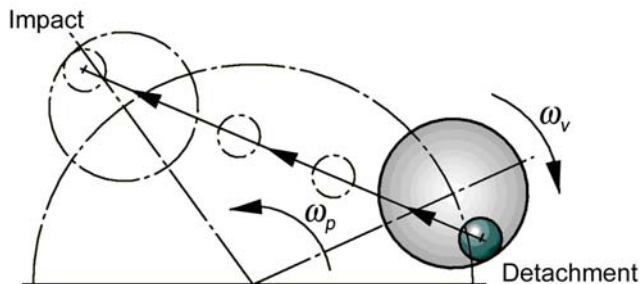


Figure 2. Movement of the ball after detachment, when  $i_{limit} \leq i \leq i_{critical}$

The above described behaviour of the milling balls is the most advantageous for carrying out effective milling, therefore it is reasonable to inspect, what set rotary speed values is the condition  $i_{limit} \leq i \leq i_{critical}$  met with the given geometrical parameters.

*Determining the detachment velocity ( $v_d$ )*

In order to be able to determine the energy released during the impact of the ball after the detachment, it is necessary to know the speed and direction of the ball. After determining the angle of detachment (2.18), the absolute point 'A' ( $X_d, Y_d$ ) of detachment, and the two components of the detachment velocity,  $v_{dx}$  and  $v_{dy}$  can be determined in directions X and Y, on supposition that the ball and the vial move together at the moment of detachment.

Detachment velocity ( $v_d$ ) at point 'A' is given by the sum of the peripheral velocity of the sun disk ( $v_{dp}$ ) and the peripheral velocity of the vial ( $v_{dv}$ ).

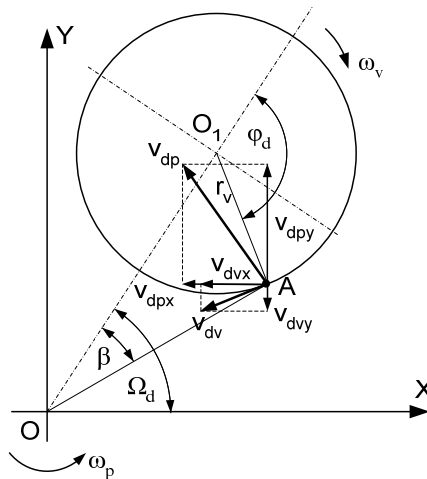


Figure 3. Interpretation of the detachment velocity

Based on the indications of Figure 3, the peripheral velocity resulting from the rotation of the vial and its X and Y direction components are:

$$v_{dv} = r_v \cdot \omega_v \tag{2.22}$$

$$v_{dvx} = - \left[ v_{dv} \cdot \cos \left( \frac{\pi}{2} - (\varphi_d - \Omega_d) \right) \right] = - [r_v \cdot \omega_v \cdot \sin(\varphi_d - \Omega_d)] \tag{2.23}$$

$$v_{dvy} = - \left[ v_{dv} \cdot \sin \left( \frac{\pi}{2} - (\varphi_d - \Omega_d) \right) \right] = - [r_v \cdot \omega_v \cdot \cos(\varphi_d - \Omega_d)] \tag{2.24}$$

Similarly, the X and Y direction components resulting from the peripheral velocity of the sun disk can be stated:

$$v_{dp} = \overline{OA} \cdot \omega_p \quad (2.25)$$

where  $OA$  is the distance between the centre of the sun disk and the detachment point 'A':

$$\overline{OA} = \sqrt{r_p^2 + r_v^2 - 2 \cdot r_p \cdot r_v \cdot \cos(\pi - \varphi_d)} \quad (2.26)$$

$$v_{dpx} = - \left[ v_{dp} \cdot \cos\left(\frac{\pi}{2} - (\Omega_d - \beta)\right) \right] = - \left[ \overline{OA} \cdot \omega_p \cdot \sin(\Omega_d - \beta) \right] \quad (2.27)$$

$$v_{dpy} = v_{dp} \cdot \sin\left(\frac{\pi}{2} - (\Omega_d - \beta)\right) = \overline{OA} \cdot \omega_p \cdot \cos(\Omega_d - \beta) \quad (2.28)$$

Based on the above the detachment velocity and its X and Y direction projections can be stated as:

$$V_{dx} = V_{dvx} + v_{dpx} \quad (2.29)$$

$$v_{dx} = -r_v \cdot \omega_v \cdot \sin(\varphi_d - \Omega_d) - \overline{OA} \cdot \omega_p \cdot \sin(\Omega_d - \beta) \quad (2.30)$$

$$V_{dy} = V_{dvy} + v_{dpy} \quad (2.31)$$

$$v_{dy} = -r_v \cdot \omega_v \cdot \cos(\varphi_d - \Omega_d) + \overline{OA} \cdot \omega_p \cdot \cos(\Omega_d - \beta) \quad (2.32)$$

Based on the relations (2.30. and 2.32.) the detachment velocity can be determined:

$$v_d = \sqrt{v_{dx}^2 + v_{dy}^2} \quad (2.33)$$

### 3. Kinetic energy of the milling ball at the moment of impact

From this step on (including detachment velocity determined above) the modell has been further built using our own algorithm. The works of others in known and available literature sources could not be followed as:

- they do not provide calculations concerning the determination of the impact point, despite the fact that this is one of the most difficult and most definitive steps of the model,
- in models related to planetary ball mills the size of the ball is neglected, i.e. it is considered to be point-like. This simplification is not acceptable. Figure 5 shows that the angle  $\varphi_c$  belonging to the real impact point ( $B$ ) may even be a multiple of the value, which would be determined in case of a point-like ball (point  $B'$ , angle  $\varphi_c'$ ).

The calculation steps of the location of impact is given in details in this chapter in a way that even the dimensions of the ball are taken into account.

In order to determine the useful kinetic energy of the ball, the absolute velocity of the point of impact should be known. The difference between the velocity calculated in the impact point and the detachment velocity gives the relative velocity of the ball and the vial, i.e. the actual impact velocity. The projection of this velocity on the radius direction of the vial will be the velocity component, which is useful from the aspect of milling, so it should be taken into account when determining kinetic energy.

As the wall detaches from the wall of the vial, it is supposed that it will move straight and even with its detachment velocity. Gravitational acceleration is perpendicular to the inspected movement plain, so only the resistance of medium influences the movement velocity of the ball, however, this influence is neglected. Kinetics of rigid bodies will be applied for the description of the free motion of the ball, until it meets the vial again. Figure 4 demonstrates the motion of the ball from the detachment to the impact, where points 'A' and 'B' indicate the location of detachment and impact.

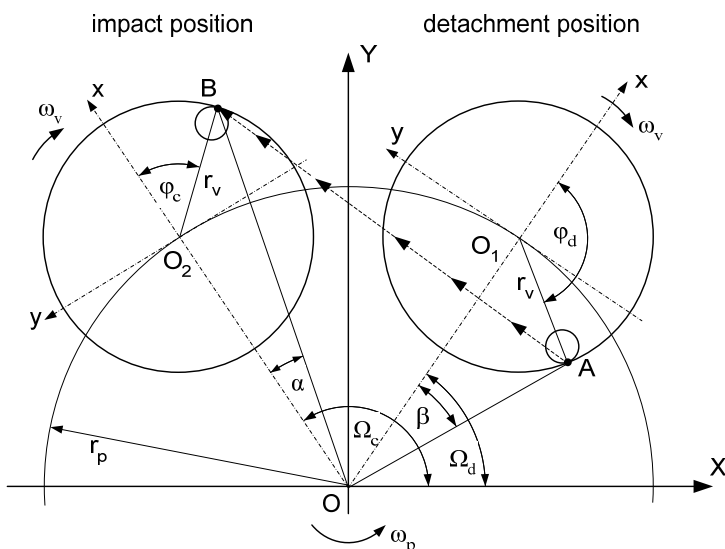


Figure 4. Motion of the ball from the detachment to the impact



Based on Figure 5 the geometrical principles concerning the triangle  $OC_2O_2$  are as follows:

$$\frac{\sin\alpha_1}{\sin(\varphi_c - \alpha_1)} = \frac{r_v - r_b}{r_p} \tag{3.2}$$

$$\overline{OC_2}^2 = r_p^2 + (r_v - r_b)^2 - 2 \cdot r_p \cdot (r_v - r_b) \cdot \cos(\pi - \varphi_c) \tag{3.3}$$

Also based on Figure 5, the following relationships are true in case of triangle  $OC_1C_2$ :

$$\frac{\sin(\pi - \gamma - (\Omega_c \pm \alpha_1))}{\sin(\Omega_c - \Omega_d \pm \alpha_1 + \beta_1)} = \frac{\overline{OC_1}}{C_1C_2} \tag{3.4}$$

$$\overline{C_1C_2}^2 = \overline{OC_1}^2 + \overline{OC_2}^2 - 2 \cdot \overline{OC_1} \cdot \overline{OC_2} \cdot \cos(\Omega_c - \Omega_d \pm \alpha_1 + \beta_1) \tag{3.5}$$

Despite the fact that these are basic mathematical and physical relationships, the relationships (3.1-3.5) together form a non-linear system of equations with five unknowns, in which the unknown parameters are the angle of impact ( $\varphi_c$ ), the angle position of the vial at the moment of impact ( $\Omega_c$ ), the distance of the ball centre from the axis of rotation of the sun disk ( $OC_2$ ) and from the point of detachment ( $C_1C_2$ ), and the angle ( $\alpha_1$ ) included between  $OC_2$  and  $OO_2$ . The determination of parameters ' $\varphi_c$ ' and ' $\Omega_c$ ' are directly, while the above mentioned other parameters are only indirectly necessary for determining the absolute velocity of the point of impact. Finding the solution for the problem is further aggravated by the fact that if the point of impact is to the right or to the left from  $OO_2$ , then  $\alpha_1$  will have a negative or positive sign in the equations.

Further attention is necessary during the solution for the fact that variables may take up values in different intervals in identical phases of the motion. Knowing the geometrical parameters of a given mill, calculations were carried out between limit values determined by designing (see later, chapter 4). The above system of equations can be solved numerically (using gradient method).

*Determining the velocity of the impact point ( $v_b$ )*

After determining the position ( $\Omega_c$ ) and angle ( $\varphi_c$ ) of impact in the previous point, the two components of the absolute velocity of the point,  $v_{bx}$  and  $v_{by}$ , can be calculated in the impact point 'B', within the X – Y co-ordinate system. The velocity of the impact point ( $v_b$ ) at point 'B' is given by the sum of the peripheral velocity of the sun disk ( $v_{bp}$ ) and the peripheral velocity of the vial ( $v_{bv}$ ).

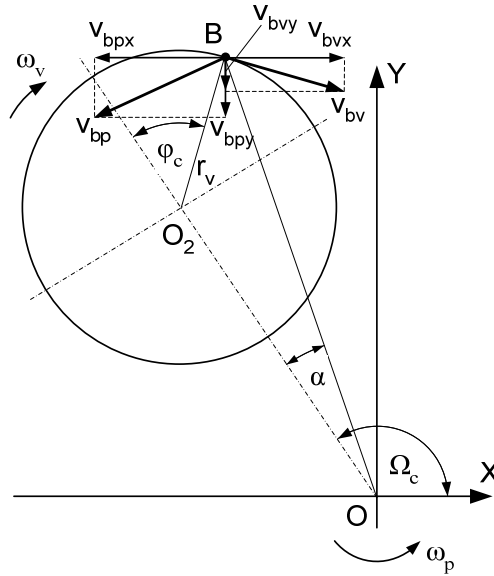


Figure 6. Interpreting the velocity of the point of impact

Based on the indications in Figure 6, the peripheral velocity resulting from the rotation of the vial, and its X- and Y-direction components are:

$$v_{bv} = r_v \cdot \omega_v \quad (3.6)$$

$$v_{bv_x} = v_{bv} \cdot \cos\left(\frac{\pi}{2} - (\Omega_c - \varphi_c)\right) = r_v \cdot \omega_v \cdot \sin(\Omega_c - \varphi_c) \quad (3.7)$$

$$v_{bv_y} = -\left[v_{bv} \cdot \sin\left(\frac{\pi}{2} - (\Omega_c - \varphi_c)\right)\right] = -[r_v \cdot \omega_v \cdot \cos(\Omega_c - \varphi_c)] \quad (3.8)$$

Similarly, X- and Y-direction components resulting from the peripheral velocity of the sun disk can also be stated:

$$v_{bp} = \overline{OB} \cdot \omega_p \quad (3.9)$$

where,  $OB$  is the distance between the centre of the sun disk and the point of impact 'B':

$$\overline{OB} = \sqrt{r_p^2 + r_v^2 - 2 \cdot r_p \cdot r_v \cdot \cos(\pi - \varphi_c)} \quad (3.10)$$

$$v_{bpx} = - \left[ v_{bp} \cdot \cos \left( (\Omega_c - \alpha) - \frac{\pi}{2} \right) \right] = - \left[ \overline{OB} \cdot \omega_p \cdot \sin(\Omega_c - \alpha) \right] \quad (3.11)$$

$$v_{bpy} = - \left[ v_{bp} \cdot \sin \left( (\Omega_c - \alpha) - \frac{\pi}{2} \right) \right] = \overline{OB} \cdot \omega_p \cdot \cos(\Omega_c - \alpha) \quad (3.12)$$

The sign of  $v_{bpx}$  (3.11) is negative in all cases. However, the sign of  $v_{bpy}$  (3.12) is positive if the point of impact falls to the right from the Y-axis of the absolute co-ordinate system, and it is negative, if it falls to the left.

Based on these the X- and Y-direction projections of the velocity of the impact point can be stated:

$$v_{bx} = v_{bv_x} + v_{bpx} \quad (3.13)$$

$$v_{bx} = r_v \cdot \omega_v \cdot \sin(\Omega_c - \varphi_c) - \overline{OB} \cdot \omega_p \cdot \sin(\Omega_c - \alpha) \quad (3.14)$$

$$v_{by} = v_{bv_y} + v_{bpy} \quad (3.15)$$

$$v_{by} = -r_v \cdot \omega_v \cdot \cos(\Omega_c - \varphi_c) + \overline{OB} \cdot \omega_p \cdot \cos(\Omega_c - \alpha) \quad (3.16)$$

The velocity components  $v_{ix}$  and  $v_{iy}$  of the absolute impact velocity are the difference between the detachment velocity (2.30, 2.32) and the corresponding velocity components of the impact point (3.14, 3.16):

$$v_{ix} = v_{dx} - v_{bx} \quad (3.17)$$

$$v_{iy} = v_{dy} - v_{by} \quad (3.18)$$

$$v_i = \sqrt{v_{ix}^2 + v_{iy}^2} \quad (3.19)$$

#### *Determining the impact energy ( $E_b$ ) and the milling power ( $P$ )*

In order to determine the kinetic energy of the ball, i.e. the impact energy, the normal direction component of the absolute impact velocity needs to be determined. The angle, where the impact of the ball is on the wall of the vial ( $\varphi_c$ ), determines the amount of energy that can be transferred to the powder particles on the wall of the vial by the ball. The effective impact velocity generating the impact energy is the normal direction component of the impact velocity, broken up into the radius direction of the vial. With the marks used in Figure 7 the normal direction component can be calculated using the relationship

$$v_{in} = v_{ix} \cdot \cos\lambda + v_{iy} \cdot \sin\lambda, \quad (3.20)$$

and the tangent direction velocity component with the relationship

$$v_{it} = -v_{ix} \cdot \sin\lambda + v_{iy} \cdot \cos\lambda \quad (3.21)$$

where  $\lambda$  is the angle demonstrated on Figure 7.

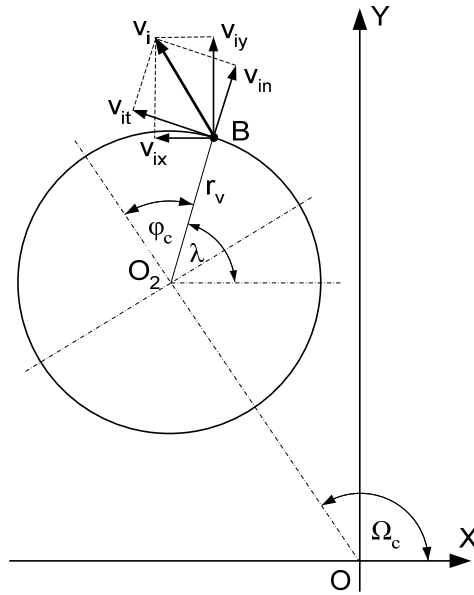


Figure 7. Interpretation of the normal and tangential direction components of the absolute impact velocity

After determining the above, the effective impact energy released at one single collision during the mechanical milling process can be calculated as follows:

$$E_b = \frac{1}{2} \cdot m_b \cdot v_{in}^2 \quad (3.22)$$

- where  $m_b$ : is the mass of the milling ball [kg]
- $v_{in}$ : is the effective impact velocity [m/s]
- $E_b$ : is the impact energy released at the collision [J].

The energy determined using the relationship 3.22. is transferred from the milling balls to the powder particles as many times as the balls hit the wall of the vial. The impact frequency is the number of times the ball hits the vial in one

second. Knowing the total period of time the time passing between the first and the second detachment should be known in order to calculate the frequency of the impacts. Each cycle can be broken down to two periods:  $T_1$  is the period of time during which the ball gets from the first detachment point to the first impact, and  $T_2$  is the period of time from the first impact until the second detachment.  $T_1$  can be calculated from (3.1), and  $T_2$  can be determined based on the following relationship:

$$T_2 = \frac{\Phi_d - \Phi_c}{\omega_v} \quad (3.23)$$

Since the period time of the cycle is the sum of  $T_1$  and  $T_2$ , the impact frequency  $f_b$  can be calculated. The impact frequency actually in this case means the number of impacts per second.

$$f_b = \frac{1}{T_1 + T_2} \quad (3.24)$$

This impact frequency corresponds with the impact of the single ball in the vial. Taking the fact into consideration that in practice milling is not carried out using one ball, that is taking the number of balls in the vial into consideration, the effective impact frequency  $f_{eff}$  can be determined. However, it is supposed that there are few balls in the vial to hinder the movement of each other.

$$f_{eff} = f_b \cdot N_b \quad (3.25)$$

where  $N_b$ : is the number of balls in the vial.

Knowing the energy released by the impact ( $E_b$ ) and the effective impact frequency ( $f_{eff}$ ), the power of the milling process ( $P$ ) can be determined.

$$P = f_{eff} \cdot E_b \quad (3.26)$$

The above described power may be suitable for comparing millings carried out using different impact energies. Greater power means that shorter milling time is necessary for the milling process.

Based on the calculation method introduced in this chapter, the impact energy of the ball and the impact frequency of the ball can be calculated, and it is apparent that these can be regulated independent from each other if the milling parameters are correctly configured. By changing the number of balls the ball impact frequency ( $f_{eff}$ ) can be changed, while the impact energy of the ball ( $E_b$ ) does not change. On the other hand, by changing the diameter ( $d_b$ ) and density ( $\rho_b$ ) of the ball, the impact energy of the ball can be changed without changing the impact frequency of the ball.

Let us note again that the model described is true and valid only if  $i_{limit} \leq i \leq i_{critical}$  is true on the rate of the rotary speeds of the sun disk and the vial (that is on the ratio ( $i$ )).

#### 4. Application of the model and calculation results

Using the calculation method described in chapters 3.1. and 3.2. the milling energy values of FRITSCH P4 planetary ball mill applicable for milling experiments were determined by different configuration parameters. Different sun disk rotary speed values and ratios were taken into consideration by the calculations and at the same time the inspection of the full rotary speed range of the mill was aimed at, together with the path of motion of the balls to comply with the impact and friction method, that is  $i_{limit} \leq i \leq i_{critical}$ . In the model set up, the breaking effect on the balls of the mill product moving together with the balls was not taken into account.

Since calculations were carried out on a given mill type, certain initial parameters were given. These were mainly the features of the device:

- distance between the sun disk and the vial:  $r_p = 0,125 \text{ m}$
- sun disk rotary speed range for test:  $n_p = 50 - 400 \text{ min}^{-1}$

Selection of further initial values determined by us was carried out based on the equipment available for the mill:

- inner radius of the vial (80 ml):  $r_v = 0,0325 \text{ m}$
- radius of the milling ball:  $r_b = 0,005 \text{ m}$
- density of the milling ball (stainless steel):  $\rho_b = 7800 \text{ kg/m}^3$

Knowing the above determined geometrical parameters ( $r_p$ ,  $r_v$ ), with the relationship 2.21. even the extreme values ( $i_{limit}$ ,  $i_{critical}$ ) of the ratio ( $i$ ) can be determined, which indirectly influence even the rotary speed of the vials together with the rotary speed of the sun disk, concerning the inspected range. Extreme values of the ratio ( $i$ ) are:

- bottom limit:  $i_{limit} = 0,96$
- upper limit:  $i_{critical} = 2,96$

Calculations using the model set up in point 3. were carried using values  $i = 1; 1,5; 2; 2,5; 2,96$ .

In the first part of the calculations, that is by the determination of the detachment angle and the detachment velocity it was found that in case of fixed geometrical conditions ( $r_p$ ,  $r_v$ ,  $r_b$ ) and ratio ( $i$ ) identical detachment angle values belong to an increasing sun disk rotary speed, while the value of the detachment velocity increases in ratio with the rotary speed of the sun disk.

After calculating the impact angle and velocity, the theoretical impact energy values belonging to the different sun disk rotary speed values were determined using the relationships of the previous subsection, for a single ball. The calculation results are shown on Figure 8.

It can be seen in Figure 8 that by increasing the rotary speed of the sun disk, the value of the impact energy increases squared up to a certain ratio. It can be

seen that by  $i=2,96$  speed ratio the curve of the impact energy is between the curves  $i=1,5$  and  $i=2$ . This results in that probably there is an optimal value between the values  $i=2$  and  $i=2,96$ , where the impact energy is the greatest possible. This assumption is verified by the set of curves shown on Figure 9. The curves indicate the change of the impact energy by increasing the ratio, belonging to different rotary speed values of the sun disk. Looking at the diagram it can be found that by given geometrical conditions and configured parameters, the greatest impact energy can be achieved by approximately  $i=2,5$ . If the impact frequency of the balls can also be taken into account, which is mainly the function of the detachment and impact angles, then using the relationship 3.25. the power of the milling process can be determined.

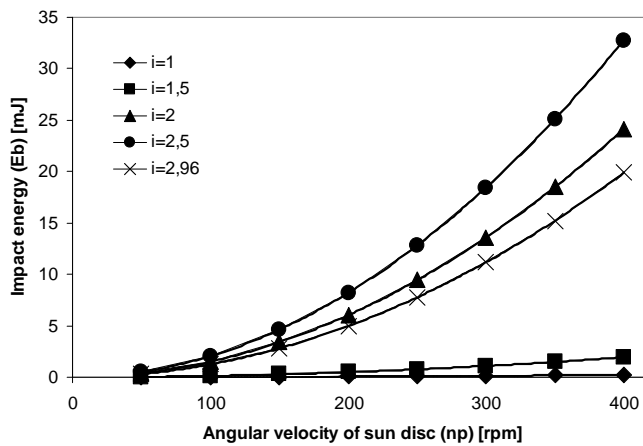


Figure 8. Change of the impact energy ( $E_b$ ) as a function of the sun disk rotary speed ( $n_p$ ) and the ratio ( $i$ )

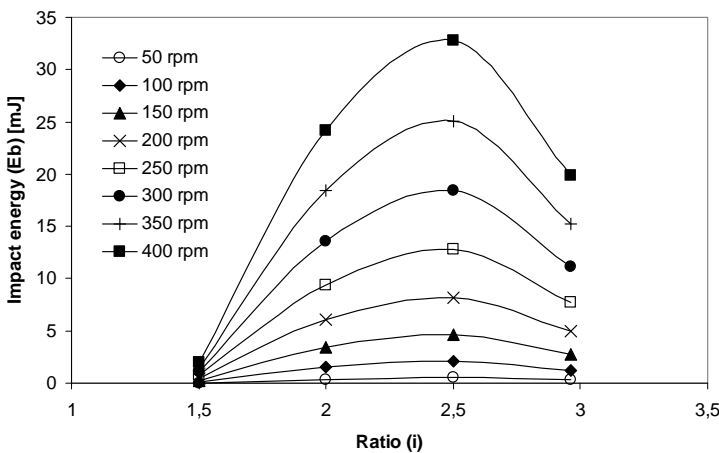


Figure 9. Changes of the impact energy ( $E_b$ ) as a function ( $E_b(i)$ ) of increasing the ratio ( $i$ ) by different rotary speeds values ( $n_p$ )

When inspecting theoretical power values belonging to different sun disk rotary speed values and velocity rates (Figure 10), it can be found that greater and greater power values belong to increasing rotary speed values. The curves calculated are cubic ones.

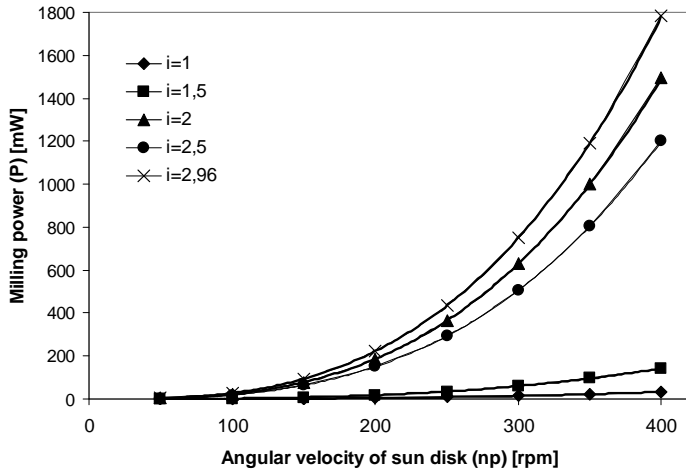


Figure 10. Changes of the milling power (P) as a function ( $P(n_p)$ ) of the sun disk rotary speed ( $n_p$ ) and the ratio (i)

In opposition to the changes of the impact energy shown in Figure 8, it can be observed on Figure 10 that the values of the curve belonging to  $i=2.5$  are lower than those belonging to  $i=2$  and  $i=2.96$ . The result is surprising as lower power belongs to a velocity ratio causing the greatest impact energy. This can be explained by the fact that in the case of this ratio ( $i=2.5$ ) the impact frequency is lower, that is the balls spend more time on the wall of the vial.

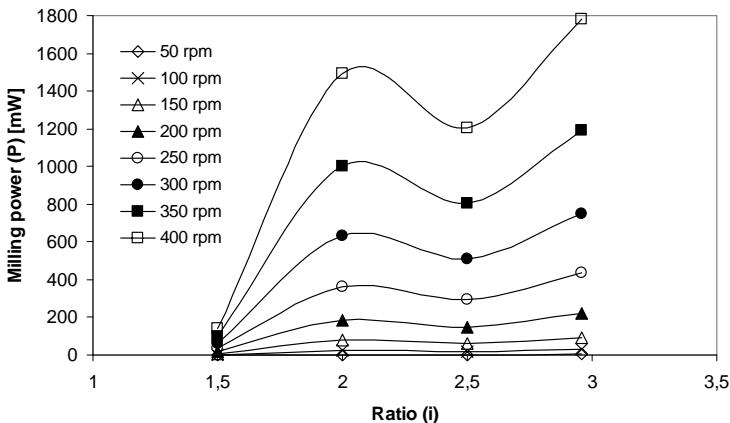


Figure 11. Changes of the milling power (P) as a function ( $P(i)$ ) of increasing the ratio (i) at different sun disk rotary speed values ( $n_p$ )

If the milling power is represented as a function of the ratio, at different sun disk rotary speed values (Figure 11), then the optimum velocity rate from the aspect of milling power can be determined. On Figure 11 this is around the value  $i=2,96$ .

Using Figures 9 and 11 such an optimum range of ratio can be highlighted, which is maximal from the aspect of both the impact energy, and the milling power. This range, by the above determined geometrical parameters, is without doubt between  $i=2-2,5$ .

The calculation results (charts) of the model we have established were determined for given initial parameters, demonstrating the applicability of the method, it is still suitable in case of arbitrarily selected other configuration and geometrical parameters for characterizing the milling process in a planetary ball mill. Of course, it is essential that the selected geometrical parameters should be like that the condition  $i_{limit} \leq i \leq i_{critical}$  is always fulfilled for the speed rate range.

*Effects of the size changes of the milling ball and the vial, and the number of balls*

The above described results were determined by fixed ball and vial sizes. In order to inspect the effect of the size changes of the milling set (ball, vial) on the impact energy and power, further calculations were carried out.

First only the size changes of the vial were inspected by the same ball size, then the size of the ball was increased, and the size of the vial remained unchanged, and finally, both the ball size and the vial size were doubled. The main initial parameters of the calculations are summarized in Table 1.

Table 1. Initial parameters of the calculations inspecting the effect of the changes of the ball size and the vial size

Studied events	Configured parameters				
	$n_p$ [rpm]	$i$	$r_p$ [m]	$r_v$ [m]	$r_b$ [m]
simple vial and ball size	400	2	0,125	0,0325	0,01
double ball size	400	2	0,125	0,0325	0,02
double vial size	400	2	0,125	0,065	0,01
double vial and ball size	400	2	0,125	0,065	0,02

The diagram showing the changes of the impact energy are illustrated in Figure 12.

It can be seen in the figure that the calculation results well demonstrate and reflect the impact energy increase expected. The results show that the increase in the vial size does not have such an effect on the increase of the impact energy, as the change of the ball size. By increasing the size of the milling set (ball, vial) together results in the greatest impact energy.

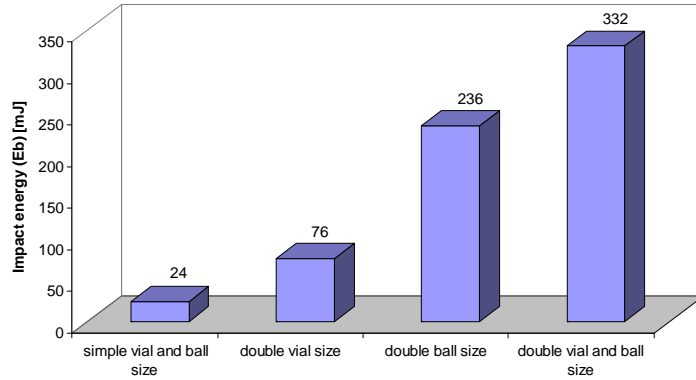


Figure 12. Development of the impact energy due to the changes of the ball size and the vial size

The change of the milling power has a slightly smaller increase (Figure 13).

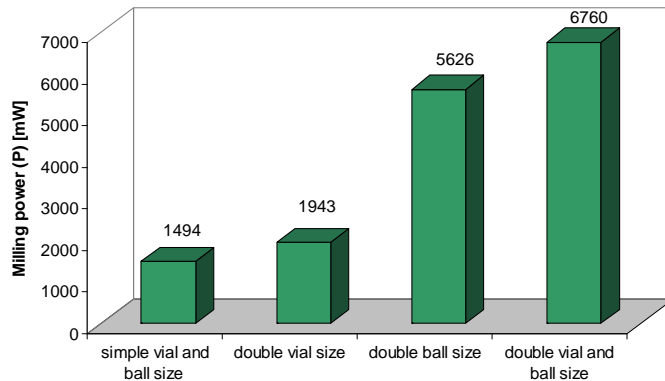


Figure 13. Development of the milling power due to the changes of the ball and the vial

Table 2. Results of the calculations inspecting the effects of ball and vial size

	simple vial and ball size	double vial size	double ball size	double vial and ball size
Impact energy [mJ]	24	76	236	332
Impact energy increase in per cent [%]	100	315	978	1375
Milling power [mW]	1494	1943	5626	6760
Milling power increase in per cent [%]	100	130	377	452

Studying Figure 13 it can be stated that increasing the dimensions of the milling set undoubtedly results in the increase of the milling power, however, this change is not of such degree as in case of increasing the impact energy. This is even proved by Table 2. comparing the calculation results.

## 5. Summary

A calculation method was introduced above on determining the performance of a planetary ball mill.

In chapter 2 the calculations of Lü and Lai were used as a starting point. In chapter 3, starting from determining the impact location of the balls we have departed from the original (Lü and Lai) model, and using our own calculations the impact location and velocity of the milling ball was determined, and from these the milling energy and power were found out. From the calculated data and diagrams, in case of a given milling task the optimal milling parameters can be highlighted, which make effective work possible. Although, calculation results described in chapter 4 were determined and shown on a certain type of mill (Fritsch Pulverisette 4) and given geometrical conditions, but the model can be used for any planetary ball mill, observing the marginal conditions we have also indicated.

As a summary, it can be stated on the effect of the sizes of the milling ball and the vial on the impact energy and power, that if further milling sets are available, then using those may help gain further energy from our planetary ball mill (by the same sun disk rotary speed and ratio), increasing the efficiency of milling and decreasing the time of milling.

Based on the calculation results and the charts (Figures 9 and 11) an optimal mill configuration can be defined, which provides for the most effective work from the aspect of the milling task. In this way, for example in case of milling certain materials, smaller impact energy can also make fast work possible, saving the milling set and the loading the mill less.

## 6. Acknowledgement

This work was supported by OTKA grants K 73776 in Hungary.

## References

- C. Suryanarayana, *Non-Equilibrium Processing of Materials* (Pergamon Press, Amsterdam, 1999)
- C.C. Koch // *Nanostructured Materials 2* (1993) 109.
- J.S. Benjamin // *Scientific American* 234 (1976) 40.

- P.S. Gilman, J.S. Benjamin // *Annual Review of Materials Science* 13 (1983) 279.
- B.S. Murty, S. Ranganathan // *International Materials Reviews* 43 (1998) 101.
- T.H. Courtney // *Mater. Trans. JIM* 36 (1995) 110.
- T.H. Courtney, D. Maurice // *Scripta Mater.* 34 (1996) 5.
- P.Le Brun, et al. // *Materials Science and Engineering A* 161 (1993) 75.
- J. Raasch // *Chemical Engineering & Technology* 15 (1992) 245.
- M. Abdellaoui, E. Gaffet // *Acta Metall. Mater.* 43 (1995) 1087.
- L. Lü, M.O. Lai: *Mechanical Alloying*, (Kluwer Academic Publishers, Massachusetts, 1998) p. 273.
- N. Burgio, et al. // *Il Nuovo Cimento* 13 (1991) 459.
- M. Abdellaoui, E. Gaffet // *Journal of Alloys and Compounds* 209 (1994) 351.
- M. Magini, et al. // *Scripta Mater.* 34 (1996) 13.
- M. Magini, A. Iasonna // *Mater. Trans. JIM*, 36 (1995) 123.
- A. Iasonna, M. Magini // *Acta Mater.* 44 (1996) 1109.
- T. Rojac, et al. // *Journal of the European Ceramic Society* 26 (2006) 3711.

# Measuring the coefficient of friction of chopped materials

Péter KAJTÁR, Péter SZENDRŐ

Szent Istvan University, Faculty of Mechanical Engineering

Andreas HAFFERT

University of Bochum, Faculty of Mechanical and Electronics Engineering

## Abstract

Forage harvesters are achieving ever great performance and throughputs. The type of material transportation means that these machines have very high friction loss levels. The product flow in the forage harvester must be analysed in order to reduce these losses. The friction coefficients of chopped grass and maize must first be determined. To obtain a precise measurement of the coefficients of friction, a test stand is constructed on which different tests can be carried out using various settings.

## Keywords

forage, chopping, cut, friction

## 1. Introduction

The forage harvester is one of the most important machines in forage harvesting. It is used to chop grass and maize to ensure better preservation. The material is picked up by an appropriate front attachment and conveyed to the chopping drum by the compression rollers. The drum cuts the product to the preset length of cut, accelerates it and conveys it onward using kinetic energy.

A modern forage harvester has a throughput of over 400 t/h and an engine performance of over 800 hp. In order to process this higher throughput, the product must be conveyed through the forage harvester at speeds of over 40 m/s. At this high performance level the losses in the product flow, e.g. friction, flow, acceleration and impact losses may be especially high and substantially increase the fuel consumption.

The aim of this project is to determine the friction losses in a forage harvester. Some improvements will then be suggested which may reduce these losses.

A test stand needs to be built to be able to determine the coefficient of friction of chopped materials. Some data is available from previous testing, though this was measured at lower speeds and loadings.

Wieneke measured friction coefficients of between 0.2 and 1.4 for grass. The big difference results from the variations in roughness of the surfaces.

Lobotka carried out tests on chopped maize. He measured friction coefficients of 0.5 - 0.6.

## 2. Test stand

Measuring the friction coefficient of chopped materials is a major challenge.

Because of the material structure, precise values for grass or maize are not possible, as they depend on several parameters. Variables include the moisture content of the material, the relative speed, the loading, length of cut and roughness of the surface. The most important parameter, however, is the material pairing. Substantial differences arise from the material sliding over different materials. By using the test stand, friction coefficients of chopped materials can be determined by with different material pairings and at different settings. The first stage of developing a test stand is drawing up a list of requirements. It should be possible to infinitely measure relative speeds up to 40 m/s and standard pressures up to 1 bar.

The test stand operates on a similar functional principle to that of a disc brake. The basic rotating disc can be fitted with various surfaces. The chopped materials in the material holder are pressed against the rotating disc from below by a pneumatic cylinder (see Fig. 1).



Figure 1. Test rig

The advantages of this principle are the even loading and the low speed differences between the inner and outer radius.

The coefficient of friction is determined by measuring the friction force tangentially to the surface and the normal force perpendicular to the surface. The material holder is attached to bars fitted with wire strain gauges (WSG), arranged to suit the relevant loadings.

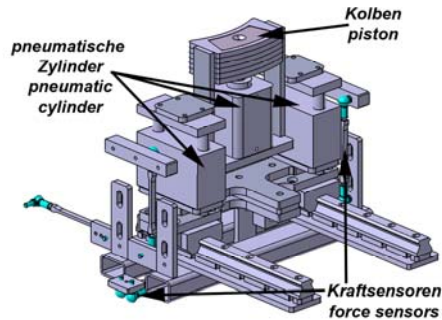


Figure 2. Material keeper

Three bars keep the material holder vertical and one governs its tangential orientation. There are two additional bars to stabilise the material holder in relation to the frame. During the test, the reaction forces are captured by the WSGs. The advantage of this solution is the ability to measure the coefficients of friction precisely, even at high speeds. The disc is driven by a hydrostatic drive, so that the relative speed between product and test surface can be set infinitely and precisely. The speed of the rotating disc is determined by a sensor and converted to an average speed over the whole radius. The pressure loading can also be infinitely adjusted by means of a special pneumatic pressure relief valve. The measurement time is adjusted by a delay valve, which returns all valves to the home position on completion of the measurement.

This also moves the material holder back to the home position.

Key technical data:

- Disc diameter 500 mm
- Width of the test surface 50 mm
- Thickness of the test disc 5 mm
- Relative speed 5-40 m/s
- Pressure 0.05-1 bar
- Measuring period 0.2-3 sec

The measurements are taken with different lengths of cut and moisture content for the same chopped material sample.

The chopped material is dried naturally to ensure that the structure of the grass remains unchanged. When measuring, only one parameter is changed at a time, in order to determine the effect of that parameter. First, the loading is kept the same and the speed changed, then the speed is kept constant and the loading varied. The test is repeated three times for each setting. The coefficient of friction is determined as an average of the data obtained.

### 3. Results

The material being tested is freshly chopped grass with a length of cut of 17 mm. In order to determine the effect of the moisture content of the material the

material was dried over a period of 4 days and a friction test carried out daily. The duration of all measurements was limited to 1 second, in order to obtain results that are as real as possible. One problematic aspect is that the product heats up substantially from the friction at high speeds and loadings. This also changes the coefficient of friction.

As stated above, during the tests the reaction forces are measured tangentially (friction force) and perpendicular to the surface (normal force) using wire strain gauges. The coefficient of friction is calculated in accordance with Coulomb's friction law.

$$\mu = \frac{F_{\text{friction force}}}{F_{\text{normal force}}}$$

Fig. 3 shows an example of the coefficient of friction trend.

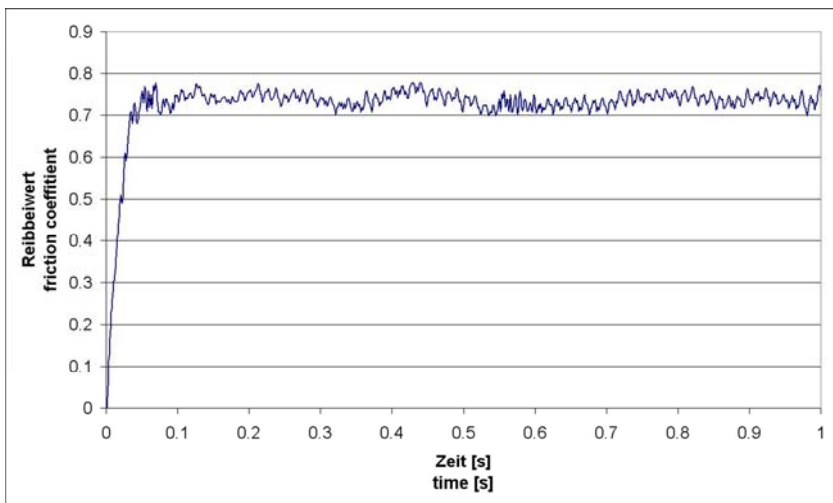


Figure 3. Trend of coefficient of friction

At the start of the measurement, the coefficient rises steeply and reaches the actual value at constant loading with a low level of fluctuation. To enable the comparison of friction coefficients from different tests a standard must be defined to govern how the measurement is read off. The coefficient of friction is read off as soon as the preset value for the normal force is reached. This is particularly important at high speeds and heavy loading, as the structure of the material changes quickly due to the heat, which means that a delayed reading will lead to incorrect results. This solution ensures that the measurement results can be compared precisely.

Fig. 4 shows the coefficient of friction trend for different lengths of cut.

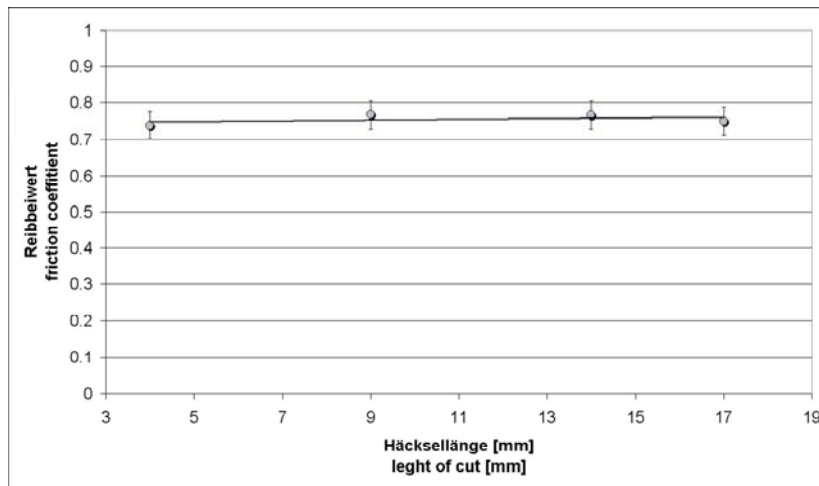


Figure 4. Friction coefficient by different length of cut

It can be seen clearly that the effect of the length of cut is very low on grass. This is an interesting result, as with smaller lengths of cut, more particles come into contact with the surface. These additional contacts and the resultant adhesive power only have a very slight effect on the coefficient of friction.

#### 4. Conclusion

In order to be able to determine the friction losses in a forage harvester, the friction coefficients of grass and maize must first be determined. To do this, a test stand is constructed, with which the coefficient of friction between chopped green forage and various surfaces can be measured. Previous tests have shown that the friction coefficient of grass is very high. It is above 0.7 and therefore increases the power requirement of the forage harvester.

Further tests must be carried out to determine the friction coefficient of chopped maize. Other tests will be undertaken at a later stage with different surfaces (roughness, profile, material). On the basis of these tests, solutions can be found for reducing the friction losses of the forage harvester.

#### References

- F. Wieneke: Reibungswerte von Pflanzen und Faserstoffen (friction coefficients of plants and fibres). Munich: Landtechnische Forschung (1956), Issue 5, p. 146
- Lobotka J.: Friction coefficients of bulk chopped fodder plants (Orig. in Czech) Zemědělska technika 81 (1967), No. 2, p. 93

# **The quality of metal surface resulted after cutting with laser**

Mircea LOBONȚIU, Ciprian MELIAN  
North University of Baia Mare, Faculty of Engineering

## **Abstract**

The metal surfaces quality resulted after cutting with laser beam have an important role in estimating the benefits with this type of processing. This paper tries to present some aspects of surfaces quality resulted after cutting with laser beam especially roughness and some parameters which influence the measured results and the roughness values calculation.

## **Keywords**

laser, cutting, surface, quality

## **1. Introduction**

Surface quality resulting after laser cutting process can be interpreted and characterized in terms of the roughness size results, the general appearance of the surface through the existence or absence dross (burr) and crater that can appear on the resulted surface after laser cutting process. Cutting applications in industry are used by processes cutting with oxygas, plasma and laser. Using laser cutting method makes possible the cutting of ferrous or nonferrous metals of different qualities and thicknesses, each method is applicable to certain types of metals having in view the price-quality operations.

## **2. Aspects of the laser cutting process**

Laser cutting: it is the technological operation through which is a made partial or total detachment of part of a material, with purpose in order to process it. Laser cutting is a process based on thermal effects of radiation without generating chip that performs the removal of material particles from a solid object without mechanical action.

Symbols under Standard ISO 9013:2002 (E)

Laser cutting is attained by movement of the laser beam along a contour of a landmark which could be cut. Ray laser is a “cutting tool” used to make very small cuts width between 0.1 .... 0.2 mm.

The cutting process setting is done according to the required precision of cut pieces, material hardness, quality and the energy consumption of the process.

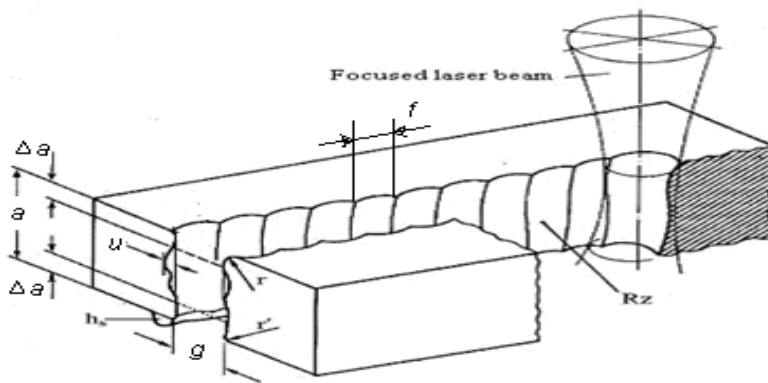


Figure 1. Laser Cutting [adapted by M. Radovanovici] ( $a$  – cut thickness,  $\Delta a$  – thickness reduction,  $g$  – bottom kerf width,  $h$  – burr on the cut base surface,  $f$  – distance between the two points of a drag line,  $r$  – melting of top edge,  $Rz$  – mean height of the profile)

Cutting operation should provide:

- a low roughness of the separated surface;
- high accuracy of the volume or of the length part;
- achieve some semi-finished products with a greater length than the cross section;
- deviations of the geometric shape of the part which must be within the limits of tolerance provided by the documentation specified.

### 3. Quality surface cutting with laser technology

*Laser cutting advantages:*

- there is no physical contact with the piece of work, internal tensions, strains and wear parts being reduced or eliminated;
- due to the very low duration of the completion of processing, the heat affected zone, adjacent to the cutting zone is minimal;
- maximum efficiency in cutting metal sheets and pipes, resulting little loss of material;
- the possibility of processing a wide range of metallic and non-metallic materials;
- minimum costs by minimizing training / discharge time;
- complete automation of the entire process;
- can be cutting pieces with high complexity form with a high degree of accuracy;
- the reduction of the finishing operation on the part resulted after this laser cutting process;
- increasing the efficiency of mass production
- high surface quality resulting from laser cutting, regarding roughness and their geometrical accuracy.

*Aspects of quality surface resulting after laser cutting process:*

In accordance with ISO 9013:2002, surface quality resulted after cutting with this thermal processing, shall be assessed according to the following :

- Perpendicular or angularity tolerance,  $u$ ;
- Mean height of the profile,  $Rz$ ;
- Drag  $n$ ;
- Melting of top edge,  $r$ ;
- Possibly occurrence of dross or melting drops on the lower edge of the cut,  $h$ ;

(see fig. 1. and fig. 2.):

*Influencing elements of the laser cutting surface quality Heat affected Zone –HAZ*

Because of during the laser cutting process, it is being actuated with a great amount of energy which can produce modification of the steel property and microstructure on a narrow area adjacent to the cutting laser. These changes are generally harmful for corrosion resistance of steel.

**Thermal deformation** is an unwanted effect caused by heat acting on the material, subject to cutting, which tend to distort.

**4. Analysis and roughnes interpretation after cutting with laser beam**

The surface resulting after the cutting with laser is mostly characterized by multiple grooves which define roughness. These grooves are parallel with a very small distance between them and they have an incline (they form a curve with the reference line) to their root towards the reference line contrary to sense of advance of cutting with laser beam. The cut surface can reveal two zones: the upper one in the area of the laser beam entrance side (zone I) and the lower one in the area of the laser beam exit side (zone II), see figure 2.

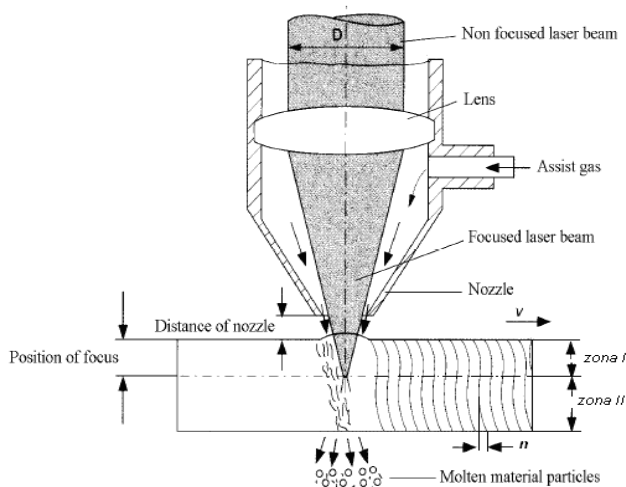


Figure 2. Principle of cutting laser process

Also due to failure or change of some parameters of cutting process, on the resulted surface can appear: crates (missing material), or dross or melting drops on the lower edge of the cut. These are considered error type appear on the surface.

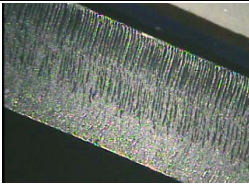
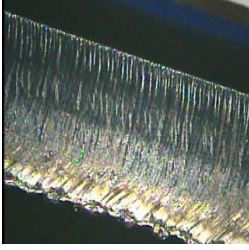
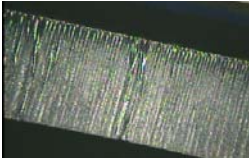
The equipment used for quality inspection of the parts resulting from laser cutting process is calibre, oprice microscopes and roughness tester. Inspection methodology is described in ISO 9013:2002 which provides for the measurement for roughness in cutting technology typically takes place at a distance of 2/3 of the cut thicknesses from upper cut edge, for laser cutting in the upper third from the upper cut edge.

*Experimental results*

To emphasize the speed parameter influence in the technological process of laser cutting, I made an experiment on the cutting machine TRUMPF L4003, I cut on the laser machine a part of sheet steel, St 37, g = 6mm. The setting parameters for this experiment are:

- Laser cutting with CO<sub>2</sub>, CW-Standard
- Focus between: 0 ....+ 0.3 mm,
- Cutting speed ranged between 1.6 .... 1.9 m / min
- Cutting gas Oxygen, pressure: the value of 0.6 bar.

Table 1. Experiment data representation

Nr.	Processing / Change parameter	Photograph of microscopic surface	Observations:
1	According [Book Machine Trumpf, 2000] Cutting Speed 1,7 m/min Cutting gas pressure 0,6 bar		Good surface quality Low values of roughness measurement. Cut surface with two zones
2	Change parameter Cutting with high speed (advance) 2,5 m/min		Deviation of the roughness. Burr, (besprinkle small area on the base material resulting from laser cutting). The grooves bend away from the direction of cutting
3	Change parameter Cutting with low speed (advance) 1,2 m/min		Crater and increased roughness. The grooves run almost parallel to the laser beam.

After the experiments with laser cutting deliberate modification of the parameter rate of cutting speed, a roughness measurements in accordance with the requirements of ISO 9013:2002 and ISO 4288 the consultation of numerous specialized works in this domain, I checked the experimental data obtained using the formula (1). We also tried to observe the correlation between Ra and Rz roughness described in formula (2).

$$R_a = 2.018 \frac{S^{0.670}}{P_L^{0.451} V^{0.330}} \quad (1)$$

$$R_z = 5.3985 R_a \quad (2)$$

#### *Roughness measurements and calculate values*

In table 2 are the roughness measurements values with the Marsurf PS1 roughness tester and the cut-off length was set at 2.5 mm/division in the roughness mode 1 (Range  $\pm 80\mu$ ).

Table 2. Roughness measurements values

Roughness measurements	Surface 1	Surface 2	Surface 3
Ra [ $\mu\text{m}$ ]	4,870	5,423	6,983
Rz [ $\mu\text{m}$ ]	29,8	31,43	35,32

In table 3 are the roughness calculate values for this three surface, with formula (1),(2).

Table 3. Roughness calculate values

Roughness calculate	Surface 1	Surface 2	Surface 3
Ra [ $\mu\text{m}$ ] calculate with formula (1)	5,187	4,565	5,811
Rz [ $\mu\text{m}$ ] calculate with formula (2)	28,2	24,644	31,370

## 5. Conclusions

After experiments and consultation of the specify literature I found that:

1. Laser cutting with high speed is diminishing the depth of penetration and decreases the accuracy and quality of processing.
2. From this experiment it can be observed that, according to the specify literature, that on a surface resulting from the laser cutting with low

- speed, the roughness are parallel to the laser beam and cutting with high-speed, the roughness have a predisposition to the side of their reference line “n” contrary the sense of advance of the cutting laser beam.
3. Comparison between the measurements values made with roughness tester and the roughness values determined by relations (1) and (2). We can see an approximation of the values

## References

- Donțu, O. – Tehnologii de prelucrare cu laser, Bucuresti: Editura tehnica 1985;
- Danilov V. I., Zuev L. B.,2006, Specific features of laser cutting of steel sheets and monitoring of sample quality after laser influence, *Journal of Applied Mechanics and Technical Physics*, Vol. 47, No. 4, pp. 608–615.
- Radovanovic, M., Dašić, P., 2006, Research on surface roughness by laser cut, *the annals of university “dunărea de jos “ of galați*, , 2006 (XII) ISSN 1221-4590;
- \* \* \* ISO 9013-2002 (E) Thermal cutting – clasification of the thermal cuts- Geometrical products specification and quality tolerances.
- \* \* \* - Book Trumpf Machine L4003. Instruction for work and using Trumpf Laser cutting Machine, 2000.
- \* \* \* [www.precolaser.com](http://www.precolaser.com)

# Opportunities of developing cooler-heater system of food industrial tanks

László SZENTESI, István OLDAL, Gábor KALÁCSKA  
Szent Istvan University, Faculty of Mechanical Engineering

## Abstract

Cooling and heating device are important parts of stainless pressure vessels. Stainless materials are expensive so low material cost is important. Hygiene requirements also influence heat surfaces. Aim of researching is determining of a heating surface according to strength and hygiene standards with low cost.

## Keywords

stainless steel, cooling, tank

## 1. Introduction

The German AD 2000 Merkblatt and the European EN 13445 standards gives specifications for design of food industrial tanks with heater shell. Calculation with these standards give thicker wall for heater shell than our products (safety factors are too high in many cases). So the products designed and manufactured by standards are more expensive because of higher cost of material, energy and bigger machines.

Requirements for products are the next:

- Low material cost
- Low cost of human labour
- Simple machine tool requirement
- Wide range application.

The heater shell type is applicable to wide range using for manufacturing of all type double walled heat exchanger and pressure vessel. Nowadays food and chemical industrial products are customized so heater shell is applicable on different products without increasing cost.

## 2. Comparing of heat exchanger types (domestic and international review)

Now in food industry the heater shell type is the common system because this is the most efficient heat exchanger. Developing of manufacturing technology is necessary which keeps energy efficient, fast and flexible, not difficult. And it has to be applicable posterior on existing products. Very important developing of a modelling-design process which is verified experiments and practical experiences.

### 3. Possibilities of developing heater-cooler surfaces, advantages, disadvantages

Heat exchangers are built on food industrial tanks because of hygiene viewpoint. Advantage of these is the next: inner structure of tank doesn't change and stays the same hygiene applicable. But strength properties change because additional outer pressure loads the wall of tank.

Common types:

*Heater pipe type:*

Attributes:

- no additional outer pressure on tank
- higher pressure (5-20 bar) in heater-cooler circle
- low chance of failure
- low heat efficiency (indirect heating)
- difficult and expensive manufacturing.

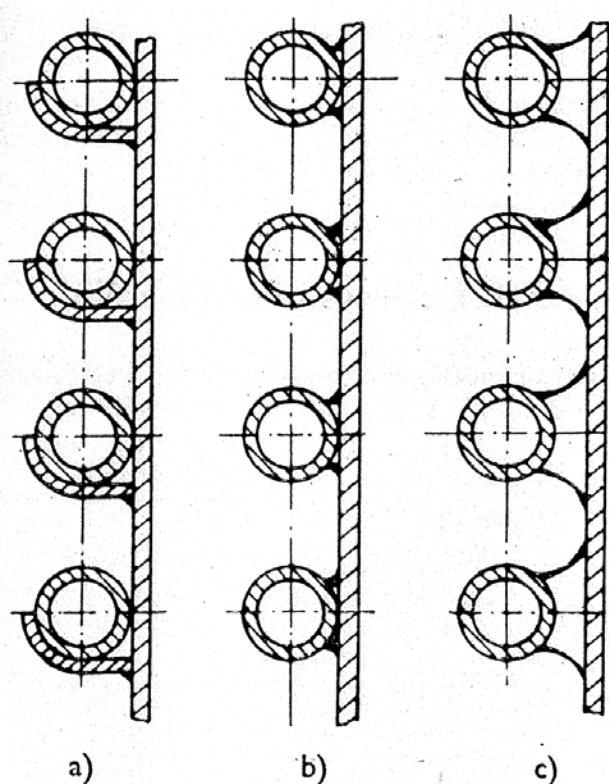


Figure 1. Heater pipe types

- a) pipe with support element, b) welded pipe,  
 c) pipe with spacer



Figure 2. Practical example of inner heater pipe with support element

*Heater channel type:*

Attributes:

- high heat efficiency (direct heating)
- additional outer pressure on tank
- difficult and expensive manufacturing,
- welding cause much harmful stress (shrinking, warp, heat stress)
- lower pressure (0-5 bar) in heater-cooler circle
- high chance of failure

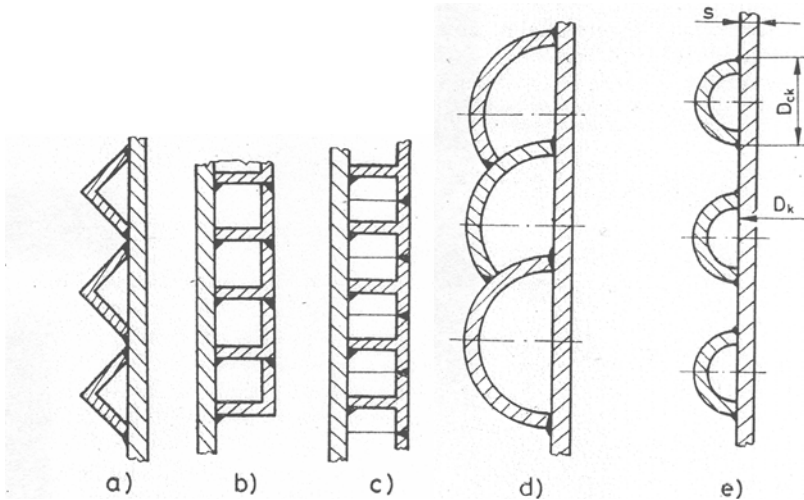


Figure 3. Heater channel types

a,b) L section, c) T section, d) half pipe channel shoulder welding, e) half pipe channel



Figure 4. Practical example of half pipe channel

*Heater shell type:*

Attributes:

- Medium level probability of failure
- high heat efficiency (direct heating)
- additional outer pressure on tank
- welding cause less harmful stress
- middling difficult and expensive manufacturing,
- lower pressure (0-5 bar) in heater-cooler circle
- middling chance of failure

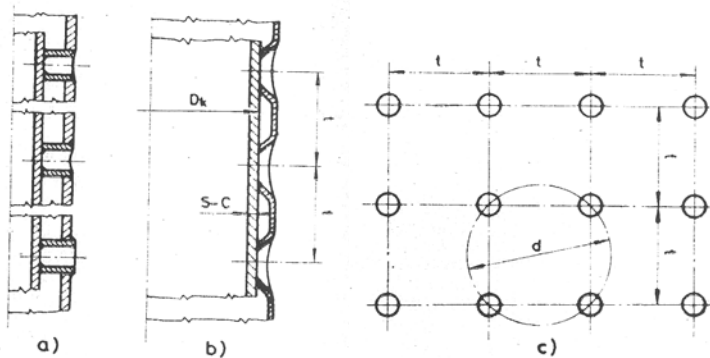


Figure 5. Heater shell supports

a) pipe ring support, b) rimmed shell support, c) grid of supports



Figure 6. Heater shell with rimmed method



Figure 7. Heater shell manufactured with laser welding

#### 4. Analysis, results of research

The European manufacturing of food industrial tanks was analysed in heat exchanger aspect. Mainly authority tested equipments are manufactured with heater channel using standard method of strength calculation. This type is suited for pressure vessel and steam heating. But material and manufacturing costs are high and require long production time. Application posterior on existing products require exceptional care, manufacturing is difficult. Common food industrial solution is laser welded point stiffed heater shell. This is a thinner and a thicker sheet welded together and after assembled it is blown up by high pressure (20-60bar) liquid. Advantages: this method can be automatized easily,

fast manufacturing. But preparation takes long time, needs difficult technology, expensive machine tools.

Product authorization is simple because of uniform technology but it isn't applicable for exist equipment. Heater fluid is thin (max 2,5 mm) with low flow capability so it needs more gates. Process is sensitive to fluid quality and clogging. Our experiences show that lead time is long and it is economy only lot size.

Measuring results show that heat efficiencies of rimmed and laser welded heater shell are same. But installation of rimmed heater shell is cheaper (less valve, less pipe, less human labour).

Product authorization is difficult because customize manufacturing. AD 2000 Merkblatt and EN 13445 standards give specification to design but results of these calculations give thicker wall than desirable.

## 5. Requirements of market, target audience, reasonableness

During our work we often meet demands for products which capable working many technology process (storage, fermentation, cooling, heating, dissolving, etc.), economy and no need technology compromise.

Common technology processes in food industry:

- Storage,
- Fermentation,
- Cooling
- Warming
- Heating
- Storage at temperature
- Dissolving

The solution is using double walled vessel but food industry have special hygienic requirements. Other specialities are expensive materials, manufacturing, exist product and plant of user.

Examined advantages and disadvantages of heat exchanger types in our opinion the heater shell type is the most suited for these purposes.

Aim of our present experiments is developed a rimmed shell technology with the mentioned advantages. It has to be saved material and statically authorial for pressure vessel.

Our experiments show that using present standard static calculation gives 25-50% more material cost and 30-40% more energy cost than necessary.

## 6. Conclusion

- outer wall heater method is applicable because of hygienic requirements
- heater shell type is economical in manufacturing aspect
- rimmed shell technology will be examined because of better heat exchange properties and flexible manufacturing

## **References**

EN 13445 standard: 13.7.4

AD 2000 Merkblatt B5 6.5

Fábry György: Vegyipari gépészek kézikönyve.

MSZ 13822/3-80. Standard Static of pressure vessels

# Ranking of various rapeseed sorts' oils by their fatty acid compositions according to the expectable physical properties

Eszter SÁRKÖZI, László JÁNOSI

Szent Istvan University, Faculty of Mechanical Engineering

## Abstract

As the industrial utilization of the vegetable oils is enlarging as biofuel stock, in the evaluation of the various oilkinds new requirements disappeared, traditionally not important physical parameters come to the front. Basically the physical properties of a vegetable oil are determined by the oil's fatty acid composition. It is considerable that whether the fatty acid compositions of the oilkinds –and so the physical properties- differ significantly not only of the various races but of the sorts within the races. In our work we measured the fatty acid compositions of 21 different rapeseeds' oils with a gaschromatograph after transesterification. By the effect of the fatty acid compositions on the physical properties (iodic value, oxidation stability, low temperature flow properties) we ranked the rapeseeds in the viewpoint of motorical application and analyzed the differences between the rapeseeds.

## Keywords

fatty acid composition, iodic value, rapeseed, gaschromatograph

## 1. Introduction

Considering environmental and energy issues the incremental utilization of renewable energy sources become a strategic aim of the European Union. Part of it the EU ordered that 5.75% (on energy content basis) of fossil fuels will be replaced by alternative fuels from renewable resources of the yearly consumption by 2010.

One of the potential methods of the large scale biofuel production and utilization is the transesterification of the vegetable oils. Through the transesterification with glycerine secession the vegetable oil's triglycerid chains are decomposing and altering into vegetable oil-methyl-ester which is similar to the diesel oil in physical properties.

In Europe one potential feedstock plant of biodiesel production is rape. Just in Hungary there were 85 sorts of rape in the National Sort Catalogue in 2007 and this number is increasing year by year. The differences of the various rape sorts was examined basically only by the aspect of agricultural utilization, but new viewpoints of the evaluation have arisen with the industrial use.

From the references and by the earlier examinations it was proven that the physical and chemical properties (iodic value, CFPP, lubrication) of the oils

extracted from various rape sorts within the rape race show differences. Analyze this differences the reason of them seems to be the variance of the fatty acid composition of the oils.

Our further aim is to determine the most appropriate rape sort for biodiesel stock in technical aspect. In this work we examined the fatty acid compositions of 21 rape sorts' oils in the viewpoint of important chemical and physical properties (iodic value, oxidation stability, cold filter plugging point) in order to explore the differences and to rank the sorts by these properties.

## 2. Experimental methods

Rapeseed oil samples

21 different rapeseeds' seeds was pressed separately by a small scale compactor. The rape sorts:

- RG section: Baldur, Bristol, Elektra, Eleonóra, Mohikán, Strauss, Triangle,
- RA section: Atrus, Dante, Rasamus, Tenno, Titán, Trabant, Viking;
- RS section: Gabriella, GK 704, GK 1103, Helena, Hybrid Star, Lilla, Saphir.

After the pressing the oils was filtered.

### *Analysis*

The fatty acid composition of the 21 rapeseed oils was determined in the Chemical Research Center of the Hungarian Academy of Sciences by gas chromatography. The measuring instrument: Agilent 6890 GC-5973 MS, the used solvent: dichlorine-methane, the esterification happened with methyl.

The iodine values was counted by the fatty acid compositions in accordance of the MSZ EN 14214 hungarian standard appendix B.

The oxidation stability and the Cold Filter Plugging Point (CFPP) was counted by the samples' saturated and unsaturated fatty acid content according to the method at Park et al.:

- oxidation stability:  $Y = 117,9295/X + 2,5905$  ( $0 < X < 100$ ), where X is the content of the linoleic and linolenic acids (wt%) and Y is the oxidation stability (h),
- CFPP:  $Y = -2,7043 * X + 232,0036$  ( $88 < X < 100$ ), where X is the content of the unsaturated fatty acid (wt%) and Y is the CFPP (°C).

## 3. Results and disussion

Table 1. shows the analysis data of the 21 rapeseed oils. All samples contain more than 90% unstarurated fatty acids (C16:1, C 17:1, C18:1, C18:2, C18:3, C20:1, C22:1, C24:1) and so less than 10 % saturated fatty acids (C14:0, C15:0, C16:0, C17:0, C18:0, C20:0, C22:0, C24:0). These data differ only a little bit between the certain rapeseed sorts as the variances of them are low. However the differences between the rapeseeds become remarkable regard to the iodine value where the grade of the unsaturation (the number of the dual bondings between the C atoms: 1, 2, 3) performs. In the viewpoint of iodine value all samples correspond to the hungarian biodiesel standard (MSZ EN 14214) with the value less than 120; in ranking of the rapeseed sorts the lowest iodine value means the best quality, that is RA5- Trabant.

Table 1. Chemical and physical properties of the 21 rapeseed oils

	Saturated fatty acids [wt%]	Unsaturated fatty acids [wt%]	Iodic value [g I <sub>2</sub> /100 g]	Ranking by iodic vaue	Oxidation stability [h]	Ranking by ox. stability	CFPP [°C]	Ranking by CFPP
RG1	8,17	91,69	103,33		6,69		-15,96	
RG2	9,20	90,80	100,56		7,03		-13,54	
RG3	6,99	93,00	105,07		6,59		-19,49	2.
RG4	7,36	92,63	101,19		7,24	3.	-18,49	
RG5	8,76	91,23	100,70		7,09		-14,71	
RG6	9,60	90,39	99,92	3.	7,09		-12,44	
RG7	6,19	93,81	107,62		6,28		-21,70	1.
RA1	9,29	90,27	101,94		6,71		-12,12	
RA2	8,81	91,11	101,33		6,97		-14,39	
RA3	9,05	90,93	99,30	2.	7,34	2.	-13,90	
RA4	7,65	92,35	103,35		6,76		-17,73	
RA5	9,36	90,62	98,62	1.	7,42	1.	-13,06	
RA6	7,99	92,01	102,70		6,83		-16,82	
RA7	7,80	92,19	105,10		6,47		-17,30	
RS1	7,27	92,75	103,61		6,79		-18,82	
RS2	9,04	90,94	102,91		6,64		-13,92	
RS3	8,67	91,33	102,92		6,67		-14,99	
RS4	7,19	92,81	104,92		6,49		-18,97	3.
RS5	7,66	92,34	105,25		6,44		-17,71	
RS6	8,57	91,34	102,59		6,72		-15,01	
RS7	8,37	91,63	104,04		6,52		-15,78	
Min.	6,19	90,27	98,62		6,28		-21,70	
Max.	9,60	93,81	107,62		7,42		-12,12	
Mean	8,24	91,72	102,71		6,80		-16,04	
Variance	0,84	0,91	4,98		0,10		6,67	

In the oxidation stability there aren't significant differences as the variance shows, all samples correspond to the hungarian standard, again the Trabant has the best value with the longest oxidation stability period.

One of the most important problem of the biodiesel is the low temperature behaviour. It can be characterized with the cold filter plugging point (CFPP, [°C]), the least temperature where the sample can be filtered in standardized conditions. Within the 21 rapesorts the CFPP differs significantly, and only one rapesort meets the requirements of the hungarian standard of -20 °C in winter period. It must be remarked that this CFPP values are more favourable than it can be found in references, so the calculation method needs further control.

The oxidation stability and the CFPP mean opposite requirements. As the greater the unsaturated fatty acid content of the sample the lower its CFPP value, and in contrast the lower the unsaturated content of the product the greater its oxidation stability.

#### **4. Conclusions**

The 21 rape sorts' oils differ only slightly in the saturated and unsaturated fatty acid content, but in iodine value and cold filter plugging point where these slight differences are added the variance is significant.

Due to the iodine value and the oxidation stability all samples correspond to the standard's requirements, but in the CFPP there is only one rapesort which is sufficient in winter conditions. Accordingly there is only one rapesort –Triangle– which is appropriate in the three parameters.

#### **References**

- Goodrum, J. W., Geller, D. P.: Influence of fatty acid methyl esters from hydroxylated vegetable oils on diesel fuel lubricity, *Bioresource Technology*, Volume 96, Issue 7, 2005, p. 851-855.
- Hancsók, J.: *Korszerű motor- és sugárhajtómű üzemanyagok III.*, Veszprém Egyetemi Kiadó, Veszprém, 2004.
- Imahara, H., E. Minami, S. Saka: Thermodynamic study on cloud point of biodiesel with its fatty acid composition, *Fuel*, Volume 85, Issues 12-13, 2006, p. 1666-1670.
- Kovács, F., Hancsók, J., Jánosi, L.: Effect of fatty acid composition on the quality of biodiesels, 2<sup>nd</sup> world conference and technology exhibition on biomass for energy, industry and climate protection, Rome, 2004.
- MSZ EN 14214 Gépjármű-hajtóanyagok. Zsírsav-metil-észter (FAME) alapú dízel-motor-hajtóanyag. Követelmények és vizsgálati módszerek (Hungarian Standard)
- Park, J. et al.: Blending effects of biodiesels on oxidation stability and low temperature flow properties, *Bioresource Technology*, Volume 99, Issue 5, 2008, p. 1196-1203.

# Numerical and experimental analysis of friction of large scale self lubricating radial bearings

Wim VAN PAEPEGEM

University Gent, Department of Materials Science and Engineering

Ali REZAEI, Wouter OST, Patrick DE BAETS,

University Gent, Department of Mechanical Construction and Production

László ZSIDAI, Gábor KALÁCSKA

Szent Istvan University, Faculty of Mechanical Engineering

## Abstract

This study includes an experimental and numerical study of the large-scale testing of fiber reinforced polymeric composite bearings. The kinematics of the test setup is simulated with two-dimensional plane-strain model with finite element method. Simulation results correspond closely to the experimental data, and provide careful investigation of stresses distribution in the bearing.

## Keywords

bearing, friction, large scale testing, finite elements

## 1. Introduction

The self-lubricating properties of some polymeric materials make them very valuable in bearing applications. When these materials are reinforced with high resistance fibers such as carbon fibers, glass fibers or polyester fibers, they are able to operate under conditions which conventional bearings cannot. At present there are few numerical studies about composite journal bearings for heavy loadings, and the degradation mechanisms of these bearings are hardly understood. In this article the mechanical behavior of a fiber reinforced polymeric composite bearing is studied. To this purpose a new test apparatus is designed and manufactured.

In conventional tribotesting, small-scale tests are mainly used because of their cost effectiveness, time efficiency, and the easiness of handling of small samples. However, because clearances and pressure distribution can not always be scaled properly, conditions can strongly differ from the real application scale, and extrapolating towards the real working conditions occasionally results in significant errors. From this point of view, experimental setups in which full-scale bearings can be tested statically and dynamically are very important. A test rig should be able to measure the friction torque accurately between journal and bearing. Usually, indirect methods are used in test rigs for journal bearings, and

only few can measure friction torques by direct methods. In indirect methods the measured torque includes the friction of both the test bearing and the shaft-supporting bearings. These two elements cannot be separated in an easy way. The developed test setup uses a direct method where the friction torque of only the test bearing is measured without any interference of the shaft-supporting bearings.

Although the experimental method provides the required information to study the magnitude of the forces on the bearing, it does not give detailed information about the distribution of stresses in the contact area between the bearing and shaft. Therefore in order to study the distribution of the shear stresses, the normal stresses, and the effects of the allocated tolerances in the set-up, numerical simulations are employed. In this article the kinematics of the test rig is modeled as a simplified two-dimensional plane strain model by FEM method.

## 2. Experimental

The experimental studies are done with a new test rig which is designed to determine the tribological behavior of large-scale journal bearings subjected to a reciprocating angular movement. Figure 1 presents the test rig and its cross-sectional view. This apparatus has been considered to test composite bearings with inner diameter of 300 millimeters. The loading conditions, rotation speed, and rotation angle can be changed by user at any time during the test. The friction torque is determined by measuring the force acting on a lever arm connected to the bushing. The tests are driven by a closed-loop servo-hydraulic system. All measuring signals are registered continuously and digitally by means of a data acquisition card. This apparatus provides measurement of the normal and friction force between the bearing and shaft, bearing's temperature during the application, and wear rate of the bearing's surface.

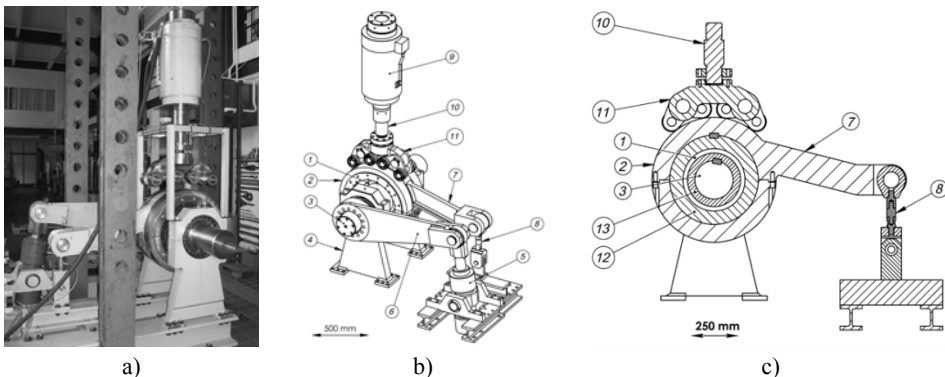


Figure 1. a) Large-scale test setup. b) Components of the test setup. c) Cross-sectional view (1-Composite bearing, 2-Bushing, 3-Shaft, 4-Shaft support, 5-Drive piston, 6-Drive lever arm, 7-Bushing lever arm, 8-load-cell(friction torque), 9-Hydraulic actuator, 10-Load-cell (vertical load), 11-Load transmission trolley, 12-Backing, 13-Shaft bushing)

The test is started by applying the vertical force on the bushing component by hydraulic actuator, and then the drive piston starts to reciprocate and makes the rotational oscillation in the shaft.

Friction force plays a very important role in tribological analyses. Therefore evaluation of the coefficient of friction (COF) of materials in tribosystems is a key factor. In this study, the COF between the composite bearing and steel shaft is calculated by using the measured signals.

Figure 2 depicts a schematic view of the loading and kinematics of the test rig. The parameters of the figure are;  $F_P$ : loading actuator force,  $F_L$ : force on the load-cell,  $F_F$ : friction force between the composite bearing and shaft,  $F_N$ : normal force on composite bearing,  $R_S$ : shaft radius,  $R_b$ : bearing radius,  $R_L$ : distance between the action points of  $F_P$  and  $F_L$ , and  $\alpha$ : rolling angle.

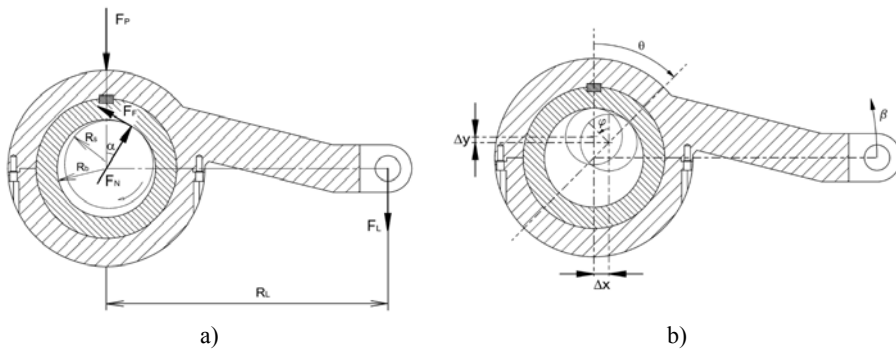


Figure 2. Schematics of the acting forces and kinematics of the setup.  
a) Acting forces, b) Kinematics

During the test  $F_P$  is assumed to be constant, and although due to a very small deviation of the hydraulic piston from its position, it is supposed to be vertical. Since the displacement of the bushing remains small, the force in the load cell  $F_L$  can also be considered vertical. According to the Coulomb law, coefficient of friction is the ratio of the tangential and normal reaction force components:

$$\mu = \frac{F_F}{F_N} \tag{1}$$

$F_F$  and  $F_N$  are derived from the following equilibrium equations:

$$F_F = \frac{R_L}{R_b} \cdot F_L \tag{2}$$

$$F_N = \left[ (F_P + F_L)^2 - \left( F_L \cdot \frac{R_L}{R_b} \right)^2 \right]^{\frac{1}{2}} \tag{3}$$

With substituting the obtained equations for  $F_F$  and  $F_N$  from Equations 2 and 3 in equation 1, the COF becomes:

$$\mu = \tan \alpha = \frac{1}{\left[ \left( \frac{R_b}{R_L} \right)^2 \cdot \left( \frac{F_P + F_L}{F_L} \right)^2 \right]^{\frac{1}{2}}} \quad (4)$$

In the journal bearing application when the shaft starts to rotate, the bearing will initially roll up to a certain angle of inclination and will then start to slip. Therefore, if the shaft rotates continuously, after the first rolling step the process reaches to the steady state sliding conditions. The tangent of the inclination angle is the COF. If the elastic deformation of the load cell and the clearances of its connections at both sides are ignored, the kinematics of the shaft rolling in the bearing can be expressed as:

$$\left( \frac{d\beta}{dt} - \frac{d\theta}{dt} \right) / \left( \frac{d\varphi}{dt} - \frac{d\theta}{dt} \right) = \frac{R_s}{R_b} \quad (5)$$

In this equation  $\frac{d\beta}{dt}$ ,  $\frac{d\theta}{dt}$ , and  $\frac{d\varphi}{dt}$  describe respectively, rotating velocity of the bushing, rotating velocity of the shaft center, and rotating velocity of the shaft around its center. Since the lever arm prevents the rotation of the bushing,  $\frac{d\beta}{dt} = 0$ , the eq.5 will be simplified into:

$$-\frac{d\theta}{dt} / \left( \frac{d\varphi}{dt} - \frac{d\theta}{dt} \right) = \frac{R_s}{R_b} \quad (6)$$

Solving the equation will result into:

$$\varphi = \theta \cdot \frac{R_s - R_b}{R_s} \quad (7)$$

Once the angle  $\theta$  reaches to  $\alpha$ , this relation is no longer valid because the shaft starts to slide instead of rolling. In practice the static COF differs from the dynamic COF. Therefore there are two rolling angles  $\alpha_S$  and  $\alpha_D$ , which correspond to the static and dynamic coefficient of friction. Once the shaft starts to rotate, it rolls up to  $\theta = \alpha_S$ , and then drops to  $\theta = \alpha_D$  and sliding occurs in the contact.

### 3. Finite element modeling

Although the experimental method provides a good estimate of the forces on the bearing, it does not give detailed information about the contact stress distribution. Therefore in order to study the stress distribution, numerical simulations are employed. In this article the kinematics of the test rig is modeled by FEM method.

The traditional method of analyzing these kinds of rolling and sliding contacts is Lagrangian formulation. In the Lagrangian approach, the nodal points are attached to material points, thus the motion of the material during the process is followed. Hence, it is easy to follow the history of material deformation. The Lagrangian analysis is computationally expensive since a transient analysis must be performed and very fine meshing is required on the shaft surface.

Another possibility to simulate this problem is the Eulerian method in which attention is focused on the motion of the material through a stationary control volume. The advantage in this method is that Eulerian elements do not deform with the material. Therefore, regardless of the magnitude of the deformation in process, Eulerian elements retain their original shape.

The limitation of the Eulerian method is simulation of the free boundaries. In this approach, it is harder to follow the material deformation history since the mesh is fixed in space and is not distorted. However, the boundary of the deformation region should be known a priori, because it can not be easily updated during the deformation. Indeed, if in an Eulerian simulation the boundaries of the model change, new control volumes have to be created, which is difficult to deal with.

An alternative approach which combines the advantages of both Lagrangian and Eulerian formulations is the Mixed Lagrangian-Eulerian method. In this approach, the mesh can have a motion independent of material deformation. Therefore, the motion of the mesh can be designed in accordance with the nature of deformation, and thus mesh distortion is avoided on one hand and the boundaries are updated on the other.

In this article two dimensional kinematics of the test setup is simulated as a quasi static model by the Mixed Lagrangian-Eulerian method.

Figure 1 demonstrates that the geometry of the bearing and bushing consists of uniformly extruded sections along the shaft's axis. In addition, the hydraulic piston applies a uniformly spread pressure on the bushing along the same axis. Therefore, considering the width of the bearing (120 mm), which is long enough to prevent the strain in the axial direction, a two-dimensional plane strain model can provide careful investigation of the stress distribution on the bearing as well as the kinematic modeling of the setup.

Figure 3 depicts the boundary conditions and meshing of the two-dimensional plane strain model for the test rig. The model contains 16939 high accuracy second order elements. This simplified assembly includes the bearing, bushing, shaft, loading actuator (piston), load transmission trolley, load-cell, support, hinge A (connection of load-cell and bushing), and hinge B (connection of load-cell and support).

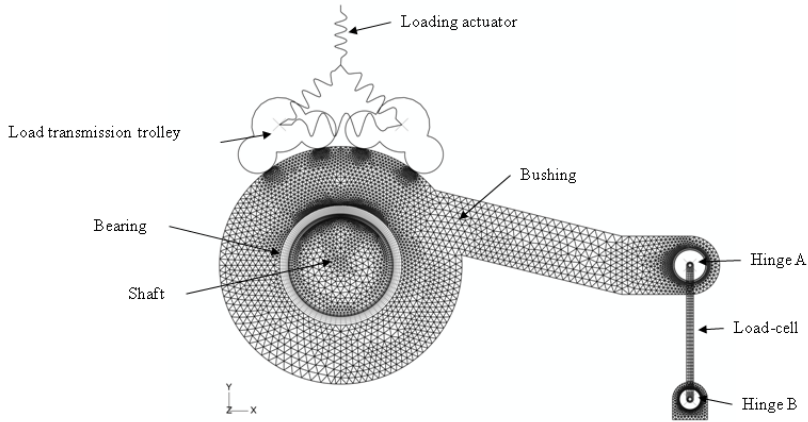


Figure 3. 2D finite element model.

#### 4. Friction and material modelling

In the numerical simulation it is assumed that the friction coefficient decays exponentially from the static value to the dynamic value (see figure 4) according to the formula:

$$\mu = \mu_D + (\mu_S - \mu_D)^{-d_c \dot{\gamma}_{eq}} \quad (8)$$

Where  $\mu_D$  is the dynamic friction coefficient,  $\mu_S$  is the static friction coefficient,  $d_c$  is a user-defined decay coefficient, and  $\dot{\gamma}_{eq}$  is the slip rate. Regarding the experimental data, parameters of the equation are defined and then the friction coefficient will be calculated correlated to the slip rate.

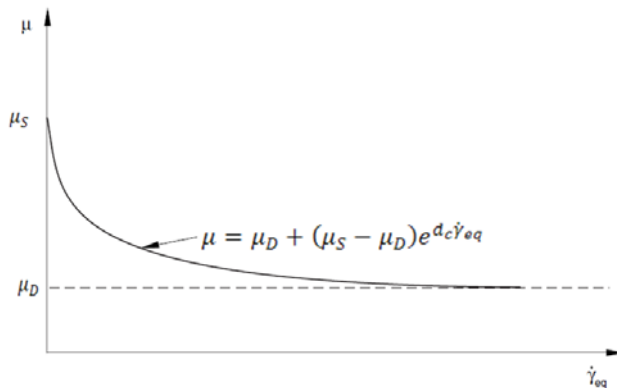


Figure 4. Relation between COF and slip rate.

The test bearing is a composite of a phenolic resin, polyester reinforcing fibers, and PTFE filling for internal lubrication (see figure 5). This bearing is an orthotropic material with the engineering constants shown in the table 1.



Figure 5. Composite bearing

Table 1. Engineering constants of the composite bearing, r: Radial coordinate, t: Tangential coordinate, z: Axial coordinate

$E_{rr}$	2.75 GPa	$G_{rt}$	1.00 GPa	$\nu_{rt}$	0.165
$E_{tt}$	10.00 GPa	$G_{tz}$	4.00 GPa	$\nu_{tz}$	0.250
$E_{zz}$	10.00 GPa	$G_{rz}$	1.00 GPa	$\nu_{rz}$	0.068

## 5. Results

The tests were performed on a composite bearing under the conditions shown in table 2:

Table 2. Test conditions.

Bearing diameter:	300 (mm)
Bearing thickness	25 (mm)
Normal load by loading actuator	100 (kN)
Driving piston amplitude	5 (mm)
Driving piston frequency	0.5 (Hz)
Clearance between shaft and bearing	1.1 (mm)
Clearance between the load cell pins and correlated bushing	0.1 (mm)

Figure 6 shows the experimental results for the coefficient of friction between the composite bearing and the shaft.

Figure 7 compares the extracted friction force ( $F_F$ ) from the experimental measurements and numerical simulations. Due to the static coefficient of friction at the start of each cycle the friction force graph shows a spike, and when sliding

occurs, it decreases. It is obvious that when direction of the rotation changes, the direction of the friction force also changes. These figures show that there is a very good agreement between numerical and experimental results. At the start of each cycle when rolling contact occurs between the shaft and bearing, the friction force rises till 14.5 kN and then it decreases to 11.5 kN in the sliding condition.

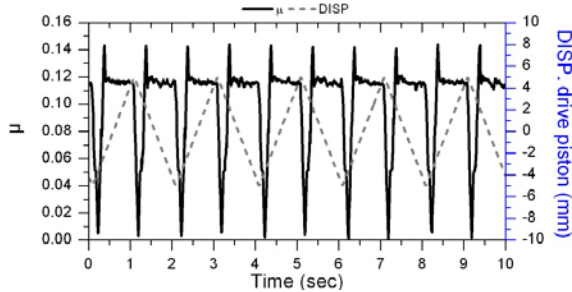
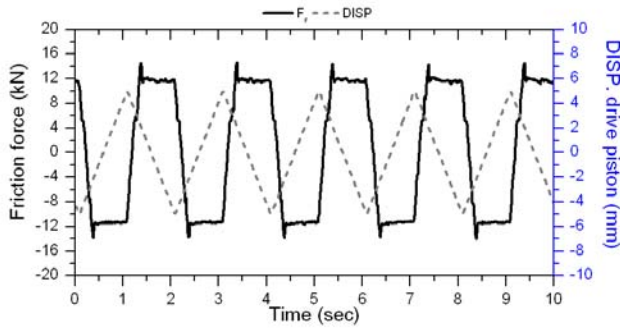
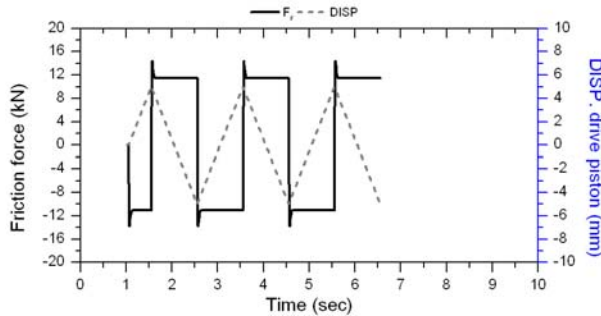


Figure 6. Measured values of the drive piston’s displacement and calculated values of the coefficient of friction between the composite bearing and shaft.



a) Experimental



b) Numerical

Figure 7. Friction force between the composite bearing and shaft.  $F_f$ : friction force, DISP: displacement of driving piston.

The fluctuation in the friction force generates a relative variation in the normal force between bearing and shaft. Once the direction of the friction force changes, the normal force reduces. The normal force at the counterclockwise rotation increases up to 101.2 kN, while it decreases to 96.7 kN in the clockwise rotation of the shaft (see figure 8).

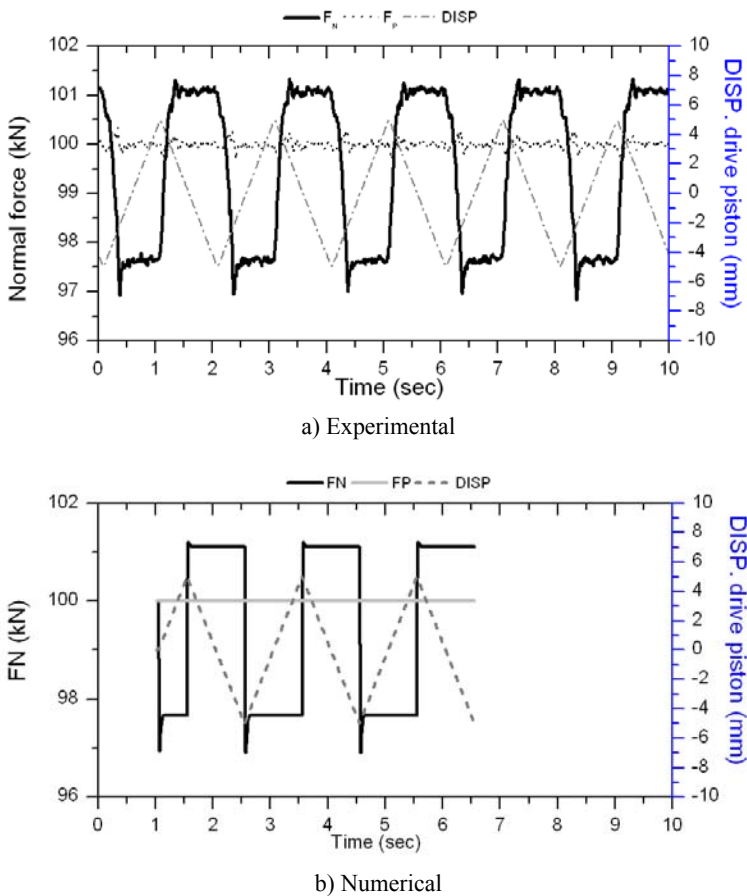


Figure 8. Normal force between the composite bearing and shaft.  
 $F_N$ : normal force, DISP: displacement of driving piston,  
 $F_p$ : applied load by loading piston.

Figure 9 shows that the simulation results of the horizontal displacement of the bushing precisely correspond with the test results. At the moment that the shaft motion tends to overcome the static friction force, the bearing sticks to the shaft. At this moment the bushing system moves forward or backward depending on the direction of rotation. Once the contact condition changes from rolling to sliding, the bearing slides back and the shaft slides against the bearing

in a fixed position. The horizontal displacement of the bushing varies between +0.1 and -0.1 mm.

Figure . 10 shows the four steps of the radial stress distribution in the composite bearing. Step 1 shows the free bearing without any loading. After applying 100 kN force, radial stress in the bearing is built up. In the second step the stresses are symmetrically distributed along the loading axis, and the maximum radial stress in the center of the contact line equals 8.5 MPa. After the loading is completed and reaches 100 kN, the shaft starts to rotate in the clockwise direction. By rotating the shaft, the stress contours starts to move to the left and at the sliding point remain fixed (see step 3), and when the shaft rotates in the counterclockwise direction, stress contours move to the right (see step 4).

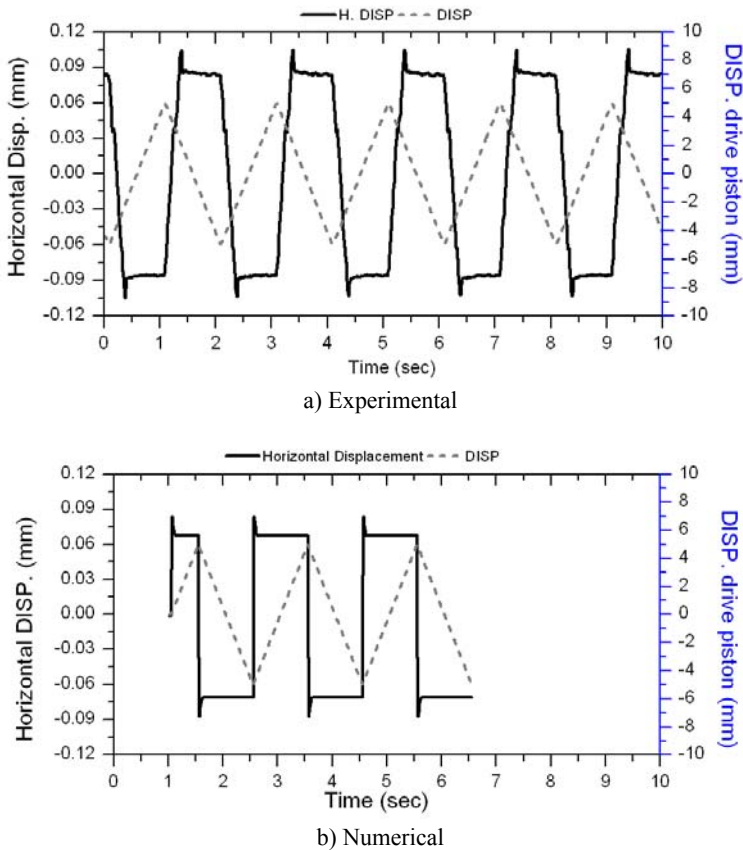


Figure 9. FEM results of the horizontal displacement of the bushing,  
H. DISP: Horizontal displacement of bushing,  
DISP: displacement of driving piston

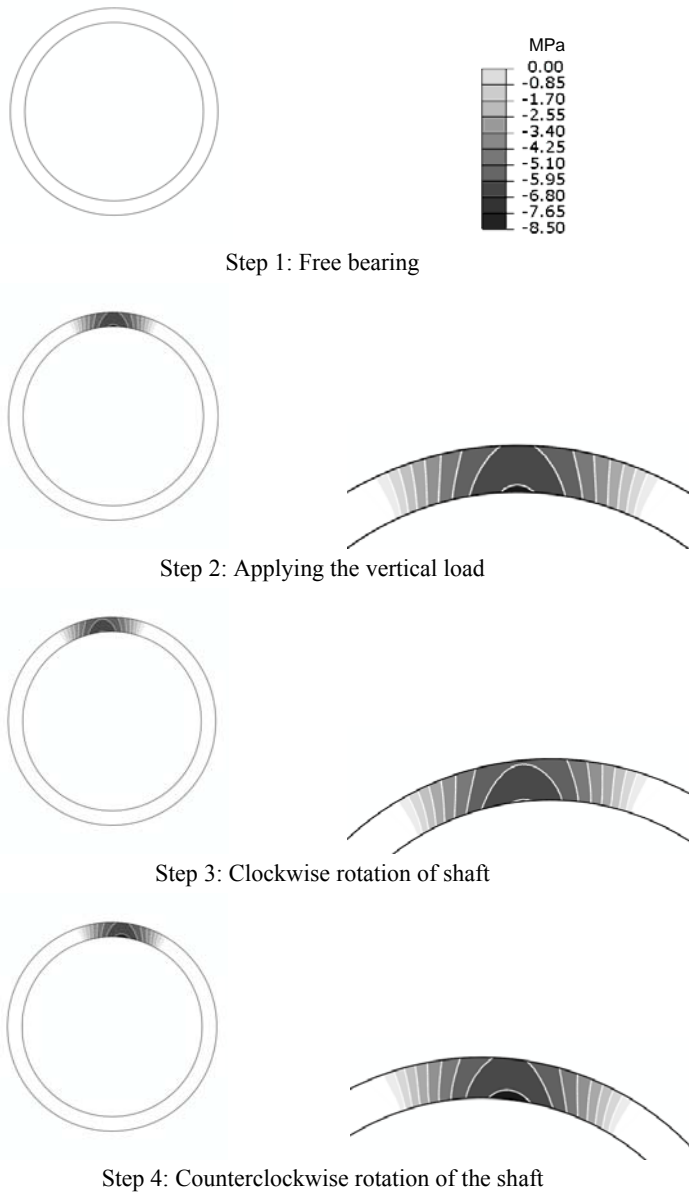


Figure 10. Radial stress distribution on the composite bearing.

## 5. Conclusion

Although the experimental method provides a general view of the friction force of the composite bearing, it does not give enough data to investigate the stress

distribution in the bearing contact area. Numerical simulations do not only include the correct kinematics of the large-scale loading set-up, but provide also the frictional shear stresses and normal stress distribution along the contact line of the bearing and shaft.

Considering the cost of the experimental methods in large scale testing, these simulation results are very helpful tools to analyze and predict the effect of the mechanical design parameters and material properties of the composite bearing in the journal bearings application.

## 6. Acknowledgements

This project is supported by Ghent University Research Fund (BOF).

## References

- Dai Gil, L. and K. Seong Su, Failure analysis of asbestos-phenolic composite journal bearing. *Composite Structures*, 2004. 65(1): p. 37-46.
- A. Biyiklioglu, H.C., H. Adatepe, H. Bas, M.S. Duman, A New Test Apparatus and Method for Friction Force Measurement in Journal Bearings under Dynamic Loading. *Experimental Techniques*, 2005.
- Persson, B.N.J., *Sliding Friction: Physical Principles and Applications*. 1998, Springer. p. 13.
- Beek, A.v., *Machine Lifetime Performance and Reliability*. 2004: Delft University of Technology. 432.
- J. Van Wittenberghe, W.Ost., A. Rezaei, P. De Baets, L. Zsidai, G. Kalácska Test Setup For Friction Force Measurements of Large-Scale COMPOSITE BEARINGS. *Experimental Techniques* 2008.
- Friedrich, K., Goda, Tibor, Varadi, Karoly, Wetzels, Bernd, Finite Element Simulation of the Fiber-Matrix Debonding in Polymer Composites Produced by a Sliding Indenter: Part I – Normally Oriented Fibers. *Journal of COMPOSITE MATERIALS*, 2004. 38(18/2004): p. 1583-1606.
- Bathe, K.-J., *Finite Element Procedures*. 1996: Prentice Hall.
- Ted Belytschko, W.K.L., Nrian Moran, *Nonlinear Finite Element for Continua and Structures*. 2000, John Wiley & Sons. p. pp. 393-443.
- Oden, J.T. and J.A.C. Martins, *Models and Computational Methods for Dynamic Friction Phenomena*. *Computer Methods in Applied Mechanics and Engineering*, 1985. 52(1-3): p. 528-634.

# New algorithm for symmetry recognition in two-dimensional case

Zoltán SZAKÁL, Ibolya ZSOLDOS

Szent Istvan University, Faculty of Mechanical Engineering

## Abstract

The origin of this work is a new method for the detection of exact and approximate reflective symmetries. The new algorithm is worked out for 2D case based on the fact that the symmetry axes cross the gravity centre. Accordingly the exact and approximate symmetry axes are selected from the set of the lines crossing the gravity centre. The searching algorithm is based on the definition of the so called symmetry-parameter which is a rate of the symmetry, a number between 0 and 1 without a dimension and its value does not depend on geometrical measures. The value of 1 corresponds to the exact symmetry and a value close to 1 corresponds to an approximate symmetry. A so called symmetry-diagram is determined from the symmetry-parameters computed for various lines crossing the gravity centre. The symmetry-diagram is applicable to find every exact and approximate symmetry axis. Beside this, the symmetry-diagram shows an individual shape property of the 2D figures, independently from geometrical measures and so it can be the base of pattern recognition methods being independent from geometrical measures.

## Keywords

2D symmetry, characterizing algorithm

## 1. Introduction

The problem of symmetry detection has been extensively studied in numerous fields including visual perception, computer vision, robotics, computational geometry and reverse engineering. Early methods concentrated on finding perfect symmetries in 2D or 3D point sets. Since the restriction to exact symmetries limits the use of these methods for real-world objects, a method was introduced for computing approximate global symmetries in 3D point sets, but the complexity of the algorithm makes it impractical for large data sets. The notion of approximate symmetry was formalized by expressing symmetry as a continuous feature. The examination of the correlation of the Gaussian image was proposed to recover global reflective and rotational symmetries. A shape descriptor was introduced that concisely encodes global reflective and rotational symmetries. Different applications based on generalized complex moments,

grouping feature points, isometric transforms, planar reflective symmetry transform and generalized symmetry transform are used in image processing and mesh processing for detecting exact local and global reflection-symmetry and rotation- symmetry of 2D and 3D images.

The symmetries are often not exactly present, but only approximately present, due to measurement errors in the scanning process, and approximation and numerical errors in model reconstruction during reverse engineering. Beside this, different CAD systems often use different tolerances, and what is symmetric in one CAD system may be only approximately symmetric in another. To solve these problems new algorithms based on the B-rep model were developed to find approximate rotational and translational symmetries of 3D forms built from simple geometric units and complex 3D forms in reverse engineering.

In the most prevalent methods of symmetry detection a number of pixels are aligned to the contour. The perpendicular bisectors of various pixel pairs are regarded as hypothetical symmetry axes. The exact and approximate symmetry axes are searched from the set of the perpendicular bisectors e.g. using a symmetry map created from the parameters of the perpendicular bisectors, or optimizing the gradient orientations of pixel pairs. In this paper a new method is shown for the detection of exact and approximate reflective symmetry. The new method is worked out for 2D case based on the fact that the symmetry axes cross the gravity centre. Accordingly the hypothetical symmetry axes are the lines crossing the gravity centre and the exact and approximate symmetry axes are selected from the set of these lines. The searching algorithm is based on the definition of the so called symmetry-parameter which is a rate of the symmetry, a number between 0 and 1 without a dimension and its value does not depend on geometrical measures. A so called symmetry-diagram is determined from the symmetry-parameters computed for various lines crossing the gravity centre. The symmetry-diagram is applicable to find every exact and approximate symmetry axis. Beside this the symmetry-diagram shows an individual property of the 2D figures, it is independent from geometrical measures but it is characteristic of the shape of the 2D figure.

## 2. The algorithm

The algorithm consists of several simple steps.

We have proceeded from the fact that the symmetry axes of a 2D figure cross the gravity centre because a symmetry axis divides the figure to two coincident parts therefore a symmetry axis is a median, too. A median has to cross the gravity centre.

The algorithm scans the multitude of the lines crossing the gravity centre and studies how favourable these lines as symmetry axes are. If there is no exact symmetry axis crossing the gravity centre, a best approximate symmetry axis crossing an area surrounding the gravity centre is searched with similar method.

Namely, since an exact symmetry axis crosses the gravity centre, an approximate symmetry axis has to cross an area surrounding the gravity centre.

In the followings we detail the steps of the algorithm.

*Step 1: Collecting of the input data*

The contour of the form is needed for the computation.

The input data set is defined as a set of points aligned to the contour. Such a point set can be created by the use of different tools of electronic image processing e.g. the MatLab. In order to decrease the measure of the point set file and the run time of the algorithm, the point set can be optimized: the points can be fixed rare or thickened depending on the complexity of the geometry. Fewer points are needed at greater curvature and more points are needed at smaller curvature, Figure 1. Such an optimization of the input point set is not required, but if we perform it, it can speed the run of the computer codes. The original contour is approximated with the stretches determined by these points. We name these stretches as perimeter stretches.

The input of the algorithm is the table of the points. The points follow each other in a clockwise direction. Such a table can be created manually and also recorded digitally from a pixel set.

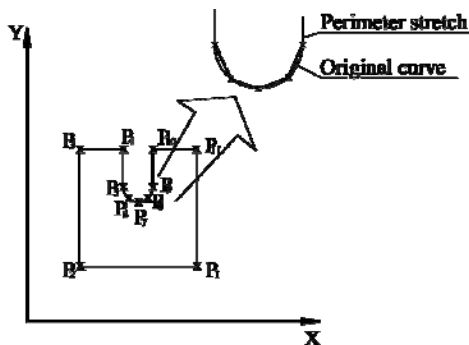


Figure 1. Collecting of points (P<sub>i</sub>) on the boundary.

*Step 2: Determination of the gravity centre*

We determine the gravity centre of the 2D figure with the method used in the geographic information systems. In order to compute the area of the 2D figure trapeziums are defined so that the points aligned to the contour are projected to the horizontal axis of the coordinate system, Figure 2.

The area of the i<sup>th</sup> trapezium is:

$$A_i = \frac{(x_{i+1} - x_i) \cdot (y_{i+1} + y_i)}{2} \tag{1}$$

where  $(x_i, y_i)$  and  $(x_{i+1}, y_{i+1})$  are the end points of the  $i^{\text{th}}$  perimeter stretch.

The points have to follow each other in a clockwise direction, in contrary case a negative value is derived for the area. The coordinate system is defined so that if the 2D figure is revolved around the gravity centre it always has to remain in the first plane quarter.

The area of the 2D figure is the sum of the areas of the trapeziums:

$$A = \sum_{i=1}^n \frac{(x_{i+1} - x_i) \cdot (y_{i+1} + y_i)}{2} \quad (2)$$

where  $n$  is the number of the trapeziums.

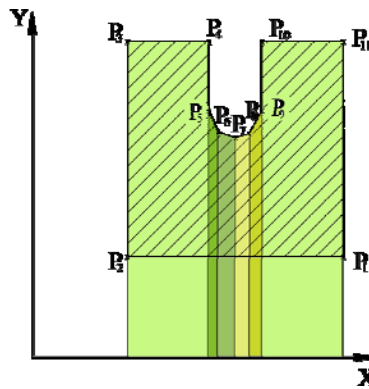


Figure 2. Definition of trapeziums for the computation of the area in the example of a hexagon.

The coordinates of the gravity centre are determined in general case by

$$x_g \cdot A = \int_A x \cdot dA \quad (3)$$

$$y_g \cdot A = \int_A y \cdot dA \quad (4)$$

In our case (because of the trapeziums) the integration reduces itself to a simple summing up:

$$x_g = \sum_{i=1}^n \left[ (y_i - y_{i+1}) \cdot \frac{(x_i^2 + x_i \cdot x_{i+1} - x_{i+1}^2)}{6 \cdot A} \right] \quad (5)$$

$$y_g = \sum_{i=1}^n \left[ (x_{i+1} - x_i) \cdot \frac{(y_i^2 + y_i \cdot y_{i+1} - y_{i+1}^2)}{6 \cdot A} \right] \quad (6)$$

*Step 3: Scanning*

The vertical line crossing the gravity centre is regarded as symmetry axis in the case of an optional starting orientation of the 2D figure, Figure 2. The algorithm analyses whether the 2D figure is symmetric for this hypothetical symmetry axis. For this purpose the algorithm scans the figure with horizontal lines (so called ‘measuring lines’) following each other with equal distances, Figure 3. The hypothetical symmetry axis is vertical and the measuring lines corresponding to the scanning levels are perpendicular to the axis namely they are horizontal.

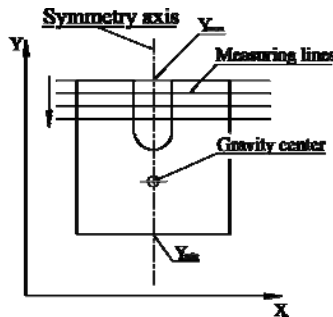


Figure 3. The horizontal measuring lines

In the course of the scanning the so called measuring stretches are determined. A measuring stretch is the distance between the vertical hypothetical symmetry axis and the intersection of a measuring line and a perimeter stretch. In Figure 4 ‘l’ and ‘r’ are the measuring stretches. In a horizontal scanning level there could be more measuring stretches, as well.

The complete area of the 2D figure is scanned with measuring lines proceeding from up to down, from the maximum ( $Y_{max}$ ) to the minimum ( $Y_{min}$ ) vertical coordinate of the points aligned to the contour. The accuracy of the method depends on the distance between the measuring lines: the shorter the distance is the more accurate the result is, however it affects the running time of the computer code as well.

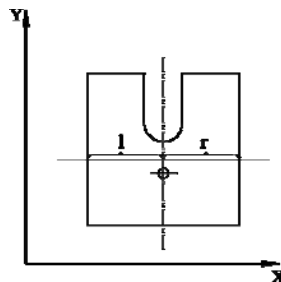


Figure 4. Definition of the measuring stretches in a simple case

*Step 4: Computing the symmetry parameter*

The symmetry parameter  $Z$  shows the deviation from the perfect symmetry numerically. This value between 0 and 1 can be a rate of the symmetry. In order to define it we introduce first a  $Z_k$  parameter for the  $k^{\text{th}}$  scanning level. In the simplest case when there is one measuring stretch on the left and on the right side of the hypothetical symmetry axis, Figure 4,  $Z_k$  can be computed simple:

$$Z_k = 1 - \frac{\text{abs}(l - r)}{L_{\max}} \quad (7)$$

where:

' $l$ ' is the measuring stretch on the link side of the symmetry axis,

' $r$ ' is the measuring stretch on the right side of the symmetry axis,

$L_{\max}$  is the maximum of the measuring stretches in the course of the scanning.

$Z_k$  is defined so that:

- $Z_k=1$  if  $l=r$  when the  $k^{\text{th}}$  scanning level is symmetrical to the hypothetical symmetry axis,
- $Z_k=0$  if  $l=0$  and  $r>0$ , or  $r=0$  and  $l>0$  when a measuring stretch does not have a pair on the other side of the hypothetical symmetry axis which is the worst case regarding the symmetry,
- $0 < Z_k < 1$  when  $l>0$  and  $r>0$  and the figure is not symmetrical to the hypothetical symmetry axis, and the closer this value is to 1 the better the  $k^{\text{th}}$  scanning level approximates the exact symmetry.

Since a ratio of lengths is used in (7)  $Z_k$  is a number without a dimension and its value does not depend on the measures.

If there are more than 2 measuring stretches in a scanning level ( $l_1, l_2, \dots, l_n$  on the left side and  $r_1, r_2, \dots, r_m$  on the right side of the hypothetical symmetry axis, Figure 5) then  $l_i$  and  $r_i$  are ordered into pairs and  $Z_k$  is defined according to (8). Let us assume that there are more measuring stretches on the left side:  $n>m$ . In this case the pairs have to be defined so that  $r_i=0$  for every  $l_i$   $i=m+1, m+2, \dots, n$ . In general case  $Z_k$  is computed as the average of the expression defined by (7) from the pairs:

$$Z_k = \frac{1}{n} \sum_{i=1}^n \left( 1 - \frac{\text{abs}(l_i - r_i)}{L_{\max}} \right) \quad (8)$$

where  $n$  is the number of the pairs in a scanning level.

The symmetry-parameter  $Z$  is defined as the average of  $Z_k$ :

$$Z = \frac{\sum_{k=1}^N Z_k}{N} \quad (9)$$

where  $N$  is the number of the scanning levels (measuring lines) from  $Y_{\max}$  to  $Y_{\min}$ .

Since  $Z$  is defined with averages according to (7), (8) and (9),  $Z$  keeps the original properties of  $Z_k$ :

- the value of  $Z$  can change between 0 and 1,
- $Z=1$  is the case of an exact symmetry,
- $Z=0$  is the worst case regarding the symmetry (e.g. the full figure is on the left side of the axis),
- in the case of  $0 < Z < 1$  the closer the value is to 1 the better the figure approximates the exact symmetry,
- $Z$  is a number without a dimension, it does not depend on the measures, it depends only on the shape.

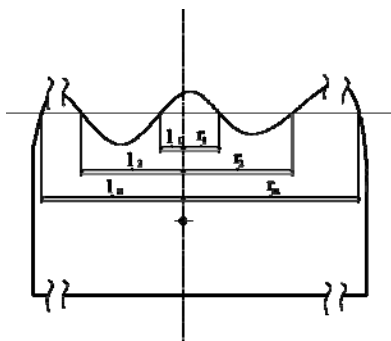


Figure 5. Definition of  $Z_k$  in general case

*Step 5: Rotation of the geometry*

After the determination of the symmetry-parameter for the starting orientation the 2D figure is scanned by rotating the hypothetical symmetry axis, as well. The computation is simpler if the hypothetical symmetry axis is fixed vertically and the figure is rotated with small angles, step by step, Figure 6. The accuracy of the computation depends on the steps (angles) of the rotation. After every step of rotation the symmetry-parameter is computed.

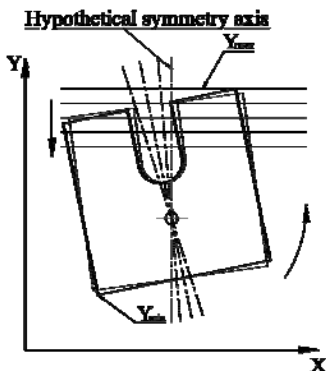


Figure 6. Rotation of the 2D figure with small angles

The method scans the entire 2D figure in such a way that it rotates the examined figure by 180 degrees. Since the algorithm examines the figure both above and below the gravity center, the rotation by 180 degrees means a complete coverage.

*Step 6: Evaluation of the results*

The symmetry-parameter  $Z$  is computed for every rotational step. The values of  $Z$  are saved together with the angles of rotation. After the full ( $180^\circ$ ) rotation a diagram is drawn where the independent variable is the angle of rotation and the dependent variable is  $Z$ . From this diagram the results can be evaluated. Let us name it symmetry-diagram. Exact symmetry exists where  $Z=1$  and the closer  $Z$  is to 1 the better the figure approximates the exact symmetry at a given angle.

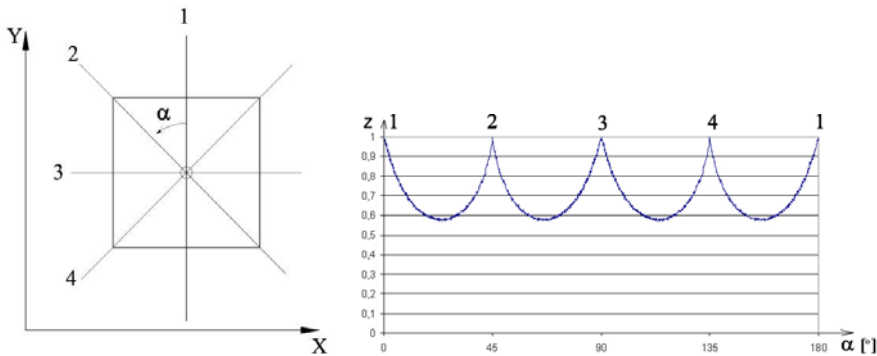


Figure 7. The definition of the symmetry-diagram

The symmetry-diagram of a square can be seen in Figure 7. The lines signed with numbers (1, 2, 3, 4) are the exact symmetry axes of the square and accordingly these correspond to the angles of rotation where  $Z=1$  ( $\alpha=0^\circ$  or  $180^\circ$ ,  $\alpha=45^\circ$ ,  $\alpha=90^\circ$  and  $\alpha=135^\circ$ ).

The symmetry-diagram shows an individual property of the 2D figures independently of the fact whether the 2D figures are symmetric (approximately symmetric) or not. Since  $Z$  is independent of geometrical measures the symmetry-diagram shows the nature of the shape of the 2D figures: it is the same for similar 2D figures having different measures, but if there is a smallest change on the shape of the 2D figure the symmetry-diagram changes, as well.

We show examples for the individuality of the symmetry-diagram in Figure 8. Three variously modified squares can be seen and the symmetry-diagrams are different, as well. In Figure 8a the corners of the square are cut, the number and the place of the original symmetry axes have not changed but the minimum values have increased from  $Z=0.58$  to  $Z=0.65$ . In Figure 8b a part of the square is cut out, only 1 symmetry axis has remained and a weakly approximate symmetry axis signed with number 3 can be found at a local maximum of the

diagram. The other two local maximums signed with number 2 and 4 correspond to only very weakly approximate symmetry axes. In Figure 8c several small parts cut out from the square, the exact symmetry axes have not changed but the curve between the maximums is basically other.

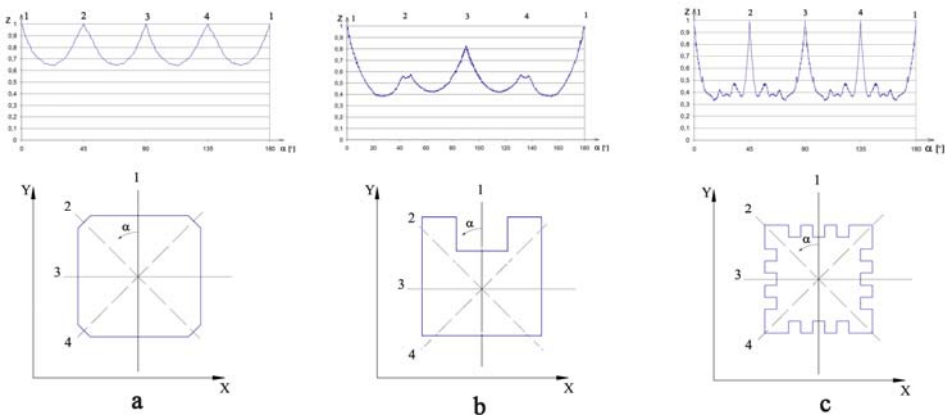


Figure 8. Symmetry-diagrams for modified squares

The algorithm does not have limits in 2D case. It is applicable even if the contour consists of several closed loops. In Figure 9 a circle with two holes can be seen.

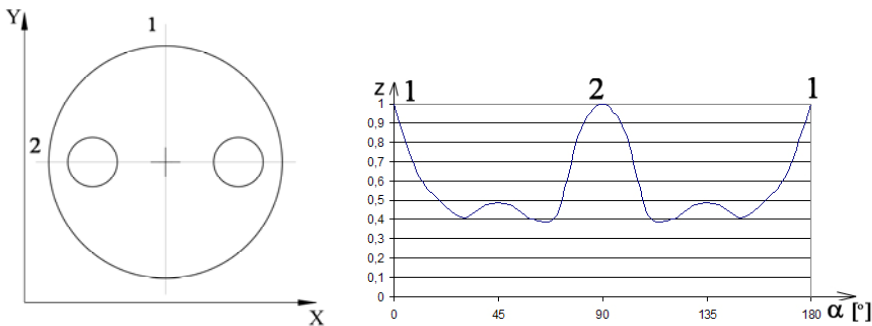


Figure 9. Example of a 2D figure having a contour with several closed loops

It is obvious that the symmetry-diagram is the constant 1 function in the case of a circle because every line crossing the centre is an exact symmetry axis. Since there are two holes on the circle in Figure 9 accordingly there are only two exact symmetry axes signed with number 1 and 2 where  $Z=1$ .

There was an exact symmetry axis in every example shown above, i.e.  $Z=1$  value(s) could be found in every symmetry-diagram computed for the lines crossing the gravity centre.

But in the case when there is no exact symmetry axis, it is not sure, that the best approximate symmetry axis can be found in the lines crossing the gravity centre. However we can assume that the best approximate symmetry axis has to pass near by the gravity centre in the case of approximate symmetrical 2D forms. In this case it is advisable to repeat the Steps 3-5 so that the symmetry-diagram is created for the points surrounding the gravity centre, as well. For the best approximate symmetry axis we have to search the symmetry-diagram where the maximum Z value can be found.

### 3. Example in the human therapy

We emphasize the significance of the study of symmetry properties on an example in the human therapy.

There are accidents when the skull is injured significantly. In the course of the reparation a prosthesis is designed and manufactured before the operation. During the design the 3D CAD model of the prosthesis is created using the model of the part remained unhurt. The design process can not be performed automatically because every injury is different. A unique design is needed where the symmetry plane (or rather the approximate symmetry plane) needs to be known. Knowing the symmetry plane the prosthesis model can be created by a simple reflection.

Since our algorithm works for 2D figures we show the symmetry detection on a plane section of the skull in the following example.

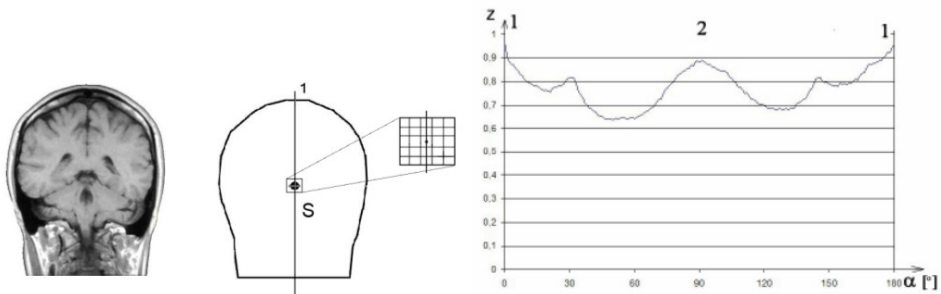


*Figure 11.* The symmetry-diagram computed from an MR photograph of the skull

In Figure 11 the study of an MR photograph of the skull can be seen. We have fixed 20 points along the external contour as input data of our algorithm. We have computed the symmetry-diagram for 6x6 points as a grid around the gravity centre as it can be seen in the enlarged detail in Figure 11. The best approximate symmetry axis (the maximum value of Z) was found in the symmetry-diagram computed for the gravity centre shown in Figure 11. In this symmetry-diagram we have got the local maximum in two places. In the position

denoted by number 1  $Z=0.95$ , thus, it is close to 1. The corresponding approximate symmetry axis is denoted by number 1. It is remarkable that even in the position denoted by number  $Z=0.97$  which is less considered to be approximate symmetric.

#### 4. Summary

The new algorithm gives a new possibility to detect exact and approximate symmetry axes of 2D figures. Beside the known methods of symmetry detection the new algorithm define the so called symmetry-parameter which can be a rate for the symmetry using a parameter between 0 and 1.

The symmetry-diagram created from the values of the symmetry-parameter computed for various lines crossing the gravity centre is independent from geometrical measures and it shows an individual, characteristic shape property of the 2D figures, which can be the base of a pattern recognition independent from geometrical measures.

#### 5. Acknowledgements

This work was supported by OTKA grants K 73776 in Hungary.

#### References

- Wolter, J.,Woo, T., and Volz, R. 1985. Optimal algorithms for symmetry detection in two and three dimensions. *The Visual Computer*.
- Atallah, M. 1985. On symmetry detection. *IEEE Trans. On Computers* 34, 7, 663–666. 2004.
- Alt, H.,Mehlhorn, K.,Wagener, H., and Welzl, E. 1988. Congruence, similarity and symmetries of geometric objects. *Discrete Comput. Geom.* 3, 237–256.
- Zabrodsky, H., Peleg, S., and Avnir, D. 1995. Symmetry as a continuous feature. *IEEE PAMI* 17.
- Sun C, Sherrah J. 3D symmetry detection using the extended Gaussian image. *IEEE Transactions on Pattern Analysis and Machine Intelligence* 1997; 19(2):164–8.
- Kazhdan, M. M., Chazelle, B., Dobkin, D. P., Finkelstein,A., and Funkhouser, T. A. 2002. A reflective symmetry descriptor. In *Proceedings of ECCV*, 642–656.
- Kazhdan, M., Funkhouser, T., and Rusinkiewicz, S. 2004. Symmetry descriptors and 3d shape matching. In *Symposium on Geometry Processing*, 116–125.

- Shen D, Ip H, Cheung K, Teoh E. Symmetry detection by generalized complex (GC) moments: A close-form solution. *IEEE Transactions on Pattern Analysis and Machine Intelligence* 1999;21(5):466–76.
- Loy G, Eklundh J. Detecting symmetry and symmetric constellations of features. In: *ECCV 2006, Part II. LNCS*, vol. 3952. Springer-Verlag; 2006. p. 508–21.
- Mitra N, Guibas L, Pauly M. Partial and approximate symmetry detection for 3D geometry. *ACM Transactions on Graphics* 2006;25(3):560–8.
- Mitra N, Guibas L, Pauly M. Symmetrization. *ACM Transactions on Graphics* 2007. 26(3): Art. No. 63
- Martinet A, Soler C, Holzschuch N, Sillion FX. Accurate detection of symmetries in 3D shapes. *ACM Transactions on Graphics* 2006;25(2): 439–64.
- Podolak J, Shilane P, Golovinskiy A, Rusinkiewicz S, Funkhouser T. A planar-reflective symmetry transform for 3D shapes. *ACM Transactions on Graphics* 2006;25(3):549–59.
- Reisfeld D, Wolfson H, Yeshurun Y. Context Free Attentional Operators: the Generalized Symmetry Transform. *Int. J. Comput. Vision* 1995; 14(2):119–130.
- Li W.H, Zhang A.M, Kleeman L. Global reflectional symmetry detection for robotic grasping and visual tracking, ACRA 05, Australasian Conference on Robotics and Automation, 2005. <http://www.visionbib.com/bibliography/journal/acr.html#ACRA05>
- Varady T, Martin R, Cox J. Reverse engineering of geometric models - an introduction. *Computer-Aided Design* 1997;29(4):255–68.
- Pratt M, Anderson B, Ranger T. Towards the standardized exchange of parameterized feature-based CAD models. *Computer-Aided Design* 2005; 37(12):1251–65.
- Mills B, Langbein F, Marshall A, Martin R. Approximate symmetry detection for reverse engineering. In: *Proc. 6<sup>th</sup> ACM symp. solid and physical modeling*. 2001. p. 241–8.
- Li M, Langbein F, Martin R. Detecting approximate symmetries of discrete point subsets. *Computer-Aided Design* 2008; 40(1):76–93.

# Energetics of the milling process in a planetary ball mill

Gyula KAKUK, Ibolya ZSOLDOS, István OLDAL

Szent Istvan University, Faculty of Mechanical Engineering

Ágnes CSANÁDY

<sup>3</sup>Bay Zoltán Foundation, Institute of Materials Science and Technology

## Abstract

*Further improving the previous models describing the operation of planetary ball mills the study determines the impact energy transmitted towards the material during the milling and the milling power. It points out relationship between the ratio between the angular velocity of the sun disk and the vials, and the geometrical parameters of the mill. By exploring the relationship between the model created for the milling process taking place in the planetary ball mill and the milling parameters depending on the mill, and using the calculations executed, data more authentic than previous ones can be obtained on the energy transferred to the mill product during the milling process, and on the efficiency of milling. This information provides a more plan able mechanical milling for researchers decomposing materials in planetary mills, and for specialists dealing with the improvement and application of these technologies.*

## Keywords

high-energy planetary ball milling, energy transfer

## 1. Introduction

Nowadays, there are several possible solutions for producing nano-structure materials using conventional and/or newly developed technologies of material science. During these processes the size, structure, composition, and morphological characteristics of “grains” and/or “phases” can be altered with the aimed selection of technological parameters. Possible ways of production include mechanical milling having been applied for decades in the production of powder materials. The improvement results of different type mills (e.g. the possibility of higher energy input) have made it possible by now to produce nano-crystalline powders by mechanical milling. However, it is inevitable to have adjustability more accurate then before, for purposive milling and the quality insurance of products intended to be produced by milling.

During the milling process (fig. 1.) carried out in the planetary mill, the impact velocity and the angle of impact has a significant effect on the energy transferred to the powder particles to be milled by the flying ball. Consequently, the

movement and impact of the balls are important factors, on the inspection of which thorough mathematical studies have been carried out.

According to Lü and Lai the greater the angular velocity of the sun disk, the greater the increase in the impact velocity as the detachment velocity of the balls increases and the flying time shortens. This impact velocity is an important parameter, which determines what energy acts upon the powder particles during the mechanical milling.

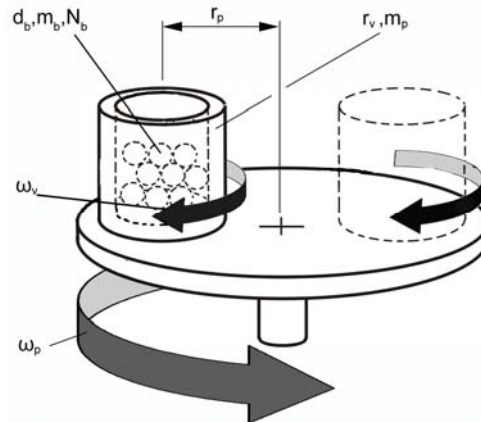


Figure 1. Process parameters of the planetary ball mill

$d_b$ : the diameter of the balls,  $m_b$ : the mass of the balls,  $N_b$ : the number of the balls,  
 $r_p$ : the distance between the rotational axes,  $r_v$ : the radius of the vial,  
 $m_p$ : the mass of the powder,  $\omega_v$ : the rotational speed of the vial,  
 $\omega_p$ : the rotational speed of the sun disk

Besides and before Lü and Lai, several authors and studies had already dealt with determining the energy transferred by the balls to the material to be milled. The study of Burgio et al. has been considered initial basis for many when determining the impact velocity of the ball and the energy transferred to the powder. Analyzing the above studies it can be stated that when determining the detachment angle and the detachment velocity they do not take into consideration forces resulting from *relative movements* (e.g. Coriolis force). Impact energy is described as the difference between the kinetic energy calculated for the moment of detachment of the ball and the velocity of the ball after the impact. No information is given on determining the location of the impact. Although, they give data of exact (measured) speed and detachment angle for a certain setup of mill type Pulverisette P5 and different ball sizes, but they provide no calculated impact energy.

P. Le Brun et al. published another relationship on determining the detachment angle of the milling ball, and they highlight the importance of the speed rate (ratio) between the sun disk and the vial, which influences the trajectory of the balls, and even the amplitude and ratio of the impact and

friction energy, which can be transferred to the material to be milled. In their study, Abdellaoui and Gaffet present the change in impact energy and power related to the angular velocity of the sun disk primarily in connection with planetary mills types G5 and G7 (but also for other milling devices) however, they do not give their calculation relationships. In another study relying upon the work of the above mentioned Burgio et al. they present calculation correlations for determining the impact energy, but no information is found on the location of the impact, furthermore, they do not take forces resulting from relative movements into consideration either in their calculations. Magini et al. give a simplified correlation for determining impact energy in their study, and they focus on inspecting the collision between the ball and the material to be milled. Iasonna and co. Magini in one of their studies examined energy transfer and power consumption during the milling process. They measured electric and mechanical power consumption on a Fritsch P5 milling device. During milling Fe-Zr powder they examined the influence of the number and size of balls, and that of the quantity of powder filled-in on the power consumption.

Several researchers have already dealt with modelling processes taking place in the planetary ball mill (Fritsch P4) used during our work, however, literature dealing with the relationship between the milling parameters regulating the process and the energy transferred to the material to be milled is incomplete. Taking this fact into consideration, it is reasonable to further clarify processes taking place in the planetary ball mill, and a more accurate exploration of the influence of some important milling parameters.

## 2. Kinetic modelling of a planetary ball mill

The description of forces acting on the milling ball in the planetary ball mill is based on the study of Lü and Lai. After a verification the calculation mentioned can be used as an initial point for the model intended to be established.

Our contributions concerning the kinetic modelling of the mechanical milling process of the planetary ball mill was started with the following statements and simplifying assumptions:

- a) the milling ball can detach from the wall of the vial, when the force acting upon it, pointing towards the radius of the vial is zero,
- b) the new junction point of the ball and the vial acts as a point of impact, disregarding the elastic impact of the ball,
- c) there is no relative movement (sliding) between the ball and the wall of the vial before the point of detachment,
- d) the resistance of the medium within the vial is neglected,
- e) any rotation of the ball is disregarded.

*Modelling steps are as follows:*

- Description of motion and force conditions
- Determining the detachment angle

- Determining the detachment velocity
- Determining the impact point
- Determining the impact velocity
- Determining the impact energy and power
- Calculating planetary ball mill working curves.

### 3. Application of the model and calculation results

Using the calculation method the milling energy values of FRITSCH P4 planetary ball mill applicable for milling experiments were determined by different configuration parameters. Different sun disk rotary speed values and ratios were taken into consideration by the calculations and at the same time the inspection of the full rotary speed range of the mill was aimed at, together with the path of motion of the balls to comply with the impact and friction method, that is  $i_{limit} \leq i \leq i_{critical}$ .

Since calculations were carried out on a given mill type, certain initial parameters were given. These were mainly the features of the device:

- distance between the sun disk and the vial:  $r_p = 0,125 \text{ m}$
- sun disk rotary speed range for test:  $n_p = 50 - 400 \text{ rpm}$

Selection of further initial values determined by us was carried out based on the equipment available for the mill:

- inner radius of the vial (80 ml):  $r_v = 0,0325 \text{ m}$
- radius of the milling ball:  $r_b = 0,005 \text{ m}$
- density of the milling ball (stainless steel):  $\rho_b = 7800 \text{ kg/m}^3$

Knowing the above determined geometrical parameters ( $r_p, r_v$ ), the extreme values ( $i_{limit}, i_{critical}$ ) of the ratio ( $i$ ) can be determined, which indirectly influence even the rotary speed of the vials together with the rotary speed of the sun disk, concerning the inspected range. Extreme values of the ratio ( $i$ ) are:

- bottom limit:  $i_{limit} = 0,96$
- upper limit:  $i_{critical} = 2,96$

Calculations using the model were carried out using values  $i = 1; 1,5; 2; 2,5; 2,96$ .

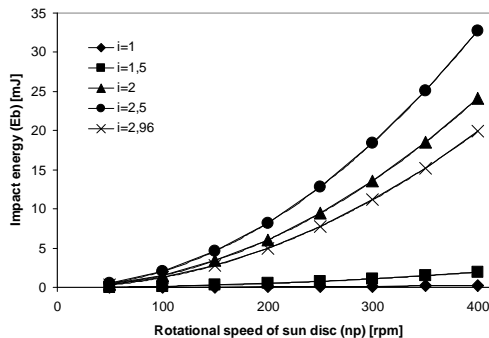


Figure 2. Change of the impact energy ( $E_b$ ) as a function of the sun disk rotational speed ( $n_p$ ) and the ratio ( $i$ )

In the first part of the calculations, that is by the determination of the detachment angle and the detachment velocity it was found that in case of fixed geometrical conditions ( $r_p$ ,  $r_v$ ,  $r_b$ ) and ratio ( $i$ ) identical detachment angle values belong to an increasing sun disk rotational speed, while the value of the detachment velocity increases in ratio with the rotational speed of the sun disk. After calculating the impact angle and velocity, the theoretical impact energy values belonging to the different sun disk rotational speed values were determined using the relationships of the previous subsection, for a single ball. The calculation results are shown on fig. 2.

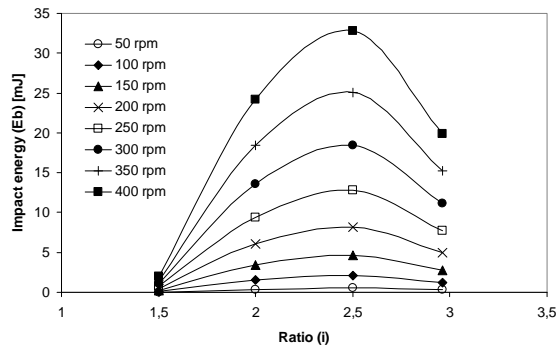


Figure 3. Changes of the impact energy ( $E_b$ ) as a function ( $E_b(i)$ ) of increasing the ratio ( $i$ ) by different rotational speeds values ( $n_p$ )

It can be seen in fig. 2. that by increasing the rotational speed of the sun disk, the value of the impact energy increases squared up to a certain ratio. It can be seen that by  $i=2,96$  speed ratio the curve of the impact energy is between the curves  $i=1,5$  and  $i=2$ . This results in that probably there is an optimal value between the values  $i=2$  and  $i=2,96$ , where the impact energy is the greatest possible. This assumption is verified by the set of curves shown on fig. 3. The curves indicate the change of the impact energy by increasing the ratio, belonging to different rotary speed values of the sun disk. Looking at the diagram it can be found that by given geometrical conditions and configured parameters, the greatest impact energy can be achieved by approximately  $i=2,5$ . If the impact frequency of the balls can also be taken into account, which is mainly the function of the detachment and impact angles, then the power of the milling process can be determined.

When inspecting theoretical power values belonging to different sun disk rotational speed values and velocity rates (fig. 4.), it can be found that greater and greater power values belong to increasing rotary speed values. The curves calculated are cubic ones.

In opposition to the changes of the impact energy shown in fig. 2., it can be observed on fig. 4. that the values of the curve belonging to  $i=2,5$  are lower than those belonging to  $i=2$  and  $i=2,96$ . The result is surprising as lower power

belongs to a velocity ratio causing the greatest impact energy. This can be explained by the fact that in the case of this ratio ( $i=2,5$ ) the impact frequency is lower, that is the balls spend more time on the wall of the vial.

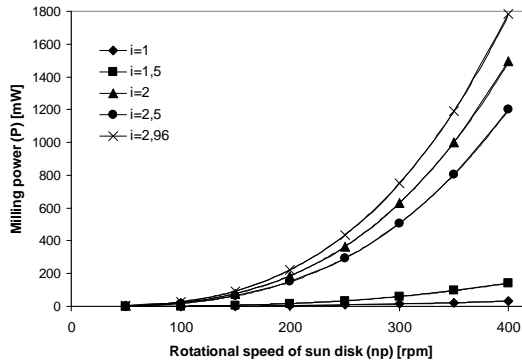


Figure 4. Changes of the milling power (P) as a function ( $P(n_p)$ ) of the sun disk rotational speed ( $n_p$ ) and the ratio (i)

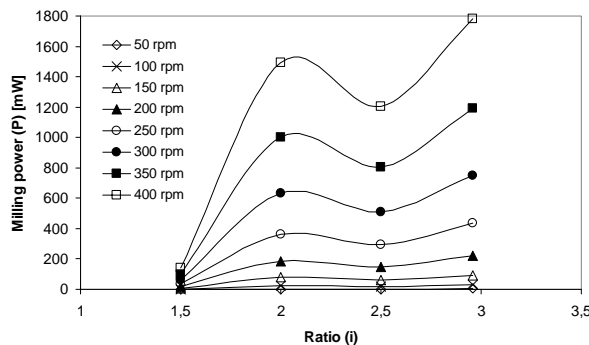


Figure 5. Changes of the milling power (P) as a function ( $P(i)$ ) of increasing the ratio (i) at different sun disk rotational speed values ( $n_p$ )

If the milling power is represented as a function of the ratio, at different sun disk rotary speed values (fig. 5.), then the optimum velocity rate from the aspect of milling power can be determined. On fig. 5. this is around the value  $i=2,96$ .

Using fig. 9. and fig. 5. such an optimum range of ratio can be highlighted, which is maximal from the aspect of both the impact energy, and the milling power. This range, by the above determined geometrical parameters, is without doubt near  $i=2$ .

The calculation results of the model we have established were determined for given initial parameters, demonstrating the applicability of the method, it is still suitable in case of arbitrarily selected other configuration and geometrical parameters for characterizing the milling process in a planetary ball mill.

### *Effects of the size changes of the milling ball and the vial*

The above described results were determined by fixed ball and vial sizes. In order to inspect the effect of the size changes of the milling set (ball, vial) on the impact energy and power, further calculations were carried out.

First only the size changes of the vial were inspected by the same ball size, then the size of the ball was increased, and the size of the vial remained unchanged, and finally, both the ball size and the vial size were doubled.

The calculation results well demonstrate and reflect the impact energy increase expected. The results show that the increase in the vial size does not have such an effect on the increase of the impact energy, as the change of the ball size. By increasing the size of the milling set (ball, vial) together results in the greatest impact energy.

Increasing the dimensions of the milling set undoubtedly results in the increase of the milling power, however, this change is not of such degree as in case of increasing the impact energy. This is even proved by table 1. comparing the calculation results.

*Table 1.* Results of the calculations inspecting the effects of ball and vial size

	simple vial and ball size	double vial size	double ball size	double vial and ball size
Impact energy [mJ]	24	76	236	332
Impact energy increase in per cent [%]	100	315	978	1375
Milling power [mW]	1494	1943	5626	6760
Milling power increase in per cent [%]	100	130	377	452

## **4. Summary**

A calculation method was introduced above on determining the performance of a planetary ball mill. In chapter 2 the calculations of Lü and Lai were used as a starting point. Calculation results described in chapter 3 were determined and shown on a certain type of mill (Fritsch Pulverisette 4) and given geometrical conditions, but the model can be used for any planetary ball mill, observing the marginal conditions we have also indicated.

As a summary, it can be stated on the effect of the sizes of the milling ball and the vial on the impact energy and power, that if further milling sets are available, then using those may help gain further energy from our planetary ball mill (by the same sun disk rotary speed and ratio), increasing the efficiency of milling and decreasing the time of milling.

Based on the calculation results and the charts (fig. 3. and 5.) an optimal mill configuration can be defined, which provides for the most effective work from the aspect of the milling task. In this way, for example in case of milling certain

materials, smaller impact energy can also make fast work possible, protecting the milling set and the loading of the mill.

## 5. Acknowledgement

The authors are grateful for the financial support of NKTH (National Office for Research and Technology) regarding the support of the NKTH/3A/004/2004 project, and OTKA grants K73776 in Hungary.

## References

- C. Suryanarayana, *Non-Equilibrium Processing of Materials*, Pergamon Press, Amsterdam, 1999.
- C.C. Koch, The synthesis and structure of nanocrystalline materials produced by mechanical attrition: a review, *Nanostructured Materials* 2 (1993) 109-129.
- J.S. Benjamin, *Mechanical Alloying*, *Scientific American* 234 (1976) 40-49.
- P.S. Gilman, J.S. Benjamin, *Mechanical alloying*, *Annual Review of Materials Science* 13 (1983) 279-300.
- B.S. Murty, S. Ranganathan, *Novel materials synthesis by mechanical alloying/milling*, *International Materials Reviews* 43 (1998) 101-141.
- T.H. Courtney, *Process modeling of mechanical alloying*, *Mater. Trans. JIM* 36 (1995) 110-122.
- T.H. Courtney, D. Maurice, *Process modeling of the mechanics of mechanical alloying*, *Scripta Mater.* 34 (1996) 5-11.
- Gy. Kakuk et al., *The influence of high-energy ball milling parameters on the traditional W-type Ba-hexaferrite properties*, *Materials Science Forum* 589 (2008) 397-402.
- P.Le Brun et al., *The modelling of the mechanical alloying process in a planetary ball mill: comparison between theory and in-situ observations*, *Materials Science and Engineering A* 161 (1993) 75-82.
- J. Raasch, *Trajectories and impact velocities of grinding bodies in planetary ball mills*, *Chemical Engineering & Technology* 15 (1992) 245-253.
- M. Abdellaoui, E. Gaffet, *The physics of mechanical alloying in a planetary ball mill: mathematical treatment*, *Acta Metall. Mater.* 43 (1995) 1087-1098.
- L. Lü, M.O. Lai, *Mechanical Alloying*, Kluwer Academic Publishers, Massachusetts, 1998.
- N. Burgio et al., *Mechanical alloying of the Fe-Zr system, Correlation between input energy and end products*, *Il Nuovo Cimento* 13 (1991) 459-476.

- 
- M. Abdellaoui, E. Gaffet, A mathematical and experimental dynamical phase diagram for ball-milled  $\text{Ni}_{10}\text{Zr}_7$ , *Journal of Alloys and Compounds* 209 (1994) 351-361.
- M. Magini et al., Ball milling: an experimental support to the energy transfer evaluated by the collision model, *Sripta Mater.* 34 (1996) 13-19.
- M. Magini, A. Iasonna, Energy-transfer in mechanical alloying, *Mater. Trans. JIM*, 36 (1995) 123-133.
- A. Iasonna, M. Magín, Power measurements during mechanical milling. An experimental way to investigate the energy transfer phenomena, *Acta Mater.* 44 (1996) 1109-1117.

## Re-constructions with engineering polymers

Otto EBERST, Sever POP

North University of Baia Mare, Faculty of Engineering

Gábor KALÁCSKA, Róbert KERESZTES

Szent Istvan University, Faculty of Mechanical Engineering

### Abstract

Engineering plastics are more often applied in industrial systems, where moving parts are subjected to severe friction and wear processes, furthermore chemical- and mechanical effects mean extra load. Compared to metals engineering plastics are used because of their good mechanical, chemical and tribological together with increased corrosion resistance and vibration damping ability. There are many sorts of technical polymers available, of which machine elements can be produced. To choose proper polymers for a given engineering application is not a simple task owing to many different parameters influencing the performance of a polymeric working element. We made some new re-constructions enhancing the advantageous material properties for a given applications. The new solutions apply machined parts made of semi-finished engineering plastics (rod, plates). At this article we show some interesting solutions mainly done from cast polyamide 6.

### Keywords

re-construction, engineering polymers, machined parts, cast polyamide 6

### 1. Solutions



Support pad of automotive crane jib, made of cast polyamide 6, replacement of bronze



Mill for fruits. Milling drums and gears are made of cast polyamide 6.  
Original parts were made of steel



Cast polyamide 6 bolts (male- female) for fixing filtration textile



Cast polyamide 6 V-belt pulley for circular saw. Earlier steel was used.



Spherical bushing made of cast polyamide 6.  
Replacement of fast wearing POM C bushing.



Cast polyamide 6 rollers of moving gates. Originally steel was applied.



Polyamide 6 pulley for flat-belts. Cast iron and wood was applied formerly.



Airport transporting belt: support wear pad, made of UHMW-PE HD 1000.  
Formerly steel and other polymer was applied.



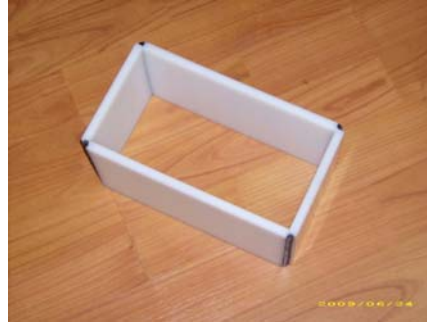
UHMW-PE HD 500 material, a part of bread slicer. Originally CrNi steel was applied.



Regulating rollers in wood processing machine, made of cast polyamide 6. Earlier steel was applied.



Wearing leg-support of food processing machine, made of cast polyamide 6. Formerly steel was used.



Casting mould, frame, in milk processing. Made of UHMW-PE HD 500. formerly CrNi steel was used.

# Landing gear leg breakdown and examination

Rajmund LEFÁNTI, József JANIK, Gábor KALÁCSKA

Szent Istvan University, Faculty of Mechanical Engineering

## Abstract

A practical problem of the gear-leg support of a small airplane can occur often. The complex premature failure of the bushing – mechanical fatigue and surface wear phenomena - caused the breakdown. To establish the proper reconstruction design we completed many data registering measurements with a real airplane in landing- and take-off, as well as flying and taxi mode. Knowing the vibration and displacement values we set the real modelling conditions. Beside the tri-axial vibration acceleration measurements we designed a bench test model for further laboratory modelling of the possible construction versions. Before the laboratory bench testing FEM analyses supported the reconstructions, for which we applied some new polymeric materials, too.

## Keywords

acceleration measurement, tribology, reconstruction

## 1. Introduction

The engineering plastics gain ground on many areas of transportation. This evolution also plays role in aerotechnics. The „ultra light structures” conception is prevailing concerning not only the large aircrafts and rocket-propelled fighters, but the small airplanes, too. With maximum concern of safety, the renovation with reconstruction is evolving regarding the civil engaged small airplane in case of the simple machine parts. First, main areas of this are the rubber/steel combinations, sealings, mechanical damping elements. At this field of that more Hungarian license was also born.

## 2. Plastic applications in the aviation engineering

Plastic machine elements are often used in the aviation engineering. A special segment of the engineering activity at that field is the maintenance of single-engines or small aircrafts having some critical elements. The figure 1. shows new single-engine polymer aircraft, which is designed and built on different composite polymers. The previous releases of such a kind of planes are considered as transitions between the traditional metal-based constructions and the new composite models. That means in the age between 20 – 30 years of a

small aircraft we can already find some hardwearing, strongly loaded polymers elements.



Figure 1. Polymer aircraft

### *Plastic machine elements in small plane*

Based on the list of the elements produced in the 1960-70-years regarding the commonly used CESSNA family, we can classify the plastic applications.

- Average contact pressure (10 – 50 MPa) applications (e.g. cable sheaves coming from the civil and mechanical engineering). Mainly tough polyamides are applied for that. (figure 2. aileron, side and depth rudder plate moving rope disc)
- High contact pressure moving surfaces: typical the rolling or rolling/sliding polymer surfaces mainly mating with steels.
- Pure sliding surfaces subjected to severe dynamic impacts (e.g. slide bearings and linear supports of landing-gear leg silent block)
- Covers and housing elements (PP, PE). Typically they are not mechanically loaded but light-weight is essential for them.

It is a fact that many of the small airplanes between 20 – 30 years are still in use worldwide. Comparing the engineering materials built in those old aircrafts to the new design versions shown in figure 1. we can find some typical engineering places to be resolved or redesigned during the maintenance.

### **3. Landing-gear leg support**

Studying the register of the maintenance activities a weak point can be found at CESSNA 172 aircraft. As time goes by the reliability of the landing-gear leg support (figure 2, 3, 4) becomes critical and after a certain number of friction load the original support pad cracks and wears extremely fast. This part is considered to be important aviation safety point, nowadays we have a good engineering possibility to renew the old structure with better and higher performance engineering polymers.



Figure 2. Position of landing gear leg on Cessna 172 type aircraft

The figure 3. and figure 4. show the landing-gear leg support.



Figure 3. Landing-gear leg support in the aircraft



Figure 4. The failed PUR component

#### 4. Cases of landing-gear leg load

To examine the different load effects of the gear leg support and to follow the time function of those loads some basic data needed that can be used for FEM analyses, too. Knowing those conditions a dynamic alternating and so-called macroscopic fretting test can be launched with a tribotester built at Szent István University, Institute for Mechanical Engineering Technology.

There are four main condition categories of the operation of landing-gear support. These cases origins from the normal use of aircraft:

- Stress during taxi mode (this load is applying with an even run on ground surface of the aerodrome: bitumen, concrete, grass)
- Stress during flying mode (large “fretting”);)
- Stress during take-off (From standing to take-off momentum. Facing of the soil. The craft would run on : bitumen, concrete, grass;)
- Stress during descent (from the first touching of ground to stop that would be on: bitumen, concrete, grass.)

*Measuring system*

To register the vibration load – as a real mechanical effect of the operation – the only legal solution was to mount a vibration sensor on the gear leg surface. I applied the register of accelerations during vibration movements.

As it is shown in fig. 5 and 6. tri-axial sensors were fixed on both legs of the plane.

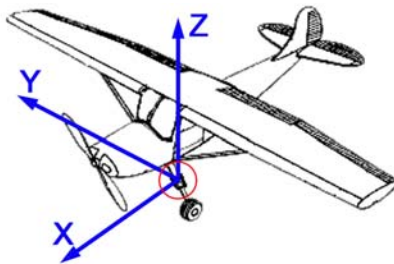


Figure 5. Loads of the unproved is tendencies



Figure 6. Acceleration sensors on the landing gear leg

The measuring system placed into the plane body during measurements consists of the followings: (Figure 7.):

- SPIDER A/D amplifier;
- laptop;
- accumulators with 12V/100Ah;
- interface adapter with 12/220V.
- tri-axial acceleration sensors on the landing gear leg.

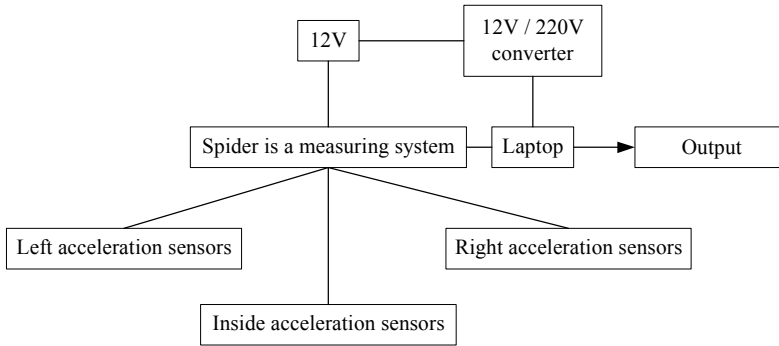


Figure 7. The schematic picture of the system

The measurements were carried out in different flying phases: during landing, take-off, taxiing and flying. The data collection was repeated 15 times in each cases.

*Results of measurements*

Some typical measured data are shown in fig. 8 and 9. The right side leg tri-axial sensors performed the graphs in “Z” direction. Fig 8. shows that the beginning of the measurement was in the flying mode (approx. 10 seconds in the air). The wheels were not in contact with the ground. After 10 seconds the touching of the grassy runway can cause high mechanical load as vibration movements of the gear leg. During the register of fig.8 graph the speed was about 30 m/s.

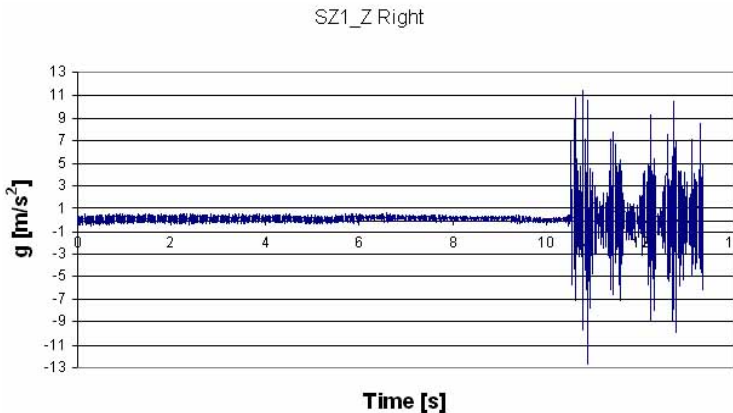


Figure 8. Right side landing gear leg z direction vibrations: flying-landing.

In fig. 9. the landing process can be monitored. First moments of touching the ground cause near “10xg” acceleration. As slowing down a damping effect of the airplane body can be monitored. The basic waves of the acceleration function are generated by the uneven surface of the soil/grass, but the decreasing tendency of “g” values is due to the decreasing speed and mechanical damping.

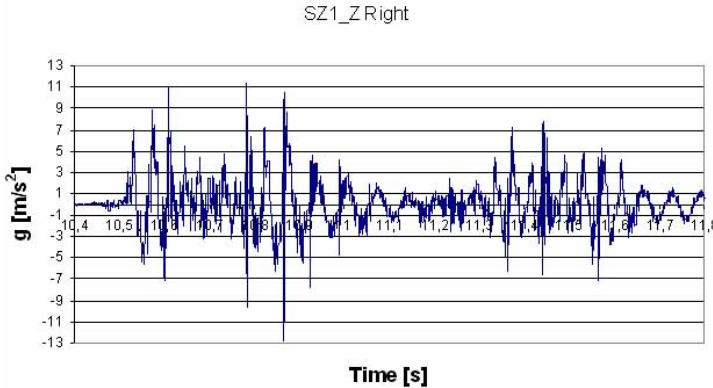


Figure 9. Right side landing gear leg z direction vibrations: landing.

*Modified bushing of gear leg*

In fig. 10. the original leg support can be seen. The steel leg – as a tubular shaft – is supported by a PUR bushing pressed in to the metal housing. The end of the leg is fixed into the plane’s body by means of bolt joints without flexible element. The real movements (vibration) of the leg in the housing are more radial than axial. Due to this effect the failure of PUR (fig.4.) is experienced caused by fatigue and friction. Knowing the relatively high friction values of PUR against steel, often there is no real surface friction in the contact area just elastic deformation with high stresses and accelerated fatigue process. The final result of those the fracture of the PUR bushing.

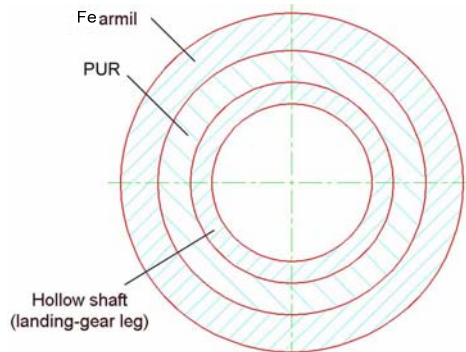


Figure 10. Section of the original underpinning

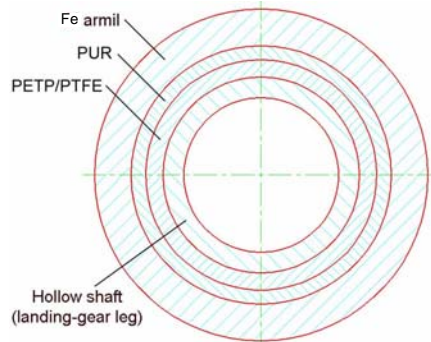


Figure 11. Section of a modified underpinning

With the modified leg's support shown in fig. 11, the high vibration stress level is reduced. By means of an internal PET/PTFE composite bushing the small oscillatory movements are guided into the real friction because of the low PET/PTFE/Steel friction and wear rate. The PET/PTFE ring is bedded into a flexible PUR ring. Those together are pressed into the steel housing. In that way a complex material model works against the operating load.

To prove the applicability of the new construction a laboratory test project is launched.

## 5. Tribology modelling of the constructions

Taking the vibration effects into account, we designed a laboratory modelling system. That model (fig.12) performs oscillatory movements when the acceleration, the normal load, the amplitude and frequency of the movements can be adjusted.

Set of the test inputs:

The already shown acceleration extremes are discovered by the real operation measurements and "10xg" acceleration is fixed as real top value. Also the frequency range can be established from the graphs.

The mechanical load effects can be calculated and put into the FEM model together with the material laws determined by measurements. The FEM model of the constructions gave the real deformations as the possible values of the amplitude of the movements.

The experimental setup of the reciprocating laboratory testrig can be seen in fig.12. The reciprocating sliding friction is created by a standing pin material sample, which has a relative motion against the reciprocating grinded steel plate in conformal contact. The tested material sample (pin) is fixed to the specimen holder. The oscillating motion of the steel plate (0 – 23 Hz) is provided by a controlled variable speed electrical motor through an eccentrically power transmission for the adjustment of the stroke. The tested steel plate is fixed to the moving steel plate holder that is supported by a roller guide way. The friction

force is measured during the movements. The testrig is equipped with a manual loading system, which consists of the weights and the loading frame. The normal displacement of the pin specimen towards the steel plate, as a result of the wear and deformation, could be measured by a contactless sensor. The pin has a diameter of 8 mm and length of 15 mm while the steel mating plate sizes is to maximum 80 mm – 150 mm. The loading system provides different normal loads: from 48 to 580 N. The possible maximum of acceleration can be set is „42xg.”

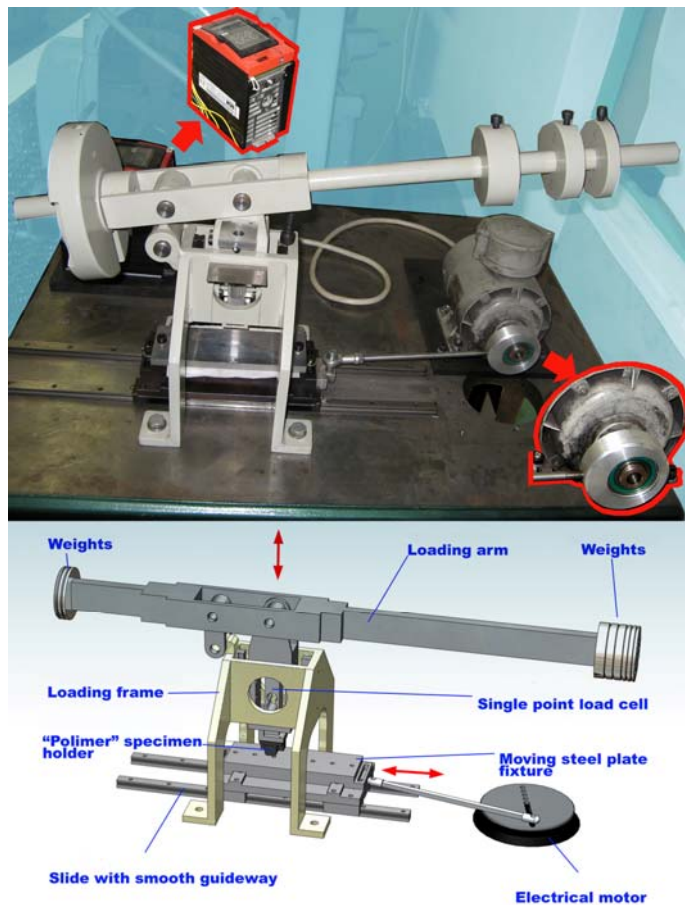


Figure 12. Upright cylinder on plate test rig

By means of the test system the different pin samples – three different PUR versions, PETP/PTFE, and PETP/PTFE/PUR combination – can be tested under the preliminary determined conditions (real airplane acceleration measurements and FEM model).

The measurements are in progress now.

---

## References

Antal, Gy. – Fledrich, G. – Kalácska, G. – Kozma, M.: Műszaki műanyagok gépészeti alapjai, Műszaki műanyagok gépészeti alapjai, Minerva-Sop Bt. Sopron, 1997

Zsidai, L. et al. (2002): The tribological behaviour of engineering plastics during sliding friction investigated with small-scale specimens, *Wear*, Vol. 253 673-688. p.

<http://index.hu/kultur/eletmod/balloszog/> Repülőgyár a homokbuckák között 2005. 07. 16.

[www.quattroplast.hu](http://www.quattroplast.hu)

# **Developing directions and utilization technology of cooling-oiling liquids from environmental effects**

Attila KÁRI-HORVÁTH, István VALASEK  
Szent Istvan University, Faculty of Mechanical Engineering

## **Abstract**

This article is about some environmental effects of cooling/lubricating materials and suggests some potential development directions of the application technologies. The construction of the emulsol is also introduced. The technology of the emulsion demolition, with a special care about the emulsion demolition with inorganic acids and inorganic salts is highlighted. Regarding cooling/lubricating materials, key expressions are: the polluting and health damaging effect, storage and transport, too. We present the developing directions of cooling lubricating technologies.

## **Keywords**

cooling/lubricating, emulsol, environmental, application technology

## **1. Introduction**

Cooling-oiling liquids (COL) are special subsidiary materials primarily used for metal-working –chipping and forming. These are named subsidiary materials, as the role of COL-s in working is indirect, therefore they can't be found in the outcome.

In the case of several procedures cooling effects of machine-oil wasn't sufficient, for this reason a fluid needed to be found that still has satisfactory oiling effect, but it also has a significantly better cooling effect than oil.

Among a lot of developing directions usage of water seemed to be the most obvious solution (a cheap material), which has approximately four-times better cooling effect than oils, however its direct oiling-effect is marginal and its suitable temperature area is narrow. Only one solution remained: if you mix water with oil, depending on mixing ratio you can have a compound having an optimal oiling, cooling and cleaning effect.

Emulsion is qualified as a dangerous chemical material, so its usage and the use of the out of used is ruled by the Chemical Safety Law (2000.year XXV. law) a 44/2000 (XII.27.) EüE-order, and the 98/2001. (VI. 15.) Government and the 16/2001. (VII. 18.) KöM order.

## **2. Emulsion dissolving**

Emulsions become really dangerous waste, if they are handled according to our national customs (without proper attention). The main groups of known procedures are summarized in table 1.

Table 1. Possible working methods of oily emulsions and oleaginous wastewater

Physical methods	Chemical methods	Physical-chemical methods	Methods without decomposition
mechanical	with inorganic acids	floated	biological
thermal	with inorganic salts	electro-chemical floated	firing
bio ultra filtration	with organic emulgator	adsorption	deposition

Among emulsion dissolving methods we introduce decomposing method with inorganic salts and metallic salts, as these are widespread in Hungary and simultaneously this method is the most dangerous one for the environment.

*Emulsion dissolving with inorganic salts and metallic salts*

Chemical methods neutralize charge developing on the edge surface of oil-water influencing emulsions stability, as its result coagulation happens. In the simplest case- in case of pH sensitive emulsions – working with acids, reaching a certain pH value emulsion decomposes and phases divide. Acidifying is often not enough for dividing emulsions, so as a pre-division and pH setting is used, then actual emulsion dissolving happens with feeding polyvalent metallic-salts. The II. and III. value metals (Fe, Al) with their strong will cations the anionic emulgator solar proton event ensues, neutralizing the two phases surface charge. The arising acid wastewater needs to be neutralized afterwards. Neutralizing can happen either with lime cream or with sodium hydrate.

Metal ions form large surface hydroxide flakes and on these large surfaces they adsorb oil and grease coagulant to fine particles. This method is called adsorb coagulation. Similar method is emulsion dissolving with iron chloride. In terms of chemical costs this method can be considered economical, but because of the increasing noxiousness costs of oleaginous hydroxide mud produced in relatively high amount, this is becoming a more and more expensive one. The oleaginous mud occurring in relatively high amount needs to be dewatered after condensation. Dewatering can happen with filter process or centrifugalization. The remaining mud depending on its oil concentration is undamaged with firing or deposition and with biological decomposition. Although you have to consider the fact that some new big stability emulsions can't always be dissolved with this method. In case of mixed collected emulsions dissolution different characters of emulsions can be used favourably as different types of emulgator weaken stability of emulsions, which means that during storage big amount of emulsion can separate out swimming up to the surface of emulsion.

Naturally this procedure depends on other factors, too: first of all the proportion of insoluble and soluble pollution in the emulsion. You have to consider developing depot storage and motive processes of emulsions; what's more you have to help emulsions dividing into water and emulsol. With developing technical equipments, using coalescences separator (fig.1.) and skimmer (fig.2.), as well as making use of gravitational force intensity of

separating oil and water can be increased. When at least two major quality of emulsion is not suitable for requirements it is considered to be incapacitated and replaced. The replaced emulsion is stored, and then it is decomposed locally or in a central decomposer.

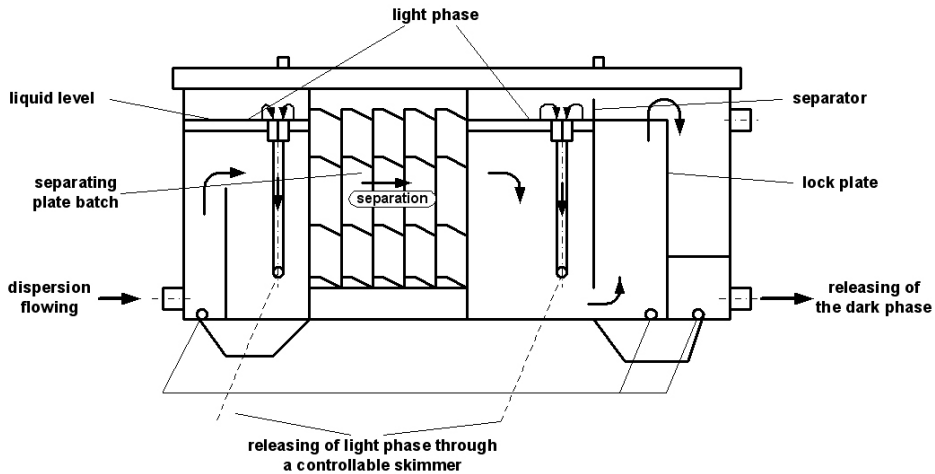


*Figure 1. The coalescences separator*

*The operation of the coalescences separator:*

Emulsion is installed into the separator where a guide vane changes the direction of current of the material in the contrary direction with gravitation. The light part of oil phase granulates significantly and it is led out through a controllable skimmer. The dark phase is guided towards through a baffle, meanwhile crushing of the roughen grains starts. Again two phases separates gradually: a fine one and rough one. The fine phase can be guided towards with a skimmer again, the darker and darker black phase flows towards through a baffle, and then it leaves the system through a releaser. The emulsion collected this way, which contains about 15-20% water, mixing with emulsol can be used for setting in concentration, if it is clean enough and doesn't contain foreign oil. This equipment needs to be often cleaned, yet it is easy to fulfil as built-in elements can be simply pulled out.

*Working of the skimmer:*

Skimmer is used for continuous removing of foreign oil or emulsion separating from emulsion floating on the liquid surface. On one hand the skimmer's effect is based on oils and oleophilic materials, on the other hand different adhesion power in water. Disk and ligamental skimmers are spread in practise. (fig.2.). The material of disks and bands is oleophilic carrier, onto which oil grains lay on during moving. From skimmer disk a pulling-down, from skimmer band two pressing rollers send the stuck oil away before it dives into liquid again.

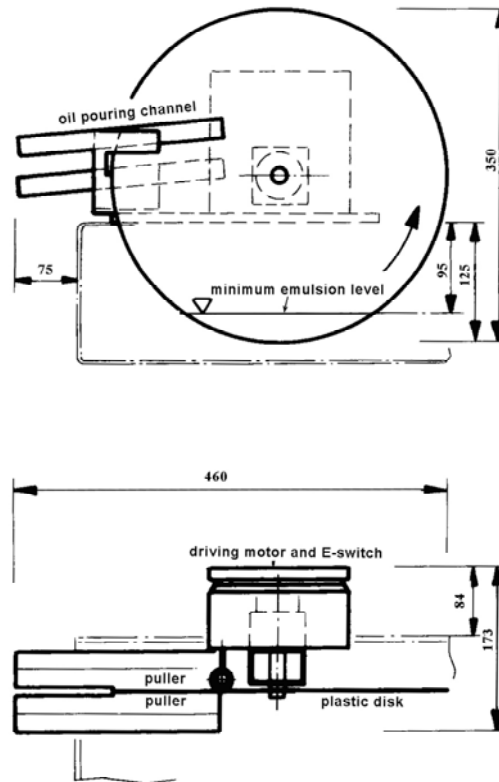


Figure 2. Operation of skimmer

### 3. Environmental and health harm of emulsions

The 98/2001 (VI.15.) Governmental regulation and the 6/2001 (VII.18.) KöM order considers emulsions dangerous waste therefore they need special usage. The problem is that firms specialized for carrying and destroying refuses oil charges a very high price for this work. So we often have to face the fact that used emulsion is poured into sewage system illegally as the stronger influence of environmental protection an environmental technology has been started, with the help of this the amount of generated dangerous waste can be decreased.

Workers' skin working with machine tools gets into contact with COL to a certain extent. COL doesn't cause any rashes or illnesses on healthy uninjured skin. Workers often clean their hands with cloth polluted by steel wool or grinder dust, in these cases sharp metal particles harm cuticle of the skin where COL can get under the skin (subcutaneous injection), where it causes inflammation. The way of contact and possible harmful effects of COL and workers are introduced in the following. The way of contact can be:

- **through air:** in form of fog, mizzle, steam, and aerosol (harmful effect: eye irritation, respiratory irritation, allergy, chemical lung cancer, illness of the digestive system)

- **direct contact:** With COL and/or solid surface covered with COL. (harmful effect: eye irritation, skin irritation, skin illness e.g. allergic eczema, toxic degenerative contact eczema, skin-cancer, etc.)

Healthcare of workers connected to COL can be totally solved by hygienic planning. In case of machine tools emulsion, as a two-phase disperse system, softens paint covering, which blisters as a result. The blistered paint covering becomes crackled, water phase penetrates through rifts and on the metal surface it calls a very intensive corrosion layer into being. As volume of oxidised metal is bigger sooner or later it forces the paint up. This phenomenon goes on still total paint covering disappears.

In case of chip shaping –if not fog lubrication is applied- oil fog allowed above the permitted level doesn't develop. In such chipping workshops where large amount of emulsion or diluted solution of COL is used you can count on emulsion-fog development. It's derived from the fact that heat of water vaporization is more than ten times higher than oil's and emulsions always contain some dissolvers as instant additive or carried in with emulgator. We can especially count on with large oil fog, if average temperature of emulsions exceeds 60-Celsius degrees, where vaporization of water becomes more intensive (development of secondary air polluting effect). Emulsion-fog is vapour, mixture of light hydrocarbon components and dissolvers inhaling, which can lead to mucous membrane injury, sickness and paint (chemical pneumonia).

Oil drips smaller than 0,5  $\mu\text{m}$  are less dangerous, as they aren't able to stick to throat and lung surface, namely at exhalation they get back to atmosphere. Oil fog concentration of air MK is allowed to be (maximum work concentration)  $<5 \text{ mg/m}^3$ . (25/2000.(IX.30.) EüM-SZCSM order). Used emulsions are produced in about 93 000  $\text{km}^2$  in the whole country, often they are made to travel several times, therefore intensive soil pollution is inevitable. Because of water component water emulsions can get into soil very deeply, where they can accumulate.

#### **4. Storage, transportation and demolition of emulsions**

You have to take care of component storage. Let's see e.g. water. Factories buy quality water for producing emulsions, they transport it in, use it, then emulsions are transported into a separator, where they are separated by some environmental-polluting acid technology, the received water, with the help of an adsorption coagulation technology, is freed from the finely dispersal oil and grease particles to make is equal to 28/2004.(XII.25.) KvVm order of wastewater release demand then it's poured into channels. Hydroxide mud remaining in the last activity is extremely harmful and its undamaging cost is so high that's just unpayable.

In the country approximately 100000 tons of used emulsions are produced a year, which are carried several times on the country road, during usage quality changes are continuously checked with more and more expensive equipment, are

separated by some expensive and environmental polluting technology, use some extra technology to make water suitable to pour into drains.

Taking these facts as a starting point we have worked out energy-saving distillatory equipment for water-regaining in the place of emulsion utilization, with the help of which from used emulsion we can distil water locally, which as a pre-treated component could be reused for emulsion making. With this technology, 17% emulsion and handling costs of present component part price would decrease with a third, to about 6%.

## 5. Developing directions of COL usage technology

### „Recycling” emulsion handling technology

The essence of new type emulsion handling technology (fig.4.) is, that with developing an emulsion supply system we can ensure emulsion stability without any special intervention. With this vulnerability of emulsion decreases yet keeping steady productivity. We have to redefine lifespan of emulsions, which isn't from infusing them into machines to removing but continuous. So lifespan isn't to be determined by producing technology but usage time calculable from material scales. This makes possible leaving the so far separately employed –in many instances distant from utilization place – mainly chemical separation and in the place with continuous, economical discharge of water expropriation we can get back 92-98% water of emulsion, as a valuable component. New technology ensures for materials not to go through the factory but circulate in it considering to possibilities.

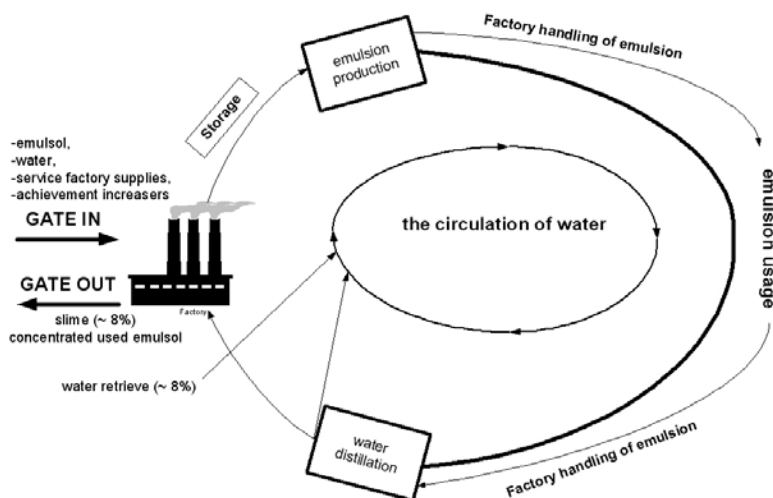


Figure 3. „Recycling” technology conceptual picture

Elements of „RECYCLING” technology:

- accepting tank with 800-1000  $\mu\text{m}$  and 100  $\mu\text{m}$  sieve filter
- prehandling tank with coalescence separator
- clean tank
- serving daily tank, in which you have to ensure technical level identity of emulsion for decomposition...

Quality requirements of emulsions for separation are the following ones:

- emulsion has to be unified, its mechanical pollution is 0,2 %
- air inclusion free (air inclusions spoil heat utilization)
- quantity of mechanical polluters is under 1  $\text{g}/\text{cm}^3$  and their size is bigger than 0,5  $\mu\text{m}$
- material composes and their components can't be connected to water
- particles connected with secondary chemical bindings have more or less continuous but decreasing repelling strength
- emulsion fed into the regainer to be an incoherent emulsion system, without exudation of disperse phase on its heat-changing wall.

#### *Development of new sliver separating technology*

Among developing directions going on at present MQL lubrication is a direction which introduction we can reach significant and instant results, but its real value is given by the fact that it's one of the factors of quantum leap change in mechanical engineering technology we are facing in some year's time. With MQL lubrication minimizing lubricators besides saving lubricator prices, caring time of work piece, implement, and machine tool can be decreased significantly. Generally speaking we can say that MQL lubrication can be used successfully at present, where producing technology can be optimized by ruled and local cooling, besides increased profitability and decreased environmental burden. Results of this new developing direction make creating new chipping technologies necessary. Target programme of my in hand PhD dissertation is getting up such chipping technology. The new chipping technology ensures simultaneously efficiency of chipping and minimizes harmful environmental effects. Tests are going on – Szent István University, Mechanical Engineer Faculty, Engineering Industry Technological Institution -, where special attention is given to MQL lubrication and reduction of environmental effects, which is realizable with combining the well chosen MQL lubricator.

#### **References**

- Bartz W. J.: és 70 szerzőtárs: Kühlschmierstoffe und Zerspannung, Renningen-Malmsheim: expert-Verlag, 2000
- Valasek I., Tóth I.: Megmunkálás tribológia, Tribotechnik Kft., Budapest, 2003. p.156-159.
- Valasek I.: Tribológiai kézikönyv, Tribotechnik Kft. Budapest, 1996.

- 
- Valasek I., Kári-Horváth A.: Az üzemi emulziókezelési technológia felülvizsgálata és fejlesztési irányának meghatározása – Gépgyártás XLVII. Évfolyam, 2007. 5.szám (I. rész) p. 18-25
- Valasek I., Kári-Horváth A.: Az üzemi emulziókezelési technológia felülvizsgálata és fejlesztési irányának meghatározása – Gépgyártás XLVII. Évfolyam, 2007. 6.szám (II. rész) p. 26-33.
- Valasek I., Kári-Horváth A.: Az üzemi emulziókezelési technológia felülvizsgálata és fejlesztési irányának meghatározása – Gépgyártás XLVIII. Évfolyam, 2008. 1-2. szám (III. rész) p. 53-59.